NASA CR-54757
VIDYA NO. 201

GPO PRICE $ _____

CFSTI PRICE(S) $ _____

Hard copy (HC) 6.00

Microfiche (MF) 1.50

ff 653 July 65

ANALYTICAL AND EXPERIMENTAL STUDY OF ABLATION MATERIAL FOR ROCKET-ENGINE APPLICATION

by

R. A. Rindal, D. T. Flood, and R. M. Kendall

prepared for

NATIONAL AERONAUTICS AND SPACE ADMINISTRATION

CONTRACT NAS 7-218

FACILITY FORM 602

N66 28545 (ACCESSION NUMBER)

287 (PAGES)

CR-54757 (NASA CR OR TMX OR AD NUMBER)

(THRU) 1

(CODE) 28

(CATEGORY)

VIDYA

A DIVISION OF Itek CORPORATION

NOTICE

This report was prepared as an account of Government sponsored work. Neither the United States, nor the National Aeronautics and Space Administration (NASA), nor any person acting on behalf of NASA:

A.) Makes any warranty or representation, expressed or implied, with respect to the accuracy, completeness, or usefulness of the information contained in this report, or that the use of any information, apparatus, method, or process disclosed in this report may not infringe privately owned rights; or

B.) Assumes any liabilities with respect to the use of, or for damages resulting from the use of any information, apparatus, method or process disclosed in this report.

As used above, "person acting on behalf of NASA" includes any employee or contractor of NASA, or employee of such contractor, to the extent that such employee or contractor of NASA, or employee of such contractor prepares, disseminates, or provides access to, any information pursuant to his employment or contract with NASA, or his employment with such contractor.

Requests for copies of this report should be referred to

National Aeronautics and Space Administration
Office of Scientific and Technical Information
Attention: AFSS-A
Washington, D.C. 20546

NASA CR-54757
VIDYA No. 201

VIDYA COPY NO. 24

FINAL REPORT

ANALYTICAL AND EXPERIMENTAL STUDY OF ABLATION MATERIAL FOR ROCKET-ENGINE APPLICATION

by

R. A. Rindal, D. T. Flood, and R. M. Kendall

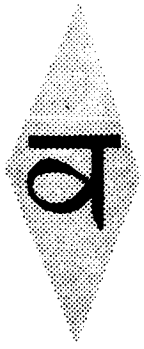
prepared for

NATIONAL AERONAUTICS AND SPACE ADMINISTRATION

May 15, 1966

CONTRACT NAS 7-218

Technical Management
NASA Lewis Research Center
Cleveland, Ohio
Liquid Rocket Technology Branch
Erwin A. Edelman



VIDYA

A DIVISION OF Itek CORPORATION

1450 PAGE MILL ROAD • PALO ALTO, CALIFORNIA
TEL: DAVENPORT 1-2455 TWX: 415 492-9270

The technical program described in this report was conducted by the Thermodynamics Department of the Vidya Division of Itek Corporation. Since completion of the program that portion of Vidya's thermodynamics capability associated with this study has been transferred to the Aerotherm Corporation, Palo Alto, California.

ACKNOWLEDGMENTS

The authors express their appreciation to the many individuals who have contributed to this study. In particular, the efforts of Vidya staff members M. W. Rubesin, R. W. Higgins, J. W. Schaefer, and P. A. McCuen are gratefully acknowledged. In addition, the many helpful suggestions of NASA technical managers D. Bachkin and E. A. Edelman are gratefully recognized.

ABSTRACT

28545

A combined theoretical-experimental program has been conducted for the purpose of developing techniques for rating the performance of ablative materials in liquid-propellant rocket engines. The theoretical studies resulted in the development of a computer program for characterizing the response of charring ablation materials in high temperature, chemically reactive environments of arbitrary chemical composition. The experimental investigations resulted in the successful modification of an arc-plasma generator so that it would operate with the necessary gases and at the conditions requisite to achieving simulation of ablative-material response in two liquid-propellant environments, namely, O_2-H_2 and N_2O_4-N_2H_4/UDMH.

SUMMARY

A combined theoretical-experimental program has been conducted for the purpose of developing techniques to rate the performance of ablative materials in liquid-propellant rocket-engine environments. A theoretical technique is developed which provides insight into basic ablative-material response phenomena and enables specification of the parameters which must be duplicated in a valid ablative-material test program.

The theoretical ablation model accounts for the primary thermochemical interactions between an ablation material and its environment. The mathematical model for subsurface thermochemical response is representative of the most realistic treatment currently available to characterize energy and mass transfer in the presence of kinetically controlled organic decomposition reactions in depth. Extensive consideration is given to thermochemical interactions between an ablation material and its environment, both of arbitrary chemical composition. The strong interdependence of the ablation-material response and boundary-layer transport phenomena is indicated and the need for a coupled solution of the boundary layer and subsurface response is stressed. Approximate equations are proposed to characterize heat and mass transfer in the multicomponent, chemically reacting boundary layer with unequal diffusion coefficients of all species, and these relations are utilized to provide the heated surface boundary condition for a numerical solution of the subsurface response. The resulting coupled solution accounts for all possible chemical reactions at the ablating surface with the assumption that chemical equilibrium is achieved. The theoretical ablation model is employed to investigate the thermochemical compatibility of a number of ablation materials in several liquid rocket-engine environments, and to make predictions which are compared to measured ablation data. The predicted ablation rates for a silica-phenolic nozzle throat are in general agreement with the data except for one firing, where material accretion was observed experimentally, and the predictions for a graphite-phenolic nozzle throat were greater than those observed experimentally by a factor of 5. The discrepancy is attributed either to the role played by chemical kinetics between the carbonaceous surface and oxygen-bearing gaseous species, or inhomogeneous boundary conditions resulting from propellant injection patterns.

The experimental investigations are directed toward developing an arc-plasma generator for testing ablative materials in a simulated rocket-engine

environment. The technique consists of arc-heating special gas mixtures and passing them through a test nozzle constructed of the ablative material. The parameters which must be duplicated to achieve experimental simulation are obtained from the theoretical considerations; they are: gas composition, enthalpy, and heat-transfer coefficient. Arc-plasma generators operating on two different principles are considered for this application: a magnetically stabilized "solenoid" unit and a gas vortex stabilized "constricted" unit. The solenoid unit was found to be suitable only for simulation of oxidation and enthalpy potential. This compromised simulation is demonstrated for one propellant system, N_2O_4-N_2H_4/UDMH. The constricted arc-plasma generator has been successfully modified to operate on the gas mixtures requisite to simulating two liquid-propellant environments, O_2-H_2 and N_2O_4-N_2H_4/UDMH.

The validity of the simulation technique was demonstrated by performing two types of verification tests, (1) measurement of the basic simulation parameters, and (2) exposure of ablative material test nozzles to the simulation environment. The basic test parameters measured were, total enthalpy, total pressure, nozzle throat heat-transfer rate, and chemical elemental concentration across the test stream. The measurements indicated all test parameters to be in the appropriate range for simulation of ablative processes in the nozzle throat. Tests of ablative nozzles further demonstrated the validity of the test technique in that uniform erosion profiles resulted and the ablation rates were observed to fall in the range anticipated for rocket-engine conditions.

TABLE OF CONTENTS

	Page No.
ACKNOWLEDGMENTS	ii
ABSTRACT	iii
SUMMARY	iv
LIST OF TABLES	ix
LIST OF FIGURES	x
LIST OF SYMBOLS	xvi
1. INTRODUCTION	1
2. THEORETICAL INVESTIGATIONS	2
2.1 Theoretical Ablation Model	2
2.1.1 Subsurface thermochemical response of charring material	6
2.1.1.1 Conservation of mass	6
2.1.1.1.1 Differential formulation of mass conservation equation	6
2.1.1.1.2 Finite-difference formulation of the mass conservation equation	9
2.1.1.2 Conservation of energy	12
2.1.1.2.1 Differential formulation of energy conservation equation	12
2.1.1.2.2 Finite-difference formulation of the energy equation	16
2.1.2 Boundary-layer transport processes	20
2.1.2.1 The differential equations of conservation for the chemically reacting multicomponent boundary layer	21
2.1.2.2 Approximate conservation equations for the multicomponent chemically reacting boundary layer in terms of parameters appropriate to an ablating material wall boundary condition	29
2.1.2.2.1 Species conservation equation	30
2.1.2.2.2 Energy equation	32
2.1.3 Coupled solution of the charring material response and the approximate boundary-layer treatment	35
2.1.3.1 Equilibrium Surface Thermochemistry Program	35
2.1.3.1.1 Basic equations of conservation at the ablating surface for chemical equilibrium	35
2.1.3.1.2 Thermochemical data for Equilibrium Surface Thermochemistry Program	39
2.1.3.1.3 Sample problem for Equilibrium Surface Thermochemistry Program	42

Page No.

2.1.3.2 Charring Material Response Program 45
2.1.3.2.1 Ablation material thermal-property data 45
2.1.3.2.2 Boundary-layer transport phenomena 46
2.1.3.2.3 Charring Material Response Program sample problem 47
2.1.3.3 Steady-state ablation 48

2.2 Material-Propellant Chemical-Interaction Studies 52
2.2.1 Material-propellant compatibility 52
2.2.1.1 Solution of the species conservation and chemical equilibrium equations 53
2.2.1.2 Energy balance solutions 55
2.2.2 Importance of particular heterogeneous reactions governing graphite ablation in the OF_2-B_2H_6 environment 57

2.3 Comparison of Predicted to Experimental Rocket-Nozzle Response 61
2.3.1 Heat-sink nozzles 61
2.3.2 Ablating nozzles 64

2.4 Summary of Theoretical Investigations 71

3. EXPERIMENTAL INVESTIGATIONS 72

3.1 Simulation Requirements 73
3.2 Experimental Approach 73
3.2.1 Simulation technique 74
3.2.1.1 Simulation gas 74
3.2.1.2 Enthalpy 77
3.2.1.3 Heat-transfer coefficient 78
3.2.1.4 Pressure 79
3.2.1.5 Simulation technique summary 79
3.2.2 Solenoid arc-plasma generator 79
3.2.3 Constrictor arc-plasma generator 82
3.2.3.1 Arc voltage 83
3.2.3.2 Thermal efficiency 84
3.2.3.3 Cathode modifications 85
3.2.3.4 Mixing plenum chamber 85
3.2.3.5 Constrictor arc-plasma generator summary 86
3.2.4 Measurement of test parameters 86
3.2.4.1 Chemical composition 86
3.2.4.2 Enthalpy 88
3.2.4.3 Pressure 89
3.2.4.4 Heat-transfer coefficient 89
3.2.4.4.1 Water-cooled calorimeter 90
3.2.4.4.2 Hot wall calorimeter 90

Page No.

3.2.5 Measurement of material response 91

3.2.5.1 Surface temperature 91
3.2.5.2 Internal temperature 92
3.2.5.3 Erosion rate 93

3.2.6 Experimental approach - summary 93

3.3 Experimental Procedure 93
3.4 Test Results 94

3.4.1 N_2O_4-N_2H_4/UDMH simulation-test series 95

3.4.1.1 Free-stream species sampling-probe test 96
3.4.1.2 Heat-transfer nozzle tests 97
3.4.1.3 Ablating nozzle tests 98

3.4.2 O_2-H_2 simulation test series 100

3.4.2.1 Heat-transfer nozzle test 101
3.4.2.2 Ablating nozzle tests 101

3.4.3 OF_2-B_2H_6 simulation attempts 102
3.4.4 Oxidation and enthalpy potential simulation 102
3.4.5 Comparison of ablation data to theoretical predictions 104

3.4.5.1 N_2O_4-N_2H_4/UDMH tests 105
3.4.5.2 O_2-H_2 test 106

3.5 Summary of Experimental Investigations 107

4. RECOMMENDATIONS 107

REFERENCES 110

TABLES I THROUGH VII

FIGURES 1 THROUGH 70

APPENDIX A - HEAT-TRANSFER COEFFICIENT EVALUATION FOR A NONABLATING SURFACE

APPENDIX B - THE ARC-PLASMA FACILITY

APPENDIX C - DISTRIBUTION LIST

LIST OF TABLES

I.- COMPARISON OF BINARY DIFFUSION COEFFICIENTS FOR VARIOUS SELECTED SPECIES AS COMPUTED BY THE PRESENT CORRELATION TECHNIQUE AND FROM KINETIC THEORY.
(a) Species typical of those encountered in the boundary layer over graphite ablating in air. Temperature = 12,000° R, pressure = 1 atm (kinetic data from method of Svehla).

I.- CONCLUDED. (b) Diffusion coefficients calculated using values for collision cross-sections suggested by Svehla (1964) which are based on the most appropriate intermolecular potential functions. Hyrogen-oxygen system, temperature = 12,000° R, pressure = 1 atm.

II.- VARIATION OF DIFFUSION FACTORS WITH TEMPERATURE.

III.- SAMPLE OUTPUT FROM THERMOCHEMICAL DATA CURVE-FIT PROGRAM.
(a) ZrO_2 liquid and solid.

III.- CONCLUDED. (b) ZrO_2 gas.

IV.- THERMOCHEMICAL DATA EMPLOYED FOR ABLATION CALCULATIONS

V.- MATERIAL PROPERTY DATA FOR COMPOSITE ABLATION MATERIALS.
(a) Graphite phenolic (32 percent phenolic, 60° and 90° fiber layup angle).

V.- CONTINUED. (b) Silica phenolic (32 percent phenolic, 60° and 90° fiber layup angle).

V.- CONCLUDED. (c) Resin decomposition gas enthalpy (h_g).

VI.- RESULTS OF MATERIAL-PROPELLANT COMPATIBILITY INVESTIGATION.
(a) OF_2-B_2H_6 environment, O/F =3.0, pressure = 100 psia.

VI.- CONTINUED. (b) O_2-H_2 environment, O/F = 4.0, pressure = 100 psia.

VI.- CONTINUED. (c) N_2O_4-N_2H_4 environment, O/F = 2.0, pressure = 100 psia.

VI.- CONCLUDED. (d) F_2/O_2-CH_4 environment, O/F = 4.0, pressure = 100 psia.

VII.- THERMAL PROPERTIES OF HEAT-SINK NOZZLE MATERIALS.
(a) 1020 Steel (ρ = 490 lb/ft^3). (b) Rokide Z (ZrO_2) (ρ = 330 lb/ft^3).
(c) Molybdenum (ρ = 639 lb/ft^3), T_{melt} = 5210° R).

LIST OF FIGURES

1.- Geometric and coordinate system for charring ablation solution.
(a) Coordinate system specification.
(b) Finite-difference representation.

2.- Comparison of exact and explicit finite-difference solution for step surface temperature at time zero.

3.- Comparison of results in charring ablation material with and without surface recession. (a) Temperature distributions. (b) Density distributions.

4.- Demonstration of the validity of the approximation, $F_i \cong m_i^{1/2} \Big/ \left(\prod_i m_i^{1/2}\right)^{1/I}$.

5.- Typical output from equilibrium Surface Thermochemistry Program for silica phenolic (68-32 percent by mass) in N_2O_4-N_2H_4/UDMH (O/F = 2.0) environment. (a) Surface temperature as a function of char recession rate with off-gas rate as a parameter.

5.- Concluded. (b) Effective wall enthalpy as a function of char recession rate with off-gas rate as a parameter.

6.- Equilibrium composition of phenolic resin gaseous pyrolysis products. Pressure = 11 atmospheres.

7.- Phenolic-resin decomposition gas equilibrium enthalpy as a function of temperature for each of three pressures.

8.- Predicted transient thermochemical response of silica phenolic (67-33 percent by mass) nozzle throat in a N_2O_4-N_2H_4/UDMH rocket engine having a 7.8-inch throat diameter and chamber pressure of 100 psia.
(a) Temperature histories for several locations in the nozzle material.
(b) Temperature distributions through the nozzle material for several times.

8.- Concluded. (c) Density distributions through nozzle material at several times. (d) Surface recession and gas generation rates.

9.- Steady-state energy equation solution for silica-phenolic material in a N_2O_4-H_2H_4/UDMH environment, comparison of results with and without equal binary diffusion coefficient assumption.

10.- Results of exact solution for transient response of slab subjected to step wall temperature rise and constant ablation rate at time zero (solution reported in Ref. 37).

11.- Noramlized surface temperature rise for transient ablation of silica phenolic (70-30) material in a N_2O_4-N_2H_4/UDMH environment, O/F = 2.0, pressure = 100 psia.

12.- Normalized surface-recession rate for transient ablation of silica phenolic (70-30) material in a N_2O_4-N_2H_4/UDMH environment, O/F = 2.0, pressure = 100 psia.

13.- Combined solution of species conservation equations and chemical equilibrium relations for OF_2-B_2H_6 propellant, O/F = 3.0, pressure = 100 psia. (a) Graphite and graphite phenolic. (b) HfB_2, HfO_2, and silica phenolic.

13.- Concluded. (c) B_4C, TiB_2, and BeO. (d) TiC, TiN, ZrC, ZrN, ZrO_2, and W.

14.- Combined solution of species conservation equations and chemical equilibrium relations for O_2-H_2 propellant, O/F = 4.0, pressure = 100 psia. (a) Graphite, graphite phenolic, TiC, TiN, ZrC, and ZrN. (b) Silica phenolic, B_4C, TiB_2, W, BeO, ZrO_2, and HfB_2.

15.- Combined solution of species conservation equations and chemical equilibrium relations for N_2O_4-N_2H_4/UDMH propellant, O/F = 2.0, pressure = 100 psia. (a) Graphite and graphite phenolic. (b) Silica phenolic, TiC, TiN, ZrC, ZrN, and ZrO_2.

15.- Concluded. (c) TiB_2, B_4C, W, BeO, HfB_2, and HfO_2.

16.- Combined solution of species conservation equations and chemical equilibrium relations for Flox-Methane propellant, O/F = 4.0, pressure = 100 psia. (a) Graphite, graphite phenolic, ZrO_2, ZrN, and ZrC. (b) Silica phenolic, TiN, HfB_2, and HfO_2.

16.- Concluded. (c) TiB_2, B_4C, BeO, and W.

17.- Steady-state energy equation solution for B' and T_w for graphite phenolic material as a function of phenolic content. (a) OF_2-B_2H_6 environment, O/F = 3.0, pressure = 100 psia. (b) O_2-H_2 environment, O/F = 4.0, pressure = 100 psia. (c) N_2O_4-N_2H_4/UDMH environment, O/F = 2.0 pressure = 100 psia. (d) Flox-Methane environment, O/F = 4.0, pressure = 100 psia.

18.- Equilibrium composition of products of combustion of OF_2-B_2H_6, O/F = 5.85, pressure = 100 psia.

19.- Equilibrium composition and temperature of products resulting from reactions between OF_2-B_2H_6 amd graphite in equilibrium with the graphite surface, O/F = 5.85, pressure = 100 psia.

20.- Equilibrium ablation rate, B', as a function of temperature for graphite in the OF_2-B_2H_6 environment, O/F = 5.85, pressure = 100 psia.

21.- Gas-phase composition for ablation of graphite in OF_2-B_2H_6, O/F = 5.85, pressure = 100 psia. (a) B' = 0.2. (b) B' = 0.4.

22.- Importance of various reactions for ablation of graphite in the OF_2-B_2H_6 environment as determined from gas phase equilibrium considerations, O/F = 5.85, pressure = 100 psia. (a) B' = 0.1. (b) B' = 0.2.

22.- Continued. (c) B' = 0.3. (d) B' = 0.4. (e) B' = 0.5. (f) B' = 0.6.

22.- Concluded. (g) B' = 0.7. (h) B' = 0.8. (i) B' = 0.9. (j) B' = 1.0.

23.- Importance of various reactions for ablation of graphite in the OF_2-B_2H_6 environment as determined from gas phase equilibrium considerations, O/F = 5.85, pressure = 100 psia. B' varies such that gas phase is in equilibrium with graphite wall.
(a) Normalized ablation versus temperature.
(b) Normalized ablation versus B'.

24.- Comparison of measured temperature histories to those predicted employing different correction factors on theory.
(a) Rokide coated steel nozzle. (b) Molybdenum nozzle.

25.- Comparison of measured temperature distributions to thos e predicted employing different correction factors on theory.
(a) Time from ignition = 10 seconds. (b) Time from igntion = 60 seconds.

26.- Enthalpy of gases in O_2-H_2 rocket engine as a function of temperature.

27.- Predicted char depth history and comparison of predicted and measured surface recession for silica phenolic nozzle throat, Engine S-4.
(a) Run No. 89; final ablated depth, predicted, 0 inch, measured, 0.2 inch.
(b) Run No. 90; final ablated depth, predicted, 0.041 inch, measured, -0.013 inch.

27.- Concluded. (c) Run No. 91; final ablated depth, predicted, 0.081 inch, measured, 0.073 inch.

28.- Predicted char depth history and comparison of predicted and measured surface recession for graphite-phenolic nozzle throat, Engine S-10.
(a) Run No. 64; final ablated depth, predicted, 0.007 inch, measured, 0.007 inch.
(b) Run No. 65; final ablated depth, predicted, 0.019 inch, measured, 0.013 inch.

28.- Concluded. (c) Run No. 66; final ablated depth, predicted, 0.52 inch, measured, 0.09 inch.

29.- Comparison of transient and steady-state ablation rates for resin off-gas, char, and total.
(a) Graphite phenolic, Run No. 66. (b) Silica phenolic, Run No. 90.

30.- Comparison of predicted to measured temperature histories for the silica-phenolic nozzle throat, Engine S-4.
(a) Run No. 89. (b) Run No. 90.

30.- Concluded. (c) Run No. 91.

31.- Comparison of predicted to measured temperature histories for the graphite-phenolic nozzle throat, Engine S-10.
(a) Run No. 64. (b) Run No. 65.

31.- Concluded. (c) Run No. 66. (d) Run No. 66, the surface was not allowed to recede for this prediction.

32.- Schematic of solenoid arc-plasma generator electrode configuration.

33.- Rocket-nozzle test model mounting scheme.

34.- Oscillograph trace for steam-hydrogen operation showing effect of hydrogen on voltage requirements.

35.- Oscillograph trace from OF_2-B_2H_6 simulation attempt showing effect of steam on arc operation.

36.- Comparison of boundary-layer enthalpy potential as a function of wall temperature for the N_2O_4-N_2H_4/UDMH propellant and the N_2-O_2-He simulation gas for different electric energy inputs.

37.- Range on actual rocket motor conditions simulated by duplicating enthalpy and oxidation potential of N_2O_4-N_2H_4/UDMH propellant.

38.- Constrictor arc-plasma generator rocket-engine environment simulation apparatus.

39.- Arc voltage as a function of mass-flow rate for two anode diameters.

40.- Arc voltage as a function of chamber pressure for hydrogen and nitrogen operation.

41.- Arc voltage as a function of mass-flow rate for H_2 and N_2 operation.

42.- Effect of anode constrictor diameter on arc voltage.

43.- Arc thermal efficiency as a function of chamber pressure.

44.- Arc thermal efficienty as a function of mass-flow rate for hydrogen operation.

45.- New cathode configuration, constrictor arc-plasma generator.

46.- Water-cooled gas-sampling probe.

47.- Schematic representation of the gas-sampling system including the heating method for the sampling tube and manifold.

48.- Pressure-tap locations in calibration nozzles.

49.- Schematic drawing of typical heat-transfer calibration nozzle.

50.- Section representation of the hot-wall calorimeter model.

51.- Thermocouple mounting scheme.

52.- Thermocouple probe.

53.- Typical X-ray photograph of thermocouple-probe locations.

54.- Schematic of gas systems for liquid engine simulation.

55.- Comparison of arc-plasma generator simulation capabilities to rocket-engine test conditions.
(a) N_2O_4-N_2H_4/UDMH propellant. (b) O_2-H_2 propellant.

56.- Comparison of measured gas composition to that which would occur if perfect mixing were obtained. Test No. 252.

57.- Typical ablating nozzle configuration; 0.3-inch-diameter nozzle shown.

58.- Constrictor arc-plasma generator with instrumented test nozzle attached.

59.- Enthalpy, pressure, and mass-flow rate histories for ablation material test in the N_2O_4-N_2H_4/UDMH environment.
(a) Test No. 295, graphite phenolic, MX 4500.

59.- Concluded. (b) Test No. 296, silica phenolic MX 2600.

60.- Throat recession data for N_2O_4-N_2H_4/UDMH simulation test series.
(a) Test No. 295, graphite phenolic, MX 4500.
(b) Test No. 296, silica phenolic, MX 2600.

61.- Post-test view of sectioned nozzles from N_2O_4-N_2H_4/UDMH simulation series.
(a) Test No. 295, graphite phenolic, MX 4500.
(b) Test No. 296, silica phenolic, MX 2600.

62.- Enthalpy, pressure, and mass-flow rate histories for ablation material Test No. 290, in the O_2-H_2 environment, silica phenolic, MX 2600.

63.- Throat recession data for O_2-H_2 simulation Test No. 290, silica phenolic, MX 2600.

64.- Post-test view of sectioned nozzles from O_2-H_2 simulation series, silica phenolic, MX 2600.

65.- Comparison of measured and predicted values of $\rho_e U_e C_H$, $D_* = 0.3$ inch, oxidation and enthalpy potential simulation, Test No. 1110.

66.- Post-test view of sectioned nozzle subjected to oxidation and enthalpy potential simulation conditions.
(a) ATJ graphite, Test No. 1105.

66.- Continued. (b) Test No. 1106, silica phenolic, MX 2600. (c) Test No. 1107, silica phenolic, MXS 75.

66.- Concluded. (d) Test No. 1108, graphite phenolic, MX 4500. (e) Test No. 1109, silica phenolic, MXS 19.

67.- Internal temperature history, Test Series IV. (a) Test No. 1105.

67.- Continued. (b) Test No. 1106. (c) Test No. 1107.

67.- Concluded. (d) Test No. 1108. (e) Test No. 1109.

68.- Comparison of predicted and measured response of graphite phenolic (MX 4500) in N_2O_4-N_2H_4/UDMH environment, Test No. 295.
(a) Surface boundary conditions evaluated from chemical equilibrium considerations.
(b) Measured surface temperature and recession rate prescribed as boundary conditions.

69.- Comparison of predicted and measured response of silica phenolic (MX 2600) in N_2O_4-N_2H_4/UDMH environment, Test No. 296.
(a) Surface boundary conditions evaluated from chemical equilibrium considerations.
(b) Measured surface temperature and recession rate prescribed as boundary conditions.

70. Comparison of predicted and measured internal-temperature history for silica phenolic (MX 2600) in O_2-H_2 environment, Test No. 290. Measured surface temperature and recession rate prescribed as boundary conditions.

LIST OF SYMBOLS

A	area
B'	normalized ablation rate, $(\rho v)_w/\rho_e U_e C_M$
B'_c	$\dot{m}_c/\rho_e U_e C_M$
B'_g	$\dot{m}_g/\rho_e U_e C_M$
$\dot{B}$	total ablation rate (Eq. (96))
C_H	heat-transfer coefficient (Stanton number), $q_w/\rho_e U_e (H_r - h_w)$
C_{k_i}	number of k atoms in molecular species i
C_N	nozzle flow coefficient
C_M	mass-transfer coefficient
D_A	anode diameter
$\bar{D}$	average diffusion coefficient (Eq. (47))
D_i^T	thermal diffusion coefficient of species i
D_{eff}	effective diffusion coefficient (Eq. (66)
D_{ij}	binary diffusion coefficient of species i into j
E	voltage
F	free energy
F_i	diffusion factor for species i (Eq. (47))
h	static enthalpy, $h_c + h_s$
h_c	chemical enthalpy, $\sum_i K_i h_i^\circ$
H_{prop}	enthalpy of propellant
h_i°	heat of formation of species i at reference temperature and 1 atm pressure
H_{inj}	enthalpy of injected simulation gases
h_s	sensible enthalpy, $\sum_i K_i \int_\circ^T C_{p_i}\, dT$
$\bar{h}$	Equation (29)
h_r	recovery enthalpy

ΔH_{arc}	energy added by electric arc
I	total number of species i, or current
j_i	diffusional mass flux of species i by virtue of a concentration gradient
J_i	total diffusional mass flux of species i (Eq. (49))
j	subdivision of node n (Eq. (10))
K	total number of k elements
k	thermal conductivity
K_B	blowing factor (Eq. (88))
K_i	mass fraction of species i
$\tilde{K}_k$	total mass fraction of element k independent of molecular configuration
K_{P_i}	equilibrium constant for formation of species i from gaseous elements
Le	Lewis number
$\dot{M}$	total mass-flow rate
$\dot{m}$	mass-flow rate per unit area
m	molecular weight
m_k	atomic weight of element k
N_i	chemical symbol for gaseous species i
N_k	chemical symbol for element k
N_ℓ	chemical symbol for condensed species ℓ
P	pressure
P_i	partial pressure of species i
Pr	Prandtl number
q_r	radiant heat-flux incident to the surface
q_w	net surface heat flux
r	radial coordinate
R	gas constant
s	streamwise coordinate
S	ablated depth (Fig. 1), or entropy
T	temperature
u	velocity component parallel to surface
v	velocity component normal to the surface

x	space coordinate (Fig. 1)
x_i	mole fraction of species i
y	coordinate normal to surface of body
Z_i	diffusion driving potential factor (Eq. (53))
$\tilde{Z}_k$	defined by Equation (59)
α_i	specific heat curve-fit coefficients (Eq. (82))
α_{ki}	mass fraction of element k in species i
β	stability factor, Equation (32)
Γ	volume fraction
Δ	finite-difference increment
ϵ	emissivity, or volume fraction
ϵ_D	eddy diffusivity (Eq. (36))
ϵ_H	eddy conductivity (Eq. (44))
ϵ_M	eddy viscosity (Eq. (42))
η	efficiency
θ	time
θ'	$\theta + \Delta\theta$
μ	viscosity
μ_1, μ_2, μ_3	factors defined by Equation (53)
ρ	density
σ	Stefan-Boltzman constant
ψ_i	mass generation of species i per unit volume as a result of chemical reaction

Subscripts

A	pertaining to arc-plasma generator
A,B,C	pertaining to resin components (Eq. (5))
a	undecomposed plastic at initial temperature
c	char or solid material
d	pertaining to decomposition (Eq. (9))
e	evaluated at edge of boundary layer
g	resin off-gas
i	gaseous species i
j	gaseous species j
k	element k
ℓ	condensed species ℓ

n	pertaining to finite-difference node n
o	evaluated in the absence of blowing
p	undecomposed plastic
R	pertaining to rocket engine
r	condensed phase removal, differentiaion at constant r, or pertaining to residual mass after decomposition (Eq. (5))
ss	steady-state value

Superscripts

κ	exponent equal to unity for axisymmetric bodies and zero for two-dimensional bodies
'	indicates fluctuating quantity, or evaluated at time θ'
$\overline{\quad}$	time averaged
*	evaluated at sonic throat conditions

NOTE: Units have been omitted from this nomenclature, but accompany numerical results presented in the text. The constant of proportionality in Newton's Second Law and the mechanical equivalent of heat have been omitted from the equations to avoid unessential repetition. Those equations requiring their use are clear from dimensional inspection. Any consistent set of units may be employed.

ANALYTICAL AND EXPERIMENTAL STUDY OF ABLATION MATERIAL FOR ROCKET-ENGINE APPLICATION

1. INTRODUCTION

Specification of the thermal insulation requirements for a large rocket motor requires reliable design information. Only a portion of this information is currently available and in many instances its reliability is questionable. This situation is due, in part, to the absence of an accurate theory for the calculation of material ablation rates for arbitrary material-propellant environment combinations. The results of subscale rocket-motor tests are often inconclusive because of chemical kinetic, and asymmetric-flow effects associated with particular injector configurations. Full-scale testing is expensive and necessary for assessing the adequacy of the final design of a thermal protection system, but does not possess enough flexibility to evaluate materials for a wide range of conditions. It is apparent that some small-scale simulation technique is desirable. For this technique to be meaningful, its design, as well as the methods of reduction and interpretation of the consequent data, must be based on a reasonably sophisticated theoretical analysis. It is these considerations which established the goals of the study reported herein. The theoretical considerations are presented first, in Section 2, and are followed, in Section 3, by a description of the experimental ablation simulation technique.

2. THEORETICAL INVESTIGATIONS

The primary objective of the theoretical investigations is to characterize mathematically the thermochemical response of ablative materials subjected to high temperature, chemically reacting environments such as those existing in a liquid-propellant rocket engine. This mathematical model may then be utilized to define the parameters which must be duplicated in a valid experimental technique. A logical byproduct of the theoretical ablation model is that it may be employed to screen candidate ablation materials proposed for utilization in various rocket combustion product environments. In addition to the specification of experimental simulation parameters and theoretical material screening calculations, it is appropriate that efforts be made to assess the validity of the theoretical ablation model by comparing the results of predictions to measured ablation data obtained from rocket-engine firings. These three considerations

correspond to the three major subdivisions in this section. The theoretical ablation model is described first in Section 2.1; the results of theoretical calculations for the thermochemical interactions between a number of potential rocket-nozzle insulation materials and several rocket combustion product environments are presented next, in Section 2.2, and are followed, in Section 2.3, by comparison of predicted and measured rocket-nozzle ablation rates.

2.1 Theoretical Ablation Model

The complexity of a mathematical model required to characterize the ablation process in its totality may be realized by considering the numerous physical processes which control the degradation of materials subjected to high temperature, reactive environments. These physical processes include: (1) the transport of mass, momentum, energy, and chemical species through the chemically reacting boundary layer, (2) possible homogeneous and heterogeneous kinetically controlled chemical reactions at and near the ablating surface, (3) removal of surface material in the gas phase resulting from chemical attack, vaporization, and sublimation, and in the condensed phase in the form of liquid-layer flow and spallation, (4) a complex interchange of energy, mass, and chemical species below the ablating surface resulting from heat conduction in a porous matrix through which a chemically reacting gas is passing, and (5) kinetically controlled reactions characterizing the decomposition of organic constituents in depth. The inclusion of all of the above phenomena in a general ablation solution is a formidable task, and if consideration is restricted to particular material types in a certain class of environmental conditions, it is not usually necessary. Even when certain of these phenomena may be rationalized as negligible, however, treatment of those remaining must be based upon a series of compromises between physical reality and practical computational considerations.

The theoretical ablation model developed here is appropriate to charring and non-charring ablation materials which undergo surface recession entirely as a result of chemical erosion, that is, no ablation is considered to occur as a result of liquid-layer flow or spallation. It is believed that thermochemical ablation is solely responsible for the material consumption occurring in rocket-engine thrust chambers for a number of materials of current interest, and, for many materials characterized by a liquid layer, or char spallation, thermochemical ablation plays a significant, if not dominant, role. The theoretical model developed herein is directed toward the general characterization of thermochemical interaction between an

ablation material and its environment, both of arbitrary chemical composition.

In order to place the present work in perspective, it is instructive to consider previous contributions in the subject area. No attempt is made to present an exhaustive search of the literature to document the historical significance of past contributions, but rather to sight specific examples which are believed representative of current state-of-the-art techniques. Past contributions in thermochemical ablation may be roughly divided into three categories: (1) investigation of high-temperature, homogeneous materials, (2) composite ablation materials, and (3) boundary-layer transport processes. Certain of these investigations are briefly described in the following paragraphs.

High-Temperature Homogeneous Materials.- The ablation of homogeneous materials (herein considered to be those which do not decompose in depth) has been the subject of numerous theoretical investigations (Refs. 1 to 5). These solutions may be placed in either of two categories: (1) those which consider a particular material-environment combination (e.g., the ablation of graphite in air) in detail including boundary-layer transport phenomena and/or chemical kinetics (Refs. 1 to 3), and (2) those which are general with respect to material and environment composition but treat boundary-layer phenomena in a more gross manner (Refs. 4 and 5). In order to retain the generality of the second category, it has been necessary to employ the simplifying boundary-layer assumptions of Lees (Ref. 6, discussed subsequently), and to consider the limiting reaction rate case of chemical equilibrium. Bartlett (Ref. 5) presents a technique for obtaining the ablation rate of and energy transfer rate to a homogeneous material of arbitrary chemical composition in an arbitrary environment within these restrictions. The technique enables considering all possible chemical reactions with effectively an unlimited number of molecular species in the boundary layer.

As pointed out by Scala and Gilbert (Ref. 1) when considering the multicomponent boundary-layer equations, practical computational limitations restrict the number of species that may be considered to about nine. When considering the ablation of graphite in a complex environment, for example, OF_2-B_2H_6 combustion products, the number of important molecular species in the boundary layer may be as high as 30 and recourse has in the past usually been taken to employing the assumption that the diffusion coefficients of all molecular species are equal.

Composite Ablation Materials.- The ablation of composite materials which decompose in depth to form a char layer near the heated surface represents a considerably more complex problem to characterize theoretically than does the ablation of homogeneous materials. There are two primary reasons responsible for the complexity: (1) many more chemical species are present in a composite material which complicates evaluating the state of the gas at the ablating surface and, (2) the chemical composition and rate of addition of ablation products to the boundary layer are not simply related to the surface recession rate. The rate of addition of gaseous decomposition products and char material to the boundary layer depends critically upon the internal material response which, in turn, is strongly dependent upon the gradients of enthalpy and chemical species in the boundary layer at the heated surface. These gradients depend upon the rates of addition of char and decomposition products. The need for a coupled solution of the subsurface response and boundary-layer surface interaction is apparent.

Kratsch, Hearne, and McChesney (Ref. 7) present a comprehensive mathematical characterization of the internal thermochemical response of composite materials and consider the chemical interactions between a particular material, nylon phenolic, and an air boundary layer. A simplified chemical model is selected to characterize consumption of the carbonaceous char by the boundary-layer gas, namely, the internal decomposition gas products are treated as an inert diluent in the boundary layer, and char consumption results from kinetically controlled oxidation in the low-temperature regime and diffusion controlled oxidation and cyano production at high temperatures. Boundary-layer transport phenomena are characterized by bulk transfer coefficients utilizing the simplifying assumptions of Lees (Ref. 6).

Quinville and Solomon (Ref. 8) present a coupled solution of the charring ablator and boundary-layer phenomena. The boundary-layer transfer coefficients are characterized by a number of parameters obtained from laminar similarity solutions or the turbulent atoms-molecules binary mixture solution of Dorrance (Ref. 9). Surface material consumption is limited to carbon oxidation by the boundary-layer-edge gas.

Efforts at Vidya directed toward mathematically characterizing ablation of charring materials of arbitrary chemical composition in arbitrary chemical environments have been conducted primarily under the subject contract and under the contractural effort reported in Reference 10. A portion of these efforts have been published in the open literature (Refs. 11 and 12).

The solution is general with respect to the chemical composition of the ablation material and its environment. Boundary-layer transport phenomena are characterized by bulk transfer coefficients with approximate modifications to include the effects of unequal diffusion coefficients of all boundary-layer species. Details of this solution are presented later in this section.

Boundary Layer.- As is apparent from the above discussions, consideration of the interactions between an ablating material and the boundary layer is an important step in evaluating the performance of an ablative material. A generalized treatment of the boundary-layer equations for a high-temperature chemically reacting gas over a chemically ablating surface is presented by Lees (Ref. 6). The solution is obtained by demonstrating similarity between the conservation equations for momentum, energy, and chemical elements. In order to reduce the equations to similar form, three simplifying assumptions are required: (1) the Prandtl and Lewis numbers are unity, (2) the streamwise derivatives of pressure, total enthalpy and chemical elemental concentration are zero, and (3) the diffusion coefficients of all species are equal. The similarity of the differential equations and boundary conditions enables expressing the diffusional transfer rate of chemical elements at the wall as the product of an elemental mass fraction difference across the boundary layer and the heat-transfer coefficient. In general, removal of the above assumptions requires that attention be given to a particular boundary-layer gas and ablation material combination. For example, Scala and Gilbert (Ref. 1) present solutions of the laminar boundary-layer equations for particular body shapes appropriate to the ablation of graphite in air. Their solution is for the similar boundary layer, but includes the effects of nonunity Lewis and Prandtl numbers, and diffusion of all significant species characterized by unequal diffusion coefficients. The correlations obtained from such a solution are restricted to the boundary layer gas-wall material composition employed in the solution.

The theoretical ablation model presented in this section has been developed with the following general objectives in mind:

(1) To select existing models and techniques based upon generality and relative accuracy and simplicity.

(2) To extend these techniques when modifications seem appropriate and can be accomplished in a straightforward manner.

(3) To program the resulting solution on a digital computer in such a manner that solutions may be obtained for a wide range of material

propellant combinations with a minimum requirement for empirical input data.

This technique has been developed and is described in the following three subsections. Mathematical characterization of the subsurface thermochemical response is presented first, in Section 2.1.1, and is followed by the boundary-layer treatment in Section 2.1.2. The coupled solution of the boundary layer and ablation material is described in Section 2.1.3.

2.1.1 Subsurface thermochemical response of charring materials

In general, because of the complex nature of the differential equations and boundary conditions which govern the thermochemical response of charring ablation materials employed for rocket-nozzle thermal protection, exact solutions may not be obtained. In order to characterize theoretically the ablation material response, recourse must be taken to numerical solutions of finite difference equations which approximate solutions of the differential equations. This section presents the difference equations which govern the internal thermochemical response of a charring ablation material having a cylindrical geometric configuration to typify a section of a rocket-engine thrust chamber. The equations are presented for the one-dimensional case; that is, the transfer of energy and mass are considered only in the direction normal to the heated surface. The effect of geometrical variation in depth, however, as it influences thermal conduction, decomposition gas generation rate, and thermal capacity, is considered in the solution.

The geometrical configuration considered in the analysis and the various space variables employed in the development are shown in Figure 1.

In the following paragraphs the differential equations and resulting finite difference equations are presented for the conservation of mass and energy.

2.1.1.1 Conservation of mass

The physical model employed to characterize mass conservation in the ablating material is presented first, and is followed by a description of the finite difference representation of the resulting differential equations.

2.1.1.1.1 Differential formulation of mass conservation equation

Decomposition of the ablation material in depth is presumed to be characterized by an irreversible reaction of the following form:

$$\text{plastic} \rightarrow \text{char} + \text{gas} \qquad (1)$$

Initially the ablation material is considered to be all plastic, and after decomposition it is all char. Intermediate states are presumed to be characterized by a mixture of pure plastic and pure char. The mass conservation equation is written neglecting the mass of the gas at any point as being small compared to the mass of solid material and assuming that the transit time of the gas from the point of decomposition to the heated surface is small. Within these constraints and referring to the coordinate system shown in Figure 1, the mass conservation equation may be written:

$$\left(\frac{\partial \dot{M}_g}{\partial r}\right)_\theta = \frac{\partial}{\partial \theta}\,(2\pi r\rho)_r = 2\pi r \left(\frac{\partial \rho}{\partial \theta}\right)_r \tag{2}$$

where the subscripts indicate variables held constant when performing partial differentiation, and $\dot{M}_g$ represents the total mass-flow rate of gas passing a point. The total gas-flow rate is related to the gas-flow rate per unit area by

$$\dot{m}_g = \frac{\dot{M}_g}{2\pi r}$$

Substitution of the above into Equation (2) yields

$$\frac{\partial}{\partial r}\,(r\dot{m}_g)_\theta = r\left(\frac{\partial \rho}{\partial \theta}\right)_r \tag{3}$$

The total gas-flow rate per unit area passing a point is obtained by integration of Equation (3)

$$\dot{m}_g = -\frac{\int_r^{r_b} r\left(\frac{\partial \rho}{\partial \theta}\right)_r dr}{r} \tag{4}$$

The gas generation rate at any point in the material, $\left(\frac{\partial \rho}{\partial \theta}\right)_r$, will depend upon the model selected to characterize decomposition of organic constituents in depth. As indicated above, the material decomposition is normally characterized by the idealized irreversible reaction of Equation (1). The choice of the actual chemical composition of the char and gas depends upon the temperature at which the reaction is complete. Further decomposition of the gas should then be allowed to occur as it passes through the char. Most

investigators have chosen to characterize the decomposition reaction by a single kinetic equation of the Arrhenius form (e.g., Refs. 13, 14, and 15), while others have assumed the decomposition reaction to occur at a fixed temperature (e.g., Ref. 16). More recently, several investigators have characterized the decomposition reaction by a series of independent reactions (Refs. 7, 8, and 17).

There is little question that the multiple part kinetic model more adequately represents the material degradation reaction for organic materials. Goldstein (Ref. 18) presents data obtained from thermogravimetric analysis of phenolic resin, nylon, and composite mixtures of the two which are well correlated by the three kinetic equations, one to characterize nylon decomposition and two for phenolic. This model is believed most general and is employed in the present analysis. The density of the composite is given by:

$$\rho = \Gamma(\rho_A + \rho_B) + (1 - \Gamma)\rho_C \tag{5}$$

where $(\rho_A + \rho_B)$ is the density of the resin, ρ_C the density of the reinforcement, and Γ the volume fraction of resin in the virgin plastic composite. The division of the resin into A and B components is a consequence of the experimentally observed two-stage decomposition process of phenolic resin (Ref. 18). The rate of change of density resulting from thermal decomposition is given by differentiating Equation (5) with respect to time

$$\left(\frac{\partial \rho}{\partial \theta}\right)_r = \Gamma \left(\frac{\partial \rho_A}{\partial \theta} + \frac{\partial \rho_B}{\partial \theta}\right)_r + (1 - \Gamma) \left(\frac{\partial \rho_C}{\partial \theta}\right)_r \tag{5a}$$

where each condensed phase reaction (A, B, or C) is given by a rate equation of the Arrhenius form.

$$\left(\frac{\partial \rho_i}{\partial \theta}\right)_r = - k_i e^{-E_i/RT} \rho_{o_i} \left(\frac{\rho_i - \rho_{r_i}}{\rho_{o_i}}\right)^{n_i} \quad \text{for } i = A,B,C \tag{5b}$$

In the energy equation to be developed subsequently, it is found most convenient to employ a coordinate system fixed to the receding surface (x rather than r). With this in mind, it is appropriate to consider the density change rate for constant x rather than constant r as given in the above equations.

At any instant in time the density may be expressed purely as a function of spatial position and time, $\rho = \rho(r,\theta)$. Then

$$d\rho = \left(\frac{\partial\rho}{\partial r}\right)_\theta dr + \left(\frac{\partial\rho}{\partial\theta}\right)_r d\theta$$

Differentiating with respect to time at constant x yields

$$\left(\frac{\partial\rho}{\partial\theta}\right)_x = \left(\frac{\partial\rho}{\partial r}\right)_\theta \left(\frac{\partial r}{\partial\theta}\right)_x + \left(\frac{\partial\rho}{\partial\theta}\right)_r$$

From Figure 1, the x and r coordinates are related to the amount of surface recession

$$r = s + x$$

from which

$$\left(\frac{\partial r}{\partial\theta}\right)_x = \frac{ds}{d\theta} \equiv \dot{s} \tag{7}$$

where the surface recession rate, $\dot{s}$, is written as an absolute derivative since $s = s(\theta)$ alone. Substituting this expression into the above equation yields

$$\left(\frac{\partial\rho}{\partial\theta}\right)_x = \left(\frac{\partial\rho}{\partial\theta}\right)_r + \left(\frac{\partial\rho}{\partial x}\right)_\theta \dot{s} \tag{8}$$

which, with Equation (5), represents the desired form of the mass conservation equation.

2.1.1.1.2 Finite-difference formulation of the mass conservation equation

The finite difference representation of the preceding differential equation is obtained by considering nodes of thickness δ_n located at specific distances below the receding surface (x = const) as shown in Figure 1(b). Differentiation at constant x, then, applies to a particular node, n, and differentiation at constant r, which characterizes the decomposition process, will be designated by the subscript d. Effectively, the finite difference nodal network may be considered as an array of constant thickness nodes moving through the material in such a manner that the distance between each node and the distance of each from the heated surface remains constant. The one exception to this system is the last ablating

node which will continually shrink as surface recession proceeds. When this node reaches a certain minimum size, its residual mass energy and volume are added to the adjacent ablating node and it is dropped.

The finite difference representation of Equation (8) is readily formulated as[1]

$$\frac{\rho_n' - \rho_n}{\Delta\theta} = \frac{(\rho_{n+1} - \rho_n)\dot{s}}{\delta_n} + \left(\frac{\partial \rho_n}{\partial \theta}\right)_d \qquad (9)$$

where the primed density, ρ', signifies evaluation at the end of the time step, $\theta' = \theta + \Delta\theta$. The final term is evaluated from Equation (5) and the subscript d refers to decomposition. The strong temperature dependence of this last term generally requires that it be treated more carefully than the terms of the energy equation. As a consequence, the mass equation has been treated at Vidya (and elsewhere) with smaller nodes (nodelets) than those for the energy equation. Rewriting Equation (9) for the nodelets, j, where j goes from 1 to J for each node n.

$$\frac{\rho_{n,j}' - \rho_{n,j}}{\Delta\theta} = \frac{(\rho_{n,j+1} - \rho_{n,j})\dot{s}}{\delta_{n,j}} + \left(\frac{\partial \rho_{n,j}}{\partial \theta}\right)_d \qquad (10)$$

The temperature $T_{n,j}$ required for the evaluation of the decomposition term with Equation (5) can be obtained via linear interpolation (with respect to volume) between the nodal volumetric centers, as in the following sketch for $J = 4$.

---

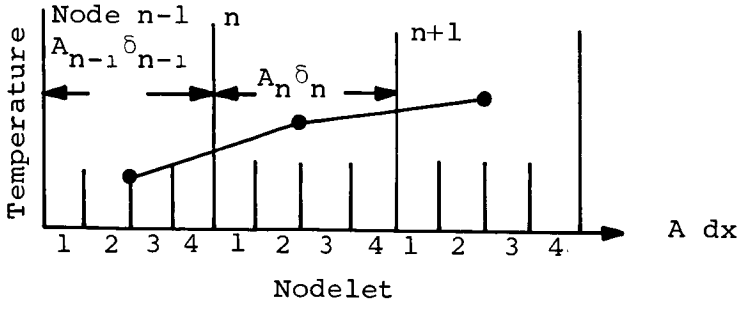
[1]The particular finite difference form used in Equation (9) was selected because of its correspondence to the finite node mass balance, that is (per unit area)

$$\text{mass in} = \rho_{n+1} \cdot \dot{s}$$

$$\text{mass out} = \rho_n \cdot \dot{s} - \delta_n \left(\frac{\partial \rho_n}{\partial \theta}\right)_d \cdot \Delta\theta$$

$$\text{accumulation} = \delta_n(\rho_n' - \rho_n)$$

Such a finite difference form guarantees the conservation of mass.



where the cross-sectional area of the node $n = A_n = 2\pi r_n$. From this sketch it is noted, for example, that

$$T_{n,2} = T_{n-1} + \frac{T_n - T_{n-1}}{(A_n\delta_n + A_{n-1}\delta_{n-1})/2} \left[\frac{A_{n-1}\delta_{n-1}}{2} + \frac{3}{8}\delta_n A_n \right]$$

or, more generally,

$$T_{n,j} = T_{n-1} + \frac{T_n - T_{n-1}}{(A_n\delta_n + A_{n-1}\delta_{n-1})/2} \left[\frac{A_{n-1}\delta_{n-1}}{2} + (j - 0.5)\frac{A_n\delta_n}{J} \right] \qquad (11)$$

for

$$j \leq \frac{J}{2}$$

and

$$T_{n,j} = T_n + \frac{T_{n+1} - T_n}{(A_{n+1}\delta_{n+1} + A_n\delta_n)/2} \left[\frac{(j - 0.5)}{J} - 0.5 \right] A_n\delta_n \qquad (12)$$

for

$$j > \frac{J}{2}$$

If there is an even number of equally sized nodelets in each node, and they are sized such that $\delta_{n,j} \cdot A_{n,j}$ = constant, that is, such that each nodelet has the same volume, the total nodal density change is the volumetric average of the density changes of all of the nodelets, therefore, averaging Equation (10) over all j.

$$\frac{\rho_n' - \rho_n}{\Delta\theta} = \frac{1}{J \cdot \Delta\theta} \sum_{j=1}^{J} \rho_{n,j}' - \rho_{n,j} = \dot{S} \left[\frac{\rho_{n,2} - \rho_{n,1}}{\delta_n} + \frac{\rho_{n,3} - \rho_{n,2}}{\delta_n} \right.$$

$$\left. + \cdots\cdots + \frac{\rho_{n+1,1} - \rho_{n,J}}{\delta_n} \right] + \frac{1}{J} \sum_{j=1}^{J} \left(\frac{\partial \rho_{n,j}}{\partial \theta} \right)_d$$

where it is noted that $\rho_{n,J+1}$ is equivalent to $\rho_{n+1,1}$. This equation can be simplified to

$$\frac{\rho_n' - \rho_n}{\Delta\theta} = \dot{S} \frac{\rho_{n+1,1} - \rho_{n,1}}{\delta_n} + \frac{1}{J} \sum_{j=1}^{J} \left(\frac{\partial \rho_{n,j}}{\partial \theta} \right)_d \qquad (13)$$

which is quite similar to Equation (9) except that the density gradient is evaluated using the nodelet densities adjacent to the nodal boundaries rather than the mean nodal density.

Since the complex decomposition process is conveniently characterized by treating the ablation material as a composite of several simply decomposing constituents (the i index of Eq. (5)), it is necessary to treat each of these constituents individually in Equation (10). As a consequence, conservational relations are established for each constituent and their individual densities are evaluated and retained for subsequent use in Equation (5).

2.1.1.2 Conservation of energy

The differential form of the energy equation is presented first and is followed by the finite difference representation.

2.1.1.2.1 Differential formulation of energy conservation equation

The energy equation is written first with respect to a spatially fixed coordinate system. For this purpose, the following functional relationships are presumed:

$$h = h(T,\rho)$$
$$T = T(r,\theta)$$
$$\rho = \rho(r,\theta)$$
$$S = S(\theta)$$

therefore

$$h = h(r,\theta)$$

The differential equation governing the conservation of energy within the charring material is obtained by considering the control volume in Figure 1(a) and equating the net energy transfer rate to the rate of energy change.

$$\overbrace{2\pi \frac{\partial}{\partial \theta} (\rho h r)_r}^{\text{storage}} = \overbrace{2\pi \frac{\partial}{\partial r} \left(kr \frac{\partial T}{\partial r} \right)_\theta}^{\text{conduction}} + \overbrace{\frac{\partial}{\partial r} \left(\dot{M}_g h_g \right)_\theta}^{\text{convection}} \qquad (14)$$

In order to develop a practical numerical solution, it is convenient to consider a coordinate system fixed to the receding surface. For this purpose, it is desired to transform the above differential equation which is written for a point, r = constant, to an equation written for the moving coordinate system, x = constant. The storage term in Equation (14) may be related to its counterpart in the moving coordinate system by expanding the energy change employing the chain rule.

$$\rho h r = \rho h r(r,\theta)$$

$$d(\rho h r) = \frac{\partial}{\partial r} (\rho h r)_\theta \, dr + \frac{\partial}{\partial \theta} (\rho h r)_r \, d\theta \qquad (15)$$

Differentiating partially with respect to time at constant x yields:

$$\frac{\partial}{\partial \theta} (\rho h r)_x = \frac{\partial}{\partial r} (\rho h r)_\theta \frac{\partial r}{\partial \theta} \Big)_x + \frac{\partial}{\partial \theta} (\rho h r)_r \qquad (16)$$

Introducing Equation (7) and rearranging obtains

$$\frac{\partial}{\partial \theta} (\rho h r)_r = r \frac{\partial}{\partial \theta} (\rho h)_x - \dot{s} \, r \frac{\partial}{\partial r} (\rho h)_\theta \qquad (17)$$

Substituting Equation (17) into Equation (14) and noting that partial differentiation with respect to x or r at constant time is equivalent results in the transformed energy equation

$$r \frac{\partial}{\partial \theta} (\rho h)_x = \frac{\partial}{\partial x} \left(k \, r \frac{\partial T}{\partial x} \right)_\theta + \dot{s} \, r \frac{\partial}{\partial x} (\rho h)_\theta + \frac{\partial}{\partial x} \left(r \, \dot{m}_g h_g \right)_\theta \qquad (18)$$

It is convenient to express the enthalpy change rate in terms of temperature and chemical composition change rates. Employing the idealization introduced by reaction 1, the density may be written

$$\rho = \epsilon_p \rho_p + (1 - \epsilon_p)\rho_c \tag{19}$$

where ϵ_p is the volume fraction of undecomposed material in the control volume $2\pi r\,dx$. For undecomposed material ϵ_p is 1, for pure char $\epsilon_p = 0$, and for intermediate states of decomposition it may be anywhere in between. The total enthalpy per unit volume may be written as the mass weighted average of the enthalpy of the parts

$$\rho h = \epsilon_p \rho_p h_p + (1 - \epsilon_p)\rho_c h_c \tag{20}$$

where

$$h_p = h_p^{\circ} + \int_{\circ}^{T} c_{p_p}\, dT \tag{21}$$

and

$$h_c = h_c^{\circ} + \int_{\circ}^{T} c_{p_c}\, dT \tag{22}$$

Differentiating Equation (20) obtains

$$\frac{\partial}{\partial\theta}(\rho h) = \rho_p h_p \frac{\partial \epsilon_p}{\partial\theta} + \rho_p \epsilon_p \frac{\partial h_p}{\partial\theta} + \rho_c \frac{\partial h_c}{\partial\theta}$$

$$- \rho_c h_c \frac{\partial \epsilon_p}{\partial\theta} - \epsilon_p \rho_c \frac{\partial h_c}{\partial\theta} \tag{23}$$

Differentiating Equations (21) and (22), and noting that the char and plastic heats of formation are constant yields

$$\frac{\partial h_p}{\partial\theta} = c_{p_p} \frac{\partial T}{\partial\theta} \quad \text{and} \quad \frac{\partial h_c}{\partial\theta} = c_{p_c} \frac{\partial T}{\partial\theta} \tag{24}$$

Differentiation of Equation (19) results in

$$\frac{\partial \epsilon_p}{\partial\theta} = \frac{1}{\rho_p - \rho_c} \frac{\partial \rho}{\partial\theta} \tag{25}$$

Substitution of Equations (24) and (25) into (23) yields the desired relation between enthalpy change rate, temperature change rate, and decomposition rate

$$\frac{\partial}{\partial\theta}(\rho h)_x = \left(\frac{\rho_p h_p - \rho_c h_c}{\rho_p - \rho_c}\right)\left(\frac{\partial\rho}{\partial\theta}\right)_x + \rho C_p \left(\frac{\partial T}{\partial\theta}\right)_x \qquad (26)$$

where

$$\rho C_p \equiv \rho_p \epsilon_p C_{p_p} + (1 - \epsilon_p)\rho_c C_{p_c} \qquad (27)$$

The specific heat, C_p, is the mass weighted average specific heat of the char and virgin plastic parts, and, as such, it represents the specific heat of the material evaluated in the absence of chemical reactions.

Considering the last term in the energy differential Equation (18) and introducing Equation (3) yields:

$$\frac{\partial}{\partial x}\left(r\dot{m}_g h_g\right)_\theta = r\dot{m}_g \frac{\partial h_g}{\partial x}\Big)_\theta + r h_g \frac{\partial\rho}{\partial\theta}\Big)_r \qquad (28)$$

Substitution of Equations (26) and (28) into Equation (18), and solving for the temperature change rate yields the desired form of the energy differential equation

$$\rho C_p \frac{\partial T}{\partial\theta}\Big)_x = \frac{1}{r}\frac{\partial}{\partial x}\left(kr\frac{\partial T}{\partial x}\right)_\theta - \bar{h}\frac{\partial\rho}{\partial\theta}\Big)_x + \dot{s}\frac{\partial}{\partial x}(\rho h)_\theta$$

$$+ \dot{m}_g \frac{\partial h_g}{\partial x} + h_g \frac{\partial\rho}{\partial\theta}\Big)_r \qquad (29)$$

where

$$\bar{h} = \frac{\rho_p h_p - \rho_c h_c}{\rho_p - \rho_c}$$

The terms in Equation (29) represent, from left to right, the sensible energy accumulation of the node, the net conduction into the node, the chemical energy accumulation of the node, net energy convected into the node as a consequence of coordinate motion, net energy convected into the node by the pyrolysis gases entering the node, and the energy convected from the node

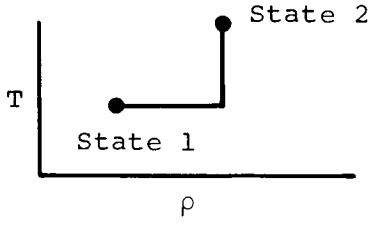
by the pyrolysis gases generated in the node. All terms are evaluated per unit volume of the node. The finite difference representation of the differential equation is given in the following section.

2.1.1.2.2 Finite-difference formulation of the energy equation

A finite difference representation of Equation (29) can be achieved in a variety of ways. As with the mass equation, however, every effort is made to preserve a correspondence with a finite nodal energy balance. For example, the total enthalpy change rate given by Equation (26),

$$\frac{\partial}{\partial\theta}(\rho h)_x = \rho C_p \left.\frac{\partial T}{\partial\theta}\right)_x + \bar{h} \left.\frac{\partial\rho}{\partial\theta}\right)_x \tag{26}$$

represents the nodal enthalpy change resulting from a change in density and a change in temperature. Since enthalpy is a function of T and ρ only in the present analysis, the path followed in going from one temperature-density state to another is inconsequential. Choosing a constant temperature path followed by a constant density path as shown in the sketch



yields the following interpretation of the two terms on the right side of Equation (26).

$$\rho C_p \left.\frac{\partial T}{\partial\theta}\right)_x + \bar{h} \left.\frac{\partial\rho}{\partial\theta}\right)_x = \rho' \bar{C}_p \frac{\Delta T}{\Delta\theta} + \bar{h} \cdot \frac{\Delta\rho}{\Delta\theta} \tag{30}$$

where $\bar{h}$ is evaluated at the initial temperature, and $\rho' \bar{C}_p$ is evaluated at the final density and initial temperature. To be precise $\bar{C}_p$ should be evaluated at some mean temperature as well as at the terminal density, but otherwise the relation is exact since $\bar{h}$ is constant at constant temperature and ρ is constant along the second segment of selected path.

Equation (29) can be written in finite difference form as

$$\left(\rho'\bar{C}_p\right)_n (T_n' - T_n) = \frac{\Delta\theta}{\delta_n r_n}\left(\frac{T_{n+1} - T_n}{\frac{\delta_{n+1}/2}{k_{n+1}r_{n+1}} + \frac{\delta_n/2}{k_n r_n}} - \frac{T_n - T_{n-1}}{\frac{\delta_n/2}{k_n r_n} + \frac{\delta_{n-1}/2}{k_{n-1}r_{n-1}}}\right)$$

$$+ \left\{ h_{g_n}\left(\frac{\partial\rho_n}{\partial\theta}\right)_d - \bar{h}\frac{\Delta\rho_n}{\Delta\theta} + \dot{m}_{g_n}\frac{h_{g_{n+1}} - h_{g_n}}{\delta_n} \right.$$

$$\left. + \frac{\dot{s}}{\delta_n}\left[(\rho h)_{T_{n+1},\rho_{n+1,1}} - (\rho h)_{T_n,\rho_{n,1}}\right]\right\}\Delta\theta \qquad (31)$$

where the use of the nodelet densities in the evaluation of ρh in the final term is motivated by the desire to maintain a consistency between this equation and the mass balances (see Eq. (13)). In effect, the node is considered to be at constant temperature but with nodelet to nodelet density variations.

The energy equation is presently solved explicitly, that is, all temperatures and enthalpies in the equation are evaluated at the beginning of the time internal, and are held constant during the time interval, $\Delta\theta$. Specification of the time interval size ($\Delta\theta$) such that the explicit solution will remain stable is obtained by a logical extension of the analysis given by Carslaw and Jaeger (Ref. 19, p. 471). For a simple conduction solution with constant thermal properties, the time interval must satisfy the following criterion in order for the solution to remain absolutely stable:

$$\Delta\theta \leq \frac{1}{2}\left(\frac{\rho C_p}{k}\right)\delta^2$$

When considering energy transfer in a material characterized by temperature and composition-dependent thermal properties, energy absorption resulting from decomposition and heat transfer to the resulting off-gas, the following criterion may be rationalized as adequate:

$$\Delta\theta = \beta\frac{(\rho C_p \delta)_n}{\frac{1}{\frac{\delta_{n+1}}{2k_{n+1}}\frac{r_n}{r_{n+1}} + \frac{\delta_n}{2k_n}} + \frac{1}{\frac{\delta_n}{2k_n} + \frac{\delta_{n-1}}{2k_{n-1}}\frac{r_n}{r_{n-1}}} + \dot{m}_{g_n}\frac{\partial h_{g_n}}{\partial T} + C_{p_n}\rho_n\dot{s}} \qquad (32)$$

where experience with this type of solution has shown that generally a stable solution will result if $\beta < 1.0$. The time increment, $\Delta\theta$, is computed for each node, except the surface node, and the minimum value so determined is employed.

The explicit procedure described above is utilized for all nodes in the solution except the surface node (n=1). The same equations are employed for nonablating, backup materials with the terms appropriate to decomposition, gas flow, and coordinate system movement set equal to zero. Because of the extremely nonlinear dependence of energy transfer on temperature for the surface node, it is believed more appropriate to treat the surface node in an implicit manner.

Utilizing the approximate boundary-layer conservation equations presented subsequently in Section 2.1.2.2 to represent the surface energy transfer rate, the following finite difference formulation of the surface energy balance results.

$$\frac{\delta_1}{\Delta\theta}\left(\rho'\bar{C}_p\right)_1(T_1' - T_1) =$$

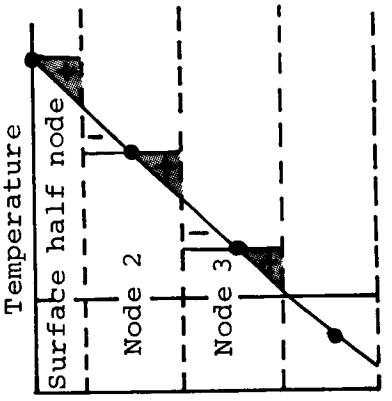
$$\rho_e u_e C_H H_r - \rho_e u_e C_H \left\{\sum K_{i_e} h_i^{\circ} + h_{s_w} - \frac{C_M}{C_H}\left[\sum_i \left(Z_{i_e} - Z_{i_w}\right) h_i^{\circ} - B' h_w\right]\right\}$$

$$+ \alpha_w q_r - \sigma\epsilon T_1^4 + \frac{T_2 - T_1}{\left(\frac{r_1 \delta_2/2}{k_2 r_2} + \frac{\delta_1}{k_1}\right)} + \dot{m}_{g_2} h_{g_2} - \bar{h}\delta_1 \frac{\Delta\rho_1}{\Delta\theta} + \dot{S}(\rho h)_{T_2, \rho_{2,1}} \qquad (33)$$

For a specified boundary-layer-edge composition, the equilibrium surface thermochemistry program described in Section 2.1.3 will provide the value of the term in braces and T_1 as functions of the normalized pyrolysis gas rate and char removal rate. Since the pyrolysis gas rate and the normalizing mass-transfer coefficient are known if an explicit mass balance is employed, this entire term can be treated as a function of $\dot{m}_{char}$ alone. Similarly, T_1 and, thus, a majority of the residual terms are also a function of $\dot{m}_{char}$. Functionally, therefore, Equation (33) becomes <u>at a given time</u> and after the solution of the mass balance equations:

$$\left(\rho'\bar{C}_p\right)_1 (T_1' - T_1)\,\frac{\delta_1}{\Delta\theta} = F(\dot{m}_{char}) + \frac{T_2}{\frac{r_1\delta_2/2}{k_2 r_2} + \frac{\delta_1}{k_1}} + \dot{m}_{g_2} h_{g_2} + \dot{S}(\rho h)_{T_2,\rho_{2,1}} \tag{34}$$

This equation is solved implicitly and iteratively. Newton's method is employed and convergence is normally obtained after one or two iterations. As shown in Figure 1(b), the surface node is treated as a "half-node" with temperature equal to surface temperature. Two characteristics of this system are significant: the extremely important surface temperature is immediately available for the surface boundary condition specification, and errors in energy content of the "constant temperature" nodes tend to cancel at successive nodal centers as indicated schematically below.



Because of this half-node concept only half as many nodelets are used with the surface node. With the exception of the surface nodelet, the density evaluation is performed according to Equation (13). In order to be consistent with the surface mass balance, however, it is presumed that material leaving (being consumed) from the surface nodelet is pure char.

In its present form, the program contains essentially three options. Option 1 is the general radiative-convective chemical boundary condition based on the results of the Equilibrium Surface Thermochemistry Program described in Section 2.1.3. Option 2 requires specification of surface temperatures and recession rates, and Option 3 is the special case of Option 1 where the convective heat-transfer coefficient is zero.

In order to determine the accuracy of the finite difference approximation of the differential equations presented in this section, several problems were constructed. Since no exact solutions of the differential equations are in existence for the general case of resin decomposition in depth, a check problem was first run without resin decomposition and compared to an exact solution. The problem selected for this case is that of a thermally semi-infinite slab with constant thermal properties and a step increase in surface temperature at time zero. The numerical and exact solutions are compared in Figure 2, where temperature distributions through the slab are shown for several times. As shown in the figure, the agreement between the solutions is excellent. Two additional check problems were constructed with resin decomposition in depth and realistic (temperature dependent) thermal properties. The first of these problems had a specified surface-temperature history with a surface-recession rate of zero. The second problem had a constant surface-recession rate with a surface-temperature history specified such that the internal temperature and density distributions in the slab should correspond to those in the first problem at any time. A comparison of the results from these two problems is shown in Figures 3(a) and 3(b), where the agreement between the two solutions is believed to be within the accuracy of the input data to the check problem.

The differential and finite difference formulation characterizing the "in depth" response of charring materials presented in this section is believed representative of the most realistic mathematical models presently in existence. Many of the details regarding the treatment of material thermal properties and resin decomposition gas properties are reserved for presentation in the subsequent section on the coupled solution (Section 2.1.3). In that section, sample input and output data will be presented for ablation material response in a typical liquid-propellant rocket engine environment. Prior to presenting the solutions, however, it is first necessary to establish the treatment of boundary-layer transport phenomena and the interactions at the ablating surface. This treatment is given in the following section.

2.1.2 Boundary-layer transport processes

A relatively comprehensive treatment of the subsurface thermochemical response of charring materials, such as presented above, is necessary to establish the heated surface boundary condition which is shared by the boundary layer and subsurface equations. Because this boundary condition is shared by the differential equations which characterize two different

regimes (subsurface and boundary layer), it is imperative that a solution be constructed to allow the mathematical coupling of the two processes.

The mathematical characterization of the subsurface response was presented in the last section, and that for the gaseous boundary layer is presented in this section. A coupled solution for the two phenomena is presented in Section 2.1.3.

2.1.2.1 The differential equations of conservation for the chemically reacting multicomponent boundary layer

The technique for characterizing the transfer of heat, mass, and chemical species in the chemically reacting, multicomponent boundary-layer has been developed, in large part, on the subject contract, and has been presented separately (Ref. 44). The development is presented here for completeness. The boundary-layer equations presented here are in a form appropriate to laminar or turbulent flow over a flat plate ($\kappa = 0$) or a body of revolution at zero angle of attack ($\kappa = 1$). The standard definitions of time-averaged turbulent quantities and relative order of magnitude are employed (Refs. 9 and 20). The turbulent transport terms are expressed in the Boussinesq form, that is, eddy viscosity, eddy diffusion, and eddy conductivity. Hence, all the terms in the equations are time-averaged quantities and no need exists for using a superscript bar. The reader is cautioned to remember that ρv represents $\overline{\rho v}$, not $\overline{\rho}\,\overline{v}$.

The equations derived are essentially an extension of those derived in Reference 9 to include a more general form for the diffusion flux including the effects of thermal diffusion (Soret effect) and unequal binary-diffusion coefficients. The diffusion introduced by pressure gradients and body forces are neglected. In the order-of-magnitude arguments, terms of the following type have been eliminated: (1) triple correlations, (2) derivatives of turbulent correlations parallel to the wall, and (3) correlations involving turbulent components of molecular transport mechanisms.

A mass balance of an individual species in a unit volume results in the relationship

$$\frac{1}{r_o^{\kappa}} \frac{\partial}{\partial s}\left(\rho u K_i r_o^{\kappa}\right) + \frac{\partial}{\partial y}\left(\rho v K_i\right) = \frac{\partial}{\partial y}\left(\rho \epsilon_{D_i} \frac{\partial K_i}{\partial y} - j_i\right) + \psi_i \qquad (35)$$

where ψ_i represents the rate of mass generation of species i per unit volume due to chemical reactions, $\rho\epsilon_{D_i}$ is defined in terms of the correlation of the fluctuating components of concentration and normal velocity, that is,

$$\rho\epsilon_{D_i} = - \frac{\overline{(\rho v)\ 'K_i'}}{\partial K_i/\partial y} \tag{36}$$

and j_i is the mass-diffusion rate of species i due to molecular processes.

When Equation (35) is summed over all the species in the system, and it is remembered that

$$\sum_i \rho\epsilon_{D_i} \frac{\partial K_i}{\partial y} = \sum_i j_i = 0 \tag{37}$$

by the definition of mass diffusion, and that

$$\sum_i \psi_i = 0 \tag{38}$$

because of conservation of mass, there results

$$\frac{1}{r_o^{\kappa}} \frac{\partial \rho u r_o^{\kappa}}{\partial s} + \frac{\partial \rho v}{\partial y} = 0 \tag{39}$$

Equation (39) is the familiar overall continuity equation.

When Equation (39) is considered together with Equation (35), the more conventional species conservation equation is obtained.

$$\rho u \frac{\partial K_i}{\partial s} + \rho v \frac{\partial K_i}{\partial y} = \frac{\partial}{\partial y} \left(\rho\epsilon_{D_i} \frac{\partial K_i}{\partial y} - j_i \right) + \psi_i \tag{40}$$

The streamwise momentum equation can be written as follows:

$$\rho u \frac{\partial u}{\partial s} + \rho v \frac{\partial u}{\partial y} = \frac{\partial}{\partial y} \left[\rho(\nu + \epsilon_M) \frac{\partial u}{\partial y} \right] - \frac{\partial p}{\partial s} \tag{41}$$

where the eddy viscosity is defined in terms of the Reynolds stresses of turbulent flow by

$$\rho\epsilon_M = - \frac{\overline{(\rho v)\ 'u'}}{(\partial u/\partial y)} \tag{42}$$

The energy equation for this general system is

$$\rho u \frac{\partial H_T}{\partial s} + \rho v \frac{\partial H_T}{\partial y} = \frac{\partial}{\partial y} \left[\rho(\epsilon_M + \nu) \frac{\partial \frac{u^2}{2}}{\partial y} + \left(\frac{k}{\bar{c}_p} + \rho\epsilon_H \right) \frac{\partial h}{\partial y} \right.$$

$$+ \sum_i \left(\rho\epsilon_{D_i} \frac{\partial K_i}{\partial y} - j_i \right) h_i - \left(\rho\epsilon_H + \frac{k}{\bar{c}_p} \right) \sum_i h_i \frac{\partial K_i}{\partial y}$$

$$\left. - \frac{RT}{\rho} \sum_i \sum_j \frac{x_j D_i^T}{m_i D_{ij}} \left(\frac{j_i}{K_i} - \frac{j_j}{K_j} \right) \right] \tag{43}$$

where the DuFour effect, the flux of heat caused by diffusion, is given in terms of the diffusion fluxes of the pertinent species in the final term within the brackets, and the turbulent enthalpy-transport coefficient is defined by

$$\rho\epsilon_H = - \frac{\sum_i K_i \overline{(\rho v)' h_i'}}{\sum_i K_i (\partial h_i / \partial y)} \tag{44}$$

The number of independent conservational equations (Eqs. (40), (41), and (43)) is I+2, where I is the number of molecular or ionic species present. The number of such species can be significant when chemically active ablating surfaces are involved. In the formulation of the solution to these relations, it is the number of required conservational equations which provides the best measure of complexity of the solution. When diffusion coefficients are equal, the Shvab-Zeldovich transformation will reduce the number of equations to K+2, where K is the number of elements present in the system. In addition, the species production term is eliminated under this transformation. This transformation, together with the requisite assumption of equal binary-diffusion coefficients, was adopted by Lees in his now classic paper (Ref. 6). A technique is presented here which affords the same reduction in the number of requisite differential equations when the diffusion coefficients of all species are not equal.

To accomplish this simplification, consideration is given to the Stefan-Maxwell equations (Eq. 8.1-3, Ref. 21) which relate the molar gradients of all species to their diffusional mass fluxes. In terms of the nomenclature adopted here, the equation becomes

$$\frac{\partial x_i}{\partial y} = \sum_{j=1}^{I} \frac{x_i x_j}{\rho \mathcal{D}_{ij}} \left[\frac{j_j + D_j^T \left(\frac{\partial \ell n\, T}{\partial y} \right)}{K_j} - \frac{j_i + D_i^T \left(\frac{\partial \ell n\, T}{\partial y} \right)}{K_i} \right] \tag{45}$$

if pressure diffusion and body forces are neglected.

In the absence of thermal diffusion and with all $\mathcal{D}_{ij}$ equal, Equation (45) reduces to Fick's law which relates the diffusional mass flux explicitly to its mass fraction gradient

$$j_i = - \rho \mathcal{D}_{ij} \frac{\partial K_i}{\partial y} \tag{46}$$

When the diffusion coefficients are not equal in a multicomponent mixture, such an explicit expression may not be obtained from the Stefan-Maxwell relations, and recourse is usually taken to utilizing the multicomponent diffusion equations with the attendant complexity of evaluating the multicomponent diffusion coefficients.

The essence of the present analysis is a simple approximation of the binary diffusion coefficients which enables solving the Stefan-Maxwell relations for the diffusional mass flux of species i explicitly in terms of gradients and properties of species i and of the system as a whole at a point. The approximation is given by

$$\mathcal{D}_{ij} = \frac{\overline{D}}{F_i F_j} \tag{47}$$

where $\overline{D}$ is effectively an average diffusion coefficient, and F_i (and F_j) might be termed diffusion factors for species i (and j). The pressure dependence of $\mathcal{D}_{ij}$ can be absorbed into the $\overline{D}$ so that the F_i are independent of pressure and have only a secondary temperature dependence. Equation (47) should be considered simply as a correlation equation to binary diffusion coefficient data. Its adequacy is best assessed by considering the accuracy with which it may be employed to correlate diffusion coefficient information derived from the most reliable sources available.

For this purpose, two high-temperature gas mixtures are considered: the first contains species of the C-N-O system, and the second of the H-O system.[2] The first system is selected because it is of interest when considering the ablation of graphite in air. The second system includes wide variations in molecular weights and molecular configurations and, as such, should represent a particularly severe test of the proposed correlation equation (Eq. (47)). Kinetic theory calculations of the binary diffusion coefficients for the C-N-O system are based on the method of Svehla (Ref. 23) utilizing the Lennard-Jones potential, and the diffusion coefficients for the H-O system are obtained using the values for collison cross sections suggested by Svehla (Ref. 24). The adequacy of the correlation equation (47) for these two systems is obtained by employing a least-squares curve fit to the diffusion coefficient data in order to evaluate F_i, F_j, and $\bar{D}$. Utilizing these values, Equation (47) is employed to compute diffusion coefficients which are compared to the diffusion coefficient data. It is noted that, with the least-squares procedure, the F_i will normally differ for a particular species for each chemical system considered. In the results reported here, $\bar{D}$ is chosen such that

$$\prod_{i=1}^{I} F_i = 1.0$$

The results of the computations are presented in Table I where the following information is given:

(1) The diffusing species i and j.

(2) The D_{ij} for each diffusing pair as computed from kinetic theory.

(3) The F_i (or F_j) for each species i (or j).

(4) The D_{ij} evaluated from Equation (47) for the F_i, F_j, and $\bar{D}$ ($\bar{D}$ is presented at the end of the table).

(5) Percent difference in D_{ij} between the result computed by Equation (47) and that computed from kinetic theory.

(6) Percent error in D_{ij} if all D_{ij} were assumed equal.

In the first case (Table I(a), nine species (O, O_2, N, N_2, CO, CO_2, C, C_3, CN) are considered (a total of 36 diffusing pairs), whereas, in the second case (Table I(b)), six species are considered (15 diffusing pairs).

---

[2]Additional correlations and diffusion coefficient evaluation techniques are presented in Reference 22 which lead to the same general conclusions.

It can be seen that the improvement over the equal diffusion coefficient model is remarkable in both cases, reducing the average absolute error in D_{ij} by more than an order of magnitude. In the first case, the average absolute error is only 1.3 percent and the maximum error in anyone single D_{ij} is only 5.2 percent. In the second case, the average absolute error is 4.8 percent and the maximum error in any one diffusion coefficient is 11.3 percent. The correlation with this set of diffusion coefficient data for a system with a species molecular weight variation of 32 to 1 is highly encouraging. Better accuracies than this are only of academic interest in view of the uncertainties in the diffusion coefficients themselves.

The utilization of Equation (47) reduces the complexity required to characterize diffusion in an I component mixture from $(I^2 - I)/2$ diffusion coefficients to I independent diffusion factors, F_i, plus the $\bar{D}$. The reduction in the number of requisite boundary-layer species conservation equations is obtained by first substituting the correlation Equation (47) into the Stefan-Maxwell Equations (45)

$$\frac{\partial x_i}{\partial y} = \sum_j \frac{x_i F_i x_j F_j}{\rho \bar{D}} \left(\frac{J_j}{K_j} - \frac{J_i}{K_i} \right) \tag{4}$$

where, for convenience, a total diffusional mass flux is defined as the sum of the molecular and thermal diffusional fluxes.

$$J_i = j_j + D_i^T \left(\frac{\partial \ell n\, T}{\partial y} \right) \tag{49}$$

Noting that $x_i = K_i \; m/m_i$, where m is the molecular weight of the mixture and m_i is the molecular weight of species i, yields:

$$\frac{\partial x_i}{\partial y} = \frac{m^2}{\rho \bar{D}} \left(\frac{K_i F_i}{m_i} \sum_j \frac{J_j F_j}{m_j} - \frac{F_i J_i}{m_i} \sum_j \frac{K_j F_j}{m_j} \right) \tag{50}$$

Multiplying each side by m_i/F_i, summing over all i and noting that

$$\sum_i J_i = 0 \quad \text{and} \quad \sum_i K_i = 1.0$$

yields:

$$\sum_j \frac{J_j F_j}{m_j} = \frac{\rho \bar{D}}{m^2} \sum_i \frac{m_i}{F_i} \frac{\partial x_i}{\partial y} \tag{51}$$

Substituting Equation (51) into (50) results in

$$\frac{\partial x_i}{\partial y} = \frac{K_i F_i}{m_i} \sum_j \frac{m_j}{F_j} \frac{\partial x_j}{\partial y} - \frac{m^2}{\rho \bar{D}} \frac{F_i J_i}{m_i} \sum_j \frac{K_j F_j}{m_j} \tag{52}$$

It is convenient to define several new quantities.

$$Z_i = \frac{m K_i}{F_1 \mu_2} = \frac{m_i x_i}{F_i \mu_2} \tag{53c}$$

$$\mu_1 = \sum_j x_j F_j = m \sum_j \frac{K_j F_j}{m_j} \tag{53b}$$

$$\mu_2 = m \sum_j \frac{K_j}{F_j} = \sum_j \frac{m_j x_j}{F_j} \tag{53c}$$

$$\mu_3 = \sum_j \frac{K_j}{F_j^2} \frac{dF_j}{dT} \tag{53d}$$

Multiplying Equation (53a) by μ_2 and differentiating with respect to y yields:

$$\frac{m_i}{F_i} \frac{\partial x_i}{\partial y} - \frac{m_i x_i}{F_i^2} \frac{\partial F_i}{\partial y} = \mu_2 \frac{\partial Z_i}{\partial y} + Z_i \frac{\partial \mu_2}{\partial y} \tag{54}$$

Employing the defining Equations (53), noting that $\sum_j Z_j = 1.0$, substituting Equation (54) into (52), and rearranging obtains:

$$J_i = - \frac{\rho \bar{D}}{m \mu_1} \left[\frac{m K_i}{F_i^2} \frac{\partial F_i}{\partial y} + \mu_2 \frac{\partial Z_i}{\partial y} + Z_i \frac{\partial \mu_2}{\partial y} - K_i \left(\sum_j \frac{m K_j}{F_j^2} \frac{\partial F_j}{\partial y} + \frac{\partial \mu_2}{\partial y} \right) \right] \tag{55}$$

Recalling that F_j is a function of temperature only and employing definitions (49) and (53a), Equation (55) may be written as follows:

$$j_i + \frac{D_i^T}{T}\frac{\partial T}{\partial y} = -\frac{\rho\bar{D}}{\mu_1}\left[\frac{\mu_2}{m}\frac{\partial Z_i}{\partial y} + \frac{(Z_i - K_i)}{m}\frac{\partial \mu_2}{\partial y} + K_i\left(\frac{1}{F_i^2}\frac{dF_i}{dT} - \mu_3\right)\frac{dT}{dy}\right] \tag{56}$$

Equation (56) provides an explicit representation of the diffusional mass flux of species i in terms of properties and gradients of species i and of the system as a whole, but not of other species. This is the functional relationship that has been sought. Consideration of the temperature dependence of F_i enables a further simplification to be obtained with little loss of accuracy.

Employing the diffusion coefficient correlation Equation (47), the F_i have been computed for the C-N-O system over a wide temperature range in order to evaluate their temperature dependence. If the F_i are assumed constant over the temperature range from 4000° R to $16{,}000^\circ$ R, the maximum error incurred is less than 1 percent. The results of the calculations are shown in Table II. Based on the extremely minor temperature dependence of the F_i for the particular system considered, it is believed reasonable to conclude that this temperature dependence will be at least of second-order importance for all systems of practical interest. Utilizing this generalization, the last term in Equation (56) may be neglected and the equation for diffusional mass flux becomes

$$j_i + \frac{D_i^T}{T}\frac{\partial T}{\partial y} = -\frac{\rho\bar{D}}{m}\frac{\mu}{\mu_1}\left[\frac{\partial Z_i}{\partial y} + \frac{(Z_i - K_i)}{\mu_2}\frac{\partial \mu_2}{\partial y}\right] \tag{57}$$

Substituting the above into the boundary-layer species conservation Equation (40), multiplying the result by the mass of element k in species i (α_{ki}), and summing over all i species yields the boundary-layer conservation equation for chemical elements in a multicomponent boundary layer with unequal diffusion coefficients.

$$\rho u\frac{\partial \tilde{K}_k}{\partial s} + \rho v\frac{\partial \tilde{K}_k}{\partial y} = \frac{\partial}{\partial y}\left(\rho\epsilon_D\frac{\partial \tilde{K}_k}{\partial y} + \frac{\rho\bar{D}\mu_2}{\mu_1 m}\frac{\partial \tilde{Z}_k}{\partial y} - \frac{\rho\bar{D}}{\mu_1}\frac{(\tilde{K}_k - \tilde{Z}_k)}{m}\frac{\partial \mu_2}{\partial y} + \frac{D_k^T}{T}\frac{\partial T}{\partial y}\right) \tag{58}$$

where

$$\tilde{K}_k \equiv \sum_{i=1}^{I} \alpha_{ki} K_i \qquad \tilde{Z}_k \equiv \sum_{i=1}^{I} \alpha_{ki} Z_i \qquad D_k^T \equiv \sum_{i=1}^{I} \alpha_{ki} D_i^T \tag{59}$$

and, for the present purpose, the ϵ_{D_i} are assumed equal.

The boundary-layer conservation equations (momentum, Eq. (41), and energy, Eq. (43)), together with modified Stefan-Maxwell Equation (57) and species conservation Equations (58), constitute a set of $(K+2)$[3] differential equations to characterize the chemically reacting, multicomponent boundary layer with unequal diffusion coefficients. This set of equations represents a gross simplification to the set of equations previously employed to characterize the multicomponent, chemically reacting boundary layer with unequal diffusion coefficients. For example, considering the H-C-N-O system, the number of significant species may be in the neighborhood of 30. The present technique requires the solution of six boundary-layer conservation equations, whereas 32 would have been required previously.

In the following section, simplified correlation equations are proposed to characterize solutions of the above equations in terms of bulk boundary-layer transfer coefficients. These approximate relationships are utilized to develop a set of equations requisite to obtaining a solution of ablation material response coupled to boundary-layer material interactions at the ablating surface.

2.1.2.2 Approximate conservation equations for the multicomponent chemically reacting boundary layer in terms of parameters appropriate to an ablating material wall boundary condition

One of the primary utilities of solutions to the boundary-layer equations is that the results may usually be generalized in terms of simplified correlation equations which, hopefully, include the effects of boundary condition variations over a relatively wide range. In this section, simplified equations are proposed to correlate solutions of the boundary-layer equations developed above. The form chosen for correlation equations of the multicomponent boundary layer with unequal diffusion coefficients is based upon analogies between the form of the present species conservation

---

[3] K represents the number of chemical elements in the system.

Equation (58) and that for the case of equal diffusion coefficients. The form chosen for the correlation equations is such that they should be valid for a wide range of boundary conditions; that is, they include parameters appropriate to transient ablation of charring as well as homogeneous material, both for arbitrary chemical composition of the ablation material and boundary-layer-edge gas.

2.1.2.2.1 Species conservation equation

In order to put the species conservation Equation (58) in a form suitable for inferring the form of its solution, some approximations are introduced. First, thermal diffusion is neglected, and, second, the laminar form of the equation is considered ($\epsilon_D = 0$). Based upon arguments set forth in Ref. 25, the form of correlation equations obtained for the laminar boundary layer are appropriate for the turbulent boundary layer as well.

$$\rho u \frac{\partial \tilde{K}_k}{\partial s} + \rho v \frac{\partial \tilde{K}_k}{\partial y} = \frac{\partial}{\partial y}\left[\frac{\rho \bar{D}}{m}\frac{\mu_2}{\mu_1}\left(\frac{\partial \tilde{Z}_k}{\partial y} + \frac{(\tilde{Z}_k - \tilde{K}_k)}{\mu_2}\frac{\partial \mu_2}{\partial y}\right)\right] \tag{60}$$

It is noteworthy that when all diffusion coefficients are equal, $F_i = F_j = 1.0$, $\bar{D} = D_{ij}$, $(\mu_2/\mu_1) = m$, $\tilde{Z}_k = \tilde{K}_k$, and Equation (60) reduces to the conventional laminar boundary-layer species conservation equation for equal diffusion coefficients.

$$\rho u \frac{\partial \tilde{K}_k}{\partial s} + \rho v \frac{\partial \tilde{K}_k}{\partial y} = \frac{\partial}{\partial y}\left(\rho D_{12}\frac{\partial \tilde{K}_k}{\partial y}\right) \tag{61}$$

Solution of the above may be correlated by an expression relating the diffusional mass flux to the product of a mass-transfer coefficient and mass-fraction difference

$$\tilde{j}_{k_w} = \rho_e U_e C_M \left(\tilde{K}_{k_w} - \tilde{K}_{k_e}\right) \tag{62}$$

where the mass-transfer coefficient may be related approximately to the heat-transfer coefficient (Stanton number).

$$C_M = C_H \, (Le)^{2/3} \tag{63}$$

Equation (60) may be put in the form of Equation (61) by generalizing an approximation which has been found to be appropriate for a number of gas

mixtures that have been considered to date. It has been observed that, the majority of the time, the second term on the right-hand side of Equation (60) is much less than the first, usually,

$$\frac{\tilde{Z}_k - \tilde{K}_k}{\mu_2} \frac{\partial \mu_2}{\partial y} << \frac{\partial \tilde{Z}_k}{\partial y} \tag{64}$$

Utilizing the above approximation, the boundary-layer species conservation equation becomes[4]

$$\rho u \frac{\partial \tilde{K}_k}{\partial s} + \rho v \frac{\partial \tilde{K}_k}{\partial y} \tilde{=} \frac{\partial}{\partial y}\left(\rho \mathcal{D}_{eff} \frac{\partial \tilde{Z}_k}{\partial y}\right) \tag{65}$$

where an effective diffusion coefficient has been defined

$$\mathcal{D}_{eff} = \frac{\overline{D}}{m} \frac{\mu_2}{\mu_1} \tag{66}$$

Clearly, the left-hand side of the differential Equations (61) and (65) represent the flow of species due to convection, and the respective right-hand sides the flow due to diffusion. Based on this observation, the similarity of Equations (61) and (65), and the form of the diffusional mass flux correlation equation for equal diffusion coefficients (62), it seems reasonable to postulate the following correlation equation to characterize solutions of the species conservation equations when the diffusion coefficients are not equal.

$$\tilde{j}_{k_w} = \rho_e U_e C_M \left(\tilde{Z}_{k_w} - \tilde{Z}_{k_e}\right) \tag{67}$$

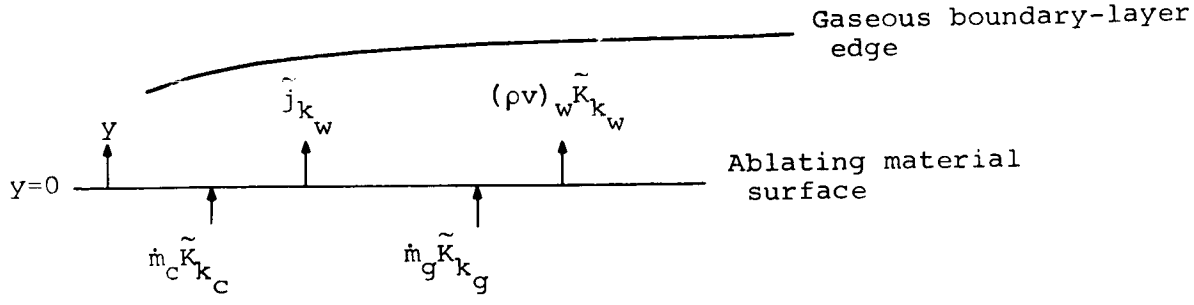
where the previous relationship (63) between heat- and mass-transfer coefficients remains valid and the Lewis number is given by

---

[4] The primary utility of neglecting the second term in Equation (60) is that the similarity between the resulting Equation (65) and Equation (61) suggests the form of a boundary-layer driving potential. Neglecting the second term is often inaccurate (for hydrogen diffusion). Until such time as numerical boundary-layer integrations are performed and correlated with Equation (60), it is felt that Equation (65) is within the uncertainty limits of the numerous approximations and compromizes which are, of necessity, made in the application of the boundary-layer equations to ablation calculations.

$$Le = \frac{\mathcal{D}_{eff}}{\alpha} \tag{68}$$

The elemental mass balance at the surface of a charring ablation material is obtained employing Equation (67) to express the diffusional flux and considering the other appropriate terms shown in the sketch below:



Requiring that chemical elements be conserved at the ablating surface yields the desired form of the ablating surface species conservation equation.

$$\dot{m}_c \tilde{K}_{k_c} + \dot{m}_g \tilde{K}_{k_g} = \rho_e U_e C_M \left(\tilde{Z}_{k_w} - \tilde{Z}_{k_e} \right) + (\rho v)_w \tilde{K}_{k_w} \tag{69}$$

2.1.2.2.2 Energy equation

An approximate correlation equation for the chemically reacting, multicomponent boundary-layer energy equation with unequal diffusion coefficients is rationalized in terms of previously employed correlation equations examined in the light of the proposed correlation Equation (67) for diffusional mass transfer with unequal diffusion coefficients.

The energy equation with <u>equal</u> diffusion coefficients for a nonablating surface is written in the form proposed by Rosner (Ref. 26).

$$\overbrace{k_g \left(\frac{\partial T}{\partial y}\right)_w - \sum_i j_{i_w} h_i^\circ}^{q_w} = \rho_e U_e C_H (H_{sr} - h_{sw})$$

$$+ \rho_e U_e C_M \sum_i (K_{ie} - K_{iw}) h_i^\circ \qquad (70)$$

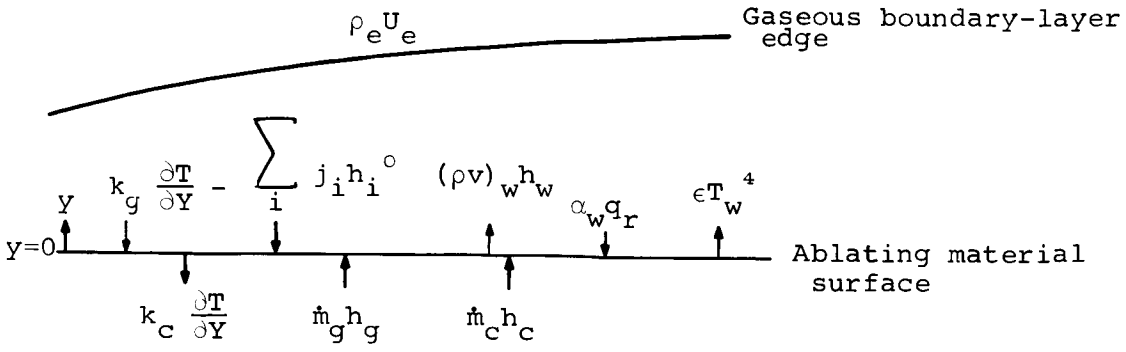
The terms on the left represent the total heat-transfer rate to the material (the wall heat flux) by molecular conduction and diffusion. The right-hand side represents the sensible and chemical energy transfer in coefficient form, the former being characterized by a heat-transfer coefficient and a sensible enthalpy driving potential, and the latter being characterized by a mass-transfer coefficient, concentration driving potentials, and the chemical enthalpies. For equal diffusion coefficients, such an equation can be rationalized on a number of semitheoretical bases or simply based on comparisons with detailed numerical boundary-layer solutions, such as those performed by Fay and Riddell (Ref. 27). For unequal diffusion coefficients, arguments analagous to those leading to Equation (70) will yield

$$\overbrace{k_g \left(\frac{\partial T}{\partial y}\right)_w - \sum_i j_{i_w} h_i^\circ}^{q_w} = \rho_e U_e C_H (H_{sr} - h_{sw})$$

$$+ \rho_e U_e C_M \sum_i (Z_{ie} - Z_{iw}) h_i^\circ \qquad (71)$$

where it is noted that chemical enthalpy transport is now characterized by the Z-driving potential of mass transfer.

The energy balance at the surface of an ablating material may be written utilizing Equation (71) to express the boundary-layer heat transfer by conduction and diffusion. Referring to the sketch below, which depicts the primary energy transfer terms appropriate to a charring material, and requiring that energy be conserved at the ablating surface yields:



$$\rho_e U_e C_H (H_{sr} - h_{sw}) + \rho_e U_e C_M \sum_i (Z_{ie} - Z_{iw}) h_i^\circ$$

$$= (\rho v)_w h_w + k_c \left.\frac{\partial T}{\partial y}\right|_w - \alpha_w q_r + \sigma \epsilon_w T_w^4 - \dot{m}_g h_g - \dot{m}_c h_c \qquad (72)$$

Employing the definition of a blowing parameter,

$$B' = (\rho v)_w / \rho_e U_e C_M \qquad (72)$$

and expressing the sensible recovery enthalpy at the boundary-layer edge as the total recovery enthalpy less the chemical enthalpy, that is,

$$H_{sr} = H_r - \sum_i K_{ie} h_i^\circ$$

the surface energy balance for a charring ablation material in a chemically reacting boundary layer with unequal diffusion coefficients is obtained.

$$\rho_e U_e C_H \left\{ H_r - \sum_i K_{ie} h_i^\circ - h_{sw} + \frac{C_M}{C_H} \left(\sum_i (Z_{ie} - Z_{iw}) h_i^\circ - B' h_w \right) \right\}$$

$$+ \dot{m}_c h_c + \dot{m}_g h_g + \alpha_w q_r - k_c \frac{dT}{dy} - \sigma \epsilon T_w^4 = 0 \qquad (74)$$

The above equation is valid for homogeneous materials as well, for which case the gas generation rate in depth, $\dot{m}_g = 0$, and the char mass-recession rate, $\dot{m}_c$, is replaced with the material mass ablation rate.

The approximate boundary-layer conservation Equations (69) and (74) for chemical elements and energy, respectively, are written in terms of fluxes at the ablating surface and represent the desired form of the boundary condition which is shared by the boundary layer and subsurface conservation equations. The details of the coupled solution are presented in the following section.

2.1.3 Coupled solution of the charring material response and the approximate boundary-layer treatment

The coupled solution has been accomplished by constructing two computer programs. The first, termed the Equilibrium Surface Thermochemistry Program, solves for the surface recession rate and state of the gas adjacent to the surface in terms of the surface temperature, the in-depth gas generation rate, the composition of the boundary-layer-edge gas, and the boundary-layer transfer coefficients. This output information is obtained in tabular form with a parametric variation of the independent variables over the range of interest. The tabular output from the Equilibrium Surface Thermochemistry Program represents the boundary condition input specification for the second computer program, termed the Charring Ablation Material Response Program.

Each of these computer programs are described briefly in the following two subsections (Sections 2.1.3.1 and 2.1.3.2); the assumptions embodied in characterizing the various requisite thermophysical property data and some typical output results are presented for each program. Finally, in Section 2.1.3.3, a simplified approach is presented for the coupled solution when steady-state ablation is assumed.

2.1.3.1 Equilibrium Surface Thermochemistry Program

The basic equations and assumptions embodied in the equations are presented first, in Section 2.1.3.1.1; characterization of requisite thermochemical property information is presented next, in Section 2.1.3.1.2; and finally, in Section 2.1.3.1.3, typical results from the program are presented.

2.1.3.1.1 Basic equations of conservation at the ablating surface for chemical equilibrium

In order to employ the species conservation Equation (69) and surface energy Equation (74), to assess the material ablation rate, it is necessary to consider the degree of chemical equilibrium at the surface, since the terms $\tilde{Z}_{kw}$, h_{sw}, and h_w, depend strongly on the molecular composition of the gases at the surface. The results presented thus far are valid independent of the

degree of chemical equilibrium achieved at the ablating surface. When consideration is given to heterogeneous (gas-solid reactions) chemical kinetics, it is necessary to restrict attention to particular boundary-layer-edge species and ablation material combinations. Recalling the ground rules of the theoretical ablation considerations herein, namely, that a degree of generality be obtained with respect to ablation material-propellant combinations, it was considered impractical to include heterogeneous chemical kinetic considerations. For many cases of practical interest, the assumption of infinite reaction rates (chemical equilibrium) appears to be quite reasonable, and it is this limiting case of reaction rates which is considered in the theoretical ablation model to be reported herein.

In order to consider the species conservation Equation (69) within the constraint of chemical equilibrium, it is convenient to express the gaseous composition at the surface in terms of partial pressures. Employing the definitions of $\tilde{Z}_{kw}$ and $\tilde{K}_{kw}$ and Dalton's law relating mole fractions to partial and total pressures, the following is obtained:

$$\tilde{K}_{kw} = m_k \frac{\sum_i C_{ki} P_i}{\sum_i m_i P_i} \tag{75}$$

and

$$\tilde{Z}_{kw} = m_k \frac{\sum_i C_{ki} P_i / F_i}{\sum_i m_i P_i / F_i} \tag{76}$$

where C_{ki} is the number of k atoms in molecular species i, P_j is the partial pressure of species i, and F_i is the diffusion factor for species i. Substitution of the above into Equation(69), followed by a normalization and rearrangement, yields an expression for the wall condition in terms of quantities at the boundary-layer edge and in the ablating material.

$$B' \frac{\sum_i C_{ki} P_{iw}}{\sum_i m_i P_{iw}} + \frac{\sum_i C_{ki} P_{iw}/F_i}{\sum_i m_i P_{iw}/F_i} = \frac{1}{m_k} \left(\tilde{Z}_{ke} + B_g' \tilde{K}_{kg} + B_c' \tilde{K}_{kc} \right) \qquad (77)$$

where

$$B_g' = \frac{\dot{m}_g}{\rho_e U_e C_M} \quad \text{and} \quad B_c' = \frac{\dot{m}_c}{\rho_e U_e C_M}$$

The chemical equilibrium relations may be written considering formation reactions of each gaseous species i from the elemental gas phase k

$$\sum_k C_{ki} N_k \rightarrow N_i \qquad (78)$$

and similarly for the formation of condensed phase species ℓ from the gaseous elements

$$\sum_k C_{k\ell} N_k \rightarrow N_\ell \qquad (79)$$

The equations of chemical equilibrium corresponding to the above formation reactions may be written in terms of the equilibrium constant $K_p(T)$ for each reaction. For gas-phase formation reactions (Eq. (78)), the following equilibrium relation applies:

$$\ell n\ P_i - \sum_k C_{ki}\ \ell n\ P_k = \ell n\ K_{pi} \qquad (80)$$

If chemical equilibrium is achieved between the gas phase and the surface material, the following equilibrium relation may be written:

$$- \sum_k C_{k\ell}\ \ell n\ P_k \leq \ell n\ K_{p\ell} \qquad (81)$$

The equality in Equation (81) implies the existence of condensed species ℓ; if the condensed phase is not present, the inequality applies (such

would be the case for water at 1 atm pressure for temperatures greater than 212° F, e.g.).

The simultaneous solution of Equations (77), (80), and (81) will yield the surface temperature and molecular composition of the gases adjacent to the surface for specified ablation rates (B'_g and B'_c) and total pressure. The number of equations and unknowns requiring solution is depicted in the table below:

Equation	Number of such equations
(77)	K
(80)	I
(81)	1

Unknown	Number of such unknowns
P_k	K
P_i	I
T_w	1

The quantities not listed as unknowns in the above table are determined prior to solution of the equations from a knowledge of the boundary-layer edge, and ablation material char and off-gas compositions. Although the wall temperature, T_w, does not appear explicitly in any of the equations, the equilibrium constant, K_p, for each of the formation reactions does appear. The above list of unknowns presumes a knowledge of the functional relationship, $K_p = K_p(T)$, for each reaction.

Within the constraint that chemical equilibrium be maintained between the gases and the surface material, one factor, in addition to those listed in the above table, is now known a priori, namely, the chemical composition of the surface material. When considering simple systems such as the ablation of graphite in air, the surface is most certainly carbon; however, when considering ablation of a composite such as silica phenolic, equilibrium considerations may dictate the presence of SiO_2, Si, SiC, or C, depending on the relative char and resin off-gas ablation rates. The equality in Equation (81) will indicate which of the possible materials is at the surface and the inequality will prevail for the remaining condensed species. The solution is accomplished by varying the temperature for a given ablation rate parameter B' until the equality in Equation (81) is obtained for one of the possible condensed-phase surface materials. By this procedure, the

chemical composition of the single surface material remaining is determined and the proper condensed-phase equilibrium equation to be employed in the solution is selected.

Solution of the general set of equations has been achieved by modification of the chemical equilibrium program described in Reference 28. The program applies the basic Newton-Rapheson iterative procedure to the equations in terms of the logarithms of the unknowns. The resulting computer program is called the Equilibrium Surface Thermochemistry Program and enables solution of the above equations by specifying a parametric array of B_c' and B_g'. The resulting output consists of the surface temperature, the enthalpy of the gas at the surface, and the quantity Z_{jw} for all j. For particular char, resin off-gas, boundary-layer-edge gas compositions, and a specified system pressure, the surface temperature, T_w, the enthalpy of the gas at the wall, h_w, and the quantity, Z_{jw}, are obtained as functions of B_c' and B_g'. The mechanics of program operation are best illustrated by considering a specific example and describing input requirements and output results. A description of requisite thermochemical data is presented next in Section 2.1.3.1.2, and is followed in Section 2.1.3.1.3, by some sample computational results obtained from the Equilibrium Surface Thermochemistry Program.

2.1.3.1.2 Thermochemical data for Equilibrium Surface Thermochemistry Program

Solution of the equations described above requires detailed, high-temperature thermochemical data for all molecular species to be considered in the analysis. The computer program employed for solving the equations requires a knowledge of the diffusion factors, F_i, and the following thermochemical data:

(1) The enthalpy of formation at 298° K, $h^{\circ}_{j_{298}}$

(2) The sensible enthalpy rise from 298° K to 3000° K,

$$\int_{298}^{3000} C_{p_j}\, dT$$

(3) The entropy at 3000° K, S_{3000}

(4) α_0, α_1, α_2

The coefficients (α_0, α_1, α_2) are defined by a specific heat-temperature curve fit relation.

$$C_p = \alpha_o + \alpha_1 T + \alpha_2 T^{-2} \tag{82}$$

A computer program has been written to "curve-fit" tabulated thermochemical data and calculate the required coefficients listed above. The program is written to accept a variety of tabulated input data. The primary data source for the current investigation is the JANAF Thermochemical Data (Ref. 29), where a free energy function is tabulated as a function of temperature. The following data, taken from the JANAF tables, are input to the curve-fit computer program.

(1) $h^o_{j_{298}}$

(2) $h_{3000} - h^o_{j_{298}} = \int_{298}^{3000} C_{p_j}\, dT$

(3) S_{3000}

(4) A free energy function, $-(F - h^o_{j_{298}})/T$

Employing Equation (82), an equation may be written relating the above data to the required specific heat coefficients:

$$-\alpha_o \left[\ell n \frac{3000}{T} + \left(1 - \frac{3000}{T}\right)\right] + \alpha_1 T \left\{\left(1 - \frac{3000}{T}\right) - \frac{1}{2}\left[1 - \left(\frac{3000}{T}\right)^2\right]\right\}$$

$$+ \alpha_2\left(\frac{1}{T^2}\right)\left\{\left(1 - \frac{T}{3000}\right) - \frac{1}{2}\left[1 - \left(\frac{T}{3000}\right)^2\right]\right\}$$

$$= \left(\frac{H_{3000} - h^o_{j_{298}}}{T}\right) - S_{3000} - \left(\frac{F - h^o_{j_{298}}}{T}\right) \tag{83}$$

The specific heat coefficients, α_i, are computed employing the above equation, with a "least squares" fit to the tabulated input data over the temperature range from 1000° K to 5000° k. Two sets of curve-fit data are obtained for each of the species over each of two temperature ranges, usually from 1000° K to 3000° K and from 3000° K to 5000° K except for condensed-phase species where the temperature break is normally chosen to correspond to the melt temperature. Besides curve-fitting the data to satisfy relations such as Equation (83), various constraints may also be imposed upon the curve-fit coefficients, such as requiring the calculated

specific heat (C_p) to be identically equal at the temperature dividing the two curve-fit ranges, for example. The accuracy of the curve-fitted data is excellent. Sample output from the program is shown in Table III where the input value of the free-energy function, $-(F - h^{\circ}_{298})/T$, is shown as a function of temperature along with the value of the free-energy function calculated employing Equation (83) with the calculated specific-heat coefficients, α_i. Also shown is the calculated value of the specific heat (C_p) as a function of temperature. The sample results are given for zirconia, liquid and solid on the first page, and the results for ZrO_2 gas on the next page.

The final output from the program for a number of chemical compounds is given in Table IV. The thermochemical data in Table IV are given according to the format described in Reference 28. In Table IV, three lines are occupied by each chemical compound. The first line indicates the data source, and the second and third lines show the thermochemical data for each of the two temperature ranges. The thermochemical data are characterized by six 6-digit numbers. The decimal point is presumed ahead of the number, and each number is followed by the exponent of 10 which multiplies it. The numbers are:

(1) $h^{\circ}_{j_{298}}$ cal/mole

(2) $\int_{298}^{3000} C_p \, dT$, cal/mole

(3) α_o
(4) α_1
(5) α_2
} See Equation (82)

(6) S_{3000}, cal/mole, $^{\circ}k$

The first six numbers are followed by two numbers indicating the lower and upper temperature range for which the data are valid. An asterisk (*) after the chemical symbol generally signifies a condensed phase (liquid or solid). The sources of thermochemical data represented are: Reference 30 for hydrocarbons, Reference 31 for hafnium compounds, and Reference 29 for the remaining compounds. The equilibrium constants, K_p, for formation of each species, as required in the Equilibrium Surface Thermochemistry Program, may be evaluated from the above thermochemical data.

The data in Table IV represents a relatively complete, comprehensive list of currently available thermochemical data and has been used for all calculations reported herein.

Evaluation of the diffusion factors, F_i, is performed in an approximate manner which has been found quite satisfactory for engineering calculations.

$$F_i = \frac{m_i^{1/2}}{\left(\prod_i m_i^{1/2}\right)^{1/I}} \tag{84}$$

The validity of the above approximation is established by considering an example. Shown in Figure 4 is a plot of the diffusion factor data (F_i) taken from Table II for the C-N-O system as a function of the right-hand side of the above equation. As shown in the figure, the maximum error in the approximate Equation (84) for the data considered is 7.3 percent. It is interesting to note the form of the factor Z_i when the diffusion factor is given by Equation (84).

$$Z_i = \frac{x_i\, m_i^{1/2}}{\sum_i x_i\, m_i^{1/2}}$$

It is noted that the value of Z_i lies between a mass and a mole fraction for species i and, as such, it is clearly seen that the utilization of ΔZ_i as the driving potential for diffusional mass transfer causes lighter species to diffuse faster than heavy species.

2.1.3.1.3 Sample problem for Equilibrium Surface Thermochemistry Program

In order to best illustrate the input requirements and output information obtained from the Equilibrium Surface Thermochemistry Program, a sample problem is described in this section. The problem considered is for the transient ablation of silica phenolic in an exhaust-product environment of N_2O_4-N_2H_4/UDMH combustion with an oxidizer-to-fuel mass ratio (O/F) of 2.0. The required input information consists of the thermochemical data for all species described in the previous section, and information pertaining to the ablation material and its environment. The input information is described first and is followed by presentation of some results.

Ablation Material Input.- The type of information required to characterize the ablation material is indicated by considering the equations being solved. These equations are given in Section 2.1.3.1.1, where it is noted that the material is characterized by the elemental mass fractions of the char and pyrolysis gases, $\tilde{K}_{k_c}$ and $\tilde{K}_{k_g}$, respectively. The ablation material being considered is 68 percent silica (SiO_2) and 32 percent phenolic resin (C_6H_6O) by mass. The following represents the effective molecular composition of the ablation material:

$$\underbrace{1.132\ SiO_2}_{68\text{ grams}} + \underbrace{0.34\ C_6H_6O}_{32\text{ grams}} \rightarrow \underbrace{\text{char + gas}}_{100\text{ grams}}$$

It is assumed that half of the resin mass is left behind in the form of pure carrbon upon decomposition of the virgin material, and that all of the silica remains in the char. The char, therefore, is composed of 16 grams of carbon and 32 grams of silica. The remaining 16 grams of material leaves in the form of gas resulting in an overall, idealized reaction of the following form:

$$\underbrace{1.132\ SiO_2 + 0.34\ C_6H_6O}_{100\text{ grams plastic}} \rightarrow \underbrace{1.132\ SiO_2 + 1.332\ C}_{84\text{ grams char}} + \underbrace{0.708\ C + 2.04\ H + 0.34\ O}_{16\text{ grams gas}}$$

The elemental mass fractions of the char and gas may be obtained directly from the above.

k	$\tilde{K}_{k_c}$ $\left(\frac{\text{mass element k}}{\text{unit mass char}}\right)$	$\tilde{K}_{k_g}$ $\left(\frac{\text{mass element k}}{\text{unit mass gas}}\right)$
H	---	0.1285
C	0.1905	.5315
O	.4315	.3400
Si	.3780	---

Boundary-Layer-Edge Input.- Referring to the equations in Section 2.1.3.1.1, it is noted that the boundary-layer edge is characterized by its elemental "Z" fractions, $\tilde{Z}_{k_e}$. These may be computed from a knowledge of the boundary-layer-edge molecular composition and the molecular diffusion factors, F_i. The effective chemical composition of the propellant may be written as follows for a 100 gram system with O/F = 2.0:

$$0.725\ N_2O_4 + 0.52\ N_2H_4 + 0.277\ C_2N_2H_8$$

The elemental mass fractions follow directly from the above.

k	$\tilde{K}_{k_e}$ $\left(\frac{\text{mass element k}}{\text{unit mass edge gas}}\right)$
H	0.0431
C	.0666
N	.4258
O	.4645

Specification of the above composition, the local pressure, and the boundary-layer-edge temperature or enthalpy enables calculation of the boundary-layer-edge molecular composition by the Equilibrium Surface Thermochemistry Program. The boundary-layer-edge molecular "Z" fractions, Z_{i_e}, are then evaluated internally in the program as well with utilization of the equation for Z in terms of the approximate diffusion factors (Eq. (85)). The elemental "Z" fractions, $\tilde{Z}_{k_e}$, are obtained directly from the defining Equation (59). The boundary-layer-edge temperature and pressure selected for the sample problem are 2790° K and 4.23 atmospheres, respectively; these values are characteristic of the rocket-nozzle throat region for an engine having a chamber pressure of 100 psia.

The resulting output from the Equilibrium Surface Thermochemistry Program, shown in Figure 5, is obtained by specifying the above input information and a parametric array of the two normalized ablation-rate parameters, B_c' and B_g'. The equilibrium surface temperature is shown in Figure 5(a) as a function of B_c' with B_g' as a parameter. The effective wall enthalpy, which is required for solution of the surface-energy Equation (74), is shown in Figure 5(b). The effective wall enthalpy is defined by rewriting the surface-energy equation.

$$\left[H_r - (H_w)_{eff}\right] + \frac{C_M}{C_H}\left(B_c'h_c + B_g'h_g\right) + \frac{\alpha_w q_r - \sigma\epsilon T_w^4 - k_c\left(\frac{dT}{dy}\right)_w}{\rho_e U_e C_H} = 0 \qquad (86)$$

The term in square brackets appears in the normal form of the driving potential for heat transfer to a nonablating surface with equal-diffusion coefficients and a Lewis number of unity. The effective wall enthalpy is defined here to include the effects of both unequal-diffusion coefficients and a non-unity Lewis number consistent with Equation (74).

$$(H_w)_{eff} = \sum_i K_{i_e} h_i^{\circ} + h_{s_w} - \frac{C_M}{C_H}\left[\sum_i \left(Z_{i_e} - Z_{i_w}\right) h_i - B' h_w\right] \qquad (87)$$

In the sample problem, the ratio C_M/C_H was evaluated from Equation (63) assuming a boundary-layer Lewis number of 0.92.

The results from the Equilibrium Surface Thermochemistry Program, shown in Figure 5, represent information necessary to evaluate the surface recession and energy-transfer rates to the ablating surface in terms of the boundary-layer heat-transfer coefficient, $\rho_e U_e C_H$, recovery enthalpy, H_r, and the ablation material response. This information represents the requisite boundary conditions for the Charring Material Response Program which is described in the next section.

2.1.3.2 Charring Material Response Program

The finite-difference equations selected to characterize the subsurface thermochemical response of charring materials were presented in Section 2.1.1. In this section, the treatment given the various requisite material thermal-property data and boundary-layer transport coefficients is described first, and is followed by a presentation of results from a sample problem.

2.1.3.2.1 Ablation material thermal-property data

The thermal-property information required in the Charring Material Response Program may be realized by considering the equations for the subsurface response presented in Section 2.1.1. The requisite data consists of the following:

(1) Reaction kinetic information for in-depth degradation of organic constituents.

(2) Enthalpy and specific heat of virgin material and char as a function of temperature.

(3) Thermal conductivity and emissivity of composite as a function of temperature.

(4) Enthalpy of internally generated decomposition gaseous products as a function of temperature.

Specification of the above information is accomplished by simple table look-up with linear interpolation between entries. An example of the above property information for typical graphite phenolic and silica phenolic materials is given in Table V. The specific heat and thermal conductivity data for the virgin material and char are usually determined experimentally

with standard high-temperature thermal property measuring techniques (see, e.g., Ref. 32). The enthalpy of the plastic and char is evaluated internally in the Charring Material Response Program by numerically integrating the specific heat-input data via Equations (21) and (22). The reaction kinetic information for in-depth degradation of organic constituents is obtained from correlating thermogravimetric analysis (TGA) data (see, e.g., Refs. 18, and 33). Characterization of the off-gas composition may not be obtained in a straightforward manner from experimental measurements. Normally it is calculated based upon some assumption regarding the kinetics of further gas-phase reactions after the initial decomposition has occurred. The assumption employed herein is consistent with that proposed in Reference 7, namely, it is assumed that the gases are in chemical equilibrium but that condensed-phase carbon not be allowed to "precipitate out." A typical resin off-gas composition based upon this model is shown in Figure 6, and the resulting gas enthalpy is shown as a function of temperature in Figure 7.

2.1.3.2.2 Boundary-layer transport phenomena

In addition to the surface thermochemistry information presented in Section 2.1.3.1, and the material thermal-property information described above, it is necessary to specify the boundary-layer heat-transfer coefficient ($\rho_e U_e C_{H_o}$), recovery enthalpy (H_r), and incident radiation energy flux (q_r) as functions of time. The treatment given boundary-layer transport phenomena was described previously in Section 2.1.2.2 where the transfer of heat and mass in the chemically reacting, multicomponent boundary layer is related to a bulk boundary-layer heat-transfer coefficient. The approach taken to evaluate this heat-transfer coefficient for a nonablating wall is illustrated in Appendix A where a sample calculation is performed to a cold, nonablating nozzle throat for a N_2O_4-N_2H_4/UDMH rocket engine having a throat diameter of 7.8 inches and a chamber pressure of 100 psia. The ratio of heat-transfer coefficient with blowing to that without blowing is evaluated from the linear approximation for low blowing rates (Ref. 35).

$$\frac{C_H}{C_{H_o}} = \frac{1}{1 + K_B B'} \quad (\text{for } B' < 0.2) \tag{88}$$

where $K_B = 0.375$ for turbulent flow. The no-blowing value of the heat-transfer coefficient, $\rho_e U_e C_{H_o}$, is input to the computer program as a table

look-up function of time, and Equation (88) is utilized for evaluating the actual heat-transfer coefficient based upon the instantaneous value of the blowing parameter, B'. The radiation heat flux, q_r, and recovery enthalpy, H_r, may also be functions of time, but for the sample problem, the following constant values were employed:

$$\rho_e U_e C_{H_o} = 0.14 \text{ lb/ft}^2\text{-sec}$$

$$q_r = 28.6 \text{ Btu/ft}^2\text{-sec}$$

$$H_r = 105 \text{ Btu/lb}$$

The above values are typical of conditions at the throat of a particular rocket engine using N_2O_4-N_2H_4/UDMH as a propellant and correspond to conditions utilized for comparing theoretical predictions to data reported in a subsequent section (Section 2.3).

2.1.3.2.3 Charring Material Response Program sample problem

In this section, some typical results from the Charring Material Response Program are presented. The data presented in Section 2.1.3.1.3, obtained from the Equilibrium Surface Thermochemistry Program, and other material property and boundary condition information presented above, represent sufficient information to enable solution of the previously developed equations which characterize the internal, thermochemical response of charring materials.

The calculations utilized the material properties for silica phenolic presented in Table V, and are for a partially pre-charred nozzle, that is, a nozzle which had been previously fired and charred to a depth 0.073 inch below the heated surface. The resultant output from the Charring Material Response Program is shown graphically in Figures 8(a) through 8(d). Figure 8(a) depicts the temperature histories of the surface and several internal locations; the temperature distribution through the material is shown for several times in Figure 8(b); the initial density distribution and the density distribution through the material is shown at several times in Figure 8(c); and the surface-recession rate and internal decomposition off-gas rate are shown as functions of time in Figure 8(d). The boundary conditions described above were applied until 104 sec, at which time firing termination occurred and the nozzle was allowed to cool by radiation. The

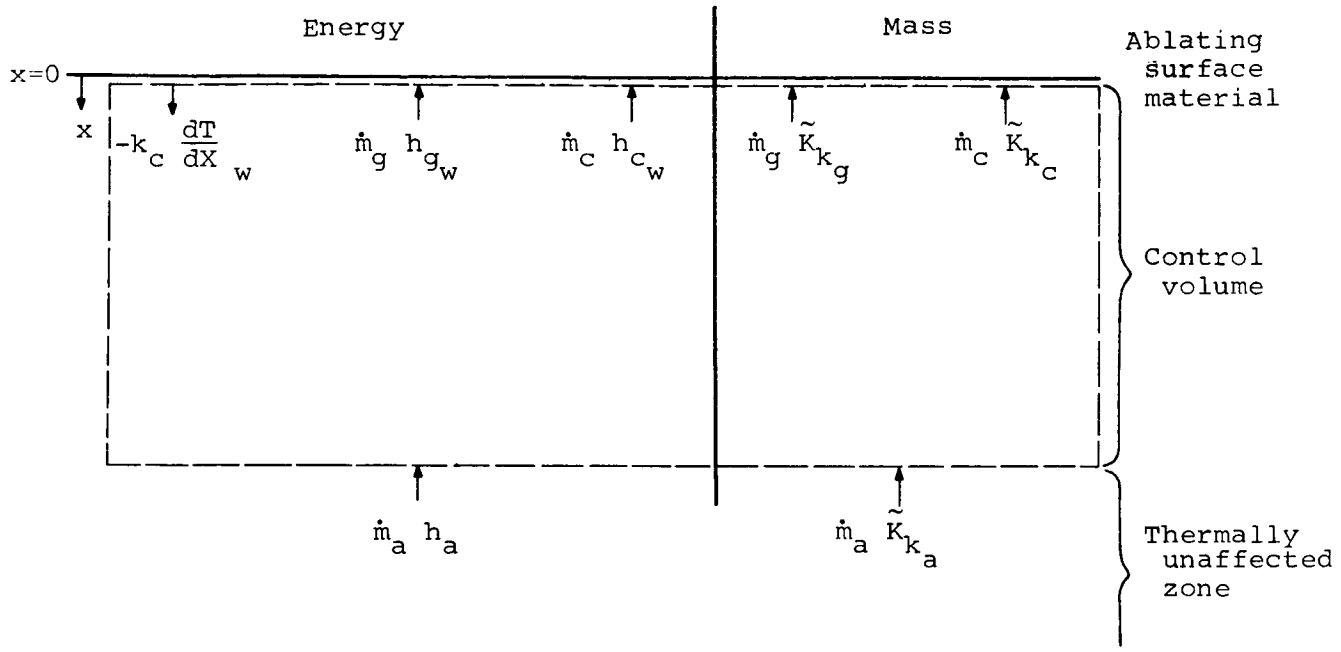
significant growth of the char layer after thrust termination is apparent from Figure 8(c).

The results shown in Figures 8(a) through (d) represent a particular solution of the equations developed previously to characterize the ablation material subsurface response subjected to boundary conditions appropriate to the chemically reacting, multicomponent boundary layer. Presentation of the results has been accompanied by a description, in rather laborious detail, of all pertinent material property and boundary-condition information. This degree of completeness has been retained here in order to enable the reader to understand, as completely as possible, the assumptions in and limitations of, the theoretical considerations reported herein.

The considerations presented thus far in this section have been directed toward the mathematical characterization of transient ablation. For certain problems of practical interest, depending on the ablation material and its environment, the ablation rate of and temperature distribution through the ablation material may become invariant with time. This situation, termed "steady-state ablation," is far simpler to characterize mathematically than transient ablation, and solution of the resulting equations requires specification of many less material thermal properties. In the following subsection, the mathematical characterization of steady-state ablation is presented.

2.1.3.3 Steady-state ablation

Steady-state ablation is best described by considering a control volume extending from the ablating surface back into the thermally unaffected zone of the virgin material. Shown in the sketch below is such a control volume depicting the various energy and mass-transfer terms crossing the control volume boundaries. To be strictly correct, the steady-state assumption applies only to flat (planer) geometries, or whenever the cross-sectional area on the two boundaries of the control volume may be assumed equal.



Steady-state ablation exists whenever the energy and chemical element content within the control volume is invariant with time. This situation will normally exist when the temperature distribution through the control volume and surface-recession rate are invariant with time. When this situation exists, we may perform an energy balance and a chemical elemental balance on the control volume to yield the following two equations:

$$\dot{m}_a h_a - k_c \frac{dT}{dx}_w = \dot{m}_g h_{g_w} + \dot{m}_c h_{c_w} \tag{89}$$

and

$$\dot{m}_g \tilde{K}_{k_g} + \dot{m}_c \tilde{K}_{k_c} = \dot{m}_a \tilde{K}_{k_a} \tag{90}$$

Substitution of Equation (89) into the surface energy Equation (74), and Equation (90) into the surface species conservation Equation (77) yields the steady-state energy balance and species conservation equations.

Energy:

$$\rho_e U_e C_H \left\{ H_r - \sum_i K_{i_e} h_i^{\circ} - h_{s_w} + \frac{C_M}{C_H} \left[\sum_i \left(Z_{i_e} - Z_{i_w} \right) h_i - B' h_w \right] \right\}$$

$$+ \alpha_w q_r - \sigma \epsilon T_w^4 + \dot{m}_a h_a = 0 \qquad (91)$$

Species:

$$B' \frac{\sum_i C_{ki} P_{iw}}{\sum_i m_i P_{iw}} + \frac{\sum_i C_{ki} P_{iw}/F_i}{\sum_i m_i P_{iw}/F_i} = \frac{1}{m_k} \left(\tilde{Z}_{ke} + B' \tilde{K}_{k_a} \right) \qquad (92)$$

The above equations do not include dependence upon terms which must be evaluated from the Charring Material Response Program, namely, the magnitude of conduction into the char ($k_c \; dT/dx$) and the relative magnitudes of the off-gas rate ($\dot{m}_g$) and char-recession rate ($\dot{m}_c$) have been eliminated from the equations. Solution of the steady-state Equations (91) and (92) may be accomplished without a knowledge of internal decomposition kinetics or material thermal properties. Solution is accomplished utilizing the Equilibrium Surface Thermochemistry Program with a parametric variation of B'. The resulting output provides sufficient information to evaluate all terms in the energy equation and solve directly for the ablation rate, B', and the corresponding surface temperature. The results of such a solution are shown in Figure 9 where the steady-state ablation rate satisfying the energy Equation (91) is shown for a silica phenolic material in a N_2O_4-N_2H_4/UDMH environment. Two solutions are shown, one for equal and one for unequal diffusion coefficients. It is noted that the steady-state ablation rate assuming equal diffusion coefficients is 38 percent greater than that considering unequal diffusion coefficients.

The substantial simplification afforded the mathematical treatment of the ablation process by assuming steady-state ablation has been demonstrated. The simplification, however, has questionable utility unless some criteria can be devised to indicate under what conditions the assumption may be applied. Such a criteria has been devised and is described in the following paragraphs.

Exact solutions exist for the transient thermal response of certain materials subjected to particular idealized boundary conditions (e.g., Refs. 37 and 38); however, it is not clear that they may be used to determine the adequacy of a steady-state solution when realistic boundary conditions and material thermal properties are employed. The approach taken here is to perform transient ablation calculations with the Charring Material Response Program, and to compare these results to the steady-state ablation solution. The time required to reach 95 percent of steady-state ablation is noted. At this time the degree of approach to steady-state ablation given by various exact, idealized solutions is determined and compared to the 95-percent figure for the charring ablator. One of the idealized solutions presented in Reference 37 has been found to yield an adequate indication of the time required to reach steady state. This solution is for the case of a slab initially at a uniform temperature, T_i, which is subjected to a step increase in surface temperature to T_w, and a constant surface-recession rate, $\dot{S}$, for time greater than zero. The result for the exact solution to the approximate problem is shown in Figure 10. Shown in Figure 10 is a parameter indicating the degree of approach to steady-state ablation as a function of normalized time. This figure is used later to compare with the results of the numerical solution.

Numerical transient ablation solutions were obtained with the Charring Material Response Program for a silica phenolic (70% - 30% by mass, respectively) material in a N_2O_4-N_2H_4/UDMH environment with heat-transfer coefficients, $\rho_e U_e C_{H_o}$ = 1.0, 0.5, 0.2, and 0.1 lb/ft^2-sec. The surface-recession rate and temperature are determined entirely from chemical-equilibrium considerations. The resulting surface temperature and recession-rate histories are shown in Figures 11 and 12, respectively. Also shown in the figures are the steady-state values determined from solution of the steady-state Equations (91) and (92). The recession-rate histories are shown as a function of the normalized time parameter.

$$\tau = \sqrt{\dot{S}_{ss}{}^2 \theta / \alpha_p}$$

where

$\dot{S}_{ss}$ steady-state surface-recession rate

θ time

α_p thermal diffusivity of the virgin plastic

The normalized time parameter is suggested from the exact solution to the approximate problem shown in Figure 10. It is noted that for all four solutions the time at which 95 percent of the steady-state ablation rate is achieved is approximately $\tau = 1.4$. It is not clear whether the char diffusivity, α_c, or the virgin plastic diffusivity, α_p, should be used in the normalized time parameter, τ. The virgin plastic diffusivity is employed here only because it results in the exact and numerical solutions approaching steady-state ablation at more nearly the same value of τ.

The results presented in this section enable evaluation of the approximate time to reach the steady-state ablation rate for charring ablation materials in a rocket-nozzle environment. Some additional calculations should be performed for different materials in different environments before the generalization may be accepted with complete confidence; however, it is believed that the results will essentially confirm those reported here.

2.2 Material-Propellant Chemical-Interaction Studies

In this section, the theoretical ablation model described above in Section 2.1 is utilized to investigate the compatibility of a number of potential rocket-nozzle insulation materials with various rocket-propellant environments, and to investigate the importance of certain chemical reactions for a particular material-environment combination. This portion of the theoretical investigations was performed prior to formulation of the approximate technique for considering boundary-layer transport processes characterized by unequal binary-diffusion coefficients, and, as a result, calculations presented in this section are based on the assumption of equal diffusion coefficients.

Results from the investigation of the chemical compatibility of a number of materials in several environments are presented first in Section 2.2.1, and are followed in Section 2.2.2 by an investigation into the importance of certain reactions controlling the ablation of graphite in the combustion product environment of OF_2-B_2H_6 rocket propellant.

2.2.1 Material-propellant compatibility

The investigation of the chemical compatibility of potential nozzle insulation materials in various environments is based upon the assumption of steady-state ablation discussed above in Section 2.1.3.3. The solutions are obtained in two steps; the combined solution of the steady-state species conservation Equation (92), and the chemical equilibrium relations (Eqs. (80) and (81)), are presented first in Section 2.2.1.1, and are followed in

Section 2.2.1.2 by solutions of the steady-state energy balance Equation (91) yielding the ablation rate and surface temperature.

2.2.1.1 Solution of the species conservation and chemical equilibrium equations

Solution of the species conservation and chemical equilibrium relations is obtained with the Equilibrium Surface Thermochemistry Program. When all diffusion coefficients are assumed equal, the surface species conservation Equation (92) may be written:

$$\frac{\sum_i C_{ki} P_{iw}}{\sum_i m_i P_{iw}} = \frac{\tilde{K}_{ke} + B' \tilde{K}_{ka}}{m_k (1 + B')} \qquad (93)$$

Solutions are obtained by specifying a range of B' for given boundary-layer-edge compositions, $\tilde{K}_{k_e}$, and material compositions, $\tilde{K}_{k_a}$. The materials and propellants considered in the study are as follows:

Propellants

Oxidizer	Fuel	O/F = mass oxidizer / mass fuel
OF_2	B_2H_6	3.0
N_2O_4	50% N_2H_4 + 50% UDMH by mass	2.0
O_2	H_2	4.0
50% O_2 + 50% F_2 by mass	CH_4	4.0

Materials

BeO	Silica phenolic 70-30	ZrO_2
TiB_2	Silica phenolic 50-50	W
Ti_2O_3	Silica phenolic 30-70	TiC
C	Graphite phenolic 70-30	ZrC
HfB_2	Graphite phenolic 50-50	TiN
HfO_2	Graphite phenolic 30-70	ZrN

The results of the solutions with the Equilibrium Surface Thermochemistry Program are shown in Figures 13(a) through 16(c) where the chemical ablation rate parameter, B', is shown as a function of surface temperature for the above material-propellant combinations. Shown in each figure is the propellant, the virgin material composition, and the composition of the surface material in equilibrium with the gaseous boundary layer. Shown in Figures 13(a) through 13(d) are the results for the 18 above materials in the OF_2-B_2H_6 environment, those for the O_2-H_2 environment in Figures 14(a) and 14(b), for the N_2O_4-Aerozine environment in Figures 15(a) through 15(c), and, finally, for the Flox-methane environment in Figures 16(a) through 16(c).

The utility of the results shown in Figures 13(a) through 16(c) is twofold. First, it provides necessary information to solve the steady-state energy balance, and, second, it provides insight into the basic chemical interactions occurring between a material and its environment. Even though chemical equilibrium is often not achieved, the results shown are representative of the equilibrium the various kinetic mechanisms are approaching. Referring to Figures 13(a), 14(a), 15(a), and 16(a), the relative susceptibility to chemical erosion of graphite phenolic may be qualitatively assessed for each of the four environments. The erosion is low in both fluorine-containing environments, OF_2-B_2H_6, and Flox-methane; moderate ablation occurs in the N_2O_4-Aerozine environment, with the ablation becoming high in the O_2-H_2 environment. In all cases considered, the performance of the material increased with increasing carbon content. Preference for graphite phenolic over pure graphite, or high phenolic content over high graphite content composites should be justified on the basis of lower thermal diffusivity or higher strength, since resistance to chemical erosion is clearly superior with increasing graphite content in all environments considered. In addition to the magnitude of the erosion rate, it is interesting to note the wall material composition in equilibrium with the boundary-layer gas. For example, the response of 30 percent silica and 70 percent phenolic in the OF_2-B_2H_6 environment shown in Figure 13(b) indicates that the surface material is B_2O_3 for $0.05 \lesssim B' \lesssim 0.175$, SiC for $0.175 \lesssim B' \lesssim 0.45$, and C for $0.45 \lesssim B' \lesssim 1.0$. Only for the high silica content composite is the surface material composed of SiO_2. Reference to Figure 14(b), the O_2-H_2 environment, however, indicates the surface material for all silica phenolic materials considered is SiO_2 for this environment. This is a result of the fact that more oxygen is available in the propellant to oxidize the carbon-containing species.

The results from the Equilibrium Surface Thermochemistry Program shown in Figures 13(a) through 16(c) are employed in the following section to obtain a steady-state energy balance for many of the materials considered.

2.2.1.2 Energy balance solutions

In this section, a steady-state energy balance is obtained for certain of the materials considered in order to yield a surface recession rate and operating surface temperature. The steady-state energy balance equation requiring solution results from rewriting Equation (91) for the special case of equal diffusion coefficients, and unity Lewis and Prandtl numbers. With these assumptions, the following simplifications apply.

$$\frac{C_M}{C_H} = 1.0$$

$$K_i = Z_i$$

If radiation is neglected, the steady-state enrgy balance becomes:

$$B'H_e - (1+B')h_w + B'h_a = 0 \qquad (94)$$

Solution of the above energy balance equation for a number of materials considered would indicate surface temperatures considerably in excess of their melting temperatures. This would be unrealistic, and, as such, steps were taken to build a greater degree of reality into the calculations by allowing removal of the liquid from the surface at the melt temperature. This is accomplished by adding a term to the energy equation to account for the energy carried from the surface in the form of liquid removal. The energy transfer rate associated with liquid removal is given by the product of the liquid layer mass removal rate ($\dot{m}_r$) and the enthalpy of the liquid at the surface temperature (h_{r_w}). Incorporation of this term to the energy balance yields

$$B'H_e - (1+B')h_w + \dot{B}h_a - (\dot{B}-B')h_{r_w} = 0 \qquad (95)$$

where a total ablation rate parameter has been defined.

$$\dot{B} \equiv B' + \frac{\dot{m}_r}{\rho_e U_e C_H} \qquad (96)$$

Solutions to Equation (95) are obtained for each of the 18 materials in each of the four propellant environments except for those cases where the surface material melts and has a composition different from the virgin material. Extra effort is required to obtain solutions for this case and it was deemed not worthwhile.

The results of the energy equation solution are shown in Tables VI(a) through VI(d), where the equilibrium steady-state values of the chemical ablation-rate parameter, B', the total ablation-rate parameter, $\dot{B}$, the surface linear recession rate, the composition of the surface material, and the surface temperature are given for a number of the materials in each of the four propellant environments. The criterion employed for mechanical removal of material from the surface is a simple one, neamely, if the surface material reaches its melt temperature before an energy balance is achieved, the liquid is presumed removed at the melt temperature. All materials considered have a well-defined melt temperature except silica and carbon. No mechanical removal of either of these materials is considered.

Materials appearing to have the most promise from a chemical resistance point of view for each of the propellants considered may be determined by referring to Tables VI(a) through VI(d). Three materials appear superior in the OF_2-B_2H_6 environment. Graphite has the minimum mass loss rate ($\dot{B} = 0.230$) with a linear surface-recession rate of 4.6 mils/sec. The minimum linear surface recession is found with TiB_2 ($\dot{S} = 3.6$ mils/sec) which has a mass recession rate of $\dot{B} = 0.422$, or about twice that of carbon. The minimum combination of mass and linear recession rate occurs with B_4C ($\dot{B} = 0.251$, $\dot{S} = 4$ mils/sec); note that B_4C operates with a surface temperature only 20° R below its melt temperature.

Five materials have no surface recession in the O_2-H_2 environment: HfB_2, HfO_2, ZrC, ZrN, and ZrO_2. It is noted that in all cases the surface material is the oxide (HfO_2 or ZrO_2) of the metal. No surface recession occurs because a protective oxide film is formed. The results are based on the assumption that the oxide film adheres to the metallic boride, carbide, or nitride.

The boride and oxide of hafnium have no surface recession in the N_2O_4-N_2H_4/UDMH environment. For this propellant, the stagnation temperature is in excess of the melt temperature of ZrO_2 which results in a melt layer forming on the surface of the zirconium materials.

The melt temperature of HfO_2 and ZrO_2 is exceeded in the Flox-CH_4 environment resulting in significant melting in both cases. Carbon yields

the minimum mass-recession rate ($\dot{B} = 0.2$) with a linear surface-recession rate $\dot{S} = 3.9$ mils/sec. The minimum linear surface-recession rate is obtained with tungsten ($\dot{S} = 0.6$ mils/sec, $\dot{B} = 0.304$).

The apparent superiority of high graphite content phenolic-graphite materials over those with a low graphite content was apparent from the equilibrium surface thermochemistry results shown in Figures 13(a) through 16(c). This trend is confirmed with the energy equation solutions tabulated in Tables VI(a) through VI(d). The surface recession rate and temperature for the graphite-phenolic materials are shown in Figures 17(a) through 17(d) as a function of phenolic content for each of the four propellants considered. In each case, the trend of increased ablation rate with increasing phenolic content is evident.

The assumptions employed in the analysis must be kept in mind when considering the above-described results. The chemical erosion rates reported are for steady-state ablation with chemical equilibrium achieved at the surface. Both of these factors tend to maximize the predicted ablation rates; however, mechanical erosion (except for the case of simple melting) is not considered.

In the following subsection some consideration is given to heterogeneous chemical kinetics at the ablating surface for a particular material-environment combination.

2.2.2 Importance of particular heterogeneous reactions governing graphite ablation in the OF_2-B_2H_6 environment

As indicated above, ablation rates predicted assuming chemical equilibrium will often be greater than are observed experimentally. The ablation rate is often dictated by the rate at which heterogeneous (gas-solid) reactions may procede. Prior to considering heterogeneous chemical kinetic mechanisms, it is necessary to define the chemical reactions requiring kinetic data over a wide range of ablation rate and surface temperature. Normally, this phase of a chemical kinetic study does not require any extensive analysis, since the reactions requiring investigation are usually apparent. When consideration is given to the reactions between graphite and the products of combustion of an OF_2-B_2H_6 propellant, however, the major reactions are not apparent. The purpose of the work described in this section is to define these major chemical reactions between graphite and the OF_2/B_2H_6 environment over a wide range of surface temperature and graphite ablation rate.

The equilibrium composition of the products of combustion of OF_2-B_2H_6 is shown in Figure 18 as a function of temperature. This composition is representative of that existing at the edge of the boundary layer. As reactions occur at the wall, the boundary-layer-edge molecular species will traverse the boundary layer, and their temperature will approach the wall temperature. The reactions of interest are those between the boundary-layer-edge species at the wall temperature (as shown in Fig. 18) and the graphite wall. The rate at which each of these many possible reactions may proceed is of interest here. The approach taken is to calculate the composition which will occur if all reaction rates are infinite (if chemical equilibrium is achieved), and, then, to assess the relative importance of each of the reactions with respect to the quantity of carbon consumed.

The equilibrium composition resulting at the graphite surface is obtained utilizing the Equilibrium Surface Thermochemistry Program described above. The resulting composition and surface temperature as a result of chemical equilibrium between the gas phase and the graphite surface are shown as functions of the normalized ablation-rate parameter, B', in Figure 19. Shown in Figure 20 is the ablation parameter, B', as a function of temperature. If complete chemical equilibrium were achieved between the gas phase and graphite surface, the ablation rate shown on the curve in Figure 20 would result for any given temperature. If, however, the gas phase is not in equilibrium with the graphite surface, the ablation rate for any given temperature will fall below the curve. The reactions requiring investigation for the kinetic study are those occurring for combinations of the ablation-rate parameter, B', and surface temperature below the curve shown in Figure 20. The approach taken in this study is to determine the important chemical reactions resulting from gas phase equilibrium for these combinations of temperature and ablation rate below the curve.

The combinations of ablation rate and temperature considered are shown as circled points in Figure 20. The gas-phase chemical equilibrium composition not in equilibrium with the graphite surface is shown in Figures 21(a) and 21(b) for B' of 0.2 and 0.4, respectively. A systematic technique has been devised for determining the important reactions which characterize the chemical composition change from that of the propellant products (Fig. 18) to that of the ablation products such as are shown in Figures 21(a) and 21(b). The technique is briefly described and is followed by a description of the results.

The gas-phase elemental composition, adjacent to a surface which is ablating as a result of chemical reactions producing gaseous products, is obtained by rewriting Equation (93) in terms of the elemental gas phase mass fraction (Eq. (75)).

$$\tilde{K}_{k_w} = \frac{\tilde{K}_{k_e} + B'\tilde{K}_{k_a}}{1 + B'} \tag{97}$$

In the OF_2-B_2H_6 environment, no carbon is present in the free stream and, for graphite, only carbon is present in the virgin material which results in the following relations for graphite ablation in the OF_2-B_2H_6 environment:

$$\tilde{K}_{k_w} = \frac{\tilde{K}_{k_e}}{1 + B'} \quad \text{for} \quad k = H,\ B,\ O,\ \text{and}\ \ F \tag{98}$$

and

$$\tilde{K}_{k_w} = \frac{B'}{1 + B'} \quad \text{for } k = C \tag{99}$$

The problem of characterizing the important chemical reactions in going from pure proepllant products (Fig. 18) to ablation products (e.g., Figs. 19 and 21) reduces to one of considering reactions between the propellant environment shown in Figure 18 with the quantity of constituents reduced by an amount dictated by Equation (98) and replaced by an amount of carbon given by Equation (99). A number of linearly independent chemical reactions are then postulated between the quantity of reactants as described above and the ablation product composition such as is shown in Figures 21(a) and 21(b). The number of linearly independent chemical reactions which may be postulated is equal to N, where N is the number of molecular species considered in the reactions less the number of chemical elements in the system (N = I - K). At this point, the problem is reduced to solving a set of (N + K) linear algebraic equations with as many unknowns where N is the number of linearly independent reactions and K is the number of elements in the system. A number of equations equal to N correspond to requiring that the N chemical reactions balance, and the remaining K equations correspond to requiring that the quantity of chemical elements in all of the reactants equal the quantity of elements considered for reaction. The relative importance of each reaction is given by the fraction of the total carbon mass consumed in that reaction.

The molecular species considered in the study include all those that appear to a significant extent in either the propellant environment or the ablation products, a list of which is given here.

C	C_6H	H_2
C_2	C_2F_2	OH
C_3	BF	H_2O
CO	BF_2	HF
CO_2	BF_3	F
C_2H	BO_2	O
C_3H	BHO_2	O_2
C_4H	H	

From the above set of 23 molecular species (I = 23) composed of 5 elements (K = 5), it is possible to construct 18 linearly independent reactions. The following set of reactions is considered in the study:

(1)	$O_2 + 2C \rightarrow 2CO$	(10)	$3C \rightarrow C_3$
(2)	$BFO + C \rightarrow CO + BF$	(11)	$2F + 2C \rightarrow C_2F_2$
(3)	$H + 2C \rightarrow C_2H$	(12)	$OH + C \rightarrow CO + H$
(4)	$H + 3C \rightarrow C_3H$	(13)	$O + C \rightarrow CO$
(5)	$H + 4C \rightarrow C_4H$	(14)	$BO_2 + F \rightarrow BFO + O$
(6)	$H + 6C \rightarrow C_6H$	(15)	$H_2O + C \rightarrow CO + H_2$
(7)	$HF \rightarrow H + F$	(16)	$BF_2 + F \rightarrow BF_3$
(8)	$H_2 \rightarrow 2H$	(17)	$BHO_2 \rightarrow H + BO_2$
(9)	$2C \rightarrow C_2$	(18)	$BF_2 \rightarrow BF + F$

The results of the reaction importance study are shown in Figures 22(a) through 22(j), where the relative importance of the most important of the 18 above reactions is shown as a function of temperature for values of B' ranging from 0.1 (Fig. 22(a)) to 1.0 (Fig. 22(j)). It is emphasized that the reactions shown in Figures 22 correspond to the regime under the equilibrium curve (Fig. 20), that is, the gas phase is not in equilibrium with the graphite surface. The results of the reaction importance study for the gas in equilibrium with the graphite surface are shown in Figures 23(a) and 23(b), where reaction importance is shown as a function of surface temperature and B', respectively.

Reference to the reaction importance results clearly define the reactions for which chemical kinetica data must be obtained to characterize

kinetically controlled ablation of graphite in an OF_2-B_2H_6 environment. In the low temperature regime with low recession rate, Reaction 15 is of prime importance. For moderate and high temperatures with low ablation rates, or low temperatures with high ablation rates, the oxidation of graphite by BFO (Reaction 2) is dominant, while the hydrocarbon formation reactions (Reactions 3, 4, and 5) become most important at high temperatures with high ablation rates.

2.3 Comparison of Predicted to Experimental Rocket-Nozzle Response

In this section, results of theoretical predictions are presented and compared to measured rocket-nozzle response data. Predicted and measured internal temperatures for nonablating (heat sink) nozzles are presented first in Section 2.3.1, and are followed in Section 2.3.2 by comparisons of predicted and measured ablation rates and temperature distributions for rocket nozzles constructed of charring-type ablation materials.

2.3.1 Heat-sink nozzles

Temperature measurements taken in two different heat-sink (nonablating) rocket nozzles are employed here to infer the rocket-nozzle throat heat-transfer rate or, more specifically, the heat- and mass-transfer coefficients. The data were obtained from Reference 40 and are for a liquid oxygen-gaseous hydrogen rocket engine having a 1.2-inch diameter throat. The nozzle geometry is the same as that described in Reference 39; it is approximated here as a hollow cylinder with an inner diameter of 1.2 inches and an outer diameter of 3.5 inches. The first of the two nozzles to be considered is made of 1020 steel with a 0.020-inch coating of "Rokide Z" on the inner diameter. The other nozzle is made of molybdenum.

Evaluation of the heat-transfer coefficient in the throat of the steel rocket nozzle was accomplished by predicting the temperature response of the nozzle employing different values of the heat-transfer coefficient and comparing these predictions to measured temperatures. The predictions were accomplished employing an IBM 7094 computer program. The program employs an explicit, finite-difference formulation of the two-dimensional axisymmetric variable thermal-property heat-conduction equations. The program will accommodate either a specified surface-temperature history yielding an internal-temperature response and surface-heating rate, or it will accommodate specified surface-heating boundary conditions yielding an internal-temperature response. The latter of these two options is employed

here. Because the thermocouple nearest the surface is 0.2 inch from the surface, it was not possible to make an accurate evaluation of the surface-temperature history required for the first option in the computer program. The thermal properties of the materials employed in the conduction solutions are given in Table VII. Axial conduction in the nozzle is neglected, as the nozzle throat is several diameters long, and the heating along its length should be reasonably uniform.

The heat-transfer coefficient was evaluated from the simplified Bartz equation as interpreted in Appendix A, resulting in a value, $\rho_e U_e C_H = 0.206$ lb/ft^2-sec. An approximate evaluation of the radiation heat transfer to the heated surface by the gas stream indicated radiation heating to be less than 5 percent of cold-wall convection heat transfer. Radiation to the surface was therefore not included in the conduction solution. The boundary-layer-edge total enthalpy was taken as the enthalpy of the propellants, O_2 Liq - H_2 Gas, at the temperature of liquid nitrogen at 1-atmosphere pressure which, for O/F of 5.9, yields $H_e = -180$ cal/gm. The wall enthalpy was taken as the equilibrium enthalpy of the propellant gases at the wall temperature and 3.8 atmospheres pressure (throat pressure for a chamber pressure of 6.8 atmospheres).

Comparisons of predicted and measured temperature histories using several values of heat-transfer coefficient are shown in Figures 24(a) and 24(b) for the steel and molybdenum nozzles, respectively. Also shown in Figures 25(a) and 25(b) are comparisons of predicted and measured temperature distributions through the steel nozzle at several times during the firing. The measured temperatures fall between the predictions using 10 percent and 30 percent of the Bartz heat-transfer coefficient for the steel nozzle, and between 50 and 70 percent for the molybdenum nozzle. All of the blame for the large difference between the measurement and prediction need not necessarily fall on the heat-transfer coefficient. Other possible causes for the difference between data and prediction are discussed briefly.

Total Enthalpy, H_e

The rocket engine (described in Ref. 39) employs a water-cooled combustion chamber. Evaluation of the heat transfer from the chamber to the cooling water (Ref. 40) indicates a heat loss of 2.15 $Btu/in.^2$-sec based on the chamber area. Assuming a chamber diameter of 2.25 inches, a length of 4 inches, and a propellant mass-flow rate of 0.52 lb/sec yields a net total-enthalpy reduction of 117 Btu/lb (65 cal/gr). Assuming complete mixing of

the gases in the chamber, the total enthalpy (H_e) is reduced from -180 cal/gr to -245 cal/gr. This amounts to a 4-percent reduction in heat-transfer driving potential ($H_e - H_w$) for a wall temperature of 2000° K, and less for lower wall temperatures.

Wall Enthalpy, H_w

The wall enthalpy for O/F = 5.9 is shown as a function of temperature in Figure 26 for three different assumptions regarding the composition of the gas adjacent to the surface:

(1) Equilibrium composition at the throat pressure (employed in the conduction solution).

(2) Composition frozen at boundary-layer-edge conditions.

(3) Composition frozen at chamber conditions.

Employing assumptions (2) and (3), and assuming a 2000° K wall temperature, results in a reduction in enthalpy potential ($H_e - H_w$) of 32 percent and 39 percent, respectively. In the tests, O/F = 5.9 for the steel nozzle and O/F = 6.7 for the molybdenum nozzle. Also shown in Figure 26 is the equilibrium wall enthalpy for O/F = 6.7.

Non-Isothermal Wall Effects

An approximate calculation of the effect of the discontinuity in wall temperature at the chamber-nozzle junction indicates a 6-percent reduction in heat-transfer rate.

Several possible explanations for the discrepancy between predicted and measured results have been proposed. All of them added together do not account for the factor of 5 discrepancy observed in the steel nozzle, however, they do fall in the range of the observed discrepancy in the molybdenum nozzle.

Concerning the above-described results, some comments are in order. First, the temperature instrumentation in the rocket nozzles was not designed for inferring the surface heat flux, but rather for the relative rating of various materials. As a result, evaluation of the surface-temperature histories along the axis of the nozzle from the subsurface measurements would be questionable, at best. Such evaluation is necessary for determining accurately the surface heat rate. Calculations performed here should therefore be interpreted as approximate indications of the magnitude of the surface heat flux. The differences between the heat-transfer rates inferred from temperature measurements in the steel and molybdenum nozzles (0.2 and

0.6 times theoretical), as well as the departure of these from the theoretical value, are believed greater than the inaccuracies associated with the data interpretation scheme. The following are offered as possible explanations of the observed discrepancies. The difference between the apparent heat-transfer rates for the steel and molybdenum nozzles could be due either to: (1) flow asymmetries in the nozzles resulting from possible incomplete propellant mixing which could produce different heat rates at the radial location corresponding to the thermocouple locations in each of the two tests, or (2) the ZrO_2 coating on the steel nozzle may have separated from the heated surface slightly, giving rise to a high thermal contact resistance, which would result in a significantly lower apparent surface heat-transfer rate (as inferred from subsurface temperature measurements in the steel). If the second of the above possibilities is presumed correct, it may be concluded that the heat-transfer rate is approximately 60 percent of theoretical, assuming gas-phase equilibrium at the surface. As indicated above, the theoretical heat-transfer rate is reduced 30 to 40 percent if the boundary-layer gas is frozen at the combustion chamber composition. This nonequilibrium effect could account for the discrepancy between the predicted and experimental heat-transfer rate within the accuracy of the data-reduction scheme. Similarly, a heat-transfer coefficient equal to approximately 0.6 times the theoretical value would explain the observed results. On the basis of the above arguments alone, it is not possible to conclude which of the two effects should be attributed with the observed discrepancy. It is believed, however, that the occurrence of nonequilibrium at the nozzle surface for the temperatures and pressures being considered is not too likely, and, as such, the discrepancy between observed and predicted heat-transfer rates is tentatively assigned to the heat-transfer coefficient being equal to 60 percent of that given by the simplified Bartz equation.

In the following section, comparisons between predicted and measured temperature histories and surface-recession rates for ablating rocket nozzles are presented.

2.3.2 Ablating nozzles

Theoretical ablation calculations have been performed corresponding to specific rocket-engine test conditions and compared to measured data. The purpose of this effort is to assess the adequacy of the theoretical ablation prediction technique for composite materials in a N_2O_4-N_2H_4/UDMH environment. The ablation data were obtained from a series of rocket-engine

firings at NASA-Lewis with each of two thrust chambers. One thrust chamber is made of silica phenolic; the other is made of graphite phenolic. The theoretical ablation model presented above, in Section 2.1, is employed for the predictions. The boundary conditions employed in the calculations are described first and are followed by prediction and data comparisons.

The values of the material property parameters utilized for predicting the transient ablation response of both graphite-phenolic and silica-phenolic materials are shown in Table V. The thermal conductivity and specific heat values tabulated have evolved from a combination of direct thermal property measurements and indirect measurements obtained from the correlation of ablation data obtained in arc-plasma, and solid-propellant rocket-engine firings. The heats of formation correspond to the mass-weighted average of the heats of formation of the constituents. The phenolic resin decomposition kinetic coefficients are taken directly from Reference 7 and the decomposition-gas enthalpy as a function of temperature results from assuming chemical equilibrium between all gaseous products.

The heat-transfer coefficient without blowing, $\rho_e U_e C_{H_o}$, is taken as 0.7 times that given by the simplified Bartz equation as interpreted in Appendix A. This correction factor is admittedly rather arbitrary, but it is applied here on the basis of the conclusion reached in the previous section for a rocket engine having a throat diameter of 1.2 inch, and on the basis of rather accurate measurements of nozzle throat heat-transfer rates in the Vidya Arc-Plasma Facility (Ref. 10). Because the surface temperatures of the ablation materials will be in the range of the boundary-layer-edge temperature, the boundary-layer-edge conditions are taken as boundary-layer-reference conditions. The resulting heat-transfer coefficent at the 7.8-inch-diameter throat of a N_2O_4-N_2H_4/UDMH rocket engine with an oxidizer-to-fuel mass ratio of 2.0 operating with a chamber pressure of 100 psia is

$$\rho_e U_e C_{H_o} = 0.14 \text{ lb/ft}^2\text{-sec}$$

and the recovery enthalpy is

$$H_r = 105 \text{ Btu/lb}$$

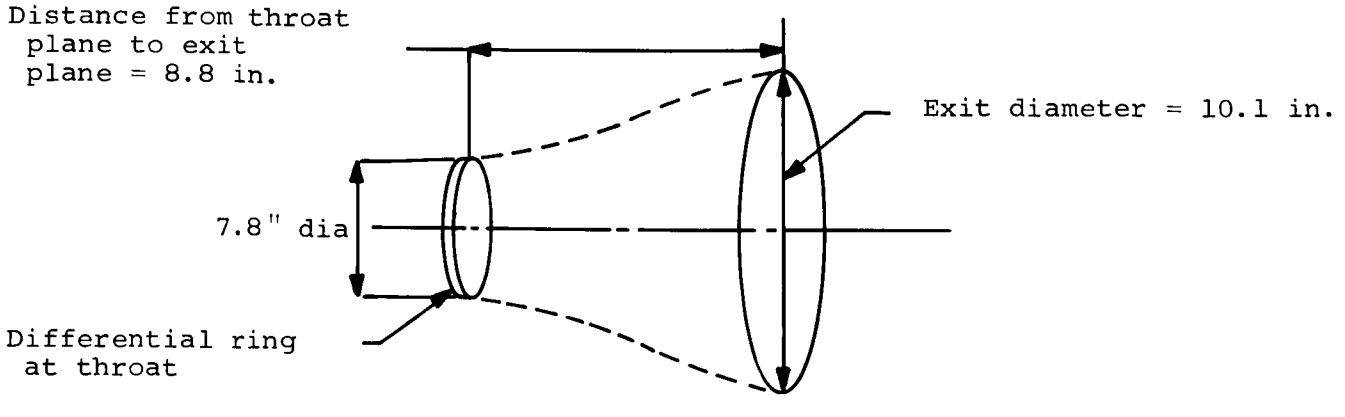
The radiation heat flux to the surface, q_{rad}, is evaluated considering the two primary radiators in the exhaust stream, H_2O and CO_2. The emissivity per unit length of a CO_2-H_2O mixture was obtained from Reference 36

by taking the mixture density to correspond to the mixture partial pressure at the free-stream temperature. The radiation heat flux was then evaluated for a one-dimensional layer of this gas having a thickness equal to the throat radius. The resulting value is

$$q_{rad} = 28.6 \text{ Btu/ft}^2\text{-sec}$$

Utilization of the throat radius as the characteristic one-dimensional length most probably yields a radiation heat flux which is too low. It is felt that utilization of the diameter would yield a heat flux that is too high, although probably more nearly correct. This radiation heat flux is less than 10 percent of the cold-wall convective heat flux and, as such, it would appear that the accuracy of the radiation heat flux is relatively inconsequential; however, this heat flux represents a substantial portion of the hot-wall convective heat flux. It is concluded that more detailed consideration should be given to evaluating the radiant heat flux in future calculations. It would be reasonable to precede such detailed evaluations with a number of transient ablation calculations having a parametric variation of the radiant heat flux in order to assess its influence upon the material recession rate and char penetration depth.

Re-radiation of energy from the ablating surface is represented in the energy equation by the term, $\sigma\epsilon T_w^4$. This representation is strictly correct only if the stream is opaque. For the present calculations the stream is relatively transparent ($\epsilon_{stream} \cong 0.1$), so consideration must be given to the geometrical view factor between the nozzle throat and the surrounding (cold) atmosphere. For this purpose, the following idealized geometrical configuration was considered to characterize the nozzle expansion cone.



Based on the above geometry, the view factor of the throat to the nozzle exit plane is $F_{1-2} = 0.23$. The surface emissivity for both ablative materials was taken as unity and, employing the above view factor, the radiation heat flux from the surface becomes

$$q_{re\text{-}rad} = 0.23\ \sigma T_w^4$$

The predicted char penetration depth and surface-recession histories are shown, together with measured surface-recession histories for the silica-phenolic nozzle throat in Figures 27(a), 27(b), and 27(c). The first run (No. 89) lasted only 5 seconds and no surface recession was predicted; however, some charring did occur and this initial char depth was employed for the subsequent firing calculation. The results for the next firing (No. 90) are shown in Figure 27(b) where it is noted that the predicted average surface-recession rate is approximately 0.4 mil/sec, but the measurement indicates negative recession (material accretion) during the 100-second firing. The measured throat surface-recession rates are obtained from choked flow calculations, and, as such, are not as reliable as pre- and post-test measurements of the ablated depth; however, it is possible that the throat diameter did decrease during firing as a result of mechanical swelling of the char, or liquid silica flow from the combustion chamber. The data from the next firing (Run No. 91) are shown in Figure 27(c) and compare favorably with the predicted surface recession.

The char penetration histories, and predicted and measured surface-recession histories for three firings with a graphite-phenolic thrust chamber are shown in Figures 28(a), 28(b), and 28(c). The first two firings (Run Nos. 64 and 65) were of short duration (5 sec) and theoretical predictions were made primarily to establish the char penetration depth for the following, long-duration firing. For the two short firings, the predicted and measured surface-recession rates compare well; however, because of the short exposure times, the indicated surface recession is very low and not much significance should be associated with the good agreement between theory and prediction. The results from the next firing (Run No. 66) are shown in Figure 28(c). The firing duration for this run is 100 seconds and the predicted surface recession exceeds the measurement by a factor of 5. The large discrepancy between predicted and measured ablation rates for the graphite-phenolic thrust chamber is attributed to either chemical kinetics, or film cooling by the fuel. Previous experience at Vidya has established

the importance of chemical kinetics at the ablating surface of graphitic materials in rocket-engine environments. The effect on ablation rate of fuel-rich and oxidizer-rich boundary layers adjacent to the ablating surface was investigated for each of these thrust chambers in order to assess the possible benefits (or detriments) of film cooling from a chemical erosion point of view. Two extremes were considered: that of all oxidizer in the boundary layer, and that of all fuel in the boundary layer. The following effects on the steady-state material ablation rates are predicted to occur:

Material	Change in Ablation Rate from O/F = 2.0	
	All Fuel, O/F = 0	All Oxidizer, O/F = ∞
Graphite phenolic	100% decrease (No recession)	71% increase
Silica phenolic	100% decrease (No recession)	100% decrease

Based on the above considerations alone, it is not possible to conclude whether film cooling or chemical kinetics are primarily responsible for the graphite-phenolic material's performing much better than would be predicted from equilibrium thermochemistry considerations; however, considering past experience, it is reasonable to conclude that chemical kinetics play a very significant if not dominating role.

Vidya has developed a computer program for the prediction of kinetically controlled ablation of graphite in solid-propellant rocket environments (Ref. 10). The development of a numerical technique for characterizing kinetically controlled erosion of composite materials could be based upon the same technique and is entirely feasible; however, rather extensive modifications to existing computer programs would be required.

In order to better present the predicted transient ablation response of the two thrust chambers and to obtain a feeling for the degree of approach to steady-state ablation, some additional predicted results are shown in Figures 29(a) and 29(b). Shown in the figures are the normalized char ablation rate, $B'_c = \dot{m}_c/\rho_e U_e C_M$, the normalized off-gas recession rate, $B'_g = \dot{m}_g/\rho_e U_e C_M$, and the normalized total ablation rate, $B' = B'_c + B'_g$ for a graphite-phenolic and a silica-phenolic thrust chamber firing. The normalized recession-rate parameters are shown as a function of time, and their steady-state values are also shown. Both of the predictions are for 100-second firings, but the degree of approach to steady-state conditions for

the two is vastly different. The graphite phenolic essentially reaches steady state after 60 seconds, whereas the silica phenolic is far from steady state after 100 seconds. It is interesting to compare these results with the steady-state ablation-rate parameter presented in Section 2.1.3.3 where it was shown that approximately 95 percent of steady-state ablation rate is reached when

$$\sqrt{\dot{s}_{ss}^2 \theta_{ss}/\alpha_p} = 1.4$$

where

$\dot{s}_{ss}$ steady-state surface-recession rate

α_p virgin plastic thermal diffusivity

θ_{ss} time to reach 95 percent of steady-state recession rate

Employing the thermal property values in Table V and the steady-state ablation rates, the following steady-state times are obtained:

Graphite phenolic	θ_{ss}	= 97 seconds
Silica phenolic	θ_{ss}	= 868 seconds

These values are quite representative of the results shown in Figure 29. It is instructive to consider the effect of the resin off-gas rate, B'_g, on the char recession rate, B'_c. In both Figures 29(a) and 29(b), the large reduction in surface recession as a result of high off-gasing rate is apparent. This fact establishes the need for detailed consideration of the kinetically controlled organic decomposition reactions in depth.

Comparison between measured and predicted subsurface temperature histories for the two thrust chambers are shown in Figures 30 and 31. The results for the three firings of the silica-phenolic chamber are shown in Figures 30(a), 30(b), and 30(c), and those for the graphite-phenolic chamber are given in Figures 31(a), 31(b), 31(c), and 31(d). The first silica-phenolic firing was only 5 seconds long and, as a result, the comparison between measured and predicted temperatures is inconclusive. Results from the second firing (Run No. 90) are shown in Figure 30(b) where it is noted that the measured temperatures lag the predictions by a significant amount. It is also noted that the thermocouple data for the cooldown portion of the firing appear inconsistent with the data obtained during the firing and, as such, the cooldown data are suspect. The reason for the discrepancy

between the temperature data and predictions during the firing is not obvious. Several possible explanations exist, the primary two being either incorrect thermal property data employed in the prediction, or erroneous thermocouple data. Based on these data alone, it is not possible to conclude which of these two factors is primarily responsible for the lack of agreement between data and prediction. The predicted and observed temperature histories for the third silica-phenolic firing (Run No. 91) are shown in Figure 30(c). No cooldown data are available for this firing and the data during the firing fall below the predictions by an amount similar to that for Run No. 90.

The predicted and measured temperature histories for the three graphite-phenolic firings are shown in Figures 31(a), 31(b), and 31(c). The predicted surface-recession rates for the first two firings (Run Nos. 64 and 65) agree well with those observed experimentally and, as such, the temperature predictions should be reasonable; however, the predicted recession rate for the third firing (Run No. 66) was so large that the first two thermocouples were predicted to be consumed. An additional prediction was made for this run in an attempt to have the surface boundary conditions correspond more closely to what was observed experimentally. For this prediction, no surface recession was allowed to occur and the predicted and measured internal-temperature histories for this case are shown in Figure 31(d).

The data presented in Figures 31(a), 31(b), and 31(d) appear quite consistent and may be employed as the basis for rationalizing discrepancies between data and theory. In each case, the data lag the predictions during the firing and come into reasonable agreement during the cooldown phase. If the discrepancy during the firing were attributed to the utilization of bad thermal property data in the prediction, then good agreement during the cooldown period would not be expected. If, on the other hand, the thermocouple installation techniques were such as to cause lags in the data during the firing, then agreement during the cooldown phase would be expected. The thermocouple probes from which these data were obtained were installed radially (thermocouple wire perpendicular to isotherms), so some lag would be anticipated between measured and actual temperatures. This type of error was investigated in Reference 41 and it was shown that significant errors can be incurred from thermocouple installations of this type. Based on the above (far from complete) arguments, it is concluded that significant temperature measurement errors exist in the data presented in this section

and the agreement between predictions and actuality is better than that indicated on the figures. The reader is cautioned that it is difficult to draw conclusions of a general nature from the comparisons presented herein since the test nozzles were of a tubular throat configuration. Subsequent scrutinization of the rocket-engine ablation data by NASA has led to the conclusion that the particular ablation tests considered here are of questionable utility because it is not possible to assess the actual location of the aerodynamic throat during the engine firing.

2.4 Summary of Theoretical Investigations

A theoretical ablation model which accounts for the primary thermochemical interactions between an ablation material and its environment has been developed and presented. The mathematical model for the subsurface thermochemical response is representative of the most realistic treatment currently available to characterize energy and mass transfer in the presence of kinetically controlled organic decomposition reactions in depth. Extensive consideration has been given the theoretical treatment of thermochemical interactions between an ablation material and its environment, both of arbitrary chemical composition. The strong interdependence of the ablation material response and boundary-layer transport phenomena is indicated and the need for a coupled solution of the boundary layer and subsurface response is stressed. A technique is presented which reduces the number of differential equations required to characterize the multicomponent, chemically reacting boundary layer with unequal diffusion coefficients from I+2 to K+2, where I is the total number of species in the boundary layer and K the number of chemical elements. Approximate equations have been proposed to characterize boundary-layer heat- and mass-transfer processes for this case. The approximate relations are utilized to provide the heated surface boundary condition for a numerical solution of the equations governing the subsurface response. The resulting coupled solution accounts for all possible chemical reactions at the ablating surface within the assumption that chemical equilibrium is achieved.

The theoretical ablation model has been employed to investigate the thermochemical compatibility of a number of ablation materials in several liquid-propellant rocket-engine environments, and to assess the validity of the often-employed assumption of steady-state ablation for a wide range of boundary conditions.

Comparisons have been made between measured ablation data and predictions utilizing the theoretical ablation model. The predicted ablation

rates for the silica-phenolic nozzle throat were in general agreement with the data, except for one firing where material accretion was observed experimentally. The predicted ablation rates for the graphite-phenolic nozzle throat were greater than those observed experimentally by a factor of 5. The discrepancy is attributed either to the role played by chemical kinetics between the carbon surface and oxygen-bearing gaseous species, or inhomogeneous boundary conditions resulting from propellant injection patterns. Discrepancies between predicted and measured subsurface temperature histories are tentatively assigned to a thermocouple installation technique which will cause low temperature readings. The need for installing thermocouple probes parallel to the isotherms is stressed, and the need for further corroboration of data so obtained and theoretical predictions is apparent.

3. EXPERIMENTAL INVESTIGATIONS

An experimental program has been performed to develop an arc-plasma generator as a liquid-propellant rocket-engine ablative material test devic The technique consists basically of adding energy to special gas mixtures with an arc-plasma generator and passing the high temperature, chemically reacting gas mixtures over the surface of an ablation material specimen. Such a technique will have two advantages over ablation material testing in a rocket engine: (1) it will be considerably more economical, and (2) it will enable detailed investigations of basic ablative material response phenomena. This latter advantage is because it will be possible to vary the parameters of primary importance one at a time. For example, the stagnation temperature may be varied over a wide range while holding O/F ratio constant, and vice versa. The majority of the experimental efforts have been directed toward modification of the arc-plasma facility to allow operation at the pressure and enthalpy levels requisite to achieving simulation with the appropriate test gases. The modification has been successfully achieved and simulation of two propellant environments (O_2-H_2, and N_2O_4-N_2H_4/UDMH) has been demonstrated.

The experimental program is described in this section. The requirements of a valid ablative-materials test program are presented first in Section 3.1; Section 3.2 presents the specific approach taken to achieve experimental duplication of the requisite simulation parameters; Section 3.3 describes the experimental procedure; and Section 3.4 presents the results of several ablative-material tests.

3.1 Simulation Requirements

Based upon the theoretical considerations introduced in Section 2.1, it is possible to list those parameters which must be duplicated in an experimental ablation test in order to obtain simulation of the material response characteristic of a particular material-propellant combination. In this section, the simulation parameters are listed and discussed with respect to the relative importance of each.

Complete simulation of the ablative material response requires duplication of the following parameters:

(1) The chemical composition of the free-stream gas.
(2) The total enthalpy of the free-stream gas.
(3) The boundary-layer heat- and mass-transfer coefficients.
(4) The local pressure.
(5) The flow-field geometry.
(6) The ablation specimen size and geometry.

The first five parameters in the above list are usually of primary importance and will be duplicated only in a full-scale test. The first four parameters may be rationalized as sufficient if chemical equilibrium is assumed and if mechanical erosion is not important; however, the influence of pressure on the chemical equilibrium composition is minor, provided the pressures between simulation test and actual do not differ by more than a factor of two.

The first three parameters are of primary importance for chemical erosion because they govern the reactivity of the chemical species approaching the surface, the rate at which chemically reactive species are transported to the surface, and the surface heat-transfer rate which, for a given ablation material, establishes the surface temperature.

Based upon the above arguments, it is reasoned that duplication of the first three simulation parameters, chemical composition, total enthalpy, and heat-transfer coefficient represents simulation of the most significant phenomena which affect thermochemical degradation of ablative materials.

In the following section, the approach taken to achieve duplication and measurement of the requisite simulation parameters is described.

3.2 Experimental Approach

In this section, a description is given of the specific objectives of the experimental program and of the particular experimental efforts undertaken to accomplish these objectives. Any experimental ablative material test program should include the following two considerations among its

primary objectives: (1) to duplicate, as nearly as possible, each of the simulation parameters, and (2) to monitor accurately each of the parameters so the observed results may be employed to infer what the material response would be in the actual application being considered. These two factors represent the primary objectives of the experimental program described herein.

The experimental simulation technique is described first in Section 3.2.1. In the two subsequent sections, the experimental efforts directed toward achieving operation of each of two arc-plasma generators in the desired range of operating conditions are described. During the first year of effort on the subject program, numerous attempts were made to achieve duplication of the requisite simulation parameters introduced above employing a magnetically stabilized arc-plasma generator to heat the simulation gases. Qualitative results of these efforts are presented in Section 3.2.2, along with the rationale leading to the decision to discontinue further efforts with the magnetically stabilized, solenoid, arc-plasma generator, and to direct subsequent efforts toward adaptation of a vortex stabilized, constrictor arc-plasma generator as the electric arc heater. During the second year of effort, the constrictor arc-plasma generator was successfully modified to operate at the desired test conditions. The design considerations and modified arc-plasma generator design are described in Section 3.2.3. Finally, in Section 3.2.4, the experimental methods for measuring the pertinent test parameters are described.

3.2.1 Simulation technique

In this section, the experimental technique is discussed in the light of the requisite simulation parameters introduced above (Section 3.1). Each of the parameters is discussed separately, and the means of achieving duplication is presented.

3.2.1.1 Simulation gas

Simulation of four liquid-propellant rocket-engine environments was considered during the subject program; they are: (1) Nitrogen tetroxide-Aerozine, (2) Oxygen-Hydrogen, (3) Oxygen Difluoride-Diborane, and (4) Flox-Methane. Experimental simulation of the first three was attempted and success was achieved with the first two. The simulation gases selected for each propellant environment are established by considering the chemical composition of the propellant. The quantity of each chemical element in the simulation gas mixture is required to be identical to that in the propellant. For the four environments listed above, the following chemical balance may be written between the propellant and the simulation gases.

(1) Nitrogen tetroxide-Aerozine, O/F = 2.0

$$0.725\ N_2O_4 + 0.520\ N_2H_4 + 0.277\ C_2N_2H_8$$

$$\rightarrow \underbrace{1.522\ N_2 + 1.212\ H_2}_{\text{Mixture F}} + \underbrace{0.554\ CO_2 + 0.43\ O_2}_{\text{Mixture G}} + \underbrace{0.933\ H_2O}_{\text{Steam}} \qquad (100)$$

The following mass fractions represent the simulation gas mixture:

$$\left.\begin{aligned} K_{N_2} &= 0.4261 \\ K_{H_2} &= 0.0244 \end{aligned}\right\} K_{\text{Mix F}} = 0.4505$$

$$\left.\begin{aligned} K_{CO_2} &= 0.2438 \\ K_{O_2} &= 0.1377 \end{aligned}\right\} K_{\text{Mix G}} = 0.3815$$

$$K_{H_2O} = 0.1680 \qquad K_{\text{steam}} = 0.1680$$

The gases designated Mix F and Mix G are commercial grade high pressure gases premixed in cylinders for laboratory use.

(2) Oxygen-Hydrogen, O/F = 4.0

$$2.5\ O_2 + 9.91\ H_2 \rightarrow 5\ H_2O + 4.91\ H_2 \qquad (101)$$

$$K_{H_2O} = 0.901$$

$$K_{H_2} = .099$$

(3) Oxygen Difluoride-Diborane, O/F = 5.85[5]

$$1.582\ OF_2 + 0.527\ B_2H_6 \rightarrow 1.054\ BF_3 + 1.581\ H_2O \qquad (102)$$

$$K_{BF_3} = 0.715$$

$$K_{H_2O} = 0.285$$

(4) Flox-Methane, O/F = 4.0

$$1.250\ O_2 + 1.053\ F_2 + 1.247\ CH_4$$

$$\rightarrow 0.526\ CF_4 + 0.721\ CO + 0.715\ H_2 + 1.779\ H_2O \qquad (103)$$

$$K_{CF_4} = 0.463$$

$$K_{CO} = 0.202$$

$$K_{H_2} = 0.014$$

$$K_{H_2O} = 0.321$$

Selection of the above simulation gas mixtures is based upon a compromise between commercial availability and nearness to the combustion chamber chemical equilibrium molecular composition. Utilization of the above gas mixtures in the indicated proportions will yield duplication of the chemical elemental composition. Duplication of the molecular composition will result if the total enthalpy and pressure match those of the rocket engine being simulated.

Each of the above idealized reactions between the propellants and simulation gas mixtures would be highly exothermic; that is, the chemical energy contained in the simulation gases is much less than that in the propellants. In order to obtain duplication of enthalpy, then, it is necessary to add energy to the simulation gas mixtures. Enthalpy duplication is discussed in the following subsection.

---

[5] O/F = 5.85 is required due to the constraint of using BF_3 for simulation; it is the only convenient Boron-containing gas for this propellant simulation.

3.2.1.2 Enthalpy

The total enthalpy of the simulation gas mixture is obtained by arc heating the gas with the appropriate amount of electric energy. The amount of arc heating required is determined by considering the enthalpy of the propellant and the enthalpy of the simulation gas mixture. The enthalpy of the simulation gas mixture, H_{inj}, is obtained from the following relation and consideration of the temperature at which they are injected, T_{inj}.

$$H_{inj} = \sum_j K_j \int_{298^\circ K}^{T_{inj}} C_{p_j} dT + h_j^\circ \qquad (104)$$

Signifying the propellant enthalpy by H_{prop}, the required arc-energy addition is:

$$\Delta H_{arc} = H_{prop} - H_{inj} \qquad (105)$$

The arc-energy input requirements for the four propellant simulations become:

Propellant	Enthalpy (Btu/lb)*		
	H_{prop}**	H_{inj}***	ΔH_{arc}
(1) N_2O_4-N_2H_4/UDMH	+105	-1895	2000
(2) O_2-H_2	-457	-5120	4663
(3) OF_2-B_2H_6	+275	-7160	6885
(4) O_2/F_2-CH_4	-641	-4296	3655

Addition of the indicated amount of energy, ΔH_{arc}, to the simulation gas mixtures will result in duplication of the total enthalpy in the test gas stream.

---

*Enthalpy base corresponds to JANAF Tables (Ref. 29).

**Propellants are assumed injected at their saturation temperature - 10 atms pressure or 298° K, whichever is less.

***Commercial simulation gases assumed injected at 298° K and steam at 300° F.

The next simulation parameter to be duplicated is the boundary-layer heat-transfer coefficient. This is discussed in the following subsection.

3.2.1.3 Heat-transfer coefficient

The relationship between the heat-transfer coefficient in the simulation test and the rocket engine may be evaluated by referring to the simplified Bartz equation as interpreted in Appendix A. This equation is admittedly approximate, but it should give a relatively accurate indication of the change in heat-transfer coefficient with chamber pressure and throat diameter. Utilizing the simplified Bartz equation and forming the ratio of heat-transfer coefficients in the arc (sub A) and rocket (sub R) yields:

$$\frac{(\rho_e U_e C_H)_A}{(\rho_e U_e C_H)_R} = \left(\frac{P_A}{P_R}\right)^{0.8} \left(\frac{D_R}{D_A}\right)^{0.2} \qquad (106)$$

where C_H is the Stanton number defined by:

$$q_w = \rho_e U_e C_H (H_r - H_w)$$

In order to duplicate the heat-transfer coefficient ($\rho_e U_e C_H$), the ratio in Equation (106) must equal unity. It is apparent that if the pressure is to be duplicated ($P_A = P_R$), then the throat diameter in the simulation test must equal that in the rocket as well ($D_A^* = D_R^*$). In an arc-plasma generator, for a given pressure and enthalpy (ΔH_{arc}), the throat diameter is limited by the available electrical power, and is generally smaller than the actual nozzle for which simulation is desired. The present Vidya constrictor arc unit is limited to throat diameters in the range of 0.3 to 0.5 inch. With this restriction on throat diameter, or for any subscale test, the simulation test pressure must be less than the actual case in order to duplicate the heat-transfer coefficient.

As discussed above in Section 3.1, duplication of the heat- and mass-transfer coefficients is of prime importance, while pressure duplication is of secondary importance. Based on this premise, it is reasonable to sacrifice pressure duplication in order to achieve heat-transfer-coefficient duplication. Duplication of the mass-transfer coefficient (C_M) will result directly if the heat-transfer coefficient is duplicated, since

$$C_M = C_H \, Le^{2/3}$$

and the boundary-layer Lewis number will be the same in the simulation test as in the rocket.

3.2.1.4 Pressure

As indicated above, pressure duplication must normally be sacrificed in a subscale test in order to achieve heat-transfer-coefficient duplication. Pressure duplication is not too important as long as differences between simulation test and actual do not differ by more than about a factor of 2.

3.2.1.5 Simulation technique summary

In this section, the requisite simulation parameters have been expressed in terms of quantities which may be measured during the conduct of a simulation test. In the following sections (Sections 3.2.2 and 3.2.3), modifications to each of two arc-plasma generators directed toward attaining operation at the desired conditions are described and are followed in Section 3.2.4 by a description of experimental techniques for measuring the simulated parameters.

3.2.2 Solenoid arc-plasma generator

During the first year of the subject contract, experimental efforts were directed toward achieving operation of a magnetically stabilized, solenoid arc-plasma generator in the range of test conditions appropriate to duplication of the simulation parameters presented in the previous section. The solenoid arc-plasma generator is described along with other major components of the Vidya Arc-Plasma Facility in Appendix B.

The solenoid arc-plasma generator was operated, and ablative material specimens were tested at test conditions which represented a compromise of the requisite simulation parameters presented above. The compromised test conditions consisted of duplicating the oxidation potential, rather than the complete chemical composition of the propellant products.

Attempts to operate the solenoid unit on the gases requisite to achieving complete duplication of chemical composition were generally unsuccessful. Major problems encountered were associated with insufficient power-supply voltage to operate on the desired test gases, and condensation of steam (one of the simulation gases for all environments considered) on the internal surfaces of the arc-plasma generator.

In this section, the solenoid arc-plasma generator is briefly described and is followed by a description of the compromised tests based on oxidation potential simulation.

The solenoid, arc-plasma generator is a high energy dc electric arc heater. The arc itself is an ionized column of the test gas rotating in a plane perpendicular to the gas flow for maximum electrical-to-thermal energy exchange. The arc travels in the annular gap between two concentric copper electrodes shown schematically in Figure 32. The outer electrode operates as the cathode and the inner as the anode. The arc zone is surrounded by a solenoidal magnetic coil external to the pressure vessel. The coil, externally excited, sets up a steady magnetic field with lines of flux perpendicular to the electric field created by the arc column traveling in the annulus. The resulting J X B body forces cause the arc to rotate around the anode at high velocity. This rotation stabilizes the arc and minimizes the local heating of the electrodes at the point of arc contact, thereby permitting the electrode surfaces to operate below their melting temperature and also minimizing gas-stream contamination

As shown in Figure 32, the test gases may be introduced both upstream of the arc zone, noted as primary injection, and downstream of the arc zone in the plenum region, noted as secondary injection. The latter mode is used for only a fraction of the total flow, and is employed when using combinations of gases which may react chemically prior to arc heating and cause deleterious effects to the electrodes. The primary test gases are injected tangentially in a direction counter to the magnetically-induced rotation of the arc. This effects a counteraction of the swirl caused by the arc motion, and thus provides a uniform flow field when the gas approaches the test section.

The plenum chamber downstream of the arc zone affords a region for mixing and equilibration of the heated gases prior to expansion to the test section. Rocket-nozzle material test specimens are affixed to the end of the plenum chamber as shown in Figure 33.

The solenoid plasma generator was used in attempts to simulate three separate propellant systems:

Propellant System	O/F	Plasma-Generator Simulation Gas
O_2-H_2	6.0	$H_2O_{(steam)}$ and H_2
N_2O_4-Aerozine	2.0	CO, CO_2, and $H_2O_{(steam)}$
OF_2-B_2H_6	5.3	BF_3 and $H_2O_{(steam)}$
N_2O_4-Aerozine	2.0	N_2, He, and O_2 (oxidation potential simulation)

The primary difficulties encountered when attempting to operate on the first three simulation gas mixtures were: (1) voltage requirements in excess of power supply capability, and (2) condensation of steam on the water-cooled surfaces of the arc-plasma generator. Typical voltage traces for the solenoid, arc-plasma generator, during operation on hydrogen and steam, are shown in Figures 34 and 35, respectively. A number of modifications to the manner in which the gases are introduced were adapted, but it was not possible to sustain arc operation on either of these gases.

In order to derive some meaningful information on material performance from the solenoid, arc-plasma test series, it was decided to relax the simulation requirements set forth earlier in Section 3.1.

The environment considered is N_2O_4-N_2H_4/UDMH, and the approach involves duplicating the erosion-producing mechanisms associated with oxidation alone, utilizing a test-gas composition simulating the oxidation potential of the propellant with other species replaced by inerts. This technique has been described in the open literature (Ref. 43). The mass fraction of oxygen is the amount contained in the propellant free to react chemically with the wall (i.e., all of the elemental oxygen except that associated with the CO which is essentially inert at the temperatures of interest).

The test-gas composition was based on a fixed oxygen mass fraction with a selection of inert gases to permit reasonable duplication of the propellant temperature-enthalpy variation. The mixture selected was comprised of nitrogen, helium, and oxygen with mass fractions as follows:

Gas	Mass Fraction
Nitrogen	0.4565
Helium	.1685
Oxygen	.3750

Determination of the electric energy to be put into the test gas is based on simulation of the enthalpy potential across the boundary layer. The enthlapy potential across the boundary layer, $(H_e - H_w)$, for a nonablating wall in the N_2O_4-N_2H_4/UDMH environment, is shown in Figure 36 as a function of wall temperature along with that for the N_2-O_2-He simulation gas for each of three values of electric energy input, ΔH_{arc} = 2000, 3000, and 4000 Btu/lb. Based on the comparisons shown in Figure 36, a value of ΔH_{arc} = 3000 Btu/lb would seem appropriate.

The gas mixture for the test was comprised of premixed nitrogen and helium which was injected into the primary gas ports of the plasma generator. Because of the high oxygen concentration, 38 percent by mass, the flow was split, routing 50 percent of the oxygen through the arc zone and introducing the balance into the downstream plenum chamber through the secondary injection ports.

The tests were run with an initial nozzle throat diameter of 0.3 inch and a chamber pressure of 190 psia. Using the simplified Bartz equation to evaluate the heat-transfer coefficient with this gas, and Equation (106) to relate arc to rocket conditions, the actual rocket-engine conditions simulated were evaluated and are shown in Figure 37. As an example, it can be seen that the test conditions simulated an engine with a 4-inch-diameter throat and a chamber pressure of 360 psia. A total of five ablation material tests were run in this test series. The test results are presented in Section 3.4.

3.2.3 Constrictor arc-plasma generator

During the first year's efforts of trying to develop techniques for simulating the chemically reactive high-temperature environment of the combustion products of various liquid-propellant rocket engines, a 400 kw constrictor arc-plasma generator[6] was developed at Vidya for a low pressure, high enthalpy air application. The characteristics of this plasma generator appeared particularly suitable for application to the rocket engine simulation. Some of the more attractive features were: (1) the arc would operate efficiently at very high enthalpy permitting an arrangement in which only certain easily handled gases would be arc heated to high enthalpy, and then diluted to combustion chamber temperature with the other required constituents, (2) the arc column voltage gradient could be changed with only minor electrode configuration changes permitting compatibility of the arc and power supply over a wide range of operating conditions and gas mixtures, (3) the plasma generator was a modular design and the components were physically small making it simple and inexpensive to modify individual parts and, (4) the plasma generator has a plenum chamber cooling circuit which is independent of the electrode cooling circuit, permitting control of the wall temperature to avoid condensation. After consideration of these points, efforts were redirected from continuing with the solenoid arc unit

[6] The general operating characteristics of the 400 kilowatt constrictor arc-plasma generator are described in Appendix B.

toward the modification of the existing air arc to a configuration compatible with the gases required to simulate the four propellant systems described in Section 3.2.1.1.

The 400 kilowatt, constrictor arc-plasma generator is shown schematically in Figure 38. The electrode configuration shown is typical and is the one developed for the liquid propellant simulation. The arc column is constrained to run along the centerline by tangential gas injection which creates a low pressure vortex core. Arc attachment is at the tungsten cathode located at the base of the cathode well and at the minimum diameter or constricted region of the tubular anode. The cathode is thoriated tungsten and serves as a thermionic emitter. The gas is introduced tangentially at the insulated ring that separates the two electrodes.

The operating characteristics of the constrictor arc are affected by electrode configuration variables such as anode constriction diameter and distance from the cathode face to the point of maximum constriction, and operating variables such as test gas composition, gas mass-flow rate, and total pressure. These variables are closely interrelated, although by examining the general dependence of one upon another, a guide for designing toward a particular operating condition is possible.

The most important operating parameter for matching the plasma generator to the power supply at specified operating conditions is arc voltage which increases with increasing pressure and mass-flow rate and decreases with increasing constriction or anode diameter and current. Another important operating parameter is the overall thermal efficiency, that is, that percentage of the electrical power input which is converted to thermal energy of the gas. This parameter limits the permissable total gas mass-flow rate for a selected gas energy content or enthalpy.

In this section, these operating variables are related to each other and to the electrode configuration. The dependence of arc voltage on the other variables is discussed first and is followed by a description of their effect on arc thermal efficiency. Next, necessary modifications to the thermionic emitting cathode are briefly discussed and are followed by a description of the mixing plenum chamber provided for simulation gas equilibration.

3.2.3.1 Arc voltage

Attention was given to achieving arc operation on hydrogen and nitrogen-hydrogen mixtures since these gases are utilized in the simulation gas

mixture for two propellant environments, N_2O_4-N_2H_4/UDMH and O_2H_2. It was desired to modify the constrictor unit to operate on these gases at the pressure and flow rate levels appropriate to rocket-environment simulation. This required tailoring the electrode configurations to sustain a stable arc with the available power supply. The considerations affecting arc voltage are disucssed here.

Figure 39 shows the dependence of voltage on mass-flow rate at two constrictor diameters, revealing that the voltage is proportional to mass-flow rate and inversely proportional to anode diameter. Figure 40 shows the dependence of voltage on chamber pressure for operation on N_2 and H_2. The effect of gas composition on arc voltage is shown in Figure 41 which represents data taken with an anode constriction diameter of 0.4 inches. It should be noted that both the slope and magnitude of the voltage differ substantially for the two gases. In both cases the trend of increasing mass-flow rate is apparent. The dependence of arc voltage on the electrical current is shown in Figure 42, wherein increasing current is shown to cause a reduction in voltage. Also shown is the effect of constrictor diameter on voltage at constant mass-flow rate. Hence, it can be seen that one of the major arc modification design guides for achieving plasma generator-to-power supply compatibility was arc voltage which follows the generalized relationship

$$E_A = f\left(\frac{P, \dot{M}}{m, D_A, I}\right)$$

3.2.3.2 Thermal efficiency

The second major consideration in the operating capabilities of an arc-plasma generator is the overall thermal efficiency which is also closely related to the variables affecting voltage. Figure 43 shows efficiency as a function of chamber pressure, anode constriction diameter and test gas revealing efficiency decreasing with increasing pressure, gas molecular weight[7] and constriction diameter. On the other hand, efficiency is found to increase with increasing mass-flow rate as shown in Figure 44. The pressure dependent data were acquired by throat diameter variation and mixing plenum back pressuring. From these data the second design guide, thermal efficiency, was found to follow the generalized relationship

[7] The actual influence of the gas is related to its ionization which generally is inversely related to the molecular weight as discussed in Reference 42.

$$\eta = f\left(\frac{\dot{M}}{P, D_A, m, I}\right)$$

Using these data and the relationships for voltage and thermal efficiency provided a basis for the successful modification of the constrictor arc-plasma generator to operate at desired conditions with the gases required to simulate certain liquid-propellant environments.

3.2.3.3 Cathode modifications

The design of the thermionic emitting cathode is critical to the successful operation of the constrictor arc-plasma generator. This situation exists because the cathode must operate at a high enough temperature to act as a thermionic emitter, yet it must be held below its melt temperature. The optimization of the cathode operating temperature is achieved by water cooling its rear surface and designing it sufficiently thick so that the temperature gradient across it will result in a surface temperature somewhat below the melt point. The cathode material employed for this application is thoriated tungsten. The cathode geometry which proved successful for operation at the desired conditions is shown in Figure 45.

3.2.3.4 Mixing plenum chamber

In order to achieve a homogeneous gas stream in the nozzle test section, a mixing plenum chamber was designed and installed downstream of the arc unit proper. Three considerations were given to the design of the mixing chamber: (1) there should be sufficient mixing of the various gases to achieve a homogeneous composition, (2) the thermal energy loss to the walls should be minimized, and (3) the walls of a plenum chamber should operate at a temperature higher than the condensation point of the gases contained therein. To satisfy requirements (1) and (2), the plenum chamber was sized to maximize the characteristic length, L_*, and to minimize the surface area while maintaining an axisymmetric geometry. The plenum chamber used for the simulation tests is 3.125 inches in diamter and 2 inches long with a characteristic length (L_*) of 18 feet based on a nozzle-throat diamter of 0.3 inch. To satisfy requirement (3), two methods were investigated: (1) a low conductivity thermal barrier, and (2) a plenum coolant having an operating temperature in excess of the condensation point of the test gas, yet low enough to work with conventional wall materials and seals. Both schemes were considered and the latter was found to be more satisfactory.

The mixing plenum chamber operated satisfactorily with heated walls. Test results with the heated plenum chamber revealed that the condensation difficulties which plagued the previous test efforts were resolved.

3.2.3.5 Constrictor arc-plasma generator summary

From the considerations of electrical compatibility, achieving the desired thermal conditions, plasma generator integrity and proper gas mixing, the 400-kilowatt constrictor arc-plasma generator was successfully modified to operate at the conditions required for simulating the environment to which certain liquid rocket-engine nozzles are exposed. Specifically, the arc-plasma generator configuration shown in Figure 38 is capable of operation on the test gases requisite to simulating two liquid-propellant rocket-engine environments, O_2-H_2 and N_2O_4-Aerozine. The former is accomplished by arc-heating hydrogen with post-injected steam, and the latter by arc heating a mixture of N_2 and H_2 (Mixture F), and post-injecting the remaining species in the mixing plenum chamber.

In the following section, the techniques developed and utilized to measure the appropriate test parameters necessary to ascertain the adequacy of the simulation test are described.

3.2.4 Measurement of test parameters

The measurable test parameters which define the chemically erosive environment of liquid engine combustion products at a particular location in a nozzle were introduced above in Section 3.2.1. These include the chemical composition, the gas enthalpy, the total pressure, and the heat-transfer coefficient. The accurate measurement of each of these parameters is necessary to demonstrate the duplication of rocket engine conditions using the arc-plasma generator simulation technique, and to compare the theoretical ablation predictions with experimental data. The methods of measurement of each of the aforementioned parameters is discussed in the succeeding paragraphs.

3.2.4.1 Chemical composition

The chemical composition of the test gas was determined by measuring the mass-flow rates of the various gases (see Section 3.2.1.1) admitted to the plasma generator. The uniformity of the gas stream composition was measured by a species sampling probe which extracted samples of the high-temperature effluent mixture from selected radial locations just downstream of the nozzle exit plane. The details of these measurements are presented along with the estimated accuracy of each measuring system.

The test gas used to duplicate the equilibrium high-temperature combustion products composition of the various liquid engines was comprised of various commercially available gases in high pressure cylinders and steam from the laboratory boilers. Some of the gases were premixed in cylinders by the gas supplier. The composition of each cylinder was checked by partial pressure measurements having an accuracy better than 1% with an acceptable tolerance of $\pm$2-percent variation between individual cylinders. Generally, only two gases were mixed in each cylinder and they were manifolded in groups of 4, 6, or 8 and allowed to further equilibrate prior to use.

The cylinder gases, that is, cylinders containing one or two gases, were admitted to the plasma generator through high-pressure metering systems consisting of standard design, radius tap ASME orifice meters accurate to approximately 2 percent. The mass-flow rate was determined by measuring the inlet pressure and temperature, and the pressure drop across an orifice of selected size. These data were used to calculate the flow coefficient and then the mass-flow rate of each gas system. The tests requiring steam utilized a similar method, however, a high-pressure mercury manometer was used to measure the differential pressure, and each orifice was calibrated by running the steam through a condenser and measuring condensate mass discharge as a function of time. In this case, the overall accuracy was found to be about 2 percent.

The gas metering systems provided a method of measuring the ambient temperature composition of the total gas mixture admitted to the arc. The composition at elevated temperature was calculated from equilibrium considerations and was based on the measured mass-flow rates selected to duplicate the rocket combustion products at equilibrium.

The gases were admitted to the plasma generator at three locations; through the arc, immediately downstream of the arc into the mixing plenum, and a special steam-injection ring also located in the mixing plenum (see Fig. 38). To assure adequate mixing of these gases, the plenum chamber and gas injection ports were carefully designed as discussed in Section 3.2.3, however, to verify the degree of mixing, the stream was sampled with a water-cooled probe. The probe, shown in Figure 46, was sufficiently small (0.125-inch outside diameter with a 0.040-inch bore) to enable local sampling of the gas stream in the region of the nozzle exit plane. This probe, designed originally for the determination of local stream enthalpy, was employed for this sampling assignment, once minor changes to its original arrangement

had been made. Since in the present case the probe and its associated equipment were to be used with test gases having condensable constituents, it was necessary to incorporate heated surfaces for the flow passageways and manifold collecting system to prevent condensation of these portions of the sampled gas. The schematic arrangement for the sampling system, including the heated elements, manifold, and collection system is shown in Figure 47.

Noncondensing surface temperatures were maintained in the sampling circuit by heating of the main collecting tube electrically. Alternating current was fed to the thin wall stainless-steel sampling tube with voltage supplied by a variable voltage autotransformer.

The remainder of the sample-collecting system was heated with variable voltage transformer controlled strip heaters. This arrangement provided effective temperature control within the temperature range from 200° F to 350° F.

The sampling probe was mounted on a manually-operated traversing system, which allowed positioning of the probe at any location along a horizontal centerline at a given axial station of the exhaust gas stream. The probe nose dimensions allowed sampling of a small filament of the gas stream when the probe is fully immersed in the stream exhaust.

The test procedure for a representative sample traverse involved establishing coolant and aspirating flows through the probe on the stream centerline with the exhaust stream flowing. A sample-bottle fill was accomplished by first terminating the aspirating flow and opening the desired toggle valve permitting gas flow into the sample bottle which was evacuated to less than 1 mm Hg absolute prior to sampling. The fill was continued until equilibrium pressure was achieved at which time the bottle was sealed, aspiration resumed, and the probe manually positioned to the next selected location.

3.2.4.2 Enthalpy

The total enthalpy added to the test gas (ΔH_{arc}) was determined by the system energy balance method. This is accomplished by measuring (1) the total electrical-input power, the product of voltage and current; (2) the energy loss to the plasma generator cooling system, the product of coolant mass-flow rate, specific heat and temperature rise through the system less frictional heating; and (3) the total mass-flow rate of the test gas through the system, discussed above in Section 3.2.4.1. These measurements were made by various sensors whose output was recorded on an analog to digital printout

system, which has a conversion accuracy from sensor to printed digital output better than 0.5 percent. The sensors consisted of a 1-percent calibrated voltage divider to detect arc voltage, a 1-percent resistance shunt for measuring current, a differential temperature thermopile calibrated to 0.2° F accuracy, and an ASME-type orifice meter or a variable area flow meter for cooling water flow rate measurement accurate to 1 percent. With these recorded measurements, the energy added to the gas was determined by the following relation

$$\Delta H_{arc} = \frac{(E)\ (I) - \dot{M}_{(coolant)} \left[C_p\ (T_{out} - T_{in}) - \left(\frac{\Delta P}{\rho} \right) \right]}{\dot{M}_{gas}}$$

The estimated overall accuracy of the ΔH_{arc} measurement is 4 percent.

3.2.4.3 Pressure

The total pressure or chamber-pressure measurement for the simulation test was made with a strain gauge type transducer and a bourdon tube-type pressure gauge of test gauge accuracy better than 1 percent. The output from the pressure transducer was recorded on an oscillograph running at a speed of 1.4 inches per second for accurate recording of the transient signal. The transducer and test gauge sensed pressure at the downstream end of the mixing plenum chamber just upstream of the test nozzle. The estimated accuracy of the pressure measurement is 2.5 percent.

To determine the axial pressure distribution and the circumferential distribution at a particular axial station (to ascertain flow uniformity), special pressure-tap instrumented nozzles were fabricated. The nozzles are uncooled heat-sink devices made from high-conductivity copper with an internal contour conforming to the test nozzle and heat-transfer nozzle contours. Pressure taps were located according to the dimensions shown in Figure 48. To detect accurately the small pressure differences in the throat region, a manometer system was connected to monitor differential pressures with an absolute pressure measurement taken at one tap.

Test firings revealed no circumferential asymmetries in the flow field and an axial pressure gradient which verified the predicted isentropic expansion.

3.2.4.4 Heat-transfer coefficient

Two techniques were considered for evaluating the heat-transfer coefficient in the throat of the nozzle test section; a water cooled and a heat-sink calorimeter nozzle. With either calorimeter, the heat-transfer coefficient is computed from a measured local heat flux and a known enthalpy

difference across the boundary layer. The edge enthalpy, H_e, is measured and the wall enthalpy is based on an estimated calorimeter surface temperature. The water-cooled calorimeter has the advantages that, (1) straightforward data-reduction techniques may be employed to evaluate the heat flux, and (2) it may be left in the stream until boundary conditions have "steadied out" thus enabling measurement independent of "start up transients." The primary disadvantage of the water-cooled calorimeter is that its heated surfaces normally operate cold, thereby promoting condensation of steam from the boundary layer which may substantially alter the measured heat flux. Due to this undesirable aspect of the water-cooled calorimeter, consideration was also given to the utilization of a "hot wall" heat-sink type calorimeter. Each device is described in the following paragraphs.

3.2.4.4.1 Water-cooled calorimeter

The water-cooled calorimeter nozzle is shown in cross section in Figure 49. The heated walls were constructed of oxygen-free high-conductivity copper, all cooled by an external high-pressure water source. The nozzle body was designed to accommodate replaceable throat inserts, an assembly which included the radius-inlet section, the three straight-throat sections, and the exit cone.

The water-cooled nozzle was designed to detect three semi-local heat fluxes in the throat region and the average heat flux in the inlet- and exit-cone sections. A 0.002-inch air gap is included between the segments to serve as an insulator barring axial heat transfer between the segments. The measurements are made by monitoring the coolant flow rate independently for each segment and the corresponding temperature rise of the coolant after passing through the flow passageway. The coolant flow rate was monitored by precision-bore rotameters, and the coolant temperature rise was measured with stainless-steel sheathed copper-constantan differential thermocouples. Using the measured values of flow rate and temperature rise, the energy transferred to the coolant was calculated and then related to the unit heat flux by introducing the total area wetted by the gas.

3.2.4.4.2 Hot wall calorimeter

Methods have been considered to provide calorimetric techniques which will eliminate the effectsof surface condensation in the determination of heat flux in the throat region of a convergent nozzle. The most effective technique available, which has additional merit because of its simplicity, involves the use of the transient temperature response of an isolated

heat-sink element. A representation of the transient temperature hot wall calorimeter is given in Figure 50. The nozzle utilizes heat-sink elements, and is fabricated in three separate sections. The nozzle contour is identical to that of the water-cooled calorimeter nozzle with only one throat segment in place. The center element, representing the throat region, is essentially one-dimensional. The isolated element is instrumented to measure the transient temperature response by means of six spring-loaded thermocouple probes located at selected and known radial locations over the downstream face of the element.

The data reduction procedure utilizes the one-dimensional transient conduction solution (heat flow in the radial, but not axial direction) to solve for the combined convective and radiative flux to the element, based on the temperature response information obtained from the thermocouple data. The solution requires the measured temperature responses of the thermocouple elements obtained at known distances apart, along the conduction paths within the heat-sink element and the thermal characteristics of the element itself, within the region of experimental interest.

In this section (Section 3.2.4), the measurement techniques to establish the test section boundary conditions have been described. In the following section (Section 3.2.5), the measurement techniques utilized to record the ablation material response are described.

3.2.5 Measurement of material response

The measurable parameters defining the response of the nozzle material to the environment are the surface temperature, the material temperature in depth, and the rate of material removal or erosion rate. These measurements are described in the succeeding paragraphs.

3.2.5.1 Surface temperature

The surface temperature was measured with a recording optical pyrometer. The sensing zone was a spot 0.080 to 0.090-inch diameter located in the nozzle throat region. The pyrometer, an Infrared Industries, "Thermodot," senses brightness temperature in the near infrared at a wavelength of about 800 millimicrons. The reported temperatures are uncorrected for surface emissivity; however, when $\epsilon \geq 0.8$ the correction amounts to less than 4 percent increase. The pyrometer was checked for interference from the exhaust gases of the simulated O_2-H_2 environment by viewing a tungsten filament through the plasma generator exhaust stream. The output of the pyrometer was unaffected by the luminous gas, hence, it was assumed the gases

would not affect temperature measurements of the nozzle wall. The pyrometer has an overall accuracy of about 5 percent at the temperatures reported.

3.2.5.2 Internal temperature

The temperature history of the nozzle material in depth was defined by several thermocouple probes accurately located in the nozzle wall. To minimize the errors induced by wire conduction and contact resistance, the smallest practical sensing junction and leadout wire were selected, and the probes spring-loaded into the nozzle material. To prevent temperature field distortion, the probes were inserted into the side of the body normal to a radius at selected distances from the heated surface. This permitted the probe to lie essentially along an isotherm in the body. The mounting scheme is shown in Figure 51.

The thermocouple probes were made from 0.035-inch OD alumina double-bore tubing, sheathed at a point starting 1 inch from the sensing junction with 0.062-inch OD stainless-steel tubing. The outer body has a small flange for spring loading. A separate retainer ring is provided to support the thermocouple probes. Two types of sensing junctions were used; the probes closest to the heated surface are 0.005-inch-diameter tungsten, 5 percent rhenium-tungsten, and 26 percent rhenium wire with a heliarc-formed junction, the other probes being commercially available 0.005-inch-diameter chromel-alumel junctions supplied by Omega Engineering Co., Springdale, Connecticut. Figure 52 shows a typical thermocouple probe. The probes are inserted into 0.039-inch-diameter holes in the ablation material nozzle. The depths are measured accurately to insure sensor contact at a point perpendicular to a radial line. X-ray examination of the drilled nozzle body is utilized to ascertain accurately the thermocouple depth beneath the surface. The x-ray beam centerline was coincident with the nozzle axis, and gauge blocks were placed at the top and bottom of the nozzle to permit determination of actual distances from photographic reproductions by eliminating the three-dimensional effects incurred at points away from the film plane. A typical x-ray is shown in Figure 53.

The thermocouples were all located at an axial position representing the center of the tubular-throat section. The distance between the thermocouple sensing junction and original unheated wall for all instrumented test models is given with the temperature data discussed in Section 3.4.

3.2.5.3 Erosion rate

The rate of material removed at the nozzle throat was measured by two methods; first, a pre- and post-test measurement of nozzle-throat diameter and the firing time to determine average rates, and second, a choked flow computation to determine nozzle-throat area as a function of the pressure history. The procedure for the latter method involves calculating an initial condition using a known throat area to establish a nozzle coefficient, usually about 0.92 to 0.98, which was then used throughout the remainder of the time-dependent computations of throat diameter. The erosion was then simply related to a diameter change. As a check, the final computation of diameter was compared with the measured value and usually agreed within about 5 percent.

3.2.6 Experimental approach - summary

A technique has been described for simulating liquid-propellant rocket-exhaust product environments. A means of achieving duplication of the primary simulation parameters, chemical composition, enthalpy, and heat-transfer coefficient, utilizing an arc-plasma generator has been presented. Efforts directed toward modification of each of two arc-plasma generators to operate in the desired range of conditions have been described. Of the two arc-plasma generators considered, a solenoid and a constrictor type, the latter was found to be more adaptable and was modified to operate in the desired range of conditions for simulation of two propellant environments, O_2-H_2, and N_2O_4-N_2H_4/UDMH. Finally, techniques were described for evaluating the accuracy with which simulation was achieved, and for measuring the response of ablative materials tested in these environments.

In the following section, Section 3.3, a brief account of the experimental procedure is given, and is followed in Section 3.4 by a presentation of results obtained from arc-plasma tests simulating each of two propellant environments.

3.3 Experimental Procedure

The procedure generally followed to conduct the rocket-engine simulation tests was somewhat dependent on the test gas composition. The hydrogen containing mixtures were treated carefully to avoid concentrations of H_2 in the arc chamber either before or after the plasma-generator firings. The use of steam required preheating to insure that the lines to the arc would not condense the small amounts of steam being used.

The gas system piping was arranged as shown schematically in Figure 54. Three separate gas metering systems were used: (1) the primary mixture, injected to the arc zone, (2) the secondary mixture, injected into the mixing plenum, and (3) steam admitted to the mixing plenum chamber through a separate injection ring. The gas mixtures employed for simulation were described in Section 3.2.1.1. For O_2-H_2 simulation, H_2 is the primary gas and the secondary system was not employed. For the N_2O_4-N_2H_4/UDMH simulation, Mixture F is the primary and Mixture G is the secondary gas. Steam is utilized for both environments. The starting procedure involved purging both the primary and secondary systems with N_2 and leaving them filled to the stop valve upstream of the arc. Downstream of the stop valves, N_2 was admitted to the gas systems and permitted to bleed into the arc chamber. Steam was circulated through the lines leading to the immediate vicinity of the arc and then bypassed to the atmosphere. The steam lines leading from the bypass valves to the mixing plenum were electrically heated to maintain their temperature above the condensation point.

With the pre-test purge flows on, the voltage potential was applied to the electrodes and the arc was started with a short pulse of high voltage RF to initiate ionization of the gas in the arc zone. Immediately after arc ignition, the primary flow was started and adjusted, requiring power system adjustments to compensate for the higher voltage associated with the H_2 in the primary gas. With stable primary flow, the secondary mixture was started and adjusted, followed closely by the introduction of the steam. Upon test completion, the primary and secondary systems were purged with nitrogen.

Once the final operating conditions had been established for each of the rocket-engine simulation cases, only a few tests were run and the speed with which the gas transferring could be accomplished was often not optimized; however, the primary considerations of starting the arc, establishing the desired gas-flow rates, reaching the desired chamber pressure and preventing explosive concentration of gases were all satisfied. Improvement in the time to reach steady state was reduced to a matter of minor piping modifications and some automatic control.

3.4 Test Results

Of the four propellant environments considered, N_2O_4-N_2H_4/UDMH, O_2-H_2, OF_2-B_2H_6, and O_2/F_2-CH_4, simulation was attempted with the first three and was successful with the first two. Duplication of the three primary

simulation parameters, chemical composition, enthalpy, and heat-transfer coefficient for these two environments was obtained utilizing the constrictor arc-plasma generator described in Section 3.2.3. Considering these three simulation parameteres to be of primary importance, the present rocket-nozzle environment simulation capabilities of the arc-plasma generator are shown in Figure 55. Since the propellant enthalpy and chemical composition are usually duplicated in all arc-plasma simulation tests, the only remaining parameter of concern is the heat-transfer coefficient. Shown in Figure 55(a) and 55(b) are the operating conditions achieved for the N_2O_4-N_2H_4/UDMH and the O_2-H_2 propellant environments, respectively. In addition, each figure indicates a line of constant heat-transfer coefficient equal to that in the simulation tests and line of constant heat-transfer coefficient equal to 25 percent greater and less than that corresponding to the arc-plasma generator simulation tests. It is apparent from the figures that a relatively broad range of rocket-engine conditions may be simulated with a subscale test. For example, referring to Figure 55(a), it is noted that, within 25 percent, the arc-plasma test of 85 psia with $D_* = 0.3$ inch yields simulation of throat conditions for rocket engines having $P_c = 138$ psia with $D_* = 8$ inches, and $P_c = 238$ psia with $D_* = 6$ inches. Rocket engines characterized by points above the constant heat-transfer-coefficient line in Figures 55(a) and 55(b) have less severe conditions than the arc-plasma test, and those below the line have more severe conditions.

A presentation of operating conditions for ablative-material tests conducted in the N_2O_4-N_2H_4/UDMH and O_2-H_2 environments, are given first in Section 3.4.1 and 3.4.2, respectively. Next, a brief description of difficulties encountered with the OF_2-B_2H_6 environment is given in Section 3.4.3, and is followed in Section 3.4.4 by the results of ablative-material tests in the solenoid-arc unit which simulated the oxidation and enthalpy potentials of the N_2O_4-N_2H_4/UDMH environment. Finally, in Section 3.4.5, the ablative-material temperature and recession-rate data are compared to predictions utilizing the theoretical ablation model described in Section 2.1.

3.4.1 N_2O_4-N_2H_4/UDMH simulation-test series

A series of five simulation tests were performed in the N_2O_4-N_2H_4/UDMH environment consisting of two calorimeter and three ablating nozzle tests. The test-gas composition and enthalpy requirements for this simulation were given in Section 3.2.1. The accuracy with which the test gas corresponds

to the desired composition may be established by considering the mass-flow rates of each gas mixture in the tests and comparing the resulting composition to that desired.

Gas	Mass-Flow Rate (lb/sec)	K_{actual}	$K_{Desired}$
Mixture F	0.0153	0.442	0.4505
Mixture G	.0134	.387	.3815
Steam	.0059	.171	.1680

It is observed that the relative mass fraction, (K) of each gas, is within 2 percent of the desired value. In order to demonstrate duplication of the gas composition adjacent to the ablation-material specimen, however, it is also necessary to insure that these gases are well mixed. The mixing plenum chamber, provided for achieving mechanical and thermal equilibration of the various gas mixtures, was described in Section 3.2.3.4. The species sampling probe, utilized to measure the degree of mixing obtained, was described in Section 3.2.4.1. The results of the species sampling measurement are presented first and are followed by calorimeter and ablation-material test results.

3.4.1.1 Free-stream species sampling-probe test

Gas samples were taken from the free stream with the species sampling probe during the course of one test to determine the degree of mixing in the plenum chamber. The results are shown in Figure 56 in the form of elemental mass fraction as a function of radial position from the stream centerline. The plot shows a comparison between the measured concentration and what should have existed had perfect mixing occurred.

The samples were taken with the probe located 0.050 inch downstream of the nozzle-exit plane to avoid entrainment of room air. The data points on Figure 56 represent the gas chemical analysis at four locations on the stream radius. The laboratory engaged to perform the quantitative gas analysis was not able to detect the expected water content (about 3 drops in a liter) due to the small volume of sampled gas. Hence, the gas-analysis data was then treated as if an unknown amount of water had existed in the sample and the comparison was based on the following reasoning. The measured hydrogen concentration in the samples was compared to the hydrogen

concentration in the complete simulation gas and the difference was presumed to have been removed in the sampling process in the form of undetected water. The amount of oxygen corresponding to the calculated quantity of water formation was also removed from the simulation gas mixture. The resulting gas composition, consisting of the initial quantities of nitrogen and carbon, a reduced quantity of oxygen, and the measured quantity of hydrogen, were compared to the measured data and are shown in Figure 56. Based on the close agreement between predicted and measured concentrations, and the flat profiles across the stream, it was concluded that the degree of gas mixing in the plenum chamber was excellent.

3.4.1.2 Heat-transfer nozzle tests

The first test in the series, No. 294, was run with the cold-wall heat-transfer nozzle simulating the N_2O_4-N_2H_4/UDMH environment. The calibration nozzle, described in Section 3.2.4.4, was used to determine the nonablating wall convective transfer coefficient, $\rho_e U_e C_H$, at the throat.

The results of this calibration test are presented below:

$$\text{Chamber pressure, } P_o = 89.96 \text{ psia}$$

$$\text{Enthalpy, } \Delta H_{arc} = 2110 \text{ Btu/lb}$$

$$\text{Throat diameter, } D_* = 0.298 \text{ inch}$$

$$\text{Throat heating rate, } q^* = 391.7 \text{ Btu/ft}^2\text{-sec}$$

A calculation of the nozzle coefficient using choked flow conditions revealed $C_N = 0.923$, reasonable for a nozzle of this size.

Using the simplified Bartz equation modified to an enthalpy driving potential, and transport properties evaluated at boundary-layer reference conditions as shown in Appendix A, the calculated value of the convective heat-transfer coefficient is $\rho_e U_e C_H = 0.384$ lb/ft^2-sec, and using a value of $T_{wall} = 200^\circ$ F, the computed throat heating is $q^* = 1158$ Btu/ft^2-sec. The ratio of the measured to computed is

$$\frac{q^*_{measured}}{q^*_{Bartz}} = 0.34$$

The low value of the measured heat-transfer rate to that predicted by the Bartz relation has been investigated to the extent that all of the raw data collected during the test was double checked and re-reduced in an effort

to uncover numerical errors. The checks verified the reported measurement within a few percent. Previous experience with nozzle-throat heat-transfer rates in the arc-plasma test device, utilizing noncondensible fluids, has generally resulted in heat fluxes equal to about 70 percent of those predicted by the Bartz simplified equation (see e.g., the test results with the N_2-He-O_2 gas mixture shown in Figure 65). It is rationalized that the low values of heat flux obtained in this environment must be a result of condensation on the cold calorimeter surface upstream of the throat section, which resulted in a liquid-water film flowing over the throat calorimeter sections.

As indicated earlier, one of the advantages of the "hot wall" heat-sink calorimeter, described in Section 3.2.4.4.2, is that its surface temperature operates high enough to insure that condensation will not occur. Two tests were run with the hot-wall heat-transfer nozzle. The test conditions were held at the desired point for about 20 seconds while transient temperature data were recorded. An analysis of the thermocouple data revealed obvious mechanical difficulties with the thermocouple probes, which were mainly attributed to improper seating of the sensing junctions against the heat-sink wall, causing erroneous measurements.

The test data were examined, however, for adequacy of conditions for nozzle environment simulation. The test data are as follows:

Test No.	Enthalpy ΔH_{arc} (Btu/lb)	Chamber Pressure, P_o (psia)	Gass Mass-Flow Rate (lb/sec)	Nozzle Coefficient*, C_N
298	2130	83.5	0.0346	0.96
299	2191	82.3	.0346	.96

*Choked flow calculation.

On the basis of the previously described test results with noncondensible fluids in the arc-plasma generator with this nozzle configuration, it seems reasonable to assume that the actual heat-transfer coefficient is approximately 0.7 times that given by the Bartz equation.

3.4.1.3 Ablating nozzle tests

Two ablation-material nozzles were tested as part of the N_2O_4-N_2H_4/UDMH propellant simulation series. The nozzle materials were graphite phenolic[8]

[8]Type MX 4500, Fiberite Corporation.

(Test No. 295), and a silica cloth phenolic[9] (Test No. 296). The nozzle configuration shown in Figure 57 was instrumented with three thermocouple probes and mounted by a retaining flange to the plenum chamber of the constrictor arc-plasma generator. Figure 58 shows a photograph of an instrumented nozzle in place for testing.

The test conditions; arc enthalpy, ΔH_{arc}, chamber pressure, P_o, and total mass-flow rate, $\dot{M}$, are shown as a function of time for Test Nos. 295 and 296 in Figure 59(a) and 59(b), respectively. The histories show the start up transient period as well as the portion of the test where the desired enthalpy and composition existed. The long transient period was due solely to slow operational procedures involved with transferring the gases and establishing the desired electrical conditions. Better control was established, and during the hot-wall heat-transfer test (Test No. 299), steady conditions were achieved in about 6 to 7 seconds. Estimates of the enthalpy and chemical composition variation during the starting period were made to provide boundary conditions for the ablation prediction presented later in Section 3.4.5. The enthalpy was computed by the energy balance method discussed in Section 3.2.4.2, using a total mass-flow rate based on the sum of the various gas flows as they were introduced into the system. The composition of the gas mixture was computed in the same manner. The temperature histories at the three thermocouple locations, along with the optically measured nozzle throat surface temperature histores, are presented in Section 3.4.5 where they are compared with predictions.

A calculation of throat erosion as a function of time was made using the pressure history and the choked flow relation. Thermodynamic properties for the choked flow calculation were based on the assumption of chemical equilibrium. The erosion data are presented in Figures 60(a) and 60(b) with a point indicating the post-test measured value at the minimum throat area, and at the mid-throat location. The choked flow calculated erosion history is shown in the figures, and is based on the assumption that erosion began when test conditions were established. Determination of steady conditions was made from the test record when all gas flows and electrical conditions were steady. Referring to Figures 59(a) and 59(b), steady-state time for Test No. 295 occurred approximately 18 seconds after arc ignition, and, for Test No. 296, steady conditions were established at 22.3 seconds. It should be noted in Figures 59(a) and 59(b) that the graphite-phenolic nozzle, Test No. 295, apparently did not start eroding until the test conditions were

[9]Type MX 2600, Fiberite Corporation.

established, since a peak pressure was reached which was comparable to that of the nonablating nozzle tests, Nos. 298 and 299. On the other hand, the silica cloth phenolic nozzle started to erode immediately due to extremely high enthalpy incurred during the starting transient, and the expected peak pressure was never achieved.

A photograph of the cross-sectioned nozzles is shown in Figures 61(a) and 61(b), wherein the dashed lines represent the pre-test contour.

The measured temperature histories of the ablating nozzles are presented and compared to predictions in Section 3.4.5.

3.4.2 O_2-H_2 simulation test series

In this test series, simulation of an O_2-H_2 rocket engine having an oxidizer-to-fuel mass ratio of 4.0 was achieved. Simulation was accomplished by arc heating the appropriate quantity of H_2 and post-injecting steam in the downstream mixing plenum chamber. As indicated in Section 3.2.1, for this environment, the desired arc enthalpy addition, ΔH_{arc} is 4663 Btu/lb. The desired and actual quantities of the simulation gases are shown below.

Gas	Mass-Flow Rate (lb/sec)	K_{actual}	$K_{desired}$
H_2	0.0033	0.0952	0.099
Steam	.0314	.9048	.901

The composition is within 4 percent of that desired.

After a number of tests required to establish stable operating conditions, three simulation tests were run for this environment. Because the voltage requirements for arc operation on hydrogen are high and because voltage requirements increase with pressure (see Fig. 40), it was possible to achieve only 65 psia chamber pressure for these simulation tests within the constraints of the present power supply capabilities and arc-plasma generator electrode geometry. Because of the lower chamber pressure, it was possible to employ a 0.4-inch-diameter-throat nozzle for these tests rather than the 0.3-inch-nozzle configuration required for the N_2O_4-N_2H_4/UDMH series.

3.4.2.1 Heat-transfer nozzle test

Test No. 287 was run with the cold-wall heat-transfer nozzle using the simulated O_2-H_2 propellant conditions. A 0.4-inch-diameter throat calorimetric nozzle was used to determine the throat heat flux.

The results of the calibration test are presented below:

$$\text{Chamber pressure, } P_o = 66.7 \text{ psia}$$

$$\text{Enthalpy, } \Delta H_{arc} = 4490 \text{ Btu/lb}$$

$$\text{Throat diameter, } D_* = 0.403 \text{ inch}$$

$$\text{Throat heat rate, } q^* = 434 \text{ Btu/ft}^2\text{-sec}$$

A calculation of the nozzle coefficient using choked flow relations revealed $C_N = 0.988$.

The predicted throat heat rate using the simplified Bartz equation was found to be $q^*_{Bartz} = 1086$ Btu/ft^2-sec. The ratio of the measured and calculated value is $q^*_{measured}/q^*_{Bartz} = 0.40$. The ratio of measured to predicted is approximately the same as that observed in the N_2O_4-N_2H_4/UDMH tests. The same rationalization of the low value of heat flux applies here, namely, condensation on the cold convergent nozzle section produced a liquid layer which effectively film cooled the throat calorimeter section.

3.4.2.2 Ablating nozzle tests

Two ablating nozzles were tested as part of the O_2-H_2 propellant system simulation demonstration. The nozzle materials were graphite[10], Test No. 289, and silica-cloth phenolic[11], Test No. 290. Both nozzles had a nominal diameter of 0.4 inch at the throat. The graphite nozzle showed no measurable erosion (Test No. 298) which was attributed to low surface temperature caused by the heat-sink effect of the nozzle. The test condition for the silica-phenolic nozzle, Test No. 290, are presented in Figure 62 which shows the enthalpy ΔH_{arc}, chamber pressure, P_o, mass-flow rate, $\dot{M}$, and estimated composition as functions of time.

The erosion history for Test No. 290, shown in Figure 63, was inferred from the chamber pressure history and choked flow calculations using equilibrium thermodynamic properties for the H_2-O_2 environment. The post-test measurement of surface recession is noted in the figure for both the minimum area and mid-throat locations. A photograph of the sectioned nozzle is

[10] GX grade Graphite Specialties Co.

[11] MX 2600 Fiberite Corp.

shown in Figure 64. The measured internal-temperature history of the nozzle is presented and compared to predicted values in Section 3.4.5.

3.4.3 OF_2-B_2H_6 simulation attempts

Tests were conducted in an attempt to simulate the OF_2-B_2H_6 propellant system using boron trifluoride gas and steam as described in Section 3.2.1.1. The first tests were run with nitrogen post-injected in place of steam in order to establish operating conditions with BF_3 as the arc-heated gas. Later tests were conducted with the BF_3-steam combination.

The results of these tests revealed that the arc could be operated on BF_3, however, there was a severe corrosive attack on the thoriated tungsten cathode surface at a chamber pressure of about 2 atmospheres. The desired gas enthalpy of 6885 Btu/lb (see Section 3.2.1.2) was achieved at 2 atmospheres chamber pressure. Severe electrode erosion was experienced when higher pressure operation was attempted.

A second problem area arose when steam was introduced to the mixing chamber downstream of the arc zone. The water and BF_3 combined to form a syrupy condensate which rapidly accumulated on the walls of the mixing plenum chamber. The corrosive characteristics of the BF_3 gas and its compounds with water attacked both the electrode surfaces and the boron-nitride electrode insulator (see Fig. 38), to a point where operation could not be sustained for more than 2 minutes. In addition to the mechanical failures experienced, there was a gross uncertainty in the gas stream composition due to the condensation in the plenum chamber.

It was encouraging to find that the arc would operate on BF_3 gas, but many corrective measures remain to be instituted before satisfactory environmental simulation can be achieved. To counteract the electrode erosion problem, thermionic emitter materials other than thoriated tungsten should be considered for a cathode surface. The electrode insulator problem probably can be resolved with an advanced grade of boron nitride which is non-hygroscopic.

Results of the ablative-material tests utilizing the solenoid arc-plasma generator, which simulated the oxidation and enthalpy potential of the N_2O_4-N_2H_4/UDMH environment, are presented in the following section.

3.4.4 Oxidation and enthalpy potential simulation

As described in Section 3.2.2, operating difficulties with the solenoid arc-plasma generator precluded obtaining duplication of the parameters requisite to complete simulation of liquid-propellant exhaust product

environments. Successful tests were run, however, with a gas mixture designed to simulate the oxidation and enthalpy potential of the N_2O_4-N_2H_4/UDMH propellant environment. Details of the gas mixture and test conditions were presented above, in Section 3.2.2.4, and the test results are presented here.

The test results consist of heat-transfer coefficient data obtained with the water-cooled calorimeter described in Section 3.2.4.4.1, ablation-material internal-temperature histories, and ablated depth for each of five nozzles tested.

Heat-flux measurements were obtained for each of the five calorimeter segments shown in Figure 49. The measured heat-transfer coefficient, $\rho_e U_e C_H$, is shown as a function of nozzle location in Figure 65. Also shown in Figure 65 is a correlation line defined by $\rho_e U_e C_H = 0.7\ (\rho_e U_e C_H)_{Bartz}$ where the latter is interpreted in Appendix A. The correlation is shown as a dashed line, and the data are shown as points. The points in the throat are located corresponding to the centers of the three tubular segments, whereas the location of the points for the inlet and exit segments are based on a calculated heat-flux distribution using the local diameter dependence of the Bartz solution.

Ablation data were obtained for each of five materials which are listed here, along with the measured total ablated depths and test times.

Test No.	Nozzle No.	Material Type	Initial Throat Diameter D_{*_i} (in.)	Wall Recession at Throat ΔS_* (in.)	Recession Rate at Throat $\dot{S}$ (in./sec$\times 10^{-3}$)	Firing Time (sec)
1105	N-15	ATJ*	0.3020	0.0950	3.125	30.4
1106	N-13	MX 2600**	.3020	.1130	8.248	13.7
1107	N-11	MXS-75**	.3015	.1402	9.163	15.3
1108	N-14	MX 4500**	.3060	.1120	5.957	18.8
1109	N-12	MXS-19**	.3050	.1260	8.129	15.5

*Manufactured by National Carbon Company.
**Manufactured by Fiberite Corporation.

All tests were run until the throat erosion caused the arc-chamber pressure to drop to approximately half its initial value. The five nozzles are shown

in Figure 66 in sectioned view. The dashed line indicates the original 0.3-inch-diameter throat nozzle contour. The ATJ Graphite model (see Fig. 66(a)) showed severe pitting or dimpling in the throat region which is characteristic of the lower density, higher permeability graphites. The other materials revealed uniform erosion throughout the throat, both in the circumferential and longitudinal directions. The ablation-material internal-temperature response histories are shown in Figure 67.

Measured temperature and recession data from the full simulation tests, utilizing the constrictor arc-plasma generator, are compared to theoretical predictions in the following section.

3.4.5 Comparison of ablation data to theoretical predictions

Temperature history and surface-recession data for the N_2O_4-N_2H_4/UDMH, and O_2-H_2 ablation-material tests are presented and compared to predictions based upon the theoretical ablation model presented in Section 2.1.

The tests were conducted for two materials, silica phenolic (MX 2600), and graphite phenolic (MX 4500), both having a fabric layup perpendicular to the heated surface in the throat region (see Figs. 61 and 64). Material thermal properties employed to characterize the thermal response of these materials, with a 90° layup angle, are shown in Table V. The time-dependent boundary conditions required for the Charring Material Response Program (Section 2.1.3.2) were generated employing the Equilibrium Surface Thermochemistry Program (Section 2.1.3.1), and the representation of gas-flow rates, chemical composition, enthalpy, and pressure presented in Figures 59 and 62 for the N_2O_4-N_2H_4/UDMH and O_2-H_2 simulation environments, respectively. The predictions for each firing were obtained with a series of three runs on the Charring Material Response Program. The first run represented the transient period required for steady operating conditions to be obtained in the test. This run utilized the assumption that the boundary-layer-edge gas was either N_2 for the N_2O_4-N_2H_4/UDMH series, or H_2 for the O_2-H_2 test. The heat-transfer coefficient employed was taken as 0.7 times that given by the simplified Bartz equation using the measured simulation gas-flow rates to obtain the boundary-layer-edge mass velocity. The second run on the Charring Material Response Program represented the period of complete simulation of the boundary-layer-edge gas composition. During this period, the total enthalpy was obtained from Figures 59 and 62, and the heat-transfer coefficient was taken as $0.7\ (\rho_e U_e C_H)_{Bartz}$ based on the measured simulation gas-flow rates and the estimated throat cross-section flow area from Figures 60 and 63. The last run on the Charring Material Response Program for each

test represented the material cooldown after test termination. This period, in all cases, is represented by a flow of room temperature nitrogen over the test sample; the purpose of which is to purge the simulation apparatus of toxic and combustable gases.

The results of the theoretical predictions are compared to the measured ablation-material response data in the following sections.

3.4.5.1 N_2O_4-N_2H_4/UDMH tests

A comparison of predicted and measured ablative-material response for graphite-phenolic and silica-phenolic test nozzles subjected to the simulated environment are shown in Figures 68 and 69, respectively. The predictions shown in Figures 68(a) and 69(a) were obtained utilizing the Equilibrium Surface Thermochemistry Program to characterize the surface boundary condition required for the subsurface response solution. For each nozzle, the predicted surface temperature and recession rate was different from that observed. This discrepancy is partially responsible for the lack of agreement between predicted and measured subsurface-temperature histories. In order to separate the errors associated with evaluating the surface boundary condition from those associated with characterizing the subsurface response, a second set of predictions was performed employing the Charring Material Response Program. This second set of predictions utilized measured surface-temperature and recession-rate histories to characterize the surface boundary conditions. The results of these calculations are shown in Figures 68(b) and 69(b) for the graphite-phenolic and silica-phenolic nozzles, respectively.

The agreement between predicted and measured surface recession for the graphite-phenolic nozzle is not bad, 0.208 predicted versus 0.150 measured. The high predicted surface-temperature peak at 13 seconds is a result of the extremely high enthalpy achieved in the simulation test prior to establishing steady operating conditions as shown in Figure 59(a). As a result of this high predicted surface temperature and somewhat high predicted surface-recession rate, the predicted temperature history of the thermocouples is substantially greater than the measurement. A modified thermocouple temperature-history prediction, utilizing the measured surface temperature and recession-rate histories as boundary conditions, is shown in Figure 68(b). The difference between predicted and measured internal-temperature histories in this figure must be attributed to the subsurface response solution. Perhaps the most likely errors would be associated with ill-defined material thermal properties. Referring to Figure 68(b), it is

noted that agreement could be substantially improved if the (high temperature) char thermal conductivity were increased and the (low temperature) virgin material thermal conductivity were decreased. Such a perturbation on the material properties of graphite phenolic, shown in Table V(a), would be in order for subsequent predictions with this material.

The agreement between predicted and measured surface recession for the silica-phenolic nozzle is poor (Fig. 69(a)). The large discrepancy is attributed to a large quantity of material removal in the liquid form prior to establishing steady operating conditions in the arc test. This occurrence is substantiated by referring to the measured chamber-pressure history for the test (Fig. 59(b)), where it is noted that the anticipated 85 psia was not reached after achieving steady operating conditions. Because of this occurrence, not much significance should be associated with the comparison in Figure 69(a). As was done for the graphite-phenolic nozzle, an additional run was made with the Charring Material Response Program, utilizing measured surface temperature and recession-rate histories as boundary conditions. The results of this computation are compared to measured internal-temperature histories in Figure 69(b). Referring to the figure, it is noted that good agreement between predicted and measured temperatures is achieved, and it is concluded that the internal response solution, including thermal properties shown in Table V(b), is adequate for characterizing the subsurface response of silica phenolic.

3.4.5.2 O_2-H_2 test

One charring ablation-material nozzle was tested in the simulated O_2-H_2 environment (Test No. 290). Because of the long transient time required to establish steady operating conditions, approximately the first 27 seconds of the test was characterized by ill-defined boundary conditions (see Fig. 62). As a result, it was not considered worthwhile to attempt prediction of the surface thermochemical boundary conditions during this period, and the Charring Material Response Program was run only with specified surface temperature and recession-rate boundary conditions. The specified surface temperature and recession rate corresponds to the measured values, and the resulting internal-temperature history is compared to the measurement in Figure 70. As was the case for the silica-phenolic nozzle tested in the N_2O_4-N_2H_4/UDMH environment, the agreement between predicted and measured internal-temperature histories is good. This gives further substantiation to the earlier conclusion that the theoretical treatment of the subsurface

thermochemical response, including material thermal properties for silica phenolic, is adequate.

3.5 Summary of Experimental Investigations

An experimental program has been conducted for the purpose of developing a laboratory technique for testing ablative materials in a simulated rocket-engine environment. The technique consists basically of adding energy to special gas mixtures with an arc-plasma generator and passing the high-temperature gas mixture through a test nozzle constructed of the ablative material. The parameters which must be duplicated to achieve experimental simulation were obtained from theoretical considerations, and related to quantities measurable in the laboratory. The parameters of primary importance are: gas composition, enthalpy, and heat-transfer coefficient.

Experimental efforts were directed toward modification of air arc-plasma generators to operate on the requisite simulation gas mixtures at the desired pressure and enthalpy levels. Arc-plasma generators operating on two different principles were considered for this modification, a magnetically stabilized "solenoid" unit, and a gas vortex stabilized "constrictor" unit. The magnetically stabilized unit was found to be suitable only for simulation of oxidation and enthalpy potential. This compromised simulation was demonstrated for one propellant system, N_2O_4-N_2H_4/UDMH. The gas stabilized, constricted, arc-plasma generator was successfully modified to operate on the requisite gas mixtures for simulating the environments of two liquid-propellant rocket-engine environments, N_2O_4-N_2H_4/UDMH, and O_2-H_2. A number of tests were run and accompanied by the measurements appropriate to demonstrating duplication of the pertinent simulation parameters. Several ablative-material tests were performed in the simulated environments in order to further demonstrate the validity of the simulation technique.

4. RECOMMENDATIONS

The studies described in this report have been directed toward developing meaningful and economical methods for rating the performance of ablative materials in liquid-propellant rocket-engine environments. The theoretical and experimental techniques adopted have been based primarily upon consideration of material removal resulting from thermochemical interactions between the material and its environment. In order to retain generality with respect

to materials and environments, it has been necessary to include certain assumptions and compromises in these techniques. Recommendations for improving the current theoretical and experimental techniques follow logically from consideration of these assumptions and limitations.

Recommendations to Improve the Theoretical Technique

It is recommended that the Charring Material Response Program be utilized to predict ablation data resulting from exposure of a variety of ablation materials to a variety of environments. On the basis of comparisons between predicted and measured material response, it will be possible to propose modifications most likely to result in agreement between prediction and data. The following modifications should be considered.

(1) The present formulation assumes that chemical equilibrium is achieved at the ablating surface. The validity of this assumption should be investigated for each material-propellant combination of interest, and, if appropriate, the program should be modified to include kinetically controlled heterogeneous reactions between the surface material and the boundary-layer reactants peculiar to each specific propellant.

(2) The present formulation considers surface recession resulting from all possible gas phase producing chemical reactions. Consideration should be given to including surface removal in liquid form to characterize silica-reinforced materials.

(3) Consideration should be given to kinetically controlled coking of the pyrolysis products in depth. This will enable theoretical characterization of the sometimes experimentally observed char densification near the ablating surface.

(4) Consideration should be given to including kinetically controlled reactions between SiO_2 fibers and carbonaceous resin residue in depth. This will enable specification of the extent of the liquid layer, a prerequisite to consideration of liquid-layer removal phenomena.

(5) Careful attention should be given to obtaining thermal property and chemical kinetic information requisite to operating the computer program with the above suggested modifications.

Recommendations to Improve the Experimental Technique.

(1) The arc-plasma generator should be modified to enable operation on the gases requisite to simulating other liquid-propellant environments of interest to NASA.

(2) Appropriate modifications should be made in the experimental operating procedure to enable achieving steady-state operating conditions within 5 seconds of arc ignition.

(3) Consideration should be given to maintaining constant chamber pressure during the conduct of an ablative material test by controlling the simulation gas-flow rate.

General Recommendations

Two recommendations which are of equal importance to both theoretical and experimental aspects of the analysis have to do with evaluating the boundary conditions to which the ablative material is exposed.

(1) Consideration should be given to utilizing numerical boundary-layer integration schemes to evaluate the heat-transfer coefficient along the particular rocket nozzle of interest. This integration should include, at the very least, the rocket thrust chamber and nozzle geometrical influence on the boundary-layer structure.

(2) It is recommended that detailed consideration be given to evaluating the state of the gas at the boundary-layer edge. The local oxidizer-to-fuel ratio strongly influences the ablation rate, and all theoretical and experimental considerations presented herein are based upon the assumption that the boundary-layer-edge gas is everywhere composed of the ideal mixture of oxidizer and fuel. There is evidence to indicate that this is rarely a valid assumption.

REFERENCES

1. Scala, S. M. and Gilbert, L. M.: The Sublimation of Graphite at Hypersonic Speeds. General Electric Doc. GE R-64-SD 55, Aug. 1964.

2. Welsh, W. E., Jr. and Chung, P. M.: Effect of Temperature on Combustion of Carbon Surfaces. Proceedings of the 1963 Heat Trans. and Fluid Mech. Inst., Stanford University Press, 1963.

3. Moore, J. A. and Zlotnick, M.: Combustion of Carbon in an Air Stream. ARS Jour., vol. 31, no. 10, Oct. 1961.

4. Denison, M. R.: The Turbulent Boundary Layer on Chemically Active Ablating Surfaces. JAS, vol. 28, no. 6, June 1961.

5. Bartlett, E. P.: A Systematic Method for Determination of Ablation Rates in a Corrosive Environment. Sixth Symposium on Ballistic Missile and Aerospace Technology, vol. III, 1961.

6. Lees, L.: Convective Heat Transfer with Mass Addition and Chemical Reactions. Third AGARD Combustion and Propulsion Colloqium, May 1958.

7. Kratsch, K. M., Hearne, L. F., and McChesney, H. R.: Thermal Performance of Heat-Shield Composites During Planetary Entry. AIAA - NASA National Meeting, Sept. 1963.

8. Quinville, J. A. and Solomon, J.: Ablating Body Heat Transfer. Aerospace Corp. SSD-TDR-63-159, Contract No. AF 94(695)-269, Jan. 15, 1964.

9. Dorrance, W. H.: Viscous Hypersonic Flow. McGraw-Hill Book Co., 1962, pp. 180-182.

10. McCuen, P. A., Schaefer, J. W., Lundberg, R. E., and Kendall, R. M.: A Study of Solid-Propellant Rocket-Motor Exposed Materials Behavior. Final Report, Contract No. AF 04(611)-9073, Vidya Project No. 9061, Feb. 26, 1965.

11. Kendall, R. M. and Rindal, R. A.: Analytical Evaluation of Rocket-Nozzle Ablation. AIAA Solid Propellant Rocket Conference, Jan. 29-31, 1964, Preprint No. 64-101.

12. Kendall, R. M., Rindal, R. A., and Bartlett, E. P.: Thermochemical Ablation. Presented at the AIAA Thermophysics Specialist Conference, Sept. 13-15, 1965, Monterey, California.

13. Munson, T. R. and Spindler, R. J.: Transient Thermal Behavior of Decomposing Materials. Part I - General Theory and Application to Convective Heating, AVCO RAD-TR-61-10, May 1961.

14. Lafazan, S. and Siegel, B.: Ablative Thrust Chambers for Space Application. Presented at the 46th National Meeting of the AIChe, Los Angeles, Calif., Feb. 5, 1962.

15. Scala, S. M. and Gilbert, L. M.: Thermal Degradation of Char-Forming Plastic During Hypersonic Flight. ARS Jour., vol. 32, p. 917, 1962.

16. McFarland, B., Joerg, P., and Taft, M.: Criteria for Plastic Ablation Materials as Functions of Environmental Parameters. Aerojet-General Corp., ASD-TR-61-439, May 1962.

17. Wells, P. B.: A Method for Predicting the Thermal Response of Charring-Ablation Materials. The Boeing Company, Document No. D2-23256, June 1964.

18. Goldstein, H. E.: Pyrolysis Kinetics of Nylon, Phenolic, and Composites. Lockheed Missiles and Space Company, TIAD 695, Feb. 11, 1964.

19. Carslaw, H. S. and Jaeger, J. C.: Conduction of Heat in Solids. Second Edition, Oxford at the Clarendon Press, 1959.

20. Van Driest, E. R.: Turbulent Boundary Layer in Compressible Fluids. Jour. Aero. Sci., vol. 18, Mar. 1951, pp. 145-161.

21. Hirschfelder, J. O., Curtiss, C. F., and Bird, R. B.: Molecular Theory of Gases and Liquids. John Wiley, 1954.

22. Kendall, R. M. and Bartlett, E. P.: An Accurate Approximation of the Stefan-Maxwell Relations for Unequal Binary Diffusion Coefficients. Vidya Tech. Note 8036-TN-1, Contract No. NAS9-4599, July 13, 1965.

23. Svehla, R. A.: Estimated Viscosities and Thermal Conductivities of Gases at High Temperatures. NASA TR R-132, 1962.

24. Svehla, R. A.: Thermodynamics and Transport Properties for the Hydrogen-Oxygen System. NASA SP-1011, 1964.

25. Chilton, T. H., and Colburn, A. P.: Correlations for Turbulent Flow Between Heat, Mass, and Momentum Transfer, Ind. Eng. Chem., 26, p. 1183, 1934.

26. Rosner, D. E.: Similitude Treatment of Hypersonic Stagnation Heat Transfer. ARS Jour., vol. 29, no. 3, Mar. 1959.

27. Fay, J. A. and Riddell, F. R.: Theory of Stagnation-Point Heat Transfer in Dissociated Air. Jour. Aero. Sci., vol. 25, Feb. 1958, p. 73.

28. Browne, H. N., Williams, M. M., and Cruise, D. R.: The Theoretical Computation of Equilibrium Compositions, Thermodynamic Properties, and Performance Characteristics of Propellant Systems. U. S. Naval Ordnance Test Station, NAVWEPS Rpt. 7043, June 1960.

29. JANAF Interim Thermochemical Tables. The Dow Chemical Company, Midland, Michigan, Sept. 1963 ed.

30. Duff, R. E., and Bauer, S. H.: Equilibrium Composition of the C/H System at Elevated Temperatures. J. Chem. Phys., vol. 36, p. 1754, April 1962.

31. Oliver, R. C., and Baier, R.: Chemical Corrosion of Rocket Liner Materials and Propellant Performance Studies. Third Quarterly Technical Summary Report. Aeronutronic Division of Ford Motor Co., Publication Number U-2045, Mar. 15, 1963.

32. Engelke, W. T.: The Thermophysical Properties of Ablative Plastic Materials from Room Temperature to Decomposition. Progress Rept. no. 3, Contract No. AF 33(657)-894, Mod. No. 3, Southern Research Institute, July 1964.

33. Farmer, R. W.: Thermogravimetry of Plastics, Part I - Empirical Homogeneous Kinetics. ASD-TDR-62-1043, Part I, Feb. 1963.

34. Bartz, D. R.: A Simple Equation for Rapid Estimation of Rocket-Nozzle Convective Heat-Transfer Coefficients. Jet Prop., Jan. 1957, p. 49.

35. Eckert, E. R. G.: Survey of Boundary-Layer Heat Transfer at High Velocities and High Temperatures. WADC Tech. Rept. 59-624, University of Minnesota, Apr. 1960.

36. McAdams, W. H.: Heat Transmission. McGraw-Hill Book Co., Inc., New York, 1954.

37. Baer, D. and Ambrosio, A.: Heat Conduction in a Semi-Infinite Slab with Sublimation at the Surface. Space Technology Laboratories, Inc., Pasadena, Calif. TR-59-0000-00610, Feb. 24, 1959.

38. Landau, H. G.: Heat Conduction in a Melting Solid. Quarterly of Applied Mechanics, 1951.

39. Rollbuhler, R. J.: Experimental Investigation of Rocket-Engine Ablative-Material Performance after Post-Run Cooling at Altitude Pressures. NASA TN D-1726, June 1963.

40. Rollbuhler, R. J.: Personal communication.

41. Dow, M. B.: Comparison of Measurements of Internal Temperatures in Ablation Material by Various Thermocouple Configurations. NASA TN D-2165, Nov. 1964.

42. Cobine, J. D.: Gaseous Conductors - Theory and Engineering Applications. Dover Publications, Inc., New York, N. Y., 1958.

43. Flood, D. T., and Schaefer, J. W.: Simulation of Rocket-Nozzle Environments with an Arc-Plasma Generator. Technical Note, AIAA Jour., vol. 3, no. 7, July 1965.

44. Kendall, R. M., Rindal, R. A., and Bartlett, E. P.: Thermochemical Ablation. AIAA Paper No. 65-642. Presented at AIAA Thermophysics Specialist Conference, Monterey, Calif., Sept. 13-15, 1965

TABLE I.- COMPARISON OF BINARY DIFFUSION COEFFICIENTS FOR VARIOUS SELECTED SPECIES AS COMPUTED BY THE PRESENT CORRELATION TECHNIQUE AND FROM KINETIC THEORY.

(a) Species typical of those encountered in the boundary layer over graphite ablating in air. Temperature = 12,000° R, Pressure = 1 atm (kinetic data from method of Svehla).

SPECIES I	SPECIES J	DIJ FROM KINETIC THEORY (FT*FT*100/SEC)	FI	DIJ FROM PRESENT CORRELATION (FT*FT*100/SEC)	ERROR USING PRESENT CORRELATION (PERCENT)	ERROR IF ALL DIJ ARE ASSUMED EQUAL (PERCENT)
O	O2	5.6458	0.7907	5.5575	- 1.6	- 16.8
O	N	7.3372		7.5274	2.6	- 36.0
O	N2	5.3995		5.3837	- 0.3	- 13.0
O	CO	5.4662		5.4379	- 0.5	- 14.1
O	CO2	4.4638		4.3762	- 2.0	5.2
O	C	8.0754		8.3663	3.6	- 41.9
O	C3	5.1820		5.0859	- 1.9	- 9.4
O	CN	5.3620		5.3697	0.1	- 12.4
O2	N	5.6566	1.0687	5.5695	- 1.5	- 16.9
O2	N2	3.9611		3.9834	0.6	18.6
O2	CO	4.0028		4.0235	0.5	17.3
O2	CO2	3.1637		3.2380	2.3	48.4
O2	C	6.3129		6.1902	- 1.9	- 25.6
O2	C3	3.7100		3.7630	1.4	26.6
O2	CN	3.9623		3.9731	0.3	18.4
N	N2	5.4277	0.7890	5.3953	- 0.6	- 13.5
N	CO	5.4763		5.4496	- 0.5	- 14.2
N	CO2	4.5136		4.3857	- 2.8	4.0
N	C	7.9727		8.3844	5.2	- 41.0
N	C3	5.2069		5.0969	- 2.1	- 9.8
N	CN	5.3784		5.3813	0.1	- 12.7
N2	CO	3.8943	1.1032	3.8977	0.1	20.6
N2	CO2	3.1114		3.1367	0.8	51.0
N2	C	6.0528		5.9967	- 0.9	- 22.4
N2	C3	3.6214		3.6454	0.7	29.7
N2	CN	3.8603		3.8488	- 0.3	21.7
CO	CO2	3.1390	1.0922	3.1683	0.9	49.7
CO	C	6.1184		6.0570	- 1.0	- 23.2
CO	C3	3.6584		3.6820	0.6	28.4
CO	CN	3.8938		3.8875	- 0.2	20.6
CO2	C	4.9902	1.3572	4.8745	- 2.3	- 5.9
CO2	C3	2.8753		2.9632	3.1	63.4
CO2	CN	3.1245		3.1286	0.1	50.3
C	C3	5.7767	0.7099	5.6649	- 1.9	- 18.7
C	CN	6.0033		5.9811	- 0.4	- 21.8
C3	CN	3.6276	1.1678	3.6359	0.2	29.5
CN			1.1061			
AVERAGE ABSOLUTE ERROR					1.3	24.2

NOTE. DIJ FROM CORRELATION EQUATION = D BAR/(FI)(FJ) WHERE D BAR AND FI ARE COMPUTED BY LEAST SQUARE CURVE FIT. D BAR=0.046966 FT*FT/SEC

TABLE I.- CONCLUDED.

(b) Diffusion coefficients calculated using values for collision cross-sections suggested by Svehla (1964) which are based on the most appropriate intermolecular potential functions. Hydrogen-oxygen system, Temperature = 12,000° R, Pressure = 1 atm.

SPECIES I	SPECIES J	DIJ FROM KINETIC THEORY (FT*FT*100/SEC)	FI	DIJ FROM PRESENT CORRELATION (FT*FT*100/SEC)	ERROR USING PRESENT CORRELATION (PERCENT)	ERROR IF ALL DIJ ARE ASSUMED EQUAL (PERCENT)
H	H2	67.6000	0.3888	74.4024	10.1	- 77.1
H	H2O	28.3200		27.0030	- 4.7	- 45.4
H	O	27.7200		30.8482	11.3	- 44.3
H	O2	24.5500		22.5734	- 8.1	- 37.1
H	OH	29.5900		27.5549	- 6.9	- 47.8
H2	H2O	19.5800	0.5342	19.6568	0.4	- 21.1
H2	O	23.6000		22.4560	- 4.8	- 34.5
H2	O2	17.1900		16.4323	- 4.4	- 10.1
H2	OH	20.1600		20.0586	- 0.5	- 23.3
H2O	O	8.2950	1.4718	8.1500	- 1.7	86.3
H2O	O2	5.7150		5.9638	4.4	170.4
H2O	OH	7.1450		7.2799	1.9	116.3
O	O2	6.8500	1.2883	6.8131	- 0.5	125.6
O	OH	8.6060		8.3166	- 3.4	79.6
O2	OH	5.5520	1.7606	6.0857	9.6	178.3
OH			1.4423			
AVERAGE ABSOLUTE ERROR					4.8	73.1

NOTE. DIJ FROM CORRELATION EQUATION = D BAR/(FI)(FJ) WHERE D BAR AND FI ARE COMPUTED BY LEAST SQUARE CURVE FIT. D BAR=0.154532 FT*FT/SEC

TABLE II.- VARIATION OF DIFFUSION FACTORS WITH TEMPERATURE

Temperature, $^{\circ}R$	4000	8000	12,000	16,000
Pressure, atm	1	1	1	1
$\bar{D} \times 10^2$, ft^2/sec	0.7597	2.3939	4.6966	7.5836
Percent error in F_i for:				
$F_O = 0.7904$	-0.06	-0.05	0.04	0.05
$F_{O_2} = 1.0682$	- .07	- .05	.05	.06
$F_N = 0.7881$	.04	.03	.11	- .19
$F_{N_2} = 1.1019$	.04	.03	.12	- .19
$F_{CO} = 1.0914$	- .04	0	.07	- .03
$F_{CO_2} = 1.3555$	- .19	- .18	.12	.25
$F_C = 0.7149$	.42	.35	- .70	- .06
$F_{C_3} = 1.1673$	- .15	- .16	.04	.27
$F_{CN} = 1.1048$	.03	.04	.12	- .17

TABLE III

SAMPLE OUTPUT FROM THERMOCHEMICAL DATA CURVE-FIT PROGRAM

(a) ZrO_2 liquid and solid.

```
CURVE FIT COMPARISON FOR O2ZR*        DATA FROM  JANAF 06/61
   TEMPERATURE        -(F-H/T)IN          -(F-H/T)OUT          CP
   1.000000E+03     2.001500E+01        2.004023E+01     2.432675E+01     O2ZR*
   1.100000E+03     2.116000E+01        2.113492E+01     2.305290E+01     O2ZR*
   1.200000E+03     2.225300E+01        2.222235E+01     2.206542E+01     O2ZR*
   1.300000E+03     2.329700E+01        2.328428E+01     2.127967E+01     O2ZR*
   1.400000E+03     2.429500E+01        2.431166E+01     2.064015E+01     O2ZR*
   1.500000E+03     2.526400E+01        2.530050E+01     2.010918E+01     O2ZR*
   1.600000E+03     2.623500E+01        2.624964E+01     1.966050E+01     O2ZR*
   1.700000E+03     2.715700E+01        2.715948E+01     1.927533E+01     O2ZR*
   1.800000E+03     2.803500E+01        2.803128E+01     1.893996E+01     O2ZR*
   1.900000E+03     2.887300E+01        2.886673E+01     1.864418E+01     O2ZR*
   2.000000E+03     2.967400E+01        2.966774E+01     1.838027E+01     O2ZR*
   2.100000E+03     3.044100E+01        3.043626E+01     1.814232E+01     O2ZR*
   2.200000E+03     3.117600E+01        3.117420E+01     1.792571E+01     O2ZR*
   2.300000E+03     3.188300E+01        3.188342E+01     1.772681E+01     O2ZR*
   2.400000E+03     3.256400E+01        3.256566E+01     1.754274E+01     O2ZR*
   2.500000E+03     3.321900E+01        3.322258E+01     1.737116E+01     O2ZR*
   2.600000E+03     3.385200E+01        3.385570E+01     1.721020E+01     O2ZR*
   2.700000E+03     3.446300E+01        3.446644E+01     1.705831E+01     O2ZR*
   2.800000E+03     3.505300E+01        3.505613E+01     1.691422E+01     O2ZR*
   2.900000E+03     3.562600E+01        3.562600E+01     1.677687E+01     O2ZR*
   3.000000E+03     3.618000E+01        3.617715E+01     1.664538E+01     O2ZR*
    CONSTRAINTS
   TEMPERATURE    TYPE        INPUT          CALCULATED
   2.9000000E+03   F      3.5626000E+01     3.5626000E+01                 O2ZR*
   2.9000000E+03   H      4.7353000E+04     4.7353001E+04                 O2ZR*
 INTERMEDIATE OUTPUT
  -.261500E+06 .487946E+05 .182127E+02-.777714E-03 .689168E+07 .524420E+0202Z
 500. 2950.2 100.                                                       O2ZR*
   TEMPERATURE        -(F-H/T)IN          -(F-H/T)OUT          CP
   2.900000E+03     4.098500E+01        4.098551E+01     2.000652E+01     O2ZR*
   3.000000E+03     4.159500E+01        4.159500E+01     2.000174E+01     O2ZR*
   3.100000E+03     4.218700E+01        4.218667E+01     1.999821E+01     O2ZR*
   3.200000E+03     4.276200E+01        4.276153E+01     1.999577E+01     O2ZR*
   3.300000E+03     4.332000E+01        4.332049E+01     1.999429E+01     O2ZR*
   3.400000E+03     4.386400E+01        4.386440E+01     1.999367E+01     O2ZR*
   3.500000E+03     4.439400E+01        4.439402E+01     1.999379E+01     O2ZR*
   3.600000E+03     4.491000E+01        4.491010E+01     1.999460E+01     O2ZR*
   3.700000E+03     4.541300E+01        4.541329E+01     1.999600E+01     O2ZR*
   3.800000E+03     4.590400E+01        4.590422E+01     1.999794E+01     O2ZR*
   3.900000E+03     4.638400E+01        4.638347E+01     2.000036E+01     O2ZR*
   4.000000E+03     4.685200E+01        4.685158E+01     2.000322E+01     O2ZR*
   4.100000E+03     4.730900E+01        4.730905E+01     2.000648E+01     O2ZR*
   4.200000E+03     4.775600E+01        4.775636E+01     2.001009E+01     O2ZR*
   4.300000E+03     4.819400E+01        4.819394E+01     2.001402E+01     O2ZR*
   4.400000E+03     4.862200E+01        4.862222E+01     2.001825E+01     O2ZR*
   4.500000E+03     4.904200E+01        4.904157E+01     2.002275E+01     O2ZR*
   4.600000E+03     4.945200E+01        4.945236E+01     2.002749E+01     O2ZR*
   4.700000E+03     4.985500E+01        4.985493E+01     2.003247E+01     O2ZR*
   4.800000E+03     5.025000E+01        5.024961E+01     2.003764E+01     O2ZR*
   4.900000E+03     5.063700E+01        5.063670E+01     2.004301E+01     O2ZR*
   5.000000E+03     5.101600E+01        5.101649E+01     2.004855E+01     O2ZR*
    CONSTRAINTS
   TEMPERATURE    TYPE        INPUT          CALCULATED
   3.0000000E+03   F      4.1595000E+01     4.1595000E+01                 O2ZR*
   3.0000000E+03   H      5.4037000E+04     5.4037000E+04                 O2ZR*
 INTERMEDIATE OUTPUT
  -.245518E+06 .540370E+05 .195658E+02 .831149E-04 .167937E+07 .596073E+0202Z
 2950. 5000.3 100.                                                      O2ZR*
```

TABLE III.- CONCLUDED.

(b) ZrO_2 gas.

```
CURVE FIT COMPARISON FOR O2ZR        DATA FROM  JANAF 06/61
   TEMPERATURE      -(F-H/T)IN      -(F-H/T)OUT          CP
   1.000000E+03     6.487300E+01    6.487294E+01    1.428676E+01    O2ZR
   1.100000E+03     6.578900E+01    6.578918E+01    1.439251E+01    O2ZR
   1.200000E+03     6.666200E+01    6.666187E+01    1.447302E+01    O2ZR
   1.300000E+03     6.749300E+01    6.749317E+01    1.453574E+01    O2ZR
   1.400000E+03     6.828600E+01    6.828565E+01    1.458557E+01    O2ZR
   1.500000E+03     6.904200E+01    6.904198E+01    1.462583E+01    O2ZR
   1.600000E+03     6.976500E+01    6.976474E+01    1.465884E+01    O2ZR
   1.700000E+03     7.045600E+01    7.045640E+01    1.468625E+01    O2ZR
   1.800000E+03     7.111900E+01    7.111923E+01    1.470927E+01    O2ZR
   1.900000E+03     7.175500E+01    7.175532E+01    1.472880E+01    O2ZR
   2.000000E+03     7.236700E+01    7.236657E+01    1.474552E+01    O2ZR
   2.100000E+03     7.295500E+01    7.295473E+01    1.475995E+01    O2ZR
   2.200000E+03     7.352100E+01    7.352139E+01    1.477250E+01    O2ZR
   2.300000E+03     7.406800E+01    7.406797E+01    1.478348E+01    O2ZR
   2.400000E+03     7.459600E+01    7.459579E+01    1.479316E+01    O2ZR
   2.500000E+03     7.510600E+01    7.510605E+01    1.480174E+01    O2ZR
   2.600000E+03     7.560000E+01    7.559984E+01    1.480939E+01    O2ZR
   2.700000E+03     7.607800E+01    7.607815E+01    1.481623E+01    O2ZR
   2.800000E+03     7.654200E+01    7.654190E+01    1.482239E+01    O2ZR
   2.900000E+03     7.699200E+01    7.699193E+01    1.482795E+01    O2ZR
   3.000000E+03     7.742900E+01    7.742900E+01    1.483299E+01    O2ZR
    CONSTRAINTS
   TEMPERATURE    TYPE         INPUT          CALCULATED
   3.0000000E+03  CP       1.4833000E+01     1.4832999E+01          O2ZR
 INTERMEDIATE OUTPUT
   -.825000E+05 .387750E+05 .148912E+02 .309724E-05-.607547E+06 .903540E+0202Z
 500. 3000.1    0.                                                  O2ZR
   TEMPERATURE      -(F-H/T)IN      -(F-H/T)OUT          CP
   3.000000E+03     7.742900E+01    7.742900E+01    1.483300E+01    O2ZR
   3.100000E+03     7.785400E+01    7.785382E+01    1.483795E+01    O2ZR
   3.200000E+03     7.826700E+01    7.826705E+01    1.484227E+01    O2ZR
   3.300000E+03     7.866900E+01    7.866930E+01    1.484604E+01    O2ZR
   3.400000E+03     7.906100E+01    7.906112E+01    1.484930E+01    O2ZR
   3.500000E+03     7.944300E+01    7.944302E+01    1.485213E+01    O2ZR
   3.600000E+03     7.981500E+01    7.981550E+01    1.485457E+01    O2ZR
   3.700000E+03     8.017900E+01    8.017900E+01    1.485666E+01    O2ZR
   3.800000E+03     8.053400E+01    8.053394E+01    1.485844E+01    O2ZR
   3.900000E+03     8.088100E+01    8.088070E+01    1.485994E+01    O2ZR
   4.000000E+03     8.122000E+01    8.121965E+01    1.486118E+01    O2ZR
   4.100000E+03     8.155100E+01    8.155113E+01    1.486220E+01    O2ZR
   4.200000E+03     8.187500E+01    8.187545E+01    1.486301E+01    O2ZR
   4.300000E+03     8.219300E+01    8.219293E+01    1.486363E+01    O2ZR
   4.400000E+03     8.250400E+01    8.250382E+01    1.486407E+01    O2ZR
   4.500000E+03     8.280800E+01    8.280841E+01    1.486437E+01    O2ZR
   4.600000E+03     8.310700E+01    8.310694E+01    1.486451E+01    O2ZR
   4.700000E+03     8.340000E+01    8.339963E+01    1.486453E+01    O2ZR
   4.800000E+03     8.368700E+01    8.368673E+01    1.486443E+01    O2ZR
   4.900000E+03     8.396800E+01    8.396842E+01    1.486422E+01    O2ZR
   5.000000E+03     8.424500E+01    8.424491E+01    1.486391E+01    O2ZR
    CONSTRAINTS
   TEMPERATURE    TYPE         INPUT          CALCULATED
   3.0000000E+03  CP       1.4833000E+01     1.4833000E+01          O2ZR
 INTERMEDIATE OUTPUT
   -.825000E+05 .387750E+05 .149990E+02-.192239E-04-.975347E+06 .903540E+0202Z
3000. 5000.1    0.                                                  O2ZR
```

TABLE IV

THERMOCHEMICAL DATA EMPLOYED FOR ABLATION CALCULATIONS

$h_{j_{298}}$	$\int_{298}^{3000} C_p\,dT$	α_o	α_1	α_2	S_{3000}	T_L	T_U	Species
1006 01 13					JANAF 12/60			ALC
209958+6	240440+5	896909+1	-757687-5	-752532+5	746650+2	500.	3000.1	ALC
209958+6	240440+5	961609+1	-128042-3	-264567+7	746650+2	3000.	5000.1	ALC
1013 01 17					JANAF 06/61			ALCL
-116200+5	244690+5	895305+1	115091-3	-929251+5	750380+2	500.	3000.1	ALCL
-116200+5	244690+5	951089+1	835189-5	-223156+7	750380+2	3000.	5000.1	ALCL
1008 01 13 01 17					JANAF 12/60			ALCLO
-550000+5	391990+5	148879+2	423287-5	-392535+6	920440+2	500.	3000.1	ALCLO
-550000+5	391990+5	158613+2	-186492-3	-400349+7	920440+2	3000.	5000.1	ALCLO
1013 02 17					JANAF 06/61			ALCL2
-780000+5	371170+5	138896+2	586012-5	-137329+6	100813+3	500.	3000.1	ALCL2
-780000+5	371170+5	136493+2	486738-4	86968+6	100813+3	3000.	5000.1	ALCL2
1013 03 17					JANAF 06/61			ALCL3
-140423+6	528160+5	199485+2	-209903-4	-446442+6	11958+3	500.	3000.1	ALCL3
-140423+6	528160+5	204484+2	-109302-3	-256062+7	11958+3	3000.	5000.1	ALCL3
01 08 01 09 01 13					JANAF 03/64		111	ALFO
-140200+6	386900+5	148800+2	650586-5	-589929+6	876980+2	1000.	3000.1	ALFO
-140200+6	386900+5	148945+2	160258-5	-588334+6	876980+2	3000.	5000.1	ALFO
1001 01 13					JANAF 06/63			ALH
620000+5	233870+5	885387+1	181289-3	-708658+6	638290+2	500.	3000.1	ALH
620000+5	233870+5	951195+1	483217-4	-304128+7	638290+2	3000.	5000.1	ALH
1001 01 08 01 13					JANAF 12/60			ALHO
-344700+4	367340+5	148073+2	231376-4	-155462+7	803550+2	500.	3000.1	ALHO
-344700+4	367340+5	143991+2	973440-4	115747+6	803550+2	3000.	5000.1	ALHO
1001 02 08 01 13					JANAF 12/60			ALHO2
-109000+6	480500+5	191451+2	162758-3	-253257+7	989760+2	500.	3000.1	ALHO2
-109000+6	480500+5	208743+2	-198656-3	-833764+7	989760+2	3000.	5000.1	ALHO2
1007 01 13					JANAF 12/60			ALN
104500+6	240670+5	892460+1	115329-3	-212370+6	742970+2	500.	3000.1	ALN
104500+6	240670+5	861677+1	172650-3	101045+7	742970+2	3000.	5000.1	ALN
1008 01 13					JANAF 03/62			ALO
213980+5	238050+5	895587+1	772498-4	-329625+6	718590+2	500.	3000.1	ALO
213980+5	238050+5	916408+1	387904-4	-116511+7	718590+2	3000.	5000.1	ALO
02 13 06 17					JANAF 03/64		111	AL2CL6
-309200+6	116290+6	437070+2	353763-5	-644812+6	211446+3	1000.	3000.1	AL2CL6
-309200+6	116290+6	437101+2	159950-5	-620287+6	211446+3	3000.	5000.1	AL2CL6
1008 02 13					JANAF 09/61			AL2O
-314400+5	359700+5	138891+2	485413-5	-663265+6	912000+2	500.	3000.1	AL2O
-314400+5	359700+5	144656+2	-108570-3	-278920+7	912000+2	3000.	5000.1	AL2O
1004 02 06					JANAF 09/62			BEC2
135000+6	367740+5	146621+2	590732-4	-161440+7	816180+2	500.	3000.1	BEC2
135000+6	367740+5	136768+2	233788-3	253563+7	816180+2	3000.	5000.1	BEC2
01 04 01 17					JANAF 03/64		111	BECL
300000+4	239830+5	893411+1	908676-4	-222435+6	719090+2	1000.	3000.1	BECL
300000+4	239830+5	894691+1	882523-4	-267069+6	719090+2	3000.	5000.1	BECL
1004 01 09					JANAF 03/63			BEF
-496780+5	234680+5	888699+1	919571-4	-421766+6	684020+2	500.	3000.1	BEF
-496780+5	234680+5	842934+1	174020-3	148137+7	684020+2	3000.	5000.1	BEF
01 04 02 09					JANAF 12/63			BEF2
-191300+6	374160+5	147905+2	289774-4	-115672+7	822830+2	500.	3000.1	BEF2
-191300+6	374160+5	138154+2	209528-3	274481+7	822830+2	3000.	5000.1	BEF2
1001 01 04					JANAF 3/63			BEH
767680+5	229360+5	877224+1	184173-3	-924908+6	607720+2	500.	3000.1	BEH
767680+5	229360+5	884739+1	160554-3	-963556+6	607720+2	3000.	5000.1	BEH
1001 01 04 01 08					JANAF 09/63			BEHO
-250000+5	321730+5	129854+2	208547-3	-239494+7	785130+2	500.	3000.1	BEHO
-250000+5	321730+5	139033+2	-916197-5	-477784+7	785130+2	3000.	5000.1	BEHO
2001 01 04					JANAF 12/60			BEH2
300000+5	345780+5	145807+2	757364-4	-277162+7	676530+2	500.	3000.1	BEH2

TABLE IV.- CONTINUED.

$h_{j_{298}}$	$\int_{298}^{3000} C_p\,dT$	α_o	α_1	α_2	S_{3000}	T_L	T_U	Species
300000+5	345780+5	153556+2	-872682-4	-534470+7	676530+2	3000.	5000.1	BEH2
2001 01	04 02 08			JANAF 09/63				BEH2O2
-158500+6	593950+5	244524+2	313890-3	-473550+7	103667+3	500.	3000.1	BEH2O2
-158500+6	593950+5	252829+2	957844-4	-632116+7	103667+3	3000.	5000.1	BEH2O2
2004 02	08			JANAF 09/63				BE2O2
-980000+5	498360+5	197854+2	208746-4	-163011+7	988560+2	500.	3000.1	BE2O2
-980000+5	498360+5	192883+2	113721-3	33709 6+6	988560+2	3000.	5000.1	BE2O2
3004 03	08			JANAF 09/63				BE3O3
-252000+6	768800+5	316149+2	406679-4	-413048+7	124702+3	500.	3000.1	BE3O3
-252000+6	768800+5	320268+2	-453443-4	-551555+7	124702+3	3000.	5000.1	BE3O3
4004 04	08			JANAF 09/63				BE4O4
-380000+6	107856+6	436112+2	233046-4	-439314+7	156562+3	500.	3000.1	BE4O4
-380000+6	107856+6	439409+2	-408308-4	-562941+7	156562+3	3000.	5000.1	BE4O4
5004 05	08			JANAF 09/63				BE5O5
-505000+6	137169+6	553874+2	617881-4	-542571+7	184299+3	500.	3000.1	BE5O5
-505000+6	137169+6	555197+2	226391-4	-555927+7	184299+3	3000.	5000.1	BE5O5
6004 06	08			JANAF 09/63				BE6O6
-636000+6	166373+6	672405+2	798827-4	-658038+7	211572+3	500.	3000.1	BE6O6
-636000+6	166373+6	665239+2	197656-3	-331145+7	211572+3	3000.	5000.1	BE6O6
01 05 02	09 01 17			JANAF 12/63				BCLF2
-211600+6	503830+5	198311+2	886329-5	-147403+7	106267+3	500.	3000.1	BCLF2
-211600+6	503830+5	195580+2	581861-4	-34753 4+6	106267+3	3000.	5000.1	BCLF2
01 05 01	09 02 17			JANAF 12/63				BCL2F
-154000+6	511180+5	198460+2	578157-5	-110178+7	110423+3	500.	3000.1	BCL2F
-154000+6	511180+5	198057+2	126436-4	-924350+6	110423+3	3000.	5000.1	BCL2F
1005 01	09			JANAF 12/60				BF
-454690+5	232890+5	887795+1	901824-4	-52610 9+6	669360+2	500.	3000.1	BF
-454690+5	232890+5	816859+1	210898-3	279334+7	669360+2	3000.	5000.1	BF
1005 02	09			JANAF 12/62				BF2
-130000+6	352490+5	137981+2	306556-4	-979515+6	874860+2	500.	3000.1	BF2
-130000+6	352490+5	148647+2	-178860-3	-507255+7	874860+2	3000.	5000.1	BF2
01 05 01	08 01 09			JANAF 12/63				BFO
-144000+6	374660+5	148017+2	227294-4	-134052+7	843900+2	500.	3000.1	BFO
-144000+6	374660+5	157870+2	-169659-3	-501345+7	843900+2	3000.	5000.1	BFO
01 05 03	09			JANAF 12/63				BF3
-270100+6	496940+5	197643+2	260131-4	-174925+7	100317+3	500.	3000.1	BF3
-270100+6	496940+5	190100+2	163117-3	133775+7	100317+3	3000.	5000.1	BF3
1001 01	05			JANAF 03/63				BH
105630+6	226370+5	871723+1	193099-3	-113880+7	593240+2	500.	3000.1	BH
105630+6	226370+5	962344+1	127652-4	-442568+7	593240+2	3000.	5000.1	BH
1001 01	05 02 08			JANAF 06/63				BHO2
-134100+6	456640+5	182280+2	425108-3	-301044+7	924900+2	500.	3000.1	BHO2
-134100+6	456640+5	168746+2	521159-3	699798+7	924900+2	3000.	5000.1	BHO2
2001 01	05			JANAF 12/60				BH2
660000+5	327480+5	131819+2	199298-3	-211346+7	728220+2	500.	3000.1	BH2
660000+5	327480+5	133411+2	907704-4	-580069+6	728220+2	3000.	5000.1	BH2
2001 01	05 02 08			JANAF 12/60				BH2O2
-450000+5	597060+5	246307+2	263481-3	-476319+7	109074+3	500.	3000.1	BH2O2
-450000+5	597060+5	246015+2	206036-3	-244306+7	109074+3	3000.	5000.1	BH2O2
3001 01	05			JANAF 12/60				BH3
180000+5	424590+5	179007+2	501613-3	-495709+7	763790+2	500.	3000.1	BH3
180000+5	424590+5	186890+2	214061-3	-464131+7	763790+2	3000.	5000.1	BH3
3001 01	05 03 08			JANAF 03/61				BH3O3
-238600+6	860730+5	356846+2	478490-3	-720419+7	131808+3	500.	3000.1	BH3O3
-238600+6	860730+5	377529+2	-105305-4	-127237+8	131808+3	3000.	5000.1	BH3O3
1005 01	07			JANAF 09/63				BN
152000+6	244620+5	880110+1	108795-3	-112446+6	699360+2	500.	3000.1	BN
152000+6	244620+5	880750+1	998189-4	723668+5	699360+2	3000.	5000.1	BN
1005 02	08			JANAF 06/63				BO2

TABLE IV.- CONTINUED.

$h_{j_{298}}$	$\int_{298}^{3000} C_p\,dT$	α_o	α_1	α_2	S_{3000}	T_L	T_U	Species
-726000+5	379300+5	148552+2	119400-4	-999435+6	856360+2	500.	3000.1	BO2
-726000+5	379300+5	118268+2	637770-3	935859+7	856360+2	3000.	5000.1	BO2
2005				JANAF 12/60				B2
199300+6	238090+5	891017+1	112093-3	-321955+6	678510+2	500.	3000.1	B2
199300+6	238090+5	724425+1	412560-3	687918+7	678510+2	3000.	5000.1	B2
1004 02 05 04 08				JANAF 12/62				B2BE04
-319600+6	902510+5	373115+2	103876-3	-543732+7	142956+3	500.	3000.1	B2BE04
-319600+6	902510+5	364687+2	244001-3	-163534+7	142956+3	3000.	5000.1	B2BE04
2005 02 08				JANAF 03/61				B2O2
-111600+6	515500+5	207885+2	370455-5	-251331+7	983970+2	500.	3000.1	B2O2
-111600+6	515500+5	196641+2	203148-3	284908+7	983970+2	3000.	5000.1	B2O2
2005 03 08				JANAF 03/61				B2O3
-210100+6	615070+5	257777+2	-153675-4	-427514+7	111710+3	500.	3000.1	B2O3
-210100+6	615070+5	239286+2	345774-3	329402+7	111710+3	3000.	5000.1	B2O3
1006				JANAF 03/61				C
170886+6	135500+5	444433+1	228125-3	409830+6	492870+2	500.	3000.1	C
170886+6	135500+5	412212+1	261908-3	262886+7	492870+2	3000.	5000.1	C
1005 01 06				JANAF 06/63				CB
198000+6	233870+5	887101+1	987600-4	-461666+6	689650+2	500.	3000.1	CB
198000+6	233870+5	864500+1	134780-3	599853+6	689650+2	3000.	5000.1	CB
1006 01 17				JANAF 12/60				CCL
132000+6	237850+5	890513+1	416720-4	-154333+6	736510+2	500.	3000.1	CCL
132000+6	237850+5	857088+1	993826-4	129567+7	736510+2	3000.	5000.1	CCL
01 06 03 09 01 17				JANAF 03/64			111	CCLF3
-166000+6	654320+5	257053+2	334186-4	-172444+7	120680+3	1000.	3000.1	CCLF3
-166000+6	654320+5	258243+2	146187-5	-193275+7	120680+3	3000.	5000.1	CCLF3
1006 01 07 01 17				JANAF 12/60				CCLN
322000+5	375090+5	415997+3	-109631-0	-651419+9	868930+2	500.	3000.1	CCLN
322000+5	375090+5	134744+2	286947-3	348958+7	868930+2	3000.	5000.1	CCLN
01 06 02 09 02 17				JANAF 03/64			111	CCL2F2
-115000+6	662240+5	257477+2	222257-4	-139026+7	125629+3	1000.	3000.1	CCL2F2
-115000+6	662240+5	258288+2	844195-6	-154245+7	125629+3	3000.	5000.1	CCL2F2
1006 01 08 02 17				JANAF 12/60				CCL2O
-526000+5	505950+5	197348+2	333599-4	-133141+7	108899+3	500.	3000.1	CCL2O
-526000+5	505950+5	189745+2	170558-3	180683+7	108899+3	3000.	5000.1	CCL2O
01 06 01 09 03 17				JANAF 03/64			111	CCL3F
-680000+5	669930+5	257811+2	137845-4	-106628+7	128911+3	1000.	3000.1	CCL3F
-680000+5	669930+5	258333+2	838371-7	-116610+7	128911+3	3000.	5000.1	CCL3F
1006 04 17				JANAF 12/60				CCL4
-259400+5	676540+5	258277+2	144070-5	-828977+6	129983+3	500.	3000.1	CCL4
-259400+5	676540+5	253023+2	998371-4	124339+7	129983+3	3000.	5000.1	CCL4
1006 01 09				JANAF 03/61				CF
744000+5	234630+5	889829+1	942918-4	-469503+6	701280+2	500.	3000.1	CF
744000+5	234630+5	810974+1	241697-3	264745+7	701280+2	3000.	5000.1	CF
1006 01 07 01 09				JANAF 06/61				CFN
-300000+4	370140+5	146756+2	528937-4	-15692+7	836950+2	500.	3000.1	CFN
-300000+4	370140+5	156821+2	-153382-3	-505794+7	836950+2	3000.	5000.1	CFN
01 06 02 09				JANAF 12/63				CF2
-300000+5	349740+5	138552+2	128704-4	-118696+7	876320+2	500.	3000.1	CF2
-300000+5	349740+5	142542+2	-646408-4	-268538+7	876320+2	3000.	5000.1	CF2
01 06 01 08 02 09				JANAF 12/63				CF2O
-152500+6	490560+5	196967+2	418619-4	-206358+7	100607+3	500.	3000.1	CF2O
-152500+6	490560+5	195291+2	621854-4	-110477+7	100607+3	3000.	5000.1	CF2O
01 06 03 09				JANAF 12/63				CF3
-116500+6	498600+5	197865+2	200977-4	-166384+7	102161+3	500.	3000.1	CF3
-116500+6	498600+5	196575+2	404917-4	-105310+7	102161+3	3000.	5000.1	CF3
01 06 04 09				JANAF 12/63				CF4
-222000+6	645420+5	243637+2	395728-3	723010+5	113627+3	500.	3000.1	CF4
-222000+6	645420+5	265430+2	-135803-3	-518966+7	113627+3	3000.	5000.1	CF4

TABLE IV.- CONTINUED.

$h_{j_{298}}$	$\int_{298}^{3000} C_p\,dT$	α_o	α_1	α_2	S_{3000}	T_L	T_U	Species
01001 01 06					JANAF 03/61			CH
142006+6	221300+5	826079+1	302211-3	-100184+7	616120+2	500.	3000.1	CH
142006+6	221300+5	707091+1	463281-3	552860+7	616120+2	3000.	5000.1	CH
1001 01 06 03 17					JANAF 12/60			CHCL3
-250000+5	634760+5	252779+2	125963-3	-287824+7	121245+3	500.	3000.1	CHCL3
-250000+5	634760+5	257850+2	237794-5	-410561+7	121245+3	3000.	5000.1	CHCL3
01 01 01 06 03 09					JANAF 12/63			CHF3
-165100+6	611030+5	252113+2	141526-3	-400405+7	109082+3	500.	3000.1	CHF3
-165100+6	611030+5	259284+2	-224709-4	-603019+7	109082+3	3000.	5000.1	CHF3
1001 01 06 01 07					JANAF 03/61			CHN
312000+5	355930+5	137023+2	552243-3	-228955+7	758620+2	500.	3000.1	CHN
312000+5	355930+5	178895+2	-295052-3	-183671+8	758620+2	3000.	5000.1	CHN
1001 01 06 01 07 01 08					JANAF 12/60			CHNO
-279000+5	461930+5	179701+2	469024-3	-200904+7	928990+2	500.	3000.1	CHNO
-279000+5	461930+5	210167+2	-229915-3	-105568+8	928990+2	3000.	5000.1	CHNO
1001 01 06 01 08					JANAF 03/61			CHO
-290000+4	323670+5	128033+2	300638-3	-201721+7	789830+2	500.	3000.1	CHO
-290000+4	323670+5	103028+2	633312-3	121615+8	789830+2	3000.	5000.1	CHO
2001 01 06					JANAF 12/62			CH2
950000+5	329960+5	132894+2	413822-3	-290273+7	684940+2	500.	3000.1	CH2
950000+5	329960+5	140728+2	132150-3	-239493+7	684940+2	3000.	5000.1	CH2
2001 01 06 02 17					JANAF 12/60			CH2CL2
-224000+5	595790+5	247355+2	249585-3	-481774+7	110269+3	500.	3000.1	CH2CL2
-224000+5	595790+5	258799+2	-161283-4	-794316+7	110269+3	3000.	5000.1	CH2CL2
02 01 01 06 02 09					JANAF 12/63			CH2F2
-107200+6	579240+5	246913+2	260835-3	-564164+7	102228+3	500.	3000.1	CH2F2
-107200+6	579240+5	256947+2	195707-4	-815777+7	102228+3	3000.	5000.1	CH2F2
2001 01 06 01 08					JANAF 03/61			CH2O
-277000+5	437910+5	184022+2	379921-3	-431982+7	848880+2	500.	3000.1	CH2O
-277000+5	437910+5	189628+2	161963-3	-372770+7	848880+2	3000.	5000.1	CH2O
3001 01 06					JANAF 12/62			CH3
319400+5	434190+5	182763+2	401025-3	-461203+7	786040+2	500.	3000.1	CH3
319400+5	434190+5	204899+2	-108028-3	-114692+8	786040+2	3000.	5000.1	CH3
3001 01 06 01 17					JANAF 12/60			CH3CL
-206340+5	560300+5	241353+2	388635-3	-654504+7	972200+2	500.	3000.1	CH3CL
-206340+5	560300+5	256598+2	197863-4	-103065+8	972200+2	3000.	5000.1	CH3CL
03 01 01 06 01 09					JANAF 12/63			CH3F
-560000+5	552230+5	241434+2	386480-3	-701904+7	935320+2	500.	3000.1	CH3F
-560000+5	552230+5	257207+2	985709-5	-110460+8	935320+2	3000.	5000.1	CH3F
4001 01 06					JANAF 03/61			CH4
-178950+5	530790+5	230948+2	677896-3	-755061+7	825970+2	500.	3000.1	CH4
-178950+5	530790+5	236053+2	374323-3	-368234+7	825970+2	3000.	5000.1	CH4
1006 01 07					JANAF 12/62			CN
109000+6	232490+5	655906+1	115326-2	479517+6	669760+2	500.	3000.1	CN
109000+6	232490+5	988013+1	313855-3	-649453+7	669760+2	3000.	5000.1	CN
2006					JANAF 12/60			C2
199026+6	246990+5	832826+1	533002-3	-470491+6	685520+2	500.	3000.1	C2
199026+6	246990+5	927643+1	274526-3	-202511+7	685520+2	3000.	5000.1	C2
01 04 02 06					JANAF 12/63			C2BF
135000+6	367740+5	174042+2	-702548-3	-572915+7	816180+2	500.	3000.1	C2BF
135000+6	367740+5	136768+2	233788-3	253563+7	816180+2	3000.	5000.1	C2BF
2006 02 09					JANAF 12/60			C2F2
-513000+5	526690+5	206993+2	383288-4	-175788+7	102918+3	500.	3000.1	C2F2
-513000+5	526690+5	212155+2	-681801-4	-352776+7	102918+3	3000.	5000.1	C2F2
2006 04 09					JANAF 06/63			C2F4
-151700+6	793120+5	316735+2	255243-4	-306132+7	134856+3	500.	3000.1	C2F4
-151700+6	793120+5	305382+2	247246-3	116982+7	134856+3	3000.	5000.1	C2F4
10 1 2 6					DUFF BAUER 6/61			C2H
117395+6	349620+5	134210+2	469100-3	-187509+7	781140+2	500.	3000.1	C2H

TABLE IV.- CONTINUED.

$h_{j_{298}}$	$\int_{298}^{3000} C_p\,dT$	α_o	α_1	α_2	S_{3000}	T_L	T_U	Species
117395+6	349620+5	148516+2	109402-3	-503862+7	781140+2	3000.	5000.1	C2H
2001 02 06				JANAF 03/61				C2H2
541900+5	482570+5	189960+2	769044-3	-409039+7	849690+2	500.	3000.1	C2H2
541900+5	482570+5	203952+2	389062-3	-645297+7	849690+2	3000.	5000.1	C2H2
2006 02 07				JANAF 12/60				C2N2
738700+5	511070+5	204183+2	105529-3	-252804+7	985480+2	500.	3000.1	C2N2
738700+5	511070+5	197380+2	212891-3	695469+6	985480+2	3000.	5000.1	C2N2
30 1 2 6				DUFF BAUER 6/61				C2H3
659250+5	562430+5	230065+2	691322-3	-499095+7	965150+2	500.	3000.1	C2H3
659250+5	562430+5	239033+2	331771-3	-335425+7	965150+2	3000.	5000.1	C2H3
4001 02 06				JANAF 12/60				C2H4
124960+5	676830+5	294887+2	526568-3	-865313+7	101790+3	500.	3000.1	C2H4
124960+5	676830+5	313872+2	616238-4	-131858+8	101790+3	3000.	5000.1	C2H4
4001 02 06 01 08				JANAF 12/60				C2H4O
-121900+5	813210+5	353747+2	546144-3	-964936+7	117211+3	500.	3000.1	C2H4O
-121900+5	813210+5	373112+2	690621-4	-141968+8	117211+3	3000.	5000.1	C2H4O
60 1 2 6				DUFF BAUER 6/61				C2H6
-203200+5	892710+5	484236+2	-169721-2	-193680+8	119447+3	500.	3000.1	C2H6
-203200+5	892710+5	393119+2	764877-3	-383891+7	119447+3	3000.	5000.1	C2H6
3006				JANAF 12/60				C3
189670+6	366220+5	146441+2	622536-4	-168227+7	798410+2	500.	3000.1	C3
189670+6	366220+5	144782+2	792232-4	-646877+6	798410+2	3000.	5000.1	C3
10 1 3 6				DUFF BAUER 6/61				C3H
127703+6	489620+5	194464+2	508379-3	-311933+7	928820+2	500.	3000.1	C3H
127703+6	489620+5	199582+2	245687-3	-63251+6	928820+2	3000.	5000.1	C3H
20 1 3 6				DUFF BAUER 6/61				C3H2
106522+6	635170+5	247444+2	992918-3	-437596+7	104666+3	500.	3000.1	C3H2
106522+6	635170+5	266623+2	364767-3	-467730+7	104666+3	3000.	5000.1	C3H2
30 1 3 6				DUFF BAUER 6/61				C3H3
764850+5	709520+5	286929+2	766031-3	-548098+7	113604+3	500.	3000.1	C3H3
764850+5	709520+5	291672+2	456238-3	-138601+7	113604+3	3000.	5000.1	C3H3
40 1 3 6				DUFF BAUER 6/61				C3H4A
442940+5	822470+5	372219+2	-528861-4	-10199+8	120293+3	500.	3000.1	C3H4A
442940+5	822470+5	344271+2	578173-3	-208515+7	120293+3	3000.	5000.1	C3H4A
50 1 3 6				DUFF BAUER 6/61				C3H5
324310+5	946210+5	397325+2	958555-3	-904683+7	141759+3	500.	3000.1	C3H5
324310+5	946210+5	395073+2	733720-3	-949766+6	141759+3	3000.	5000.1	C3H5
3006 02 08				JANAF 12/60				C3O2
-830000+4	652120+5	263775+2	103904-3	-350368+7	112723+3	500.	3000.1	C3O2
-830000+4	652120+5	263543+2	882201-4	-287091+7	112723+3	3000.	5000.1	C3O2
4006				JANAF 12/60				C4
242321+6	511230+5	205903+2	623436-4	-257703+7	986760+2	500.	3000.1	C4
242321+6	511230+5	210714+2	-434895-4	-404939+7	986760+2	3000.	5000.1	C4
10 1 4 6				DUFF BAUER 6/61				C4H
155196+6	645030+5	252172+2	574336-3	-339547+7	113166+3	500.	3000.1	C4H
155196+6	645030+5	249358+2	402513-3	377676+7	113166+3	3000.	5000.1	C4H
20 1 4 6				DUFF BAUER 6/61				C4H2
111715+6	763230+5	298897+2	735927-3	-430646+7	119311+3	500.	3000.1	C4H2
111715+6	763230+5	301707+2	456896-3	69812+6	119311+3	3000.	5000.1	C4H2
30 1 4 6				DUFF BAUER 6/61				C4H3
101975+6	851450+5	343217+2	855861-3	-624935+7	130072+3	500.	3000.1	C4H3
101975+6	851450+5	345194+2	564141-3	-151557+6	130072+3	3000.	5000.1	C4H3
40 1 4 6				DUFF BAUER 6/61				C4H4A
737050+5	971240+5	398132+2	961427-3	-792442+7	139440+3	500.	3000.1	C4H4A
737050+5	971240+5	395899+2	720956-3	577880+6	139440+3	3000.	5000.1	C4H4A
4006 02 07				JANAF 12/60				C4N2
127500+6	801240+5	322151+2	131902-3	-416604+7	133064+3	500.	3000.1	C4N2
127500+6	801240+5	332891+2	-100253-3	-756393+7	133064+3	3000.	5000.1	C4N2
5006				JANAF 12/60				C5

TABLE IV.- CONTINUED.

$h_{j_{298}}$	$\int_{298}^{3000} C_p\,dT$	α_o	α_1	α_2	S_{3000}	T_L	T_U	Species
242374+6	656230+5	264706+2	806528-4	-337125+7	111641+3	500.	3000.1	C5
242374+6	656230+5	271156+2	-580271-4	-543183+7	111641+3	3000.	5000.1	C5
10 1 5	6			DUFF BAUER 6/61				C5H
185980+6	776470+5	299470+2	946114-3	-430591+7	121859+3	500.	3000.1	C5H
185980+6	776470+5	291522+2	690014-3	976229+7	121859+3	3000.	5000.1	C5H
20 1 5	6			DUFF BAUER 6/61				C5H2
165230+6	933660+5	369008+2	965961-3	-583890+7	137191+3	500.	3000.1	C5H2
165230+6	933660+5	370835+2	638028-3	137088+7	137191+3	3000.	5000.1	C5H2
30 1 5	6			DUFF BAUER 6/61				C5H3
135414+6	100517+6	405377+2	799736-3	-675863+7	147599+3	500.	3000.1	C5H3
135414+6	100517+6	396951+2	706570-3	334017+7	147599+3	3000.	5000.1	C5H3
60 6 0	0			DUFF BAUER 6/61				C6
291342+6	772700+5	303965+2	607305-3	-475660+7	128958+3	500.	3000.1	C6
291342+6	772700+5	308488+2	643430-4	583350+7	128958+3	3000.	5000.1	C6
10 1 6	6			DUFF BAUER 6/61				C6H
213164+6	942310+5	374677+2	420482-3	-474514+7	148238+3	500.	3000.1	C6H
213164+6	942310+5	351470+2	661760-3	962699+7	148238+3	3000.	5000.1	C6H
20 1 6	6			DUFF BAUER 6/61				C6H2
169683+6	105052+6	412157+2	896814-3	-569006+7	153063+3	500.	3000.1	C6H2
169683+6	105052+6	409176+2	665591-3	323615+7	153063+3	3000.	5000.1	C6H2
30 1 6	6			DUFF BAUER 6/61				C6H3
158461+6	114839+6	461927+2	874250-3	-738470+7	164599+3	500.	3000.1	C6H3
158461+6	114839+6	450580+2	812263-3	450167+7	164599+3	3000.	5000.1	C6H3
60 1 6	6			DUFF BAUER 6/61				C6H6
197700+5	147317+6	626122+2	117808-2	-139277+8	172317+3	500.	3000.1	C6H6
197700+5	147317+6	595572+2	140760-2	737034+7	172317+3	3000.	5000.1	C6H6
70 6 0	0			DUFF BAUER 6/61				C7
292116+6	909770+5	359795+2	669838-3	-579638+7	140555+3	500.	3000.1	C7
292116+6	909770+5	355785+2	210202-3	102222+8	140555+3	3000.	5000.1	C7
10 1 7	6			DUFF BAUER 6/61				C7H
241752+6	108509+6	434324+2	412328-3	-55929+7	160749+3	500.	3000.1	C7H
241752+6	108509+6	402025+2	823782-3	123670+8	160749+3	3000.	5000.1	C7H
20 1 7	6			DUFF BAUER 6/61				C7H2
220830+6	119871+6	479372+2	119639-2	-828438+7	166034+3	500.	3000.1	C7H2
220830+6	119871+6	479388+2	825569-3	171374+7	166034+3	3000.	5000.1	C7H2
80 6 0	0			DUFF BAUER 6/61				C8
344891+6	104684+6	415594+2	733634-3	-683462+7	159275+3	500.	3000.1	C8
344891+6	104684+6	402894+2	359448-3	146984+8	159275+3	3000.	5000.1	C8
10 1 8	6			DUFF BAUER 6/61				C8H
288875+6	122402+6	489887+2	527442-3	-644448+7	174023+3	500.	3000.1	C8H
288875+6	122402+6	454317+2	953953-3	140527+8	174023+3	3000.	5000.1	C8H
20 1 8	6			DUFF BAUER 6/61				C8H2
226156+6	133849+6	528472+2	975801-3	-710651+7	180289+3	500.	3000.1	C8H2
226156+6	133849+6	511890+2	960881-3	821940+7	180289+3	3000.	5000.1	C8H2
90 6 0	0			DUFF BAUER 6/61				C9
340665+6	118391+6	471410+2	796582-3	-787328+7	170872+3	500.	3000.1	C9
340665+6	118391+6	450207+2	505033-3	190813+8	170872+3	3000.	5000.1	C9
10 1 9	6			DUFF BAUER 6/61				C9H
293122+6	137308+6	546536+2	609606-3	-683518+7	189983+3	500.	3000.1	C9H
293122+6	137308+6	507642+2	106604-2	158457+8	189983+3	3000.	5000.1	C9H
20 1 9	6			DUFF BAUER 6/61				C9H2
272220+6	148147+6	592585+2	135861-2	-988554+7	194630+3	500.	3000.1	C9H2
272220+6	148147+6	585236+2	106325-2	470277+7	194630+3	3000.	5000.1	C9H2
100 6 0	0			DUFF BAUER 6/61				C10
400439+6	132098+6	527202+2	860613-3	-891076+7	189592+3	500.	3000.1	C10
400439+6	132098+6	497439+2	651908-3	235109+8	189592+3	3000.	5000.1	C10
10 1 10	6			DUFF BAUER 6/61				C10H
346750+6	151795+6	605449+2	627977-3	-760351+7	208392+3	500.	3000.1	C10H
346750+6	151795+6	562113+2	115764-2	170972+8	208392+3	3000.	5000.1	C10H

TABLE IV.- CONTINUED.

$h_{j_{298}}$	$\int_{298}^{3000} C_p\,dT$	α_o	α_1	α_2	S_{3000}	T_L	T_U	Species
20 1 10 6				DUFF BAUER 6/61				C1OH2
284031+6	163084+6	643258+2	109715-2	-831845+7	214369+3	500.	3000.1	C1OH2
284031+6	163084+6	620020+2	115832-2	109441+8	214369+3	3000.	5000.1	C1OH2
1001 01 17				JANAF 03/61				CLH
-219700+5	218640+5	839693+1	214828-3	-125475+7	623640+2	500.	3000.1	CLH
-219700+5	218640+5	837177+1	193261-3	-446002+6	623640+2	3000.	5000.1	CLH
1001 01 08 01 17				JANAF 12/60				CLHO
-220000+5	329450+5	130281+2	197747-3	-200191+7	828260+2	500.	3000.1	CLHO
-220000+5	329450+5	143860+2	-989737-4	-621082+7	828260+2	3000.	5000.1	CLHO
1 12 1 17				JANAF 12/60				CLMG
100000+4	244690+5	894214+1	114589-3	-712398+5	763170+2	1000.	3000.1	CLMG
100000+4	244690+5	894376+1	114417-3	-811970+5	763170+2	3000.	5000.1	CLMG
1007 01 08 01 17				JANAF 12/60				CLNO
126200+5	371090+5	138156+2	387830-3	-101834+7	925450+2	500.	3000.1	CLNO
126200+5	371090+5	146390+2	226016-3	-405949+7	925450+2	3000.	5000.1	CLNO
1007 02 08 01 17				JANAF 12/60				CLNO2
631000+4	499320+5	197869+2	190793-4	-171145+7	105068+3	500.	3000.1	CLNO2
631000+4	499320+5	197732+2	214466-4	-165191+7	105068+3	3000.	5000.1	CLNO2
1008 01 17				JANAF 12/60				CLO
241920+5	240570+5	889291+1	123702-3	-171206+6	740940+2	500.	3000.1	CLO
241920+5	240570+5	810727+1	268314-3	299502+7	740940+2	3000.	5000.1	CLO
2008 01 17				JANAF 12/60				CLO2
250000+5	365780+5	138491+2	190480-3	-689759+6	911340+2	500.	3000.1	CLO2
250000+5	365780+5	131788+2	311873-3	206608+7	911340+2	3000.	5000.1	CLO2
01 17 01 22				JANAF 03/64			111	CLTI
111200+6	249690+5	894340+1	213417-3	-509498+5	803570+2	1000.	3000.1	CLTI
111200+6	249690+5	894312+1	213789-3	-584666+5	803570+2	3000.	5000.1	CLTI
2017				JANAF 03/61				CL2
000000-0	244290+5	852234+1	273227-3	287718+6	737600+2	500.	3000.1	CL2
000000-0	244290+5	100329+2	-141907-4	-554731+7	737600+2	3000.	5000.1	CL2
1 12 2 17				JANAF 12/60				CL2MG
-100700+6	396840+5	149008+2	100259-5	-205509+6	948640+2	1000.	3000.1	CL2MG
-100700+6	396840+5	149032+2	194830-6	-205888+6	948640+2	3000.	5000.1	CL2MG
1008 02 17				JANAF 12/60				CL2O
181000+5	363600+5	138650+2	123715-4	-433229+6	937110+2	500.	3000.1	CL2O
181000+5	363600+5	137574+2	285555-4	982909+5	937110+2	3000.	5000.1	CL2O
02 17 01 22				JANAF 03/64			111	CL2TI
-723000+5	399290+5	149045+2	-165309-6	-117562+6	101672+3	1000.	3000.1	CL2TI
-723000+5	399290+5	149094+2	-837104-6	-143133+6	101672+3	3000.	5000.1	CL2TI
03 17 01 22				JANAF 03/64			111	CL3TI
-129300+6	527610+5	198678+2	118482-5	-327898+6	120469+3	1000.	3000.1	CL3TI
-129300+6	527610+5	198703+2	381686-6	-328488+6	120469+3	3000.	5000.1	CL3TI
04 17 01 14				JANAF 03/64			111	CL4SI
-157100+6	684000+5	258251+2	217101-5	-501042+6	136244+3	1000.	3000.1	CL4SI
-157100+6	684000+5	25833 +2	14 692-6	-525380+6	136244+3	3000.	5000.1	CL4SI
04 17 01 22				JANAF 03/64			111	CL4TI
-182410+6	688660+5	258301+2	104658-5	-327011+6	142161+3	1000.	3000.1	CL4TI
-182410+6	688660+5	258330+2	192447-6	-329597+6	142161+3	3000.	5000.1	CL4TI
04 17 01 40				JANAF 12/63				CL4ZR
-207030+6	691300+5	258750+2	-109792-4	-307300+6	146706+3	500.	3000.1	CL4ZR
-207030+6	691300+5	256762+2	298633-4	379778+6	146706+3	3000.	5000.1	CL4ZR
01 01 01 09				JANAF 12/63				FH
-648000+5	210540+5	775546+1	348201-3	-122460+7	586970+2	500.	3000.1	FH
-648000+5	210540+5	888981+1	799284-4	-419038+7	586970+2	3000.	5000.1	FH
1001 01 08 01 09				JANAF 12/60				FHO
-261000+5	326680+5	127356+2	288514-3	-180501+7	799420+2	500.	3000.1	FHO
-261000+5	326680+5	154100+2	-262264-3	-118814+8	799420+2	3000.	5000.1	FHO
3001 01 09 01 14				JANAF 12/60				FH3SI
-105000+6	601620+5	252368+2	138197-3	-462130+7	102818+3	500.	3000.1	FH3SI

TABLE IV.- CONTINUED.

$h_{j_{298}}$	$\int_{298}^{3000} C_p\,dT$	α_0	α_1	α_2	S_{3000}	T_L	T_U	Species
-105000+6	601620+5	256480+2	317924-4	-544889+7	102818+3	3000.	5000.1	FH3SI
1007 01 09				JANAF 12/60				FN
586000+5	234380+5	900098+1	-168131-4	-400908+6	683510+2	500.	3000.1	FN
586000+5	234380+5	822584+1	144314-3	222486+7	683510+2	3000.	5000.1	FN
1007 01 08 01 09				JANAF 06/61				FNO
-157000+5	351800+5	137563+2	383019-4	-105557+7	878110+2	500.	3000.1	FNO
-157000+5	351800+5	129742+2	179442-3	217276+7	878110+2	3000.	5000.1	FNO
1007 02 08 01 09				JANAF 12/62				FNO2
-190000+5	494740+5	197065+2	401052-4	-183510+7	101532+3	500.	3000.1	FNO2
-190000+5	494740+5	189123+2	183090-3	145259+7	101532+3	3000.	5000.1	FNO2
1008 01 09				JANAF 12/60				FO
324000+5	234380+5	880849+1	432306-4	-157315+6	701930+2	500.	3000.1	FO
324000+5	234380+5	763129+1	227095-3	585122+7	701930+2	3000.	5000.1	FO
01 09 01 14				JANAF 12/63				FSI
-100000+4	240290+5	895860+1	799739-4	-238769+6	739700+2	500.	3000.1	FSI
-100000+4	240290+5	878956+1	112585-3	402157+6	739700+2	3000.	5000.1	FSI
1009 01 22				JANAF 06/61				FTI
-560000+5	240420+5	895043+1	762007-4	-198326+6	759700+2	500.	3000.1	FTI
-560000+5	240420+5	903459+1	608954-4	-542534+6	759700+2	3000.	5000.1	FTI
1009 01 74				JANAF 09/62				FW
978960+5	239730+5	889454+1	818076-4	-125716+6	799860+2	500.	3000.1	FW
978960+5	239730+5	-108153-0	182936-2	337146+8	799860+2	3000.	5000.1	FW
1009 01 40				JANAF 06/61				FZR
-110000+5	242180+5	895817+1	841853-4	-150585+6	785080+2	500.	3000.1	FZR
-110000+5	242180+5	100042+2	-116989-3	-413340+7	785080+2	3000.	5000.1	FZR
2009				JANAF 12/60				F2
000000-0	244320+5	874852+1	271736-3	-634340+5	685700+2	500.	3000.1	F2
000000-0	244320+5	591497+1	736861-3	137204+8	685700+2	3000.	5000.1	F2
2001 02 09 01 14				JANAF 12/60				F2H2SI
-194000+6	614140+5	253865+2	104534-3	-389856+7	109548+3	500.	3000.1	F2H2SI
-194000+6	614140+5	255753+2	457219-4	-400920+7	109548+3	3000.	5000.1	F2H2SI
1007 02 09				JANAF 12/62				F2N
890000+4	357860+5	138490+2	160322-4	-676379+6	888700+2	500.	3000.1	F2N
890000+4	357860+5	124793+2	272689-3	472085+7	888700+2	3000.	5000.1	F2N
1008 02 09				JANAF 03/61				F2O
760000+4	361580+5	138318+2	250576-4	-489744+6	888610+2	500.	3000.1	F2O
760000+4	361580+5	134205+2	770492-4	205378+7	888610+2	3000.	5000.1	F2O
2009 01 14				JANAF 09/63				F2SI
-149000+6	362180+5	138735+2	958362-5	-497462+6	902140+2	500.	3000.1	F2SI
-149000+6	362180+5	134292+2	906293-4	131251+7	902140+2	3000.	5000.1	F2SI
2009 01 22				JANAF 12/60				F2TI
-132000+6	361020+5	138654+2	119966-4	-553278+6	948640+2	500.	3000.1	F2TI
-132000+6	361020+5	133715+2	100616-3	149953+7	948640+2	3000.	5000.1	F2TI
2009 01 40				JANAF 06/30				F2ZR
-146700+6	366930+5	138525+2	160322-4	-248456+6	918940+2	500.	3000.1	F2ZR
-146700+6	366930+5	134449+2	876927-4	-148464+7	918940+2	3000.	5000.1	F2ZR
1001 03 09 01 14				JANAF 12/60				F3HSI
-283000+6	639320+5	255972+2	538924-4	-269045+7	117049+3	500.	3000.1	F3HSI
-283000+6	639320+5	259082+2	-136809-4	-366501+7	117049+3	3000.	5000.1	F3HSI
01 07 03 09				JANAF 03/64			111	F3N
-304000+5	508060+5	198144+2	151977-4	-110734+7	103342+3	1000.	3000.1	F3N
-304000+5	508060+5	198669+2	781936-6	-119096+7	103342+3	3000.	5000.1	F3N
3009 01 14				JANAF 09/63				F3SI
-267500+6	517390+5	198724+2	-614607-6	-797647+6	109545+3	500.	3000.1	F3SI
-267500+6	517390+5	196925+2	342949-4	-120736+6	109545+3	3000.	5000.1	F3SI
3009 01 22				JANAF 12/60				F3TI
-255300+6	516620+5	199053+2	-952653-5	-844253+6	110675+3	500.	3000.1	F3TI
-255300+6	516620+5	201929+2	-621437-4	-201208+7	110675+3	3000.	5000.1	F3TI
3009 01 40				JANAF 12/61				F3ZR

TABLE IV.- CONTINUED.

$h_{j_{298}}$	$\int_{298}^{3000} C_p\,dT$	α_0	α_1	α_2	S_{3000}	T_L	T_U	Species
-271100+6	524200+5	199038+2	-841175-5	-52775 6+6	115320+3	500.	3000.1	F3ZR
-271100+6	524200+5	200219+2	-306387-4	-989995+6	115320+3	3000.	5000.1	F3ZR
02 07 04 09					JANAF 03/64		111	F4N2
-200000+4	806720+5	316906+2	272636-4	-201121+7	136599+3	1000.	3000.1	F4N2
-200000+4	806720+5	317863+2	152639-5	-217755+7	136599+3	3000.	5000.1	F4N2
1008 04 09 01 74					JANAF 06/62			F4OW
-337580+6	815040+5	317472+2	118742-4	-176306+7	143702+3	500.	3000.1	F4OW
-337580+6	815040+5	313193+2	903628-4	-306807+5	143702+3	3000.	5000.1	F4OW
4009 01 14					JANAF 09/63			F4SI
-385980+6	663400+5	258339+2	-145249-5	-14633 9+7	121328+3	500.	3000.1	F4SI
-385980+6	663400+5	249018+2	181814-3	197696+7	121328+3	3000.	5000.1	F4SI
4009 01 22					JANAF 09/61			F4TI
-371400+6	675400+5	259060+2	-204668-4	-100503+7	128682+3	500.	3000.1	F4TI
-371400+6	675400+5	270399+2	-230624-3	-55355 4+7	128682+3	3000.	5000.1	F4TI
04 09 01 40					JANAF 12/63			F4ZR
-397200+6	681540+5	258533+2	-533097-5	-659853+6	135530+3	500.	3000.1	F4ZR
-397200+6	681540+5	265254+2	-130738-3	-332339+7	135530+3	3000.	5000.1	F4ZR
06 09 01 74					JANAF 12/63			F6W
-421000+6	987810+5	377756+2	-531038-5	-126632+7	163054+3	500.	3000.1	F6W
-421000+6	987810+5	264572+2	203394-2	482389+8	163054+3	3000.	5000.1	F6W
1001					JANAF 12/60			H
521020+5	134230+5	480223+1	555469-4	173095+6	388620+2	500.	3000.1	H
521020+5	134230+5	308752+1	315025-3	929744+7	388620+2	3000.	5000.1	H
1 1 1 12					JANAF 12/60			HMG
407000+5	233800+5	886108+1	126543-3	-537426+6	652080+2	1000.	3000.1	HMG
407000+5	233800+5	893706+1	106477-3	-679513+6	652080+2	3000.	5000.1	HMG
1 1 1 8 1 12					JANAF 12/60			HMGO
-122000+5	329390+5	126194+2	313624-3	-143430+7	840270+2	1000.	3000.1	HMGO
-122000+5	329390+5	137829+2	173595-4	-390653+7	840270+2	3000.	5000.1	HMGO
1001 01 07					JANAF 12/60			HN
792000+5	217660+5	823133+1	281555-3	-126896+7	609290+2	500.	3000.1	HN
792000+5	217660+5	765457+1	359853-3	180778+7	609290+2	3000.	5000.1	HN
1001 01 07 01 08					JANAF 12/60			HNO
238000+5	327550+5	133820+2	122061-3	-232403+7	783850+2	500.	3000.1	HNO
238000+5	327550+5	141523+2	-470424-4	-469135+7	783850+2	3000.	5000.1	HNO
1001 01 07 02 08					JANAF 06/63			HNO2
-183400+5	468800+5	190278+2	189744-3	-308752+7	962310+2	500.	3000.1	HNO2
-183400+5	468800+5	210284+2	-229017-3	-978618+7	962310+2	3000.	5000.1	HNO2
1001 01 07 03 08					JANAF 06/63			HNO3
-321000+5	609120+5	253548+2	608154-4	-450532+7	110851+3	500.	3000.1	HNO3
-321000+5	609120+5	266283+2	-145785-3	-102656+8	110851+3	3000.	5000.1	HNO3
1001 01 08					JANAF 12/60			HO
933000+4	214040+5	773193+1	394386-3	-973561+6	613820+2	500.	3000.1	HO
933000+4	214040+5	965144+1	-443528-4	-686115+7	613820+2	3000.	5000.1	HO
01 01 02 08					JANAF 03/64		111	HO2
500000+4	325340+5	127161+2	292770-3	-172279+7	799790+2	1000.	3000.1	HO2
500000+4	325340+5	138028+2	147088-4	-399551+7	799790+2	3000.	5000.1	HO2
1001 01 14					JANAF 12/60			HSI
114000+6	230100+5	879959+1	194499-3	-972882+6	659960+2	500.	3000.1	HSI
114000+6	230100+5	995466+1	-335662-4	-521070+7	659960+2	3000.	5000.1	HSI
4001 01 14					JANAF 12/60			H4SI
780000+4	584380+5	250841+2	172839-3	-560393+7	924370+2	500.	3000.1	H4SI
780000+4	584380+5	254616+2	695862-4	-621356+7	924370+2	3000.	5000.1	H4SI
1009 01 72					AERONUT U-2045 3/63			HAFF
-210000+5	238040+5	899071+1	-135220-4	-208349+6	793280+2	500.	3000.1	HAFF
-210000+5	238040+5	991818+1	-187198-3	-386628+7	793280+2	3000.	5000.1	HAFF
2009 01 72					AERONUT U-2045 3/63			HAFF2
-143000+6	395280+5	148828+2	588453-5	-247694+6	983630+2	500.	3000.1	HAFF2
-143000+6	395280+5	142543+2	123301-3	223897+7	983630+2	3000.	5000.1	HAFF2

TABLE IV.- CONTINUED.

$h_{j_{298}}$	$\int_{298}^{3000} C_p\,dT$	α_0	α_1	α_2	S_{3000}	T_L	T_U	Species
3009 01 72				AERONUT U-2045 3/63				HAFF3
-280000+6	525590+5	198611+2	297024-5	-414350+6	120914+3	500.	3000.1	HAFF3
-280000+6	525590+5	186354+2	235933-3	432668+7	120914+3	3000.	5000.1	HAFF3
2008 01 72				AERONUT U-2045 3/63				HAF02
-850000+5	388820+5	149184+2	-435346-5	-597146+6	925400+2	500.	3000.1	HAF02
-850000+5	388820+5	155883+2	-132986-3	-315382+7	925400+2	3000.	5000.1	HAF02
4009 01 72				AERONUT U-2045 3/63				HAFF4
-410000+6	683420+5	259241+2	-252420-4	-688150+6	138810+3	500.	3000.1	HAFF4
-410000+6	683420+5	258881+2	-917862-5	-797631+6	138810+3	3000.	5000.1	HAFF4
1008 01 09 01 72				AERONUT U-2045 3/63				HAF0F
-109000+6	392280+5	148930+2	288115-5	-401960+6	984030+2	500.	3000.1	HAF0F
-109000+6	392280+5	144062+2	959603-4	146589+7	984030+2	3000.	5000.1	HAF0F
1008 02 09 01 72				AERONUT U-2045 3/63				HAF0F2
-248000+6	521840+5	199057+2	-950324-5	-641316+6	117538+3	500.	3000.1	HAF0F2
-248000+6	521840+5	204068+2	-998477-4	-271146+7	117538+3	3000.	5000.1	HAF0F2
1 12				JANAF 9/62				MG
352810+5	134390+5	480812+1	676706-4	106780+6	469800+2	1000.	3000.1	MG
352810+5	134390+5	-665525-0	124139-2	176789+8	469800+2	3000.	5000.1	MG
1 7 1 12				JANAF 3/64				MGN
690000+5	242620+5	893597+1	119070-3	-154670+6	739500+2	1000.	3000.1	MGN
690000+5	242620+5	893270+1	118848-3	-119243+6	739500+2	3000.	5000.1	MGN
1007				JANAF 03/61				N
112965+6	134370+5	486944+1	383516-4	958460+5	480900+2	500.	3000.1	N
112965+6	134370+5	428957+1	240844-3	-417273+6	480900+2	3000.	5000.1	N
1007 01 08				JANAF 06/63				NO
215800+5	227000+5	877623+1	899031-4	-789656+6	688490+2	500.	3000.1	NO
215800+5	227000+5	916260+1	657885-5	-212519+7	688490+2	3000.	5000.1	NO
1007 02 08				JANAF 06/63				NO2
801100+4	345800+5	137819+2	315611-4	-133765+7	848890+2	500.	3000.1	NO2
801100+4	345800+5	130154+2	172586-3	175340+7	848890+2	3000.	5000.1	NO2
1007 01 14				JANAF 12/60				NSI
121000+6	235110+5	893357+1	603803-4	-411466+6	711560+2	500.	3000.1	NSI
121000+6	235110+5	883779+1	815057-4	-119769+6	711560+2	3000.	5000.1	NSI
2007 01 08				JANAF 12/60				N2O
195000+5	365450+5	144686+2	120489-3	-153478+7	815900+2	500.	3000.1	N2O
195000+5	365450+5	123036+2	459018-3	942382+7	815900+2	3000.	5000.1	N2O
1008				JANAF 06/62				O
595590+5	135220+5	497228+1	380768-5	154749+5	500960+2	500.	3000.1	O
595590+5	135220+5	657489+1	-224268-3	-891782+7	500960+2	3000.	5000.1	O
2008				JANAF 03/61				O2
000000-0	234460+5	804370+1	510872-3	-152718+6	679730+2	500.	3000.1	O2
000000-0	234460+5	103071+2	290991-4	-783079+7	679730+2	3000.	5000.1	O2
2008 01 14				JANAF 12/62				O2SI
-762000+5	382950+5	148272+2	207464-4	-777200+6	858950+2	500.	3000.1	O2SI
-762000+5	382950+5	133320+2	289052-3	571139+7	858950+2	3000.	5000.1	O2SI
2008 01 22				JANAF 12/60				O2TI
-798000+5	385860+5	148550+2	129468-4	-656075+6	880860+2	500.	3000.1	O2TI
-798000+5	385860+5	138669+2	200463-3	317357+7	880860+2	3000.	5000.1	O2TI
2008 01 74				JANAF 06/62				O2W
210000+5	364020+5	138442+2	177526-4	-364856+6	959960+2	500.	3000.1	O2W
210000+5	364020+5	130756+2	159997-3	271226+7	959960+2	3000.	5000.1	O2W
2008 01 40				JANAF 06/61				O2ZR
-825000+5	387750+5	148912+2	309724-5	-607547+6	903540+2	500.	3000.1	O2ZR
-825000+5	387750+5	149990+2	-192239-4	-975347+6	903540+2	3000.	5000.1	O2ZR
3008 01 74				JANAF 3/63				O3W
-700000+5	518660+5	198723+2	-425236-6	-720531+6	111374+3	500.	3000.1	O3W
-700000+5	518660+5	190447+2	158010-3	245041+7	111374+3	3000.	5000.1	O3W
9008 03 74				JANAF 3/63				O9W3
-468510+6	178044+6	676402+2	-219384-4	-183063+7	278001+3	500.	3000.1	O9W3

TABLE IV.- CONTINUED.

$h_{j_{298}}$	$\int_{298}^{3000} C_p\,dT$	α_o	α_1	α_2	S_{3000}	T_L	T_U	Species
-468510+6	17804+6	672619+2	551037-4	-506619+6	278001+3	3000.	5000.1	O9W3
12008 04	74			JANAF 3/63				O12W4
-648740+6	241378+6	914477+2	-117941-4	-219886+7	360115+3	500.	3000.1	O12W4
-648740+6	241378+6	914708+2	-143699-4	-233768+7	360115+3	3000.	5000.1	O12W4
2014				JANAF 12/62				SI2
130900+6	243430+5	891154+1	102582-3	-354376+5	753940+2	500.	3000.1	SI2
130900+6	243430+5	106398+2	-190701-3	-845149+7	753940+2	3000.	5000.1	SI2
1013				JANAF 03/61				AL
780000+5	134610+5	492905+1	113634-4	706967+5	508440+2	500.	3000.1	AL
780000+5	134610+5	395674+1	204094-3	361777+7	508440+2	3000.	5000.1	AL
1004				JANAF 09/61				BE
782550+5	134380+5	464695+1	112298-3	334374+6	440210+2	500.	3000.1	BE
782550+5	134380+5	105297-0	109147-2	147714+8	440210+2	3000.	5000.1	BE
1005				JANAF 12/60				B
132618+6	134240+5	506024+1	-307108-4	-985641+5	481210+2	500.	3000.1	B
132618+6	134240+5	507458+1	-121838-4	-726353+6	481210+2	3000.	5000.1	B
1072				AERONUT U-2045 3/63				HAF
145500+6	181790+5	759511+1	169886-4	-132371+7	588610+2	500.	3000.1	HAF
145500+6	181790+5	183004+1	130824-2	156981+8	588610+2	3000.	5000.1	HAF
1014				JANAF 12/62				SI
106000+6	140180+5	457930+1	301346-3	142859+6	519920+2	500.	3000.1	SI
106000+6	140180+5	478318+1	141019-3	259988+7	519920+2	3000.	5000.1	SI
1022				JANAF 12/60				TI
112490+6	156330+5	242864+1	157423-2	116689+7	558710+2	500.	3000.1	TI
112490+6	156330+5	479336+1	106517-2	-637108+7	558710+2	3000.	5000.1	TI
1074				JANAF 12/61				W
201799+6	216540+5	512206+1	439362-3	683863+7	594080+2	500.	3000.1	W
201799+6	216540+5	108518+1	147027-2	153357+8	594080+2	3000.	5000.1	W
1040				JANAF 06/61				ZR
145417+6	184270+5	606392+1	593613-3	-861888+6	585830+2	500.	3000.1	ZR
145417+6	184270+5	538554+1	770890-3	457018+6	585830+2	3000.	5000.1	ZR
1006 02	08			JANAF 03/61				CO2
-940540+5	365350+5	144559+2	210386-3	-182392+7	798480+2	500.	3000.1	CO2
-940540+5	365350+5	156451+2	-381561-4	-602768+7	798480+2	3000.	5000.1	CO2
1005 01	08			JANAF 06/62				BO
574400+4	226450+5	862197+1	136981-3	-631704+6	670240+2	500.	3000.1	BO
574400+4	226450+5	803486+1	210252-3	264653+7	670240+2	3000.	5000.1	BO
1006 01	08			JANAF 03/61				CO
-264170+5	223570+5	865040+1	117021-3	-898211+6	653700+2	500.	3000.1	CO
-264170+5	223570+5	115496+2	-424139-3	-131563+8	653700+2	3000.	5000.1	CO
2008 02	13			JANAF 12/61				AL2O2
-953970+5	504970+5	198593+2	224091-5	-134144+7	105665+3	500.	3000.1	AL2O2
-953970+5	504970+5	-185468+2	738440-2	144995+9	105665+3	3000.	5000.1	AL2O2
01 04 01	08			JANAF 09/63				BEO
310000+5	231840+5	885450+1	909641-4	-552570+6	661420+2	500.	3000.1	BEO
310000+5	231840+5	894167+1	685229-4	-731204+6	661420+2	3000.	5000.1	BEO
1001 01	05 01 08			JANAF 12/60				BHO
-471270+5	356030+5	142974+2	167620-3	-201136+7	764730+2	500.	3000.1	BHO
-471270+5	356030+5	112392+2	644865-3	134967+8	764730+2	3000.	5000.1	BHO
1017				JANAF 03/61				CL
289220+5	140280+5	508338+1	-272037-4	290013+6	516230+2	500.	3000.1	CL
289220+5	140280+5	539251+1	-770696-4	-114573+7	516230+2	3000.	5000.1	CL
1009				JANAF 06/61				F
188600+5	136830+5	489030+1	256070-4	215413+6	497910+2	500.	3000.1	F
188600+5	136830+5	583971+1	-157585-3	-365876+7	497910+2	3000.	5000.1	F
1 2								HE
000000+0	134230+5	496780+1	000000+0	000000+0	415956+2	500.	3000.1	HE
000000+0	134230+5	496780+1	000000+0	000000+0	415956+2	3000.	5000.1	HE
2001				JANAF 03/61				H2

TABLE IV.- CONTINUED.

$h_{j_{298}}$	$\int_{298}^{3000} C_p\,dT$	α_o	α_1	α_2	S_{3000}	T_L	T_U	Species
000000-0	212100+5	711963+1	621950-3	-71269+6	484650+2	500.	3000.1	H2
000000-0	212100+5	681794+1	589854-3	265106+7	484650+2	3000.	5000.1	H2
2001 01	08			JANAF 03/61				H2O
-577980+5	302010+5	112254+2	811397-3	-260800+7	684210+2	500.	3000.1	H2O
-577980+5	302010+5	157278+2	-191548-3	-173599+8	684210+2	3000.	5000.1	H2O
1008 01	72			AERONUT U-2045 3/63				HAFO
300000+5	235310+5	898778+1	-129961-4	-331141+6	759550+2	500.	3000.1	HAFO
300000+5	235310+5	103422+2	-267763-3	-564287+7	759550+2	3000.	5000.1	HAFO
1 8 1	12			JANAF 12/60				MGO
419000+4	240930+5	893540+1	100696-3	-19347 9+6	709950+2	1000.	3000.1	MGO
419000+4	240930+5	894423+1	987260-4	-219685+6	709950+2	3000.	5000.1	MGO
2007				JANAF 03/61				N2
000000-0	221650+5	862699+1	116090-3	-103715+7	637650+2	500.	3000.1	N2
000000-0	221650+5	984175+1	-116232-3	-612728+7	637650+2	3000.	5000.1	N2
1008 01	14			JANAF 09/63				OSI
-242000+5	233590+5	891444+1	545951-4	-452091+6	697470+2	500.	3000.1	OSI
-242000+5	233590+5	850773+1	132710-3	109918+7	697470+2	3000.	5000.1	OSI
1008 01	22			JANAF 12/60				OTI
151000+5	236840+5	894324+1	524336-4	-319889+6	754390+2	500.	3000.1	OTI
151000+5	236840+5	940250+1	-354311-4	-208089+7	754390+2	3000.	5000.1	OTI
1008 01	74			JANAF 3/63				OW
105000+6	238640+5	900466+1	349295-4	-310058+6	811400+2	500.	3000.1	OW
105000+6	238640+5	997145+1	-142914-3	-420935+7	811400+2	3000.	5000.1	OW
1008 1	40			JANAF 06/61				OZR
211000+5	215190+5	708186+1	-324544-4	297703+6	741580+2	500.	3000.1	OZR
211000+5	215190+5	696436+1	-798961-6	538861+6	741580+2	3000.	5000.1	OZR
1013				JANAF 03/61				AL*
240000+4	189130+5	696390+1	125221-4	347759+5	251963+2	500.	3000.3	AL*
240000+4	189130+5	744466+1	-758263-4	-210774+7	251963+2	3000.	5000.3	AL*
1007 01	13			JANAF 12/62				ALN*
-760000+5	312665+5	122768+2	-178828-4	-673685+6	299013+2	500.	2790.2	ALN*
-760000+5	314405+5	408674+2	-915846-4	-230400+9	299601+2	2790.	5000.2	ALN*
3008 02	13			JANAF 09/61				AL2O3*
-400400+6	811817+5	319699+2	120451-4	-217514+7	772577+2	500.	2318.2	AL2O3*
-366770+6	759318+5	351153+2	-192777-4	-555942+6	893107+2	2318.	5000.3	AL2O3*
1004				JANAF 09/61				BE*
000000-0	193025+5	828125+1	-288958-5	-173046+7	170595+2	500.	1556.2	BE*
288100+4	182708+5	769547+1	-257476-5	-213324+7	184265+2	1556.	5000.3	BE*
01 04 02	09			JANAF 12/63				BEF2*
-241957+6	546211+5	207446+2	-139307-4	558937+6	583302+2	500.	2000.2	BEF2*
-241957+6	548613+5	210844+2	256246-5	-533447+6	584292+2	2000.	5000.2	BEF2*
2 6 1	12			JANAF 12/60				C2MG*
210000+5	517619+5	169984+2	154993-2	-351115+6	544512+2	1000.	1800.2	C2MG*
210000+5	51754 4+5	169721+2	155315-2	-284690+6	544482+2	1800.	5000.2	C2MG*
3 6 2	12			JANAF 12/60				C3MG2*
190000+5	862753+5	283405+2	257631-2	-57641 3+6	931018+2	1000.	1800.2	C3MG2*
190000+5	862671+5	283535+2	256721-2	-56558 4+6	930986+2	1800.	5000.2	C3MG2*
1 12 2	17			JANAF 12/60				CL2MG*
-144979+6	597109+5	221001+2	-472014-7	-127269+3	790377+2	1000.	2500.3	CL2MG*
-144979+6	597109+5	220994+2	128785-6	172774+4	790377+2	2500.	5000.3	CL2MG*
02 05 01	72			AERONUT U-2045 3/63	111			HAFB2*
-742000+5	523605+5	188865+2	595324-3	205403+6	517723+2	1000.	3520.2	HAFB2*
-742000+5	786811+5	210046+2	-753793-6	-256927+5	592471+2	3520.	5000.3	HAFB2*
02 08 01	72			AERONUT U-2045 3/63	111			HAFO2*
-266100+6	544461+5	221881+2	-960937-5	-344362+7	577316+2	1000.	3170.2	HAFO2*
-266100+6	734450+5	218000+2	000-0	000-0	637251+2	3170.	5000.3	HAFO2*
04 09 01	72			AERONUT U-2045 3/63	111			HAFF4*
-461400+6	107118+6	226023+2	103650-1	-625330+5	111481+3	1000.	1201.2	HAFF4*
-461400+6	110446+6	362001+2	-254286-7	-126009+3	120302+3	1201.	5000.3	HAFF4*

TABLE IV.- CONTINUED.

$h_{j_{298}}$	$\int_{298}^{3000} C_p\,dT$	α_o	α_1	α_2	S_{3000}	T_L	T_U	Species
01 07 01 72					AERONUT U-2045 3/63 111			HAFN*
-882400+5	353567+5	151750+2	-181568-3	-330157+7	391997+2	1000.	3580.2	HAFN*
-882400+5	532571+5	142746+2	-753941-6	-256972+5	442002+2	3580.	5000.3	HAFN*
01 04 01 08					JANAF 09/63			BEO*
-143100+6	337038+5	160771+2	-434631-3	-593740+7	291887+2	500.	2820.2	BEO*
-129562+6	359122+5	153149+2	182960-3	-190747+6	347723+2	2820.	5000.3	BEO*
2004 01 06					JANAF 03/62			BE2C*
-222000+5	519028+5	229814+2	-271974-5	-635112+7	430672+2	500.	2401.2	BE2C*
-653500+4	526826+5	195224+2	723914-5	-483551+6	499909+2	2401.	5000.3	BE2C*
3004 02 07					JANAF 03/63			BE3N2*
-137800+6	863645+5	386258+2	-227477-3	-117238+8	776686+2	500.	2473.2	BE3N2*
-110735+6	916598+5	288203+2	-194536-3	779046+8	907280+2	2473.	5000.3	BE3N2*
1005 01 07					JANAF 9/63			BN*
-595100+5	291896+5	119161+2	239906-4	-891069+6	257049+2	500.	2500.2	BN*
-595100+5	290739+5	117157+2	257181-5	-240029+6	256618+2	2500.	5000.2	BN*
2005 03 08					JANAF 12/60			B2O3*
-300978+6	811530+5	299659+2	700906-3	-130981+7	828910+2	500.	3000.2	B2O3*
-300978+6	811530+5	288865+2	659184-3	884491+7	828910+2	3000.	5000.2	B2O3*
2005 01 40					JANAF 03/63			B2ZR*
-715000+5	520398+5	218849+2	598057-3	-804156+7	488198+2	500.	3323.2	B2ZR*
-606270+5	541024+5	250051+2	117452-4	-472366+6	527046+2	3323.	5000.3	B2ZR*
1006 01 14					JANAF 12/62			CSI*
-206400+5	334219+5	152771+2	-222607-3	-503627+7	296828+2	500.	2773.2	CSI*
-756200+4	348054+5	152568+2	-219419-4	-170023+7	348989+2	2773.	5000.3	CSI*
04 17 01 40					JANAF 12/63			CL4ZR*
-234700+6	750873+5	219283+2	-112411-3	155115+8	108878+3	500.	1500.2	CL4ZR*
-234700+6	855218+5	307042+2	-120868-4	529248+7	113634+3	1500.	5000.2	CL4ZR*
2009 01 72					ASSUMED SAME AS F2ZR*			F2HAF*
-220380+6	810550+5	306608+2	-210271-3	-798369+6	927673+2	500.	3000.3	F2HAF*
-220380+6	810550+5	266045+2	599714-3	154320+8	927673+2	3000.	5000.3	F2HAF*
3009 01 72					ASSUMED SAME AS F3ZR*			F3HAF*
-330000+6	971206+5	429874+2	242608-4	-136903+8	102064+3	500.	1601.2	F3HAF*
-317884+6	864581+5	319981+2	126208-5	-241831+5	105028+3	1601.	5000.3	F3HAF*
06 09 01 74					JANAF 12/63			F6W*
-427000+6	-140109+7	-120974+4	-196796	-2150687+10	-559815+3	500.	1200.2	F6W*
-427000+6	-275680+6	-379896+3	-119768-2	758620+9	-138661+2	1200.	5000.2	F6W*
01 06 01 72					AERONUT U-2045 3/63 111			HAFC*
-447000+5	348462+5	158602+2	-236443-3	-472110+7	379296+2	1000.	4160.2	HAFC*
-447000+5	556756+5	146049+2	740357-6	33672+5	429385+2	4160.	5000.3	HAFC*
1 12					JANAF 9/62			MG*
215800+4	258340+5	527980+1	260008-2	113964+3	293394+2	1000.	1700.3	MG*
215800+4	258339+5	528113+1	259962-2	-142858+4	293394+2	1700.	5000.3	MG*
1 8 1 12					JANAF 12/60			MGO*
-143700+6	336077+5	127331+2	173473-3	-660586+6	337049+2	1000.	2000.2	MGO*
-143700+6	335780+5	131367+2	327353-4	-114877+7	336939+2	2000.	5000.2	MGO*
3 8 1 12 1 14					JANAF 12/60			MGO3SI*
-362750+6	856395+5	243532+2	484199-2	-533715+6	822449+2	1000.	1798.2	MGO3SI*
-352067+6	903202+5	373061+2	133609-4	-430019+7	908099+2	1798.	5000.3	MGO3SI*
4 8 2 12 1 14					JANAF 12/60			MG2O4SI
-512980+6	123432+6	352288+2	680283-2	-506108+6	118377+3	1000.	2158.2	MG2O4SI
-496527+6	128026+6	526253+2	103634-4	-580849+7	128170+3	2158.	5000.3	MG2O4SI
2 12 1 14					JANAF 12/60			MG2SI
-186000+5	625345+5	177141+2	346801-2	-291684+6	683951+2	1000.	1375.2	MG2SI
-792000+3	607920+5	225001+2	-422729-7	-189417+3	815087+2	1375.	5000.3	MG2SI
2 7 3 12					JANAF 12/60			MG3N2*
-110200+6	789750+5	292742+2	113991-3	196192+6	867454+2	1000.	1800.2	MG3N2*
-110200+6	789220+5	295378+2	686471-6	295585+4	867250+2	1800.	5000.2	MG3N2*
1007 01 22					JANAF 12/60			NTI*
-805000+5	353992+5	139516+2	224921-3	-237365+7	355579+2	500.	3201.2	NTI*

TABLE IV.- CONTINUED.

$h_{j_{298}}$	$\int_{298}^{3000} C_p\,dT$	α_o	α_1	α_2	S_{3000}	T_L	T_U	Species
-652420+5	364550+5	134058+2	130614-4	776741+6	406524+2	3201.	5000.3	NTI*
1007 01 40				JANAF 12/61				NZR*
-873000+5	368412+5	147403+2	405595-3	-385238+7	384591+2	500.	3225.2	NZR*
-694890+5	357007+5	136845+2	315953-4	330586+7	436372+2	3225.	5000.3	NZR*
2008 01 14				JANAF 12/62				O2SI*
-217500+6	468950+5	176582+2	549817-3	-236409+7	473990+2	500.	1883.2	O2SI*
-215948+6	507890+5	217500+2	-193988-4	-282763+6	499160+2	1883.	5000.3	O2SI*
2008 01 22				JANAF 12/60				O2TI*
-225500+6	488351+5	190821+2	-102491-4	-143270+7	519395+2	500.	2128.2	O2TI*
-212320+6	513349+5	190035+2	-412635-5	117753+6	592964+2	2128.	5000.3	O2TI*
2008 01 74				JANAF 06/62				O2W*
-140940+6	547956+5	233094+2	-361730-4	-538143+7	551090+2	500.	2000.2	O2W*
000000-0	569078+5	287018+2	186655-4	-267082+8	559378+2	2000.	5000.3	O2W*
2008 01 40				JANAF 06/61				O2ZR*
-261500+6	487946+5	182127+2	-777714-3	689168+7	524420+2	500.	2950.2	O2ZR*
-245518+6	540370+5	195658+2	831149-4	167937+7	596073+2	2950.	5000.3	O2ZR*
3008 02 22				JANAF 12/60				O3TI2*
-362900+6	946320+5	364500+2	-320380-5	-150722+7	962115+2	500.	2401.2	O3TI2*
-334661+6	972696+5	359848+2	-104734-5	196485+6	109086+3	2401.	5000.3	O3TI2*
3008 01 74				JANAF 3/63				O3W*
-201460+6	651377+5	248215+2	-220326-4	-120178+6	714102+2	500.	1745.2	O3W*
-187801+6	775349+5	314980+2	149772-5	-331027+5	851294+2	1745.	5000.3	O3W*
1014				JANAF 12/62				SI*
000000-0	172470+5	652874+1	838825-4	-32216+6	185450+2	500.	1685.2	SI*
120920+5	165620+5	600789+1	234623-4	356236+6	254280+2	1685.	5000.3	SI*
1074				JANAF 12/61				W*
000000-0	189545+5	775752+1	991652-4	-217322+7	231570+2	500.	3650.2	W*
720200+4	196127+5	874838+1	-706194-5	421056+7	252882+2	3650.	5000.3	W*
1040				JANAF 06/61				ZR*
000000-0	203287+5	575035+1	-102844-3	639457+7	266635+2	500.	2128.2	ZR*
526900+4	219819+5	851208+1	-197639-5	-291700+5	297680+2	2128.	5000.3	ZR*
1006				JANAF 03/61				C*
000000-0	144120+5	586075+1	953976-4	-766621+6	121290+2	500.	3000.2	C*
000000-0	144120+5	485134+1	291605-3	307202+7	121290+2	3000.	5000.2	C*
2005 01 22				JANAF 12/62				B2TI*
-700000+5	560966+5	226476+2	104772-2	-711450+7	489143+2	500.	3193.2	B2TI*
-603800+5	585292+5	269415+2	126484-4	274920+6	526893+2	3193.	5000.3	B2TI*
4005 01 06				JANAF 12/60				B4C*
-122000+5	754141+5	302324+2	472313-4	-219585+7	650380+2	500.	2620.2	B4C*
109420+5	771144+5	298788+2	-116769-4	128251+6	745221+2	2620.	5000.3	B4C*
1006 01 22				JANAF 12/60				CTI*
-438000+5	344230+5	138258+2	127229-3	-250262+7	332904+2	500.	3410.2	CTI*
-268660+5	351837+5	131769+2	-101042-4	-242423+7	384818+2	3410.	5000.3	CTI*
1006 01 40				JANAF 03/62				CZR*
-450000+5	360105+5	149082+2	928757-4	-321715+7	374877+2	500.	3765.2	CZR*
-247880+5	361377+5	153317+2	-712238-5	-587717+7	428784+2	3765.	5000.3	CZR*
2009 01 40				JANAF 06/61				F2ZR*
-220380+6	810550+5	306608+2	-210271-3	-798369+6	927673+2	500.	3000.3	F2ZR*
-220380+6	810550+5	266045+2	599714-3	154320+8	927673+2	3000.	5000.3	F2ZR*
3009 01 40				JANAF 06/61				F3ZR*
-330000+6	971206+5	429874+2	242608-4	-136903+8	102064+3	500.	1601.2	F3ZR*
-317884+6	864581+5	319981+2	126208-5	-241831+5	105028+3	1601.	5000.3	F3ZR*
04 09 01 40				JANAF 12/63				F4ZR*
-456800+6	-676661+6	-597645+3	-992990-3	758743+9	-265363+3	500.	1200.2	F4ZR*
-456800+6	-758602+5	-134613+3	-213939-3	281649+9	236126+2	1200.	5000.2	F4ZR*
1008 01 22				JANAF 12/60				OTI*
-123900+6	435561+5	182106+2	-534802-4	-154252+7	417253+2	500.	2010.2	OTI*
-108682+6	391724+5	145141+2	267716-5	-206837+6	474256+2	2010.	5000.3	OTI*
1022				JANAF 12/60				TI*

TABLE IV.- CONCLUDED.

$h_{j_{298}}$	$\int_{298}^{3000} C_p\,dT$	α_o	α_1	α_2	S_{3000}	T_L	T_U	Species
000000-0	193899+5	471612+1	-708316-4	839470+7	240622+2	500.	1950.2	TI*
387800+4	216130+5	800196+1	165771-5	-732318+5	269556+2	1950.	5000.3	TI*
02 17 01	22			JANAF 03/64			111	CL2TI*
-123500+6	634211+5	160221+2	451891-2	-107738+4	744972+2	1000.	1500.2	CL2TI*
-123500+6	634211+5	160265+2	451745-2	-604510+4	744972+2	1500.	5000.2	CL2TI*
03 17 01	22			JANAF 03/64			111	CL3TI*
-172400+6	731540+5	233586+2	234506-2	-199751+6	930391+2	1000.	1200.2	CL3TI*
-172400+6	734036+5	230170+2	255718-2	-744078+5	931445+2	1200.	5000.2	CL3TI*
06 09 01	74			JANAF 12/63			111	F6W*
-427000+6	113478+6	419996+2	223527-6	150363+3	157378+3	1000.	1200.3	F6W*
-427000+6	113483+6	419852+2	738808-5	846970+4	157380+3	1200.	5000.3	F6W*

TABLE V

MATERIAL PROPERTY DATA FOR COMPOSITE ABLATION MATERIALS[1]

(a) Graphite phenolic (32 percent phenolic, 60° and 90° fiber layup angle).

Virgin Plastic

$\rho_p = 88.17$ lb/ft^3

$h_p^o = -352$ Btu/lb

Temperature (°R)	Specific Heat (Btu/lb-°R)	Thermal Conductivity (Btu/ft-sec-°R)	
		60° Layup Angle	90° Layup Angle
530	0.210	0.46×10^{-3}	0.50×10^{-3}
1000	.430	$.46\times10^{-3}$	$.50\times10^{-3}$
1500	.472	$.46\times10^{-3}$	$.50\times10^{-3}$
2000	.484	$.46\times10^{-3}$	$.50\times10^{-3}$
3000	.493	$.46\times10^{-3}$	$.50\times10^{-3}$
4000	.498	$.46\times10^{-3}$	$.50\times10^{-3}$
5000	.500	$.46\times10^{-3}$	$.50\times10^{-3}$
7000	.500	$.46\times10^{-3}$	$.50\times10^{-3}$

Char

$\rho_c = 71.24$ lb/ft^3

$h_c^o = 0$

Temperature (°R)	Specific Heat (Btu/lb-°R)	Thermal Conductivity (Btu/ft-sec-°R)	
		60° Layup Angle	90° Layup Angle
530	0.210	0.717×10^{-3}	0.781×10^{-3}
1000	.430	$.766\times10^{-3}$	$.834\times10^{-3}$
1500	.472	$.817\times10^{-3}$	$.888\times10^{-3}$
2000	.484	$.868\times10^{-3}$	$.944\times10^{-3}$
3000	.493	$.981\times10^{-3}$	1.070×10^{-3}
4000	.498	1.113×10^{-3}	1.210×10^{-3}
5000	.500	1.287×10^{-3}	1.400×10^{-3}
6000	.500	1.565×10^{-3}	1.707×10^{-3}
7000	.500	2.074×10^{-3}	2.260×10^{-3}

[1]Data based on fragmentary information obtained from several sources.

TABLE V.- CONTINUED

(b) Silica phenolic (32 percent phenolic, 60° and 90° fiber layup angle).

Virgin Plastic

$\rho_p = 106.49$ lb/ft^3

$h_p^{\circ} = -4782$ Btu/lb

Temperature ($^{\circ}$R)	Specific Heat (Btu/lb-$^{\circ}$R)	Thermal Conductivity (Btu/ft-sec-$^{\circ}$R)	
		60° Layup Angle	90° Layup Angle
530	0.210	0.189×10^{-3}	0.205×10^{-3}
1000	.430	$.189\times10^{-3}$	$.205\times10^{-3}$
1500	.472	$.189\times10^{-3}$	$.205\times10^{-3}$
2000	.484	$.189\times10^{-3}$	$.205\times10^{-3}$
3000	.493	$.189\times10^{-3}$	$.205\times10^{-3}$
4000	.498	$.189\times10^{-3}$	$.205\times10^{-3}$
5000	.500	$.189\times10^{-3}$	$.205\times10^{-3}$
7000	.500	$.189\times10^{-3}$	$.205.10^{-3}$

Char

$\rho_c = 89.45$ lb/ft^3

$h_c^{\circ} = -5274$ Btu/lb

Temperature ($^{\circ}$R)	Specific Heat (Btu/lb-$^{\circ}$R)	Thermal Conductivity (Btu/ft-sec-$^{\circ}$R)	
		60° Layup Angle	90° Layup Angle
530	0.210	0.294×10^{-3}	0.32×10^{-3}
1000	.430	$.314\times10^{-3}$	$.342\times10^{-3}$
1500	.472	$.335\times10^{-3}$	$.364\times10^{-3}$
2000	.484	$.356\times10^{-3}$	$.387\times10^{-3}$
3000	.493	$.403\times10^{-3}$	$.438\times10^{-3}$
4000	.498	$.456\times10^{-3}$	$.496\times10^{-3}$
5000	.500	$.528\times10^{-3}$	$.574\times10^{-3}$
6000	.500	$.642\times10^{-3}$	$.699\times10^{-3}$
7000	.500	$.851\times10^{-3}$	$.925\times10^{-3}$

TABLE V.- CONCLUDED.

(c) Resin decomposition gas enthalpy (h_g).

Temperature ($^{\circ}R$)	900	1800	2700	3600	4500	5400	6300
Enthalpy (Btu/lb)	-1810	-870	521	2780	3760	5130	7350

(d) Phenolic resin decomposition kinetic coefficients (see Eq. (5(b)) (taken from Ref. 7).

Resin Part	k_i (sec^{-1})	n_i	E_i ($^{\circ}R$)	ρ_{o_i} (lb/ft^3)	ρ_{r_i} (lb/ft^3)
A	0.140×10^{5}	3	0.154×10^{5}	20.25	0
B	$.448\times10^{+10}$	3	$.368\times10^{5}$	60.75	40.5

TABLE VI

RESULTS OF MATERIAL-PROPELLANT COMPATIBILITY INVESTIGATION

(a) OF_2-B_2H_6 environment, O/F = 3.0, pressure = 100 psia.

Virgin Material	Density (lb/ft^3)	Melt Temperature ($^\circ R$)	Surface Temperature ($^\circ R$)	Surface Material	B'	$\dot{B}$	$\dot{S}$* (in/sec)
BeO	191	5070	5070	BeO	0.1559	0.7011	0.0088
TiB_2	281	5730	5450	B_2Ti	.4224	.4224	.00360
B_4C	151	4710	4690	B_4C	.2507	.2507	.00398
C	120	---	5400	C	.2300	.2300	.00459
HfB_2	650	6340		HfO_2	melts, no solution		
HfO_2	630	5710	5710	HfO_2	.2610	2.6624	.0105
ZrO_2	327	5320	5320	ZrO_2	0	2.5945	.0190
W	1203	6570	6570	W	0	2.7452	.0054
70% SiO_2 30% Ph	120	---	3940	SiO_2	.8025	.8025	.01605
50% SiO_2 50% Ph	100	---	4010	SiC	.651	.651	.01550
30% SiO_2 70% Ph	80	---	4410	C	.503	.503	.01500
70% C 30% Ph	88	---	5240	C	.2480	.2480	.00677
50% C 50% Ph	86	---	5180	C	.2700	.2700	.00753
30% C 70% Ph	84	---	5125	C	.2900	.2900	.00827
CTi	307	6140	3785	Ti_2O_3	.9125	.9125	.00714
CZr	420	6770		O_2Zr	melts, no solution		
NTi	338	5760		Ti_2O_3	melts, no solution		
NZr	442	5805		O_2Zr	melts, no solution		

*Based on value for mass-transfer coefficient, $\rho_e u_e C_M = 0.2$ lb/ft^2-sec.

TABLE VI.- CONTINUED.

(b) O_2-H_2 environment, O/F = 4.0, pressure = 100 psia.

Virgin Material	Density (lb/ft^3)	Heat Temperature (^oR)	Surface Temperature (^oR)	Surface Material	B'	$\dot{B}$	$\dot{S}$* (in./sec)
BeO	191	5070	5070	BeO	0	0.0195	0.0002
TiB_2	281	5730		TiO_3	melts, no solution		
B_4C	151	4710	4220	B_4C	.4136	.4136	.00657
C	120	---	2340	C	.6030	.6030	.01206
HfB_2	650	6340	5120	HfO_2	0	0	0
HfO_2	603	5170	5120	HfO_2	0	0	0
ZrO_2	327	5320	5120	ZrO_2	0	0	0
W	1203	6570	5025	W	.2764	.2764	.00552
70% SiO_2 30% Ph	120	---	4680	SiO_2	.1368	.1368	.002736
50% SiO_2 50% Ph	100	---	4600	SiO_2	.1506	.1506	.00362
30% SiO_2 70% Ph	80	---	4500	SiO_2	.1701	.1701	.00511
70% C 30% Ph	88	---	2310	C	.6800	.6800	.0180
50% C 50% Ph	86	---	2247	C	.7300	.7300	.0204
30% C 70% Ph	84	---	2190	C	.7800	.7800	.0223
CTi	307	6140		Ti_2O_3	melts, no solution		
CZr	420	6770	5120	ZrO_2	0	0	0
NTi	338	5760		Ti_2O_3	melts, no solution		
NZr	442	5805	5120	ZrO_2	0	0	0

*Based on value of mass-transfer coefficient, $\rho_e u_e C_M$ = 0.2 lb/ft^2-sec.

TABLE VI.- CONTINUED.

(c) N_2O_4-N_2H_4 environment, O/F = 2.0, pressure = 100 psia.

Virgin Material	Density (lb/ft^3)	Melt Temperature ($^\circ R$)	Surface Temperature ($^\circ R$)	Surface Material	B'	$\dot{B}$	$\dot{S}$ * (in.sec)
BeO	191	5070	5070	BeO	0	0.2049	0.0025
TiB_2	281	5730		TiO_2	melts, no solution		
B_4C	151	4710	4710	B_4C	0	.3554	.0056
C	120	---	3225	C	.2800	.2800	.00559
HfB_2	650	6340	5600	HfO_2	0	0	0
HfO_2	603	5710	5600	HfO_2	0	0	0
ZrO_2	327	5320	5320	ZrO_2	0	.4317	.00316
W	1203	6570	4910	W	.6499	.6499	.00130
70% SiO_2 30% Ph	120	---	5200	SiO_2	.1242	.1242	.002484
50% SiO_2 50% Ph	100	---	5020	SiO_2	.1546	.1546	.00371
30% SiO_2 70% Ph	80	---	4780	SiO_2	.1775	.1775	.00533
70% C 30% Ph	88	---	3050	C	.3130	.3130	.00849
50% C 50% Ph	86	---	2900	C	.3400	.3400	.00949
30% C 70% Ph	84	---	2705	C	.3650	.3650	.0104
CTi	307	6140		TiO_2	melts, no solution		
CZr	420	6770		ZrO_2	melts, no solution		
NTi	338	5760		TiO_2	melts, no solution		
NZr	442	5805		ZrO_2	melts, no solution		

*Based on value of mass-transfer coefficient, $\rho_e u_e C_M$ = 0.2 lb/ft^2-sec.

TABLE VI.- CONCLUDED.

(d) F_2/O_2-CH_4 environment, O/F = 4.0, pressure = 100 psia.

Virgin Material	Density (lb/ft^3)	Melt Temperature (^oR)	Surface Temperature (^oR)	Surface Material	B'	$\dot{B}$	$\dot{S}$* (in./sec)
BeO	191	5070	5070	BeO	0.3249	0.1406	0.004
TiB_2	281	5730	4720	B_2Ti	.610	.610	.00521
B_4C	151	4710	4710	B_4C	.3003	.3266	.0051
C	120	---	5530	C	.196	.196	.0039
HfB_2	650	6340		HfO_2	melts, no solution		
HfO_2	603	5710	5710	HfO_2	.0800	1.86	.00740
ZrO_2	327	5320	5320	ZrO_2	0	1.536	.0112
W	1203	6570	5870	W	.3043	.3043	.0006
70% SiO_2 30% Ph	120	---	4960	SiO_2	.3699	.3699	.0074
50% SiO_2 50% Ph	100	---	4570	SiO_2	.3570	.3570	.00857
30% SiO_2 70% Ph	80	---	3840	C	.5077	.5077	.01515
70% C 30% Ph	88	---	5410	C	.2100	.2100	.00573
50% C 50% Ph	86	---	5280	C	.2200	.2200	.00572
30% C 70% Ph	84	---	5040	C	.2250	.2250	.00642
CTi	307	6140		TiO_2	melts, no solution		
CZr	420	6770		ZrO_2	melts, no solution		
NTi	338	5760		TiO_2	melts, no solution		
NZr	442	5805		ZrO_2	melts, no solution		

*Based on value of mass-transfer coefficient, $\rho_e u_e C_M$ = 0.2 lb/ft^2-sec.

TABLE VII

THERMAL PROPERTIES OF HEAT-SINK NOZZLE MATERIALS

(a) 1020 Steel (ρ = 490 lb/ft^3).

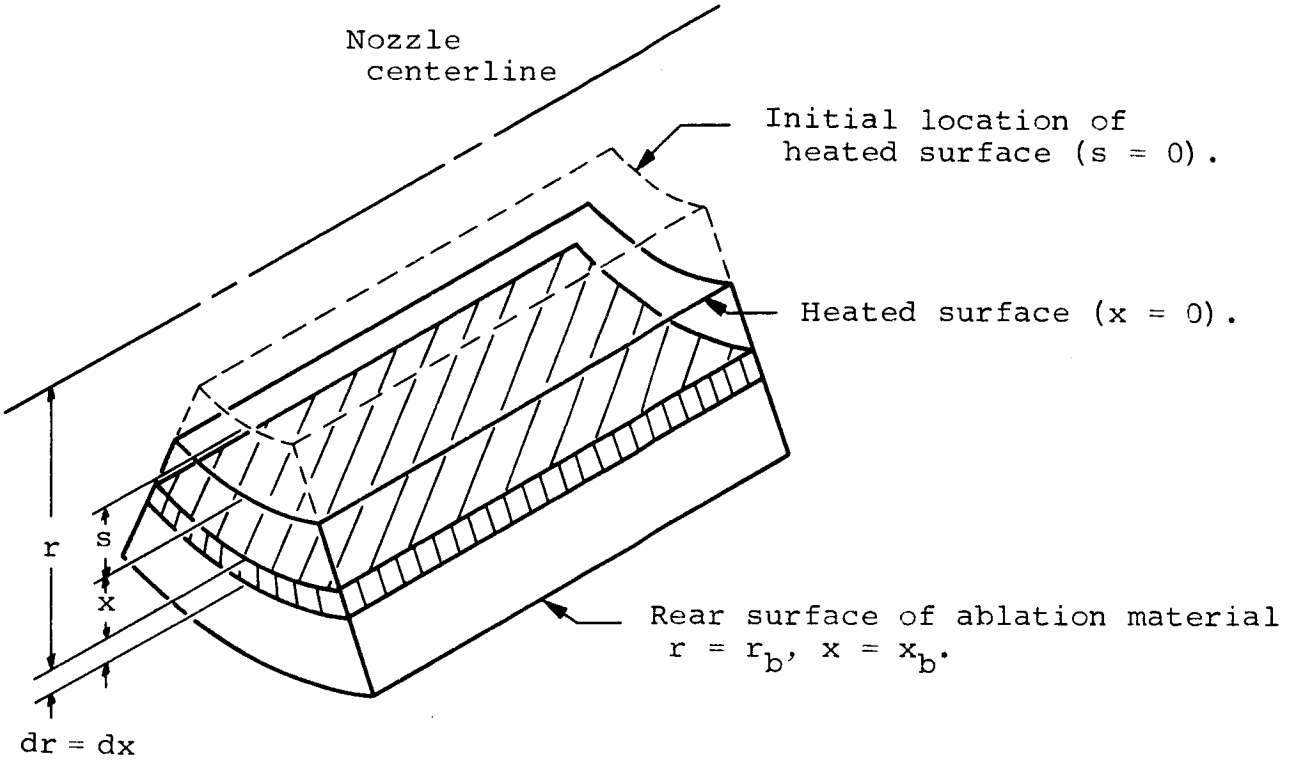
T ($^\circ$R)	k (Btu/ft-sec-$^\circ$R)	C_p (Btu/lb-$^\circ$R)
500	1.04×10^{-2}	0.10
1000	$.829\times10^{-2}$	.13
1500	$.625\times10^{-2}$	.18
1750	$.547\times10^{-2}$	.20
2000	$.484\times10^{-2}$	.17
3000	$.334\times10^{-2}$	.16

(b) Rokide Z (ZrO_2) (ρ = 330 lb/ft^3).

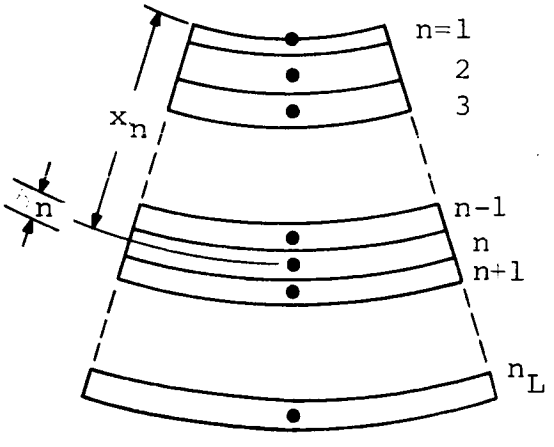
T ($^\circ$R)	k (Btu/ft-sec-$^\circ$R)	C_p (Btu/lb-$^\circ$R)
500	2.67×10^{-4}	0.104
750	2.72×10^{-4}	.122
1000	2.75×10^{-4}	.134
1500	2.89×10^{-4}	.144
2000	3.06×10^{-4}	.149
2660	3.30×10^{-4}	.155
2661	3.30×10^{-4}	.144
6000	4.86×10^{-4}	.144

(c) Molybdenum (ρ = 639 lb/ft^3, T_{melt} = 5210° R).

T ($^\circ$R)	k (Btu/ft-sec-$^\circ$R)	C_p (Btu/lb-$^\circ$R)
400	2.78×10^{-2}	0.0605
500	2.20×10^{-2}	.0620
1000	2.075×10^{-2}	.0650
1250	2.015×10^{-2}	.0655
2000	1.755×10^{-2}	.0700
3000	1.423×10^{-2}	.083
3500	1.270×10^{-2}	.091
3750	1.217×10^{-2}	.095
4000	1.175×10^{-2}	.100
4500	1.120×10^{-2}	.110
5000	1.090×10^{-2}	.120
5500	1.083×10^{-2}	.133



(a) Coordinate system specification.



(b) Finite-difference representation.

Figure 1.- Geometric and coordinate system for charring ablation solution.

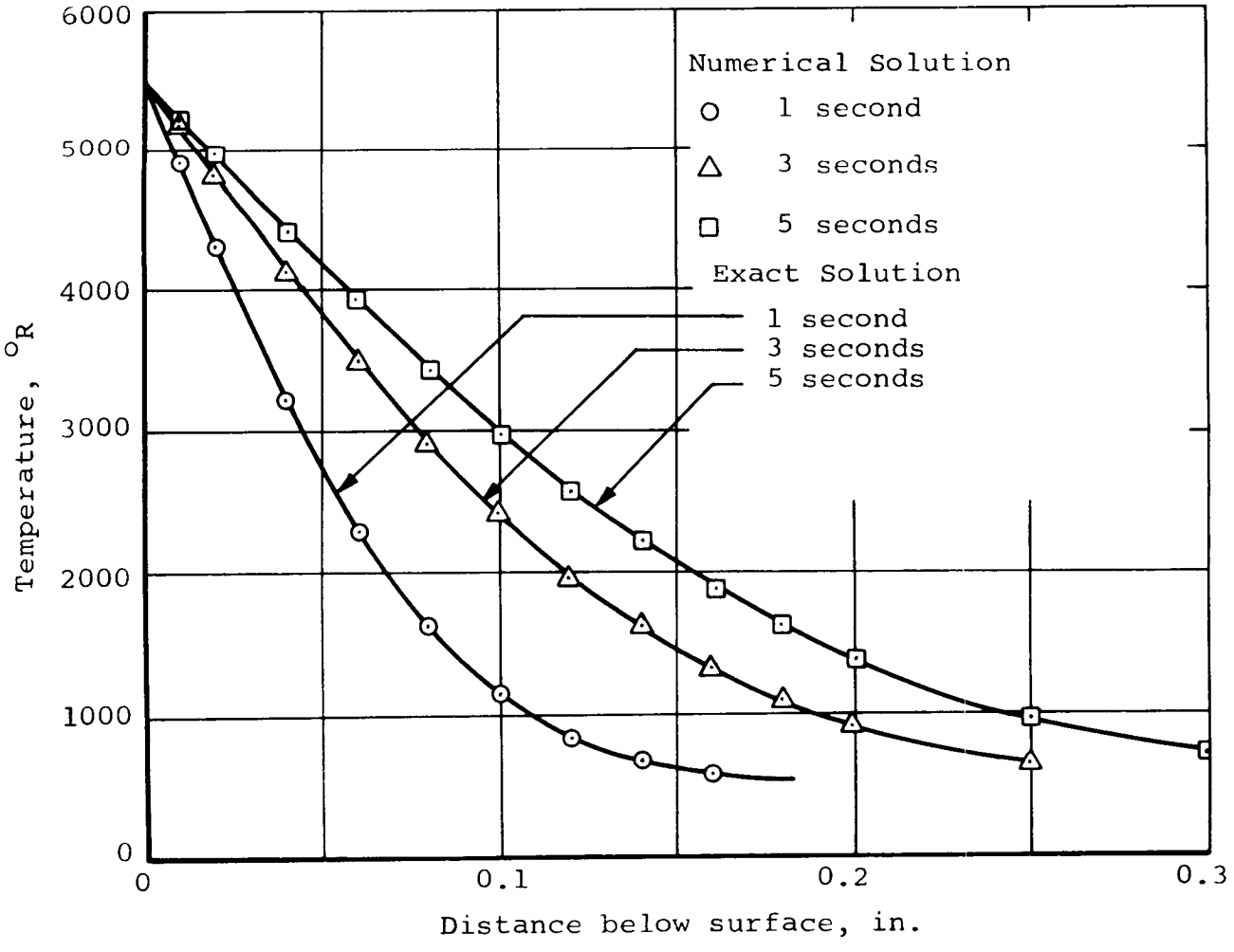
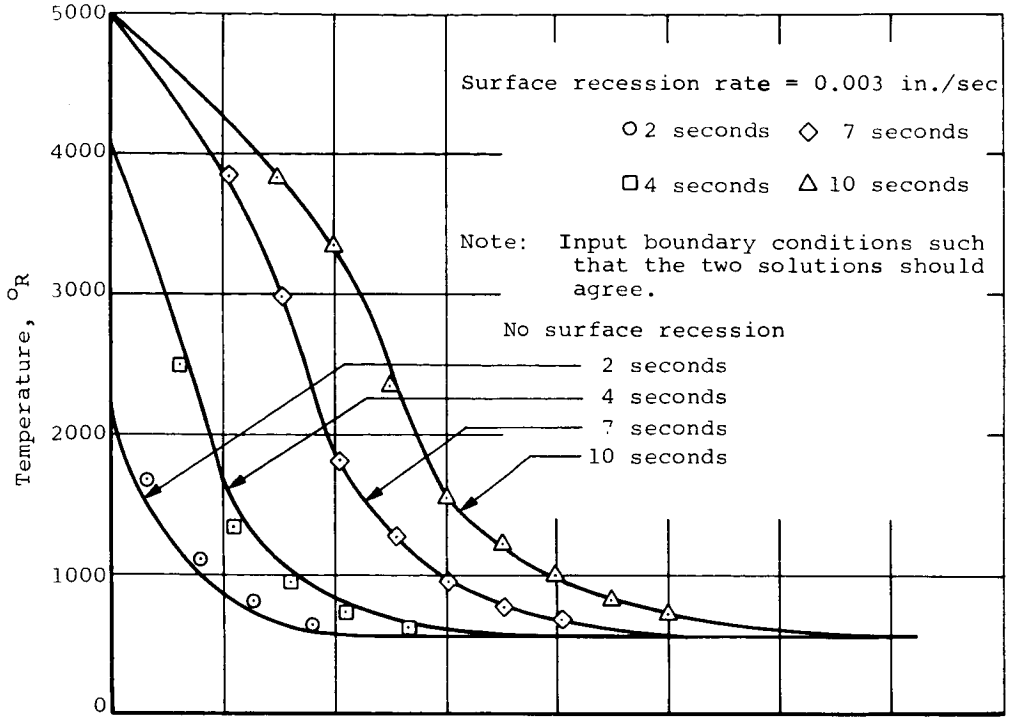
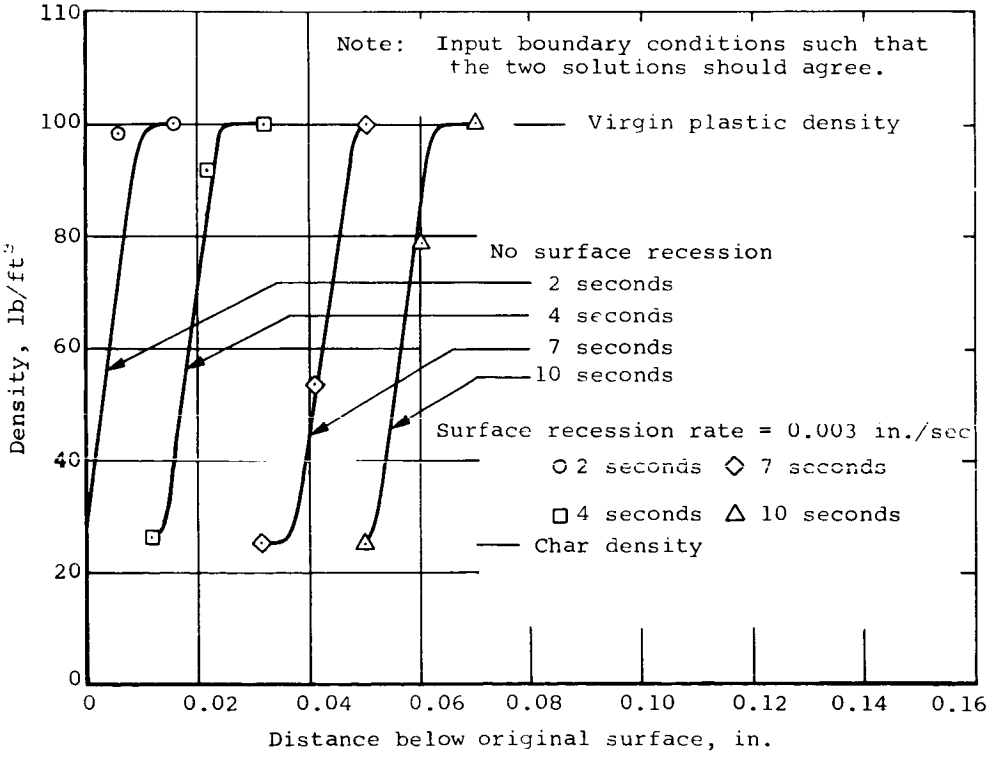


Figure 2.- Comparison of exact and explicit finite-difference solution for step surface temperature at time zero.



(a) Temperature distributions.



(b) Density distributions.

Figure 3.- Comparison of results in charring ablation material with and without surface recession.

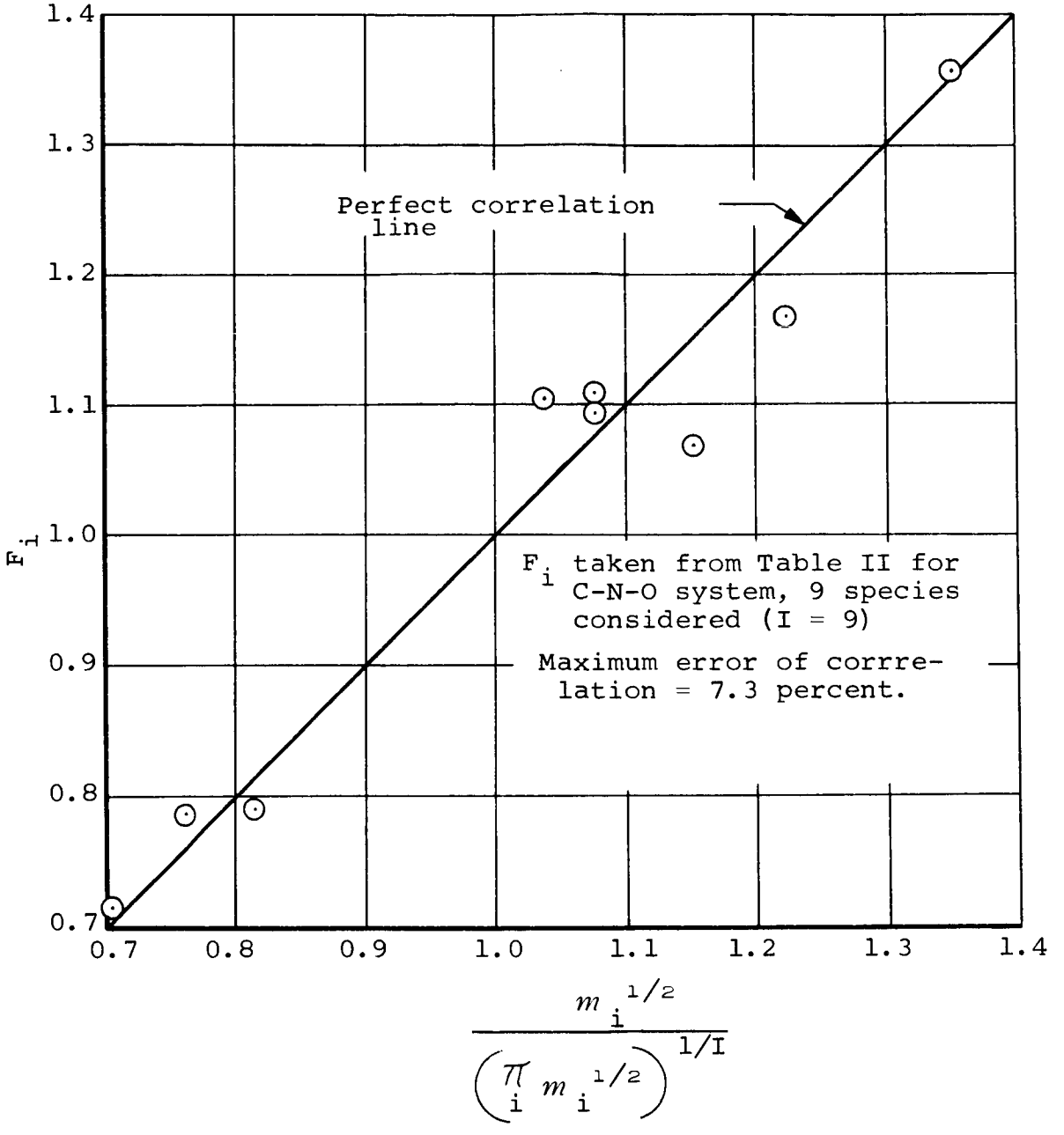
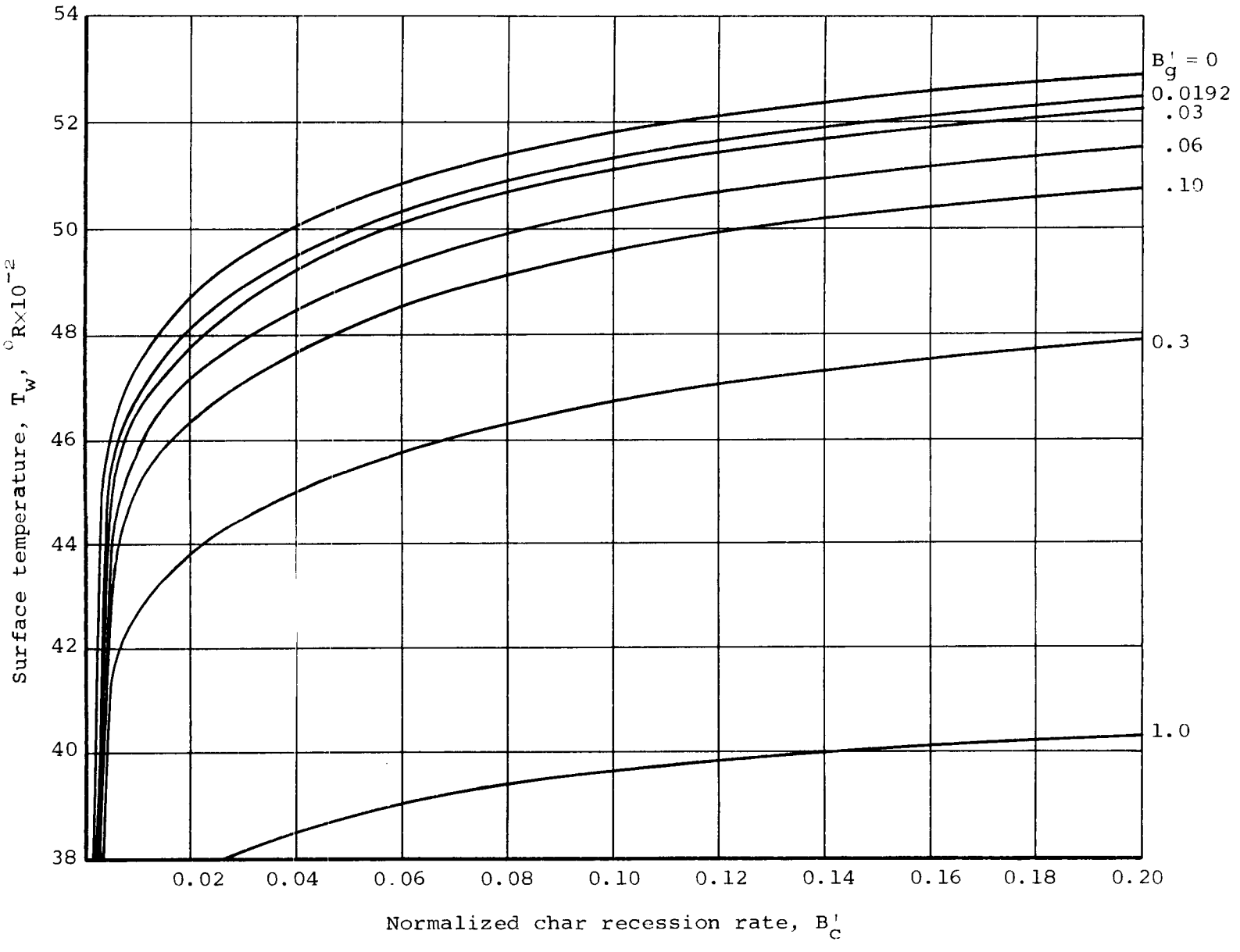
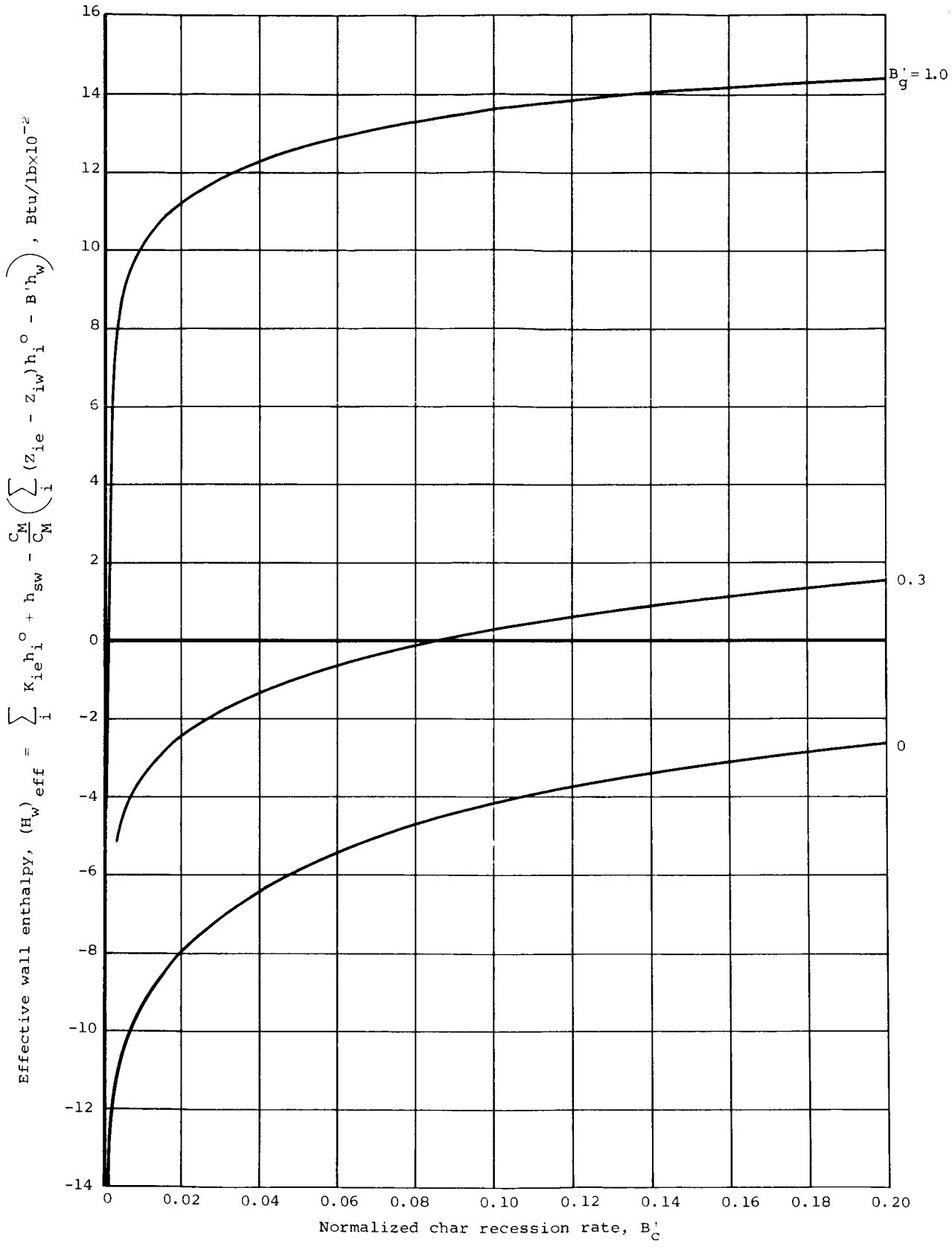


Figure 4.- Demonstration of the validity of the approximation, $F_i \cong m_i^{1/2} \Big/ \left(\prod_i m_i^{1/2}\right)^{1/I}$.



(a) Surface temperature as a function of char recession rate with off-gas rate as a parameter.

Figure 5.- Typical output from equilibrium Surface Thermochemistry Program for silica phenolic (68-32 percent by mass) in a N_2O_4-N_2H_2/UDMH (O/F = 2.0) environment.



(b) Effective wall enthalpy as a function of char recession rate with off-gas rate as a parameter.

Figure 5.- Concluded.

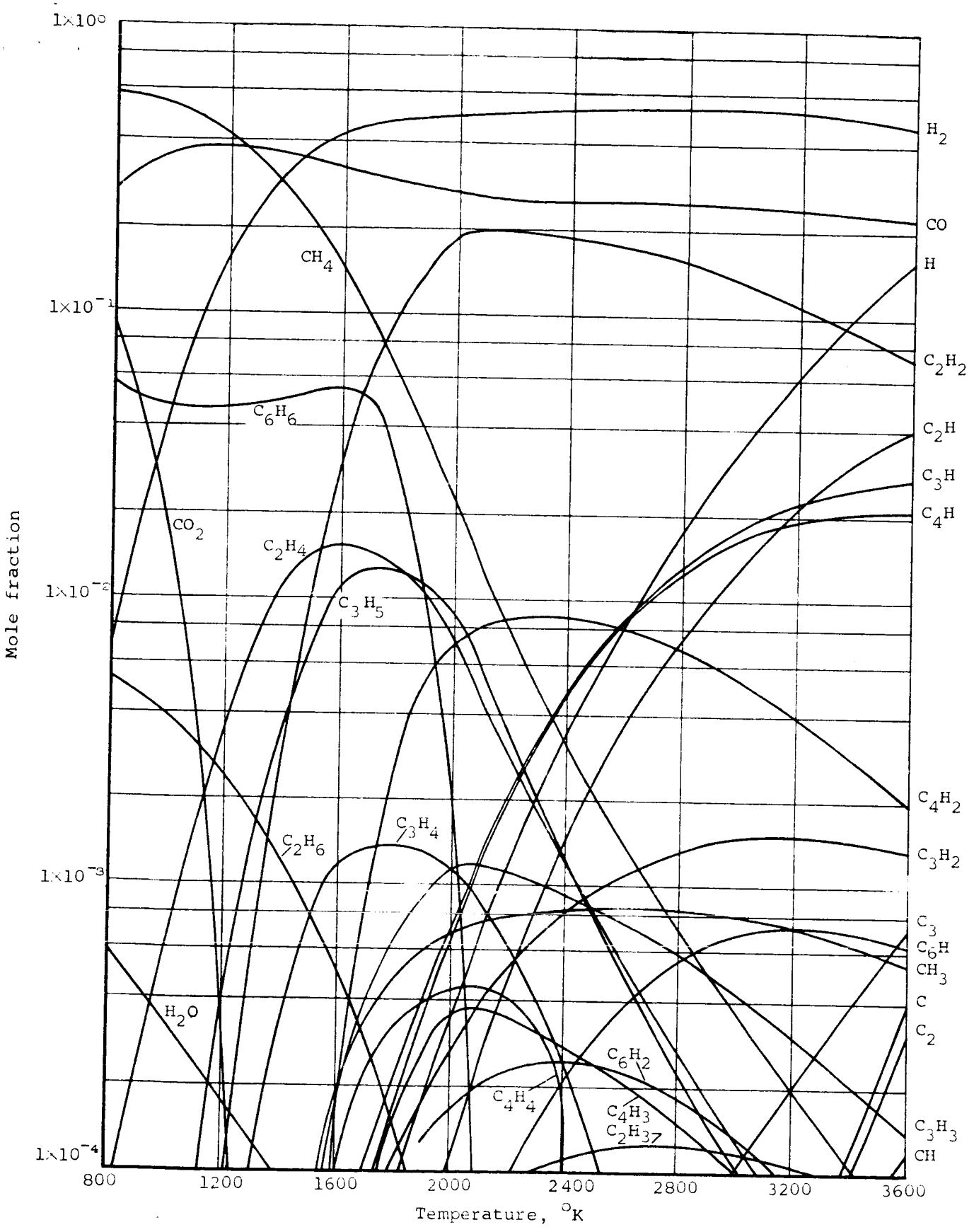


Figure 6.- Equilibrium composition of phenolic resin gaseous pyrolysis products. Pressure = 11 atmospheres.

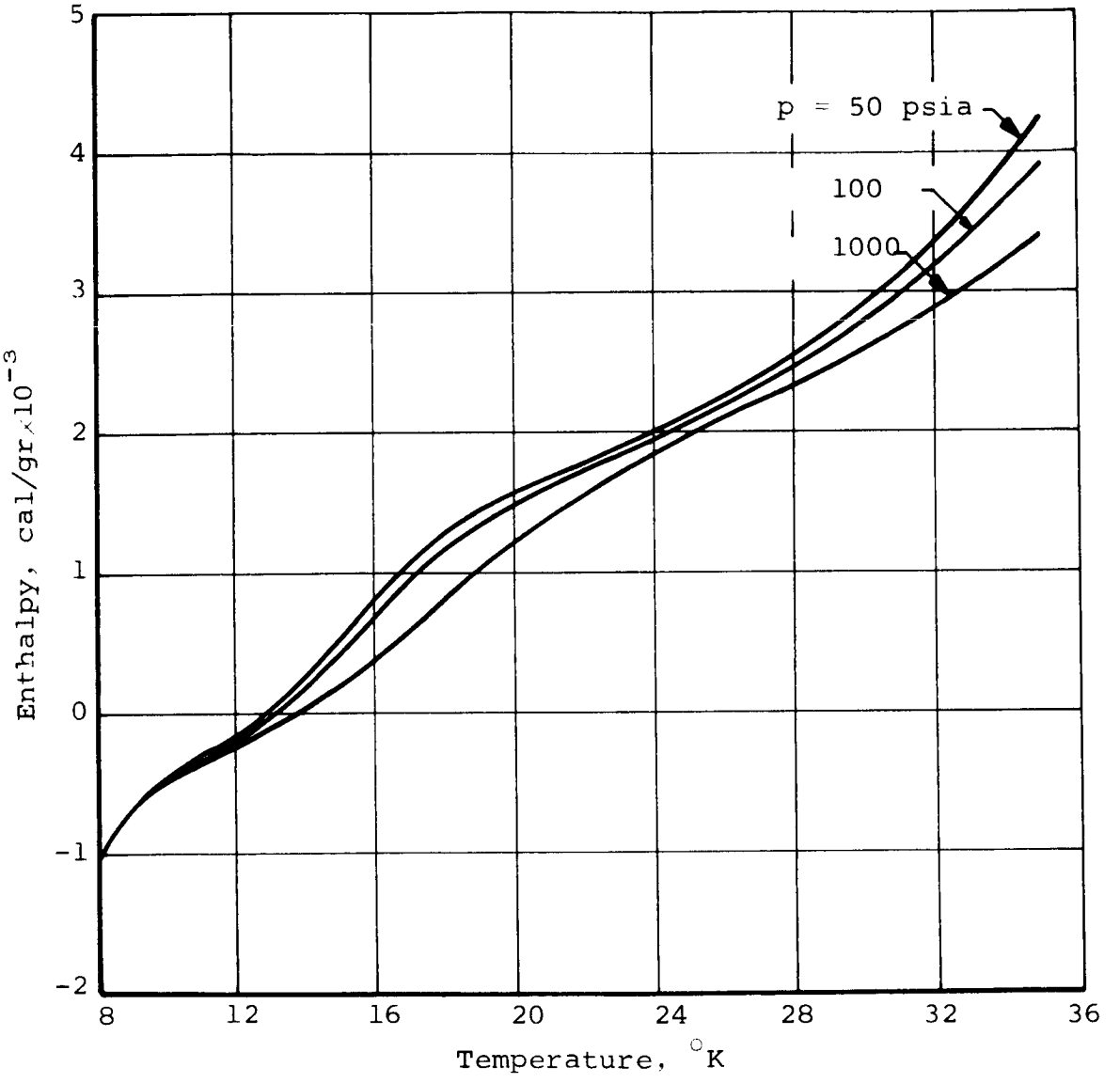
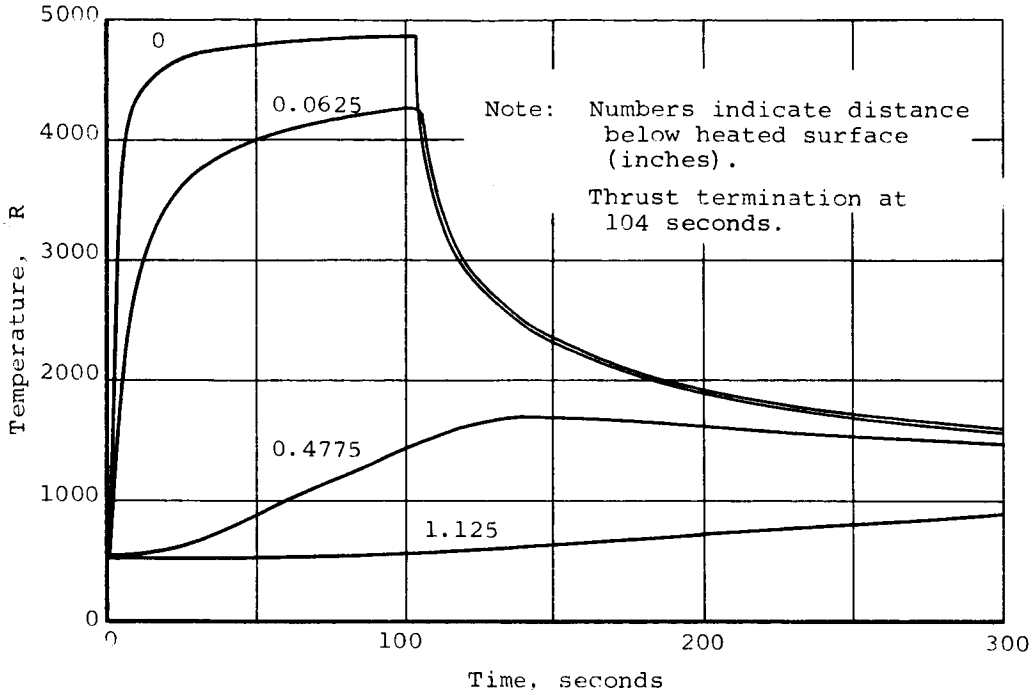
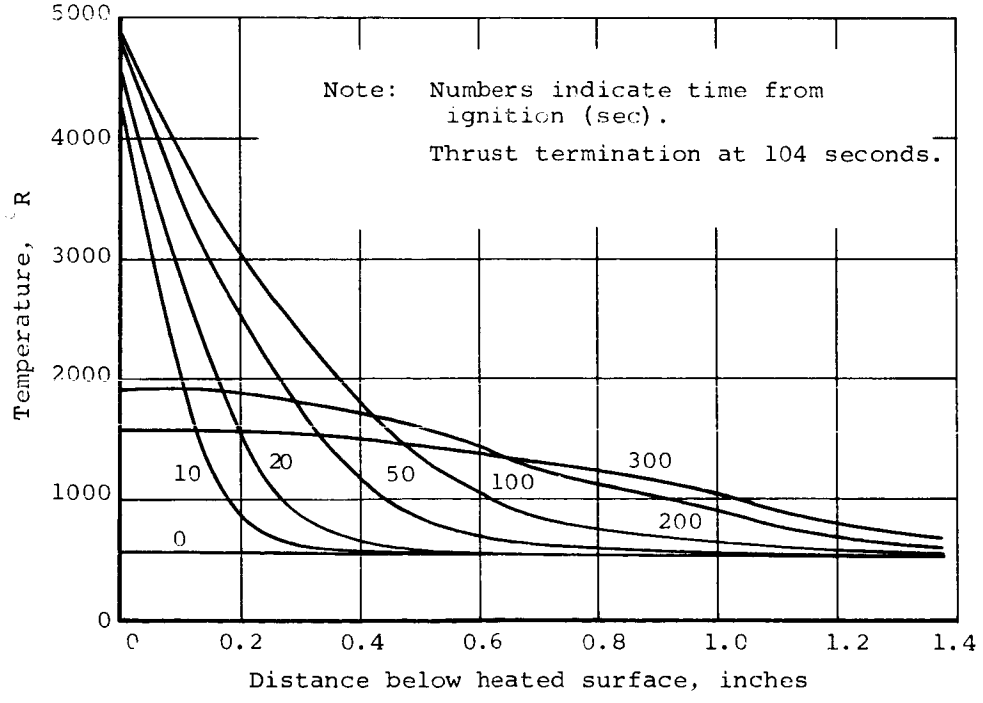


Figure 7.- Phenolic-resin decomposition gas equilibrium enthalpy as a function of temperature for each of three pressures.

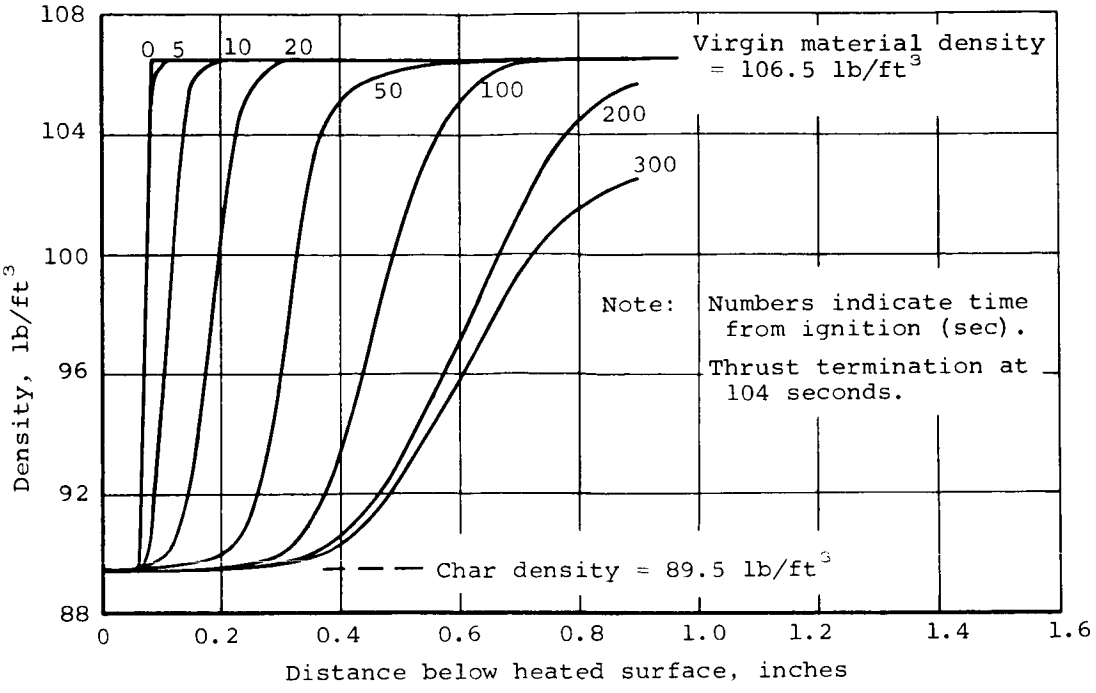


(a) Temperature histories for several locations in the nozzle material.

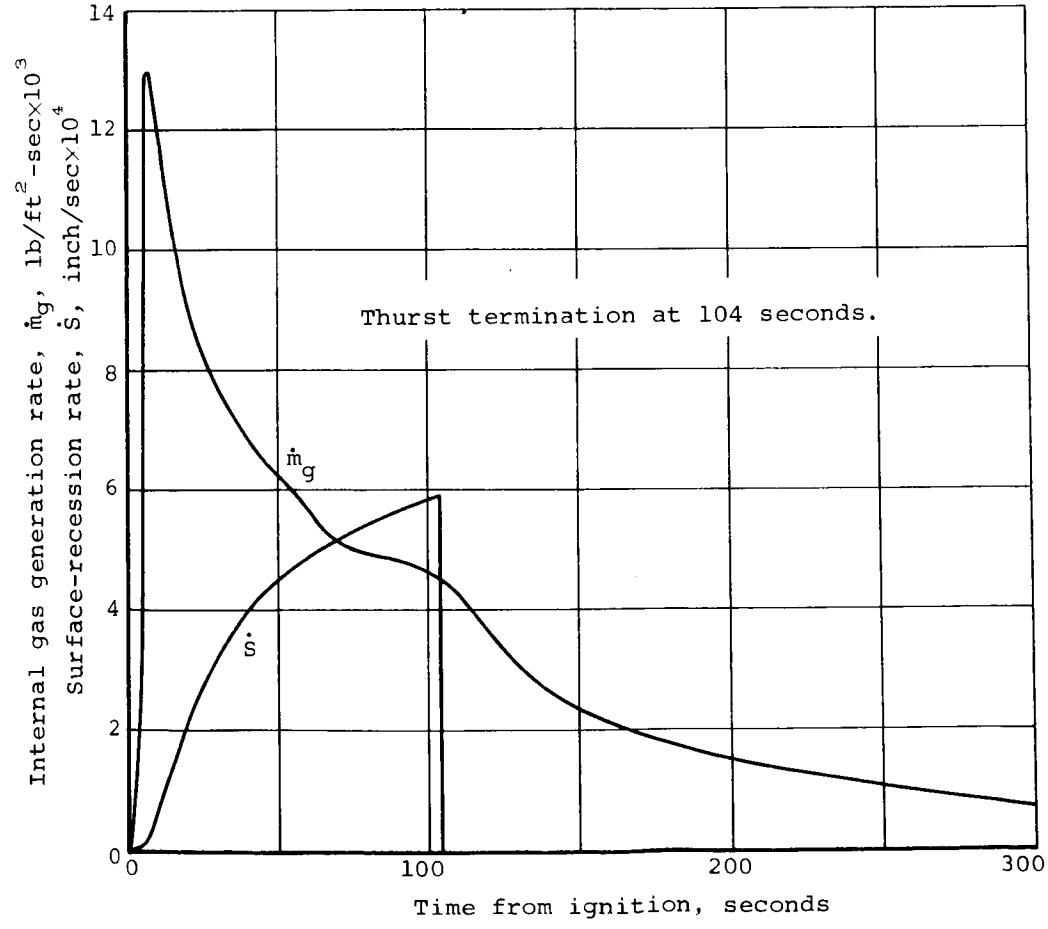


(b) Temperature distributions through the nozzle material for several times.

Figure 8.- Predicted transient thermochemical response of silica phenolic (67-33 percent by mass) nozzle throat in a N_2O_4-N_2H_4/UDMH rocket engine having a 7.8-inch throat diameter and chamber pressure of 100 psia.



(c) Density distributions through nozzle material at several times.



(d) Surface recession and gas generation rates.

Figure 8.- Concluded.

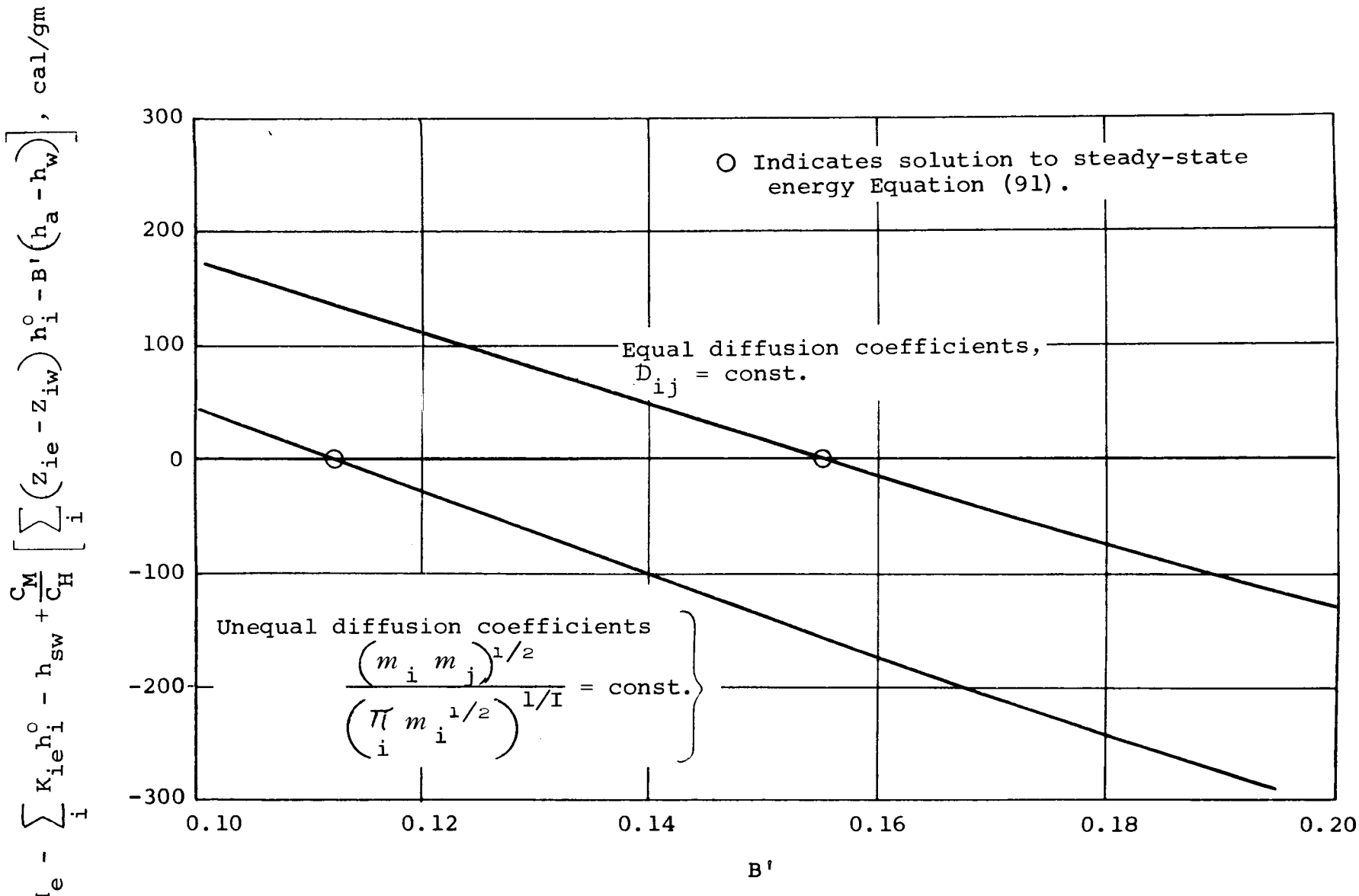


Figure 9.- Steady-state energy equation solution for silica-phenolic material in a N_2O_4-N_2H_4/UDMH environment, comparison of results with and without equal binary diffusion coefficient assumption.

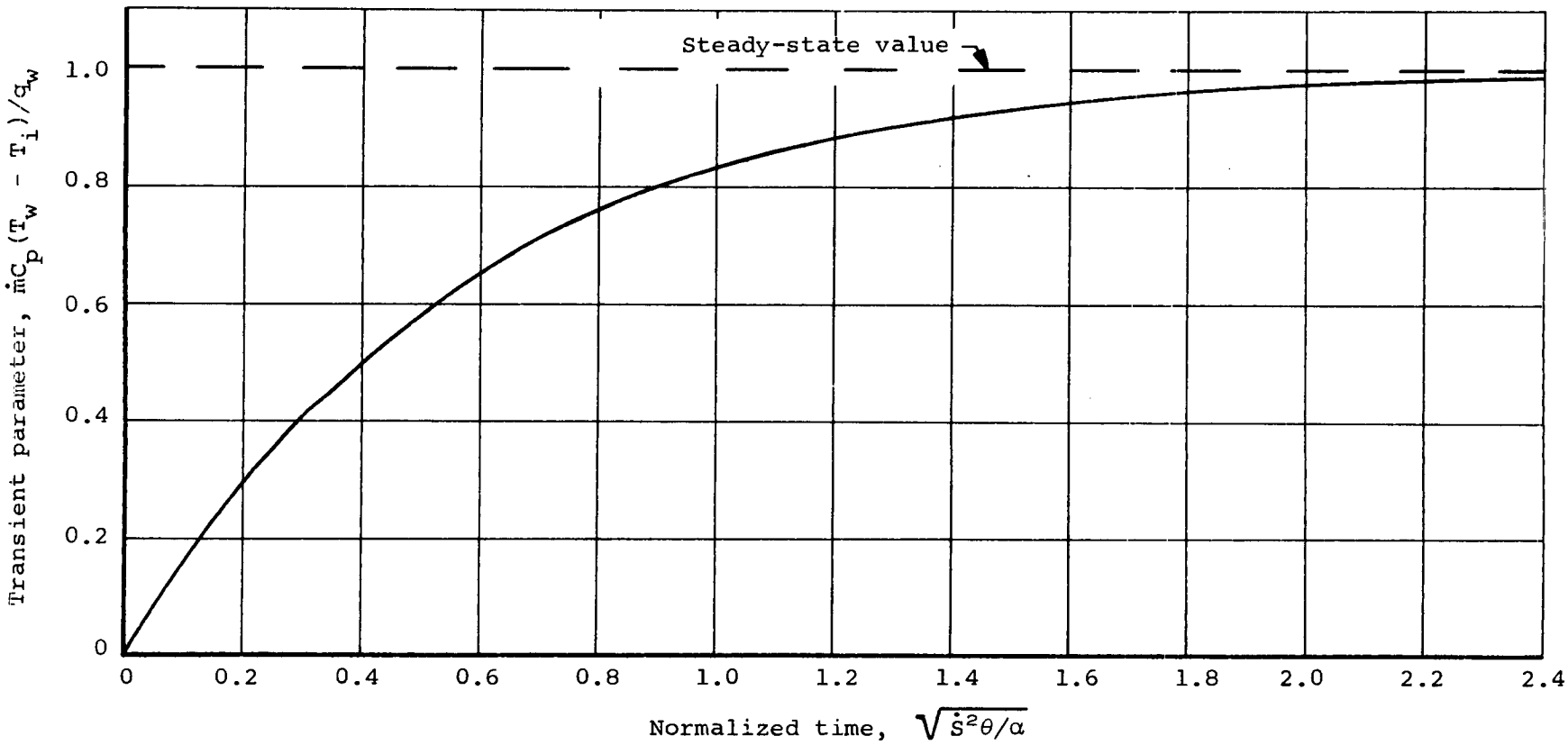


Figure 10.- Results of exact solution for transient response of slab subjected to step wall temperature rise and constant ablation rate at time zero (solution reported in Ref. 37).

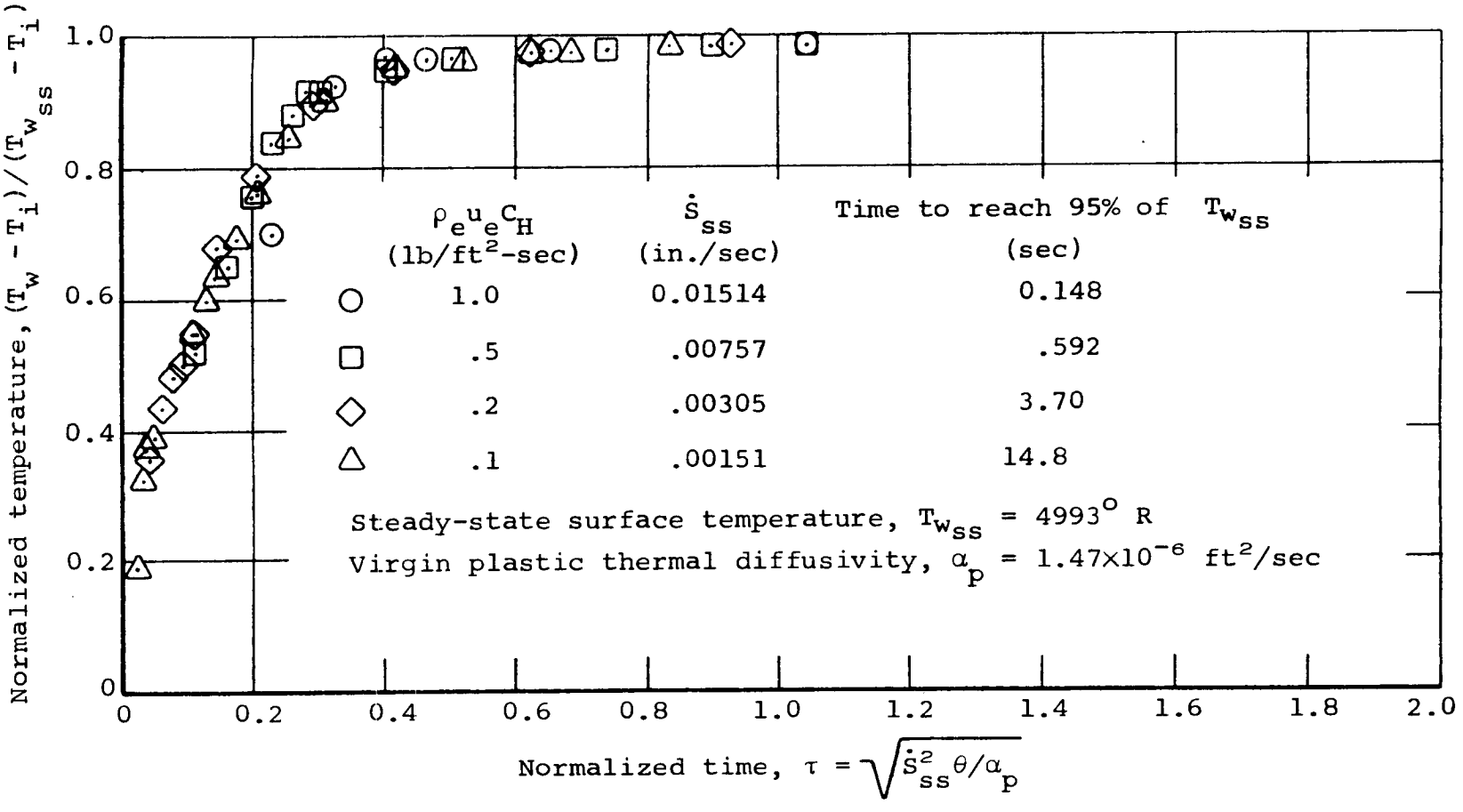


Figure 11.- Normalized surface temperature rise for transient ablation of silica phenolic (70-30) material in a N_2O_4-N_2H_4/UDMH environment, O/F = 2.0, pressure = 100 psia.

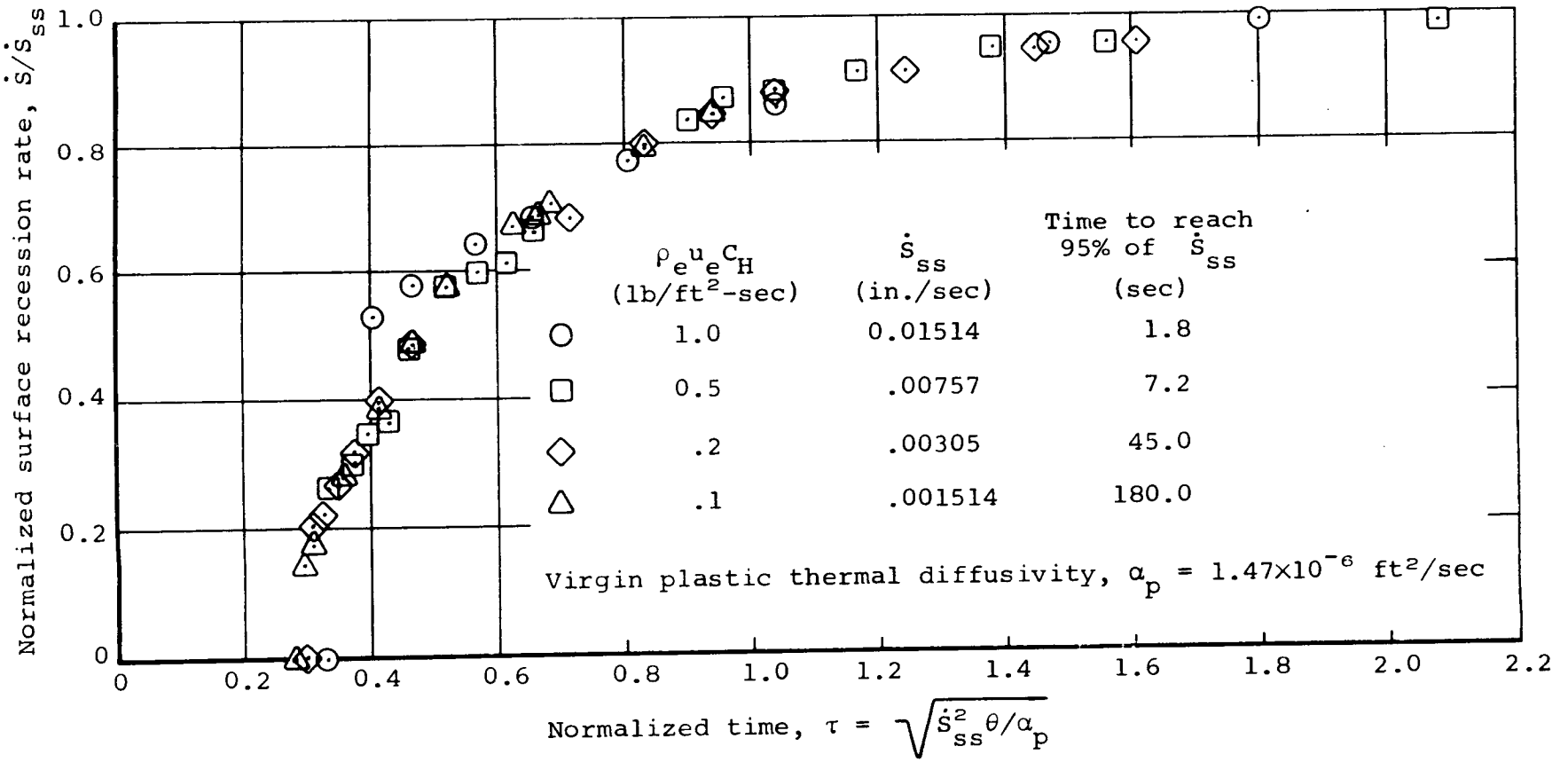
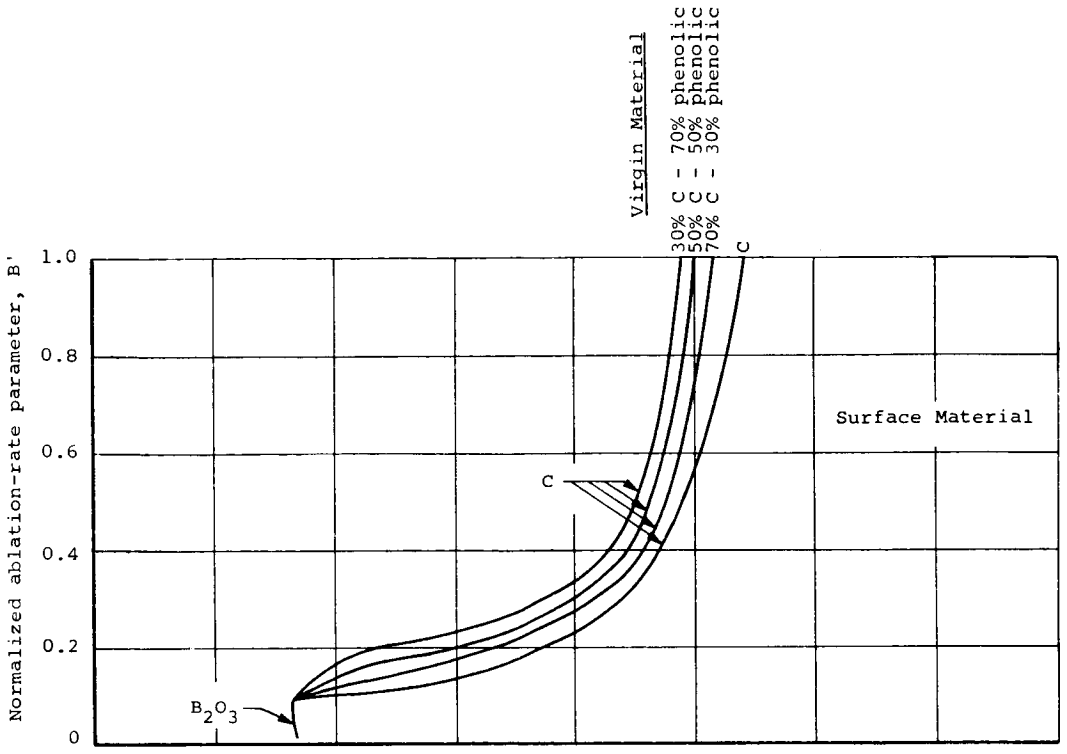
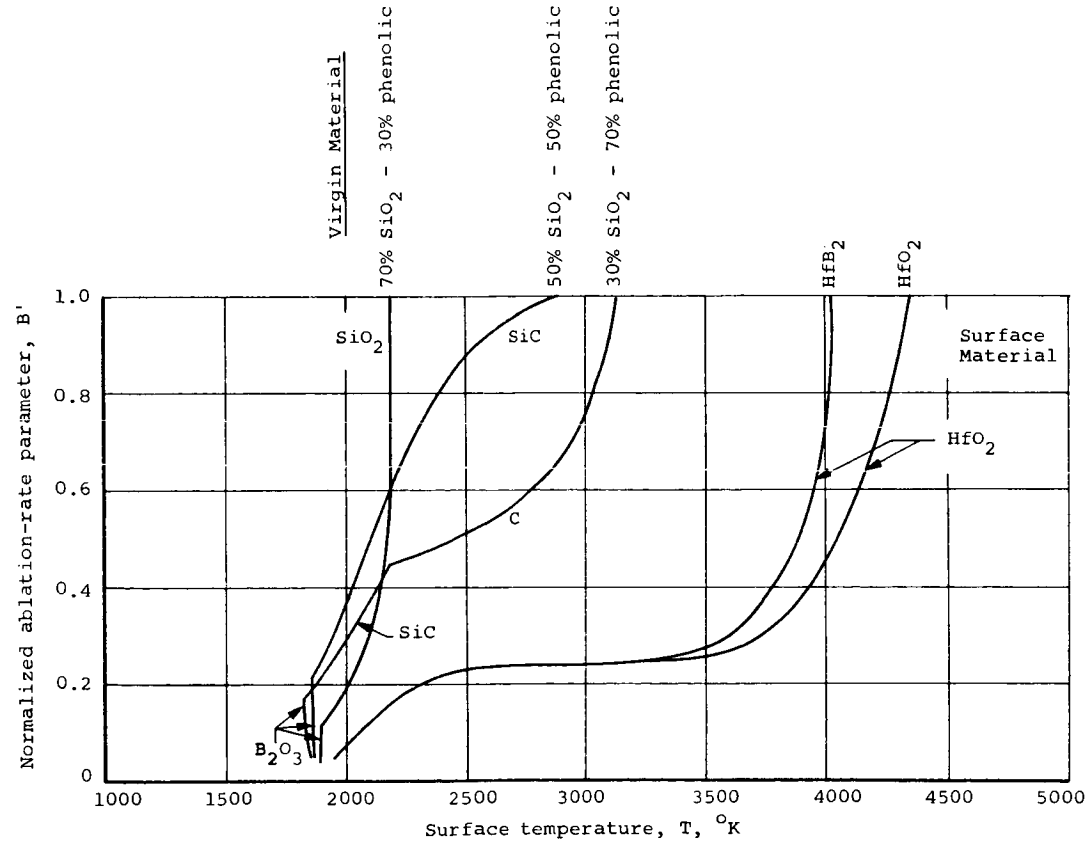


Figure 12.- Normalized surface-recession rate for transient ablation of silica phenolic (70-30) material in a N_2O_4-N_2H_4/UDMH environment, O/F = 2.0, pressure = 100 psia.

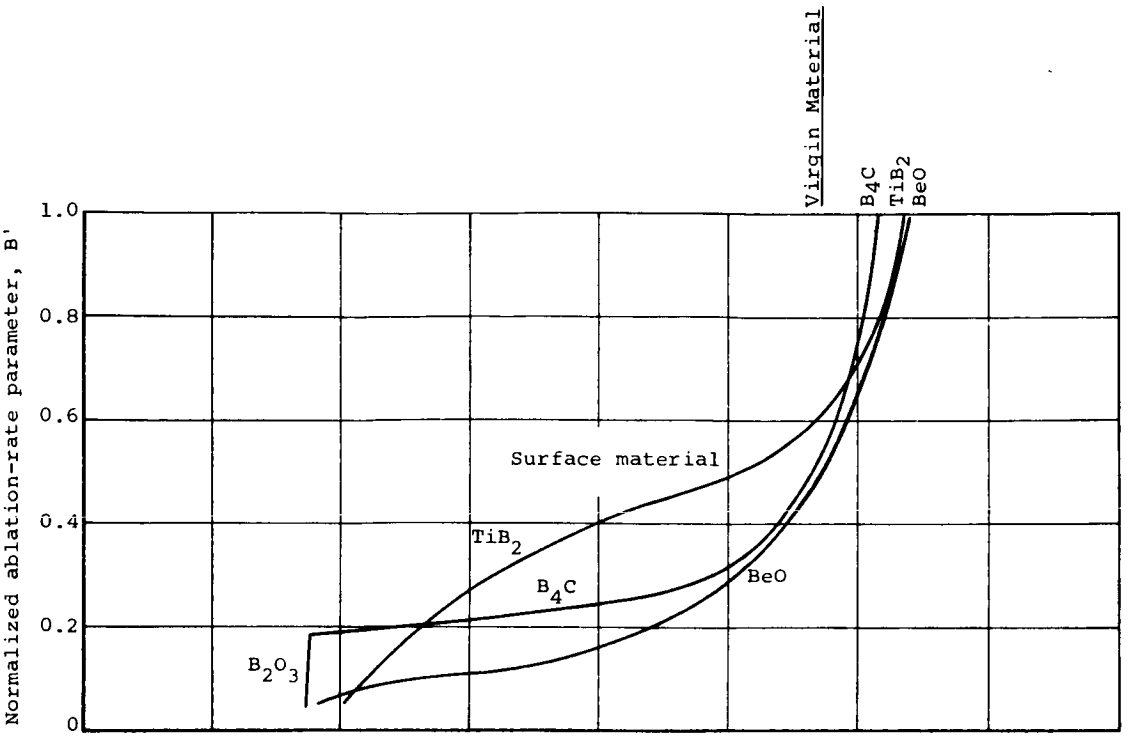


(a) Graphite and graphite phenolic.

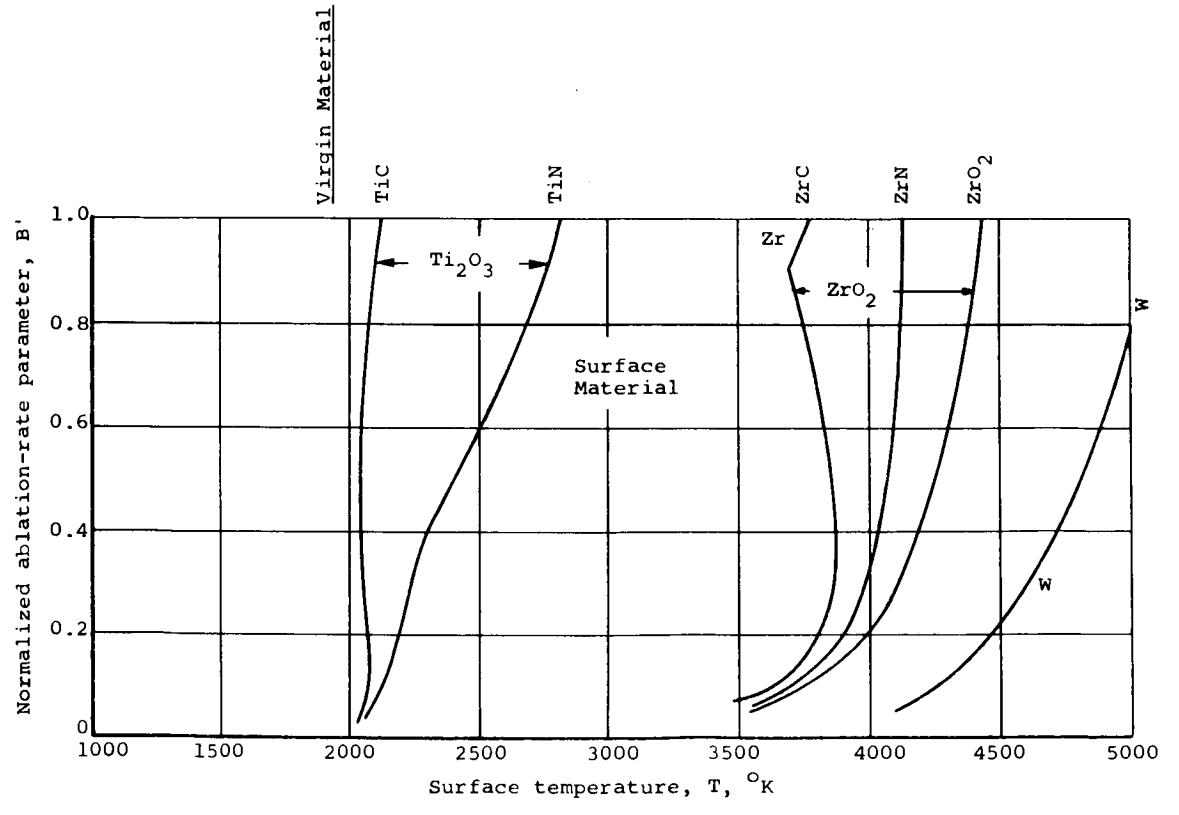


(b) HfB_2, HfO_2, and silica phenolic.

Figure 13.- Combined solution of species conservation equations and chemical equilibrium relations for OF_2-B_2H_6 propellant, O/F = 3.0, pressure = 100 psia.

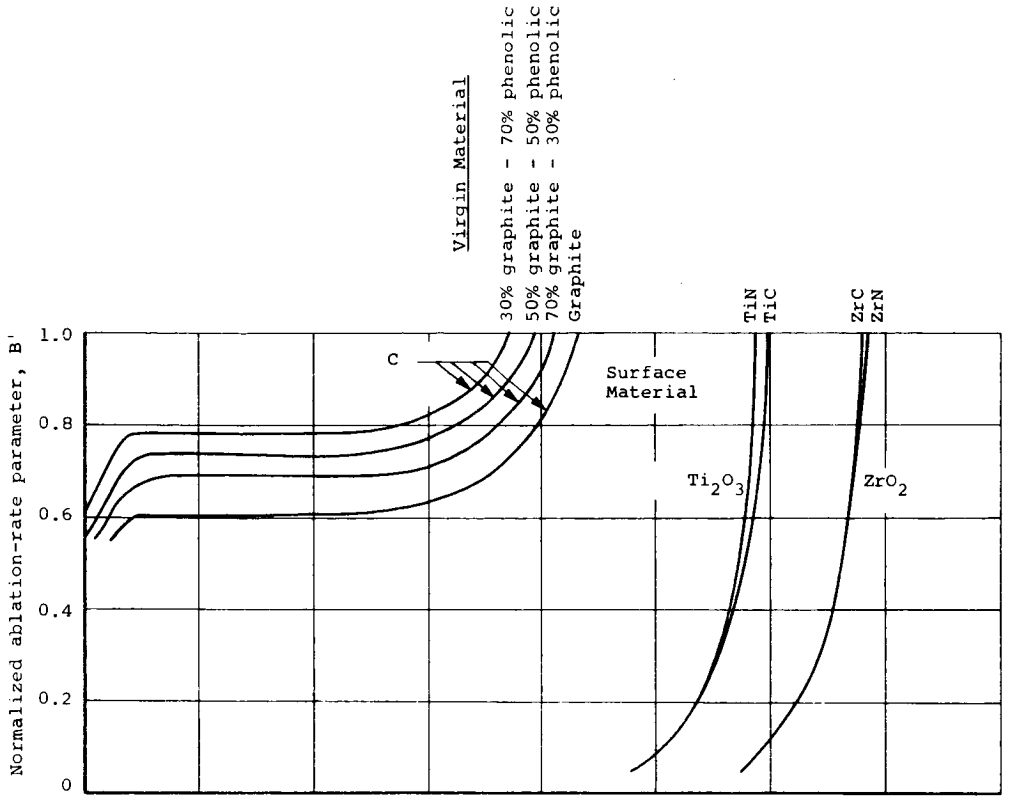


(c) B_4C, TiB_2, and BeO.

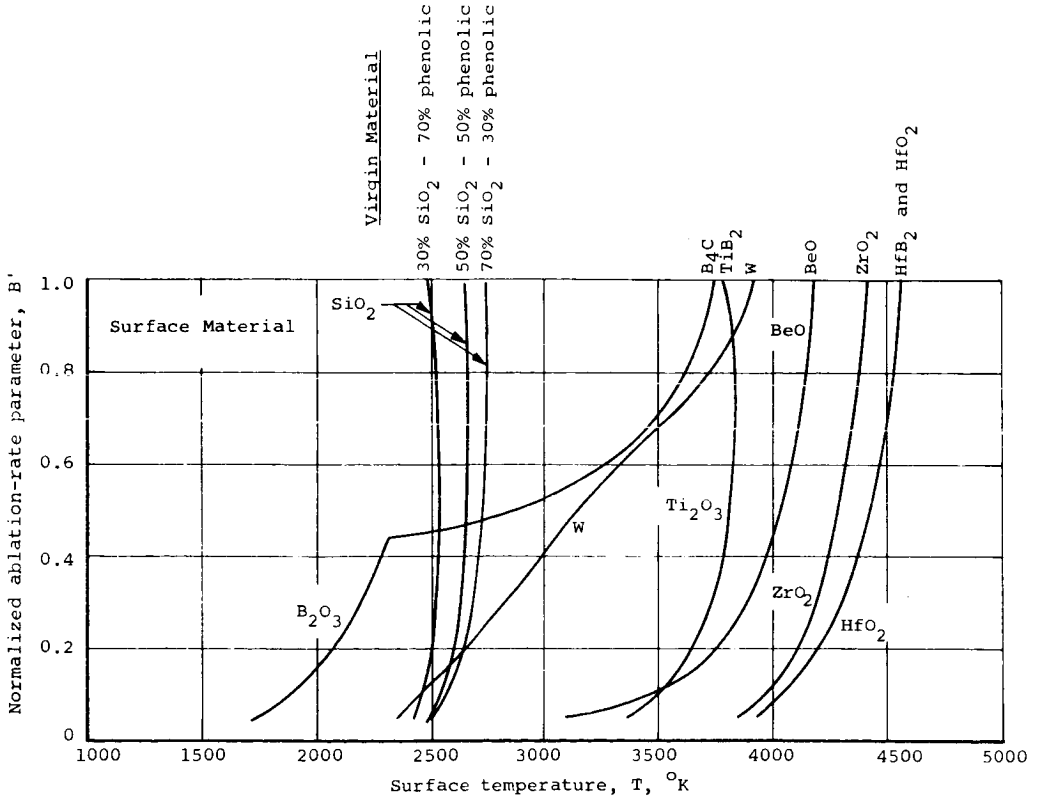


(d) TiC, TiN, ZrC, ZrN, ZrO_2, and W.

Figure 13.- Concluded.

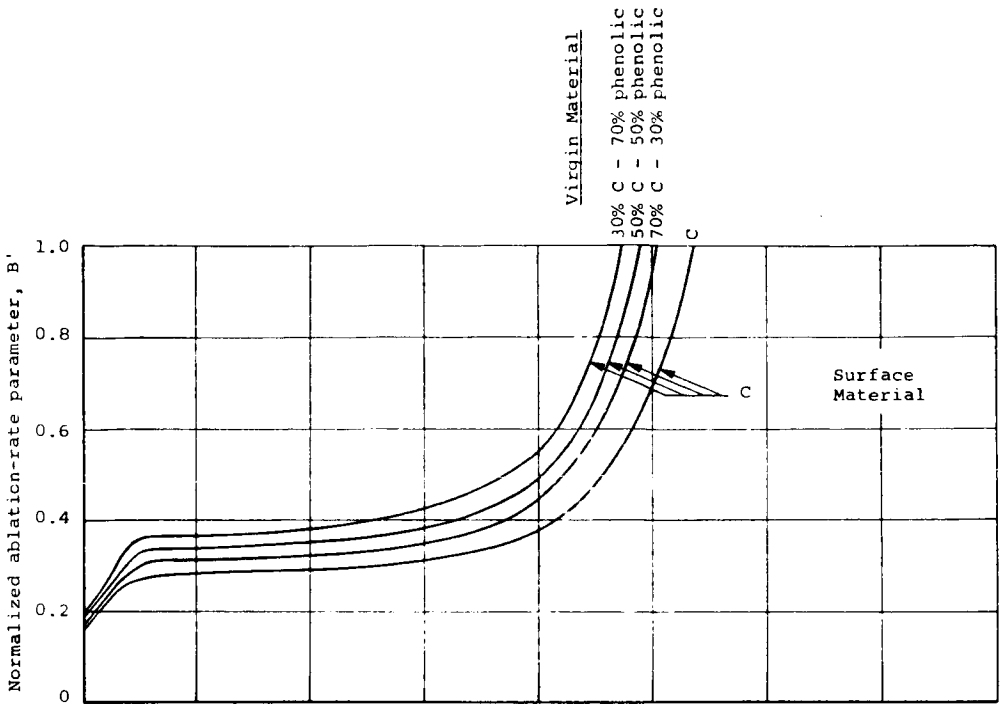


(a) Graphite, graphite phenolic, TiC, TiN, ZrC, and ZrN.

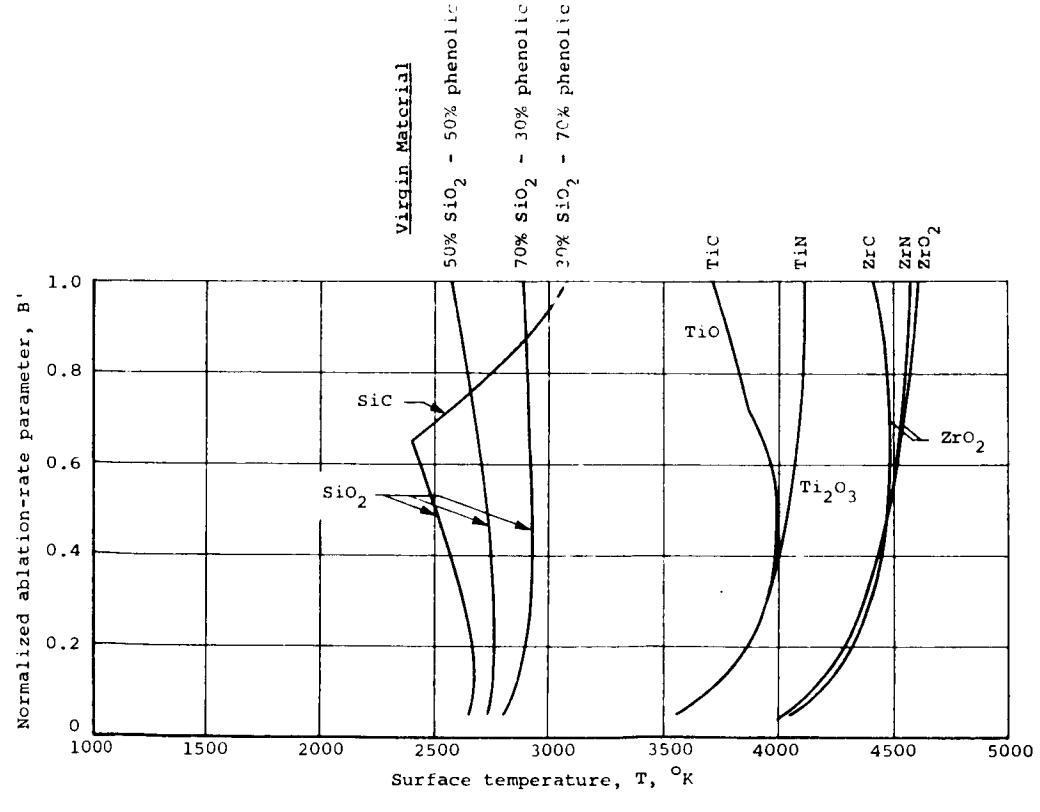


(b) Silica phenolic, B_4C, TiB_2, W, BeO, ZrO_2, and HfB_2.

Figure 14.- Combined solution of species conservation equations and chemical equilibrium relations for O_2-H_2 propellant, O/F = 4.0, pressure = 100 psia.

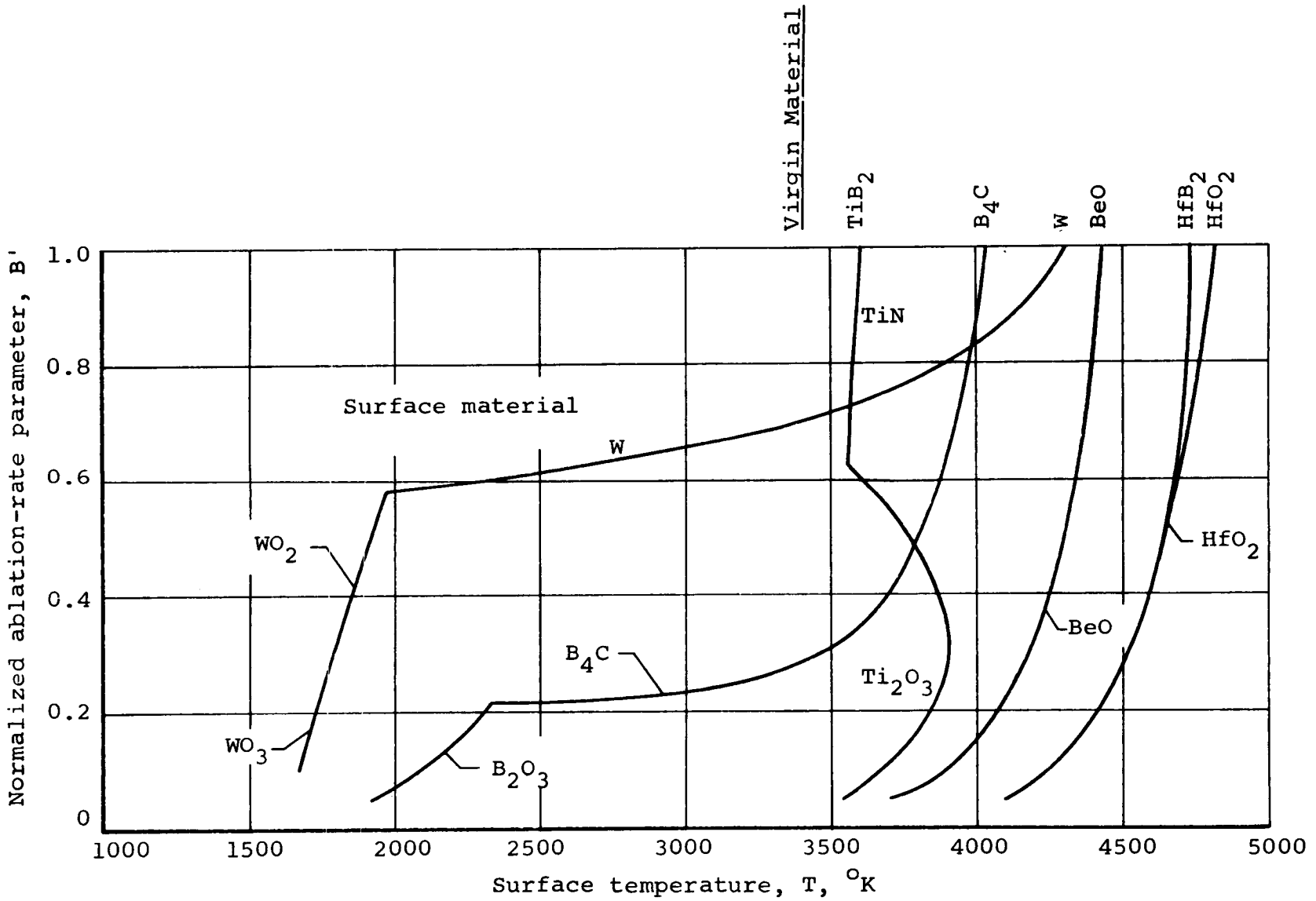


(a) Graphite and graphite phenolic.



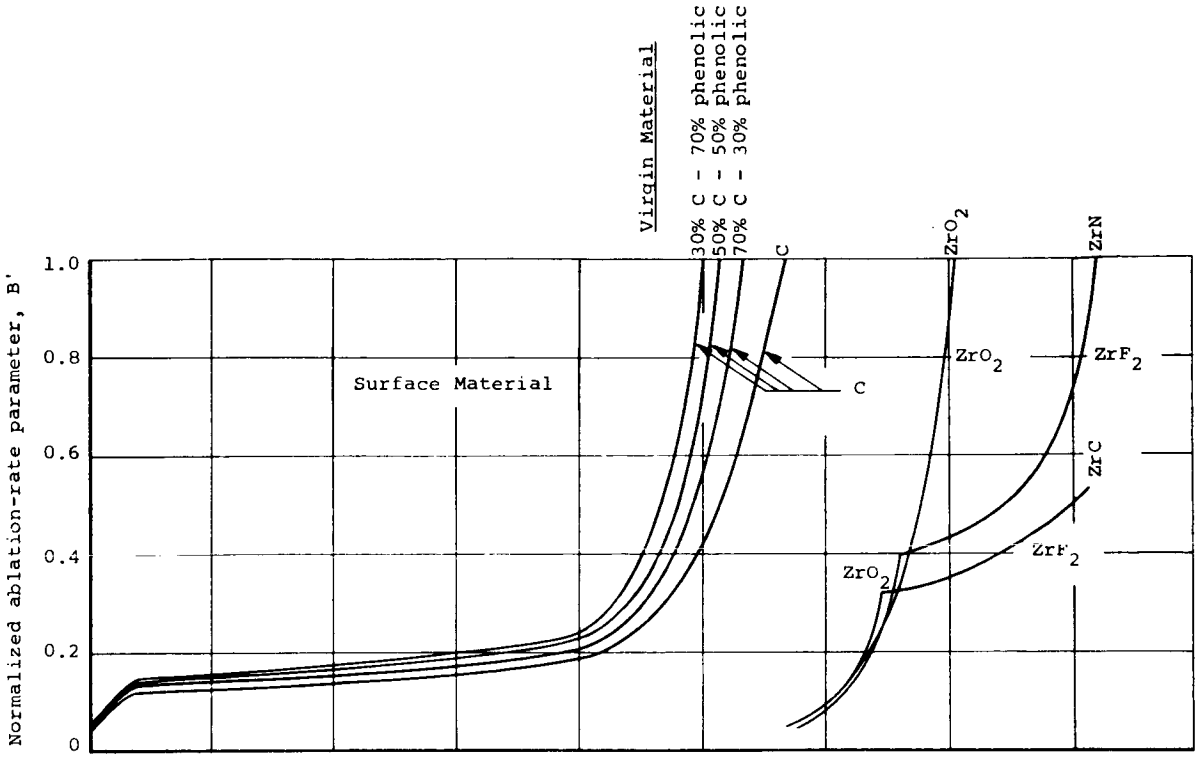
(b) Silica phenolic, TiC, TiN, ZrC, ZrN, and ZrO_2.

Figure 15.- Combined solution of species conservation equations and chemical equilibrium relations for N_2O_4-N_2H_4/UDMH propellant, O/F = 2.0, pressure = 100 psia.

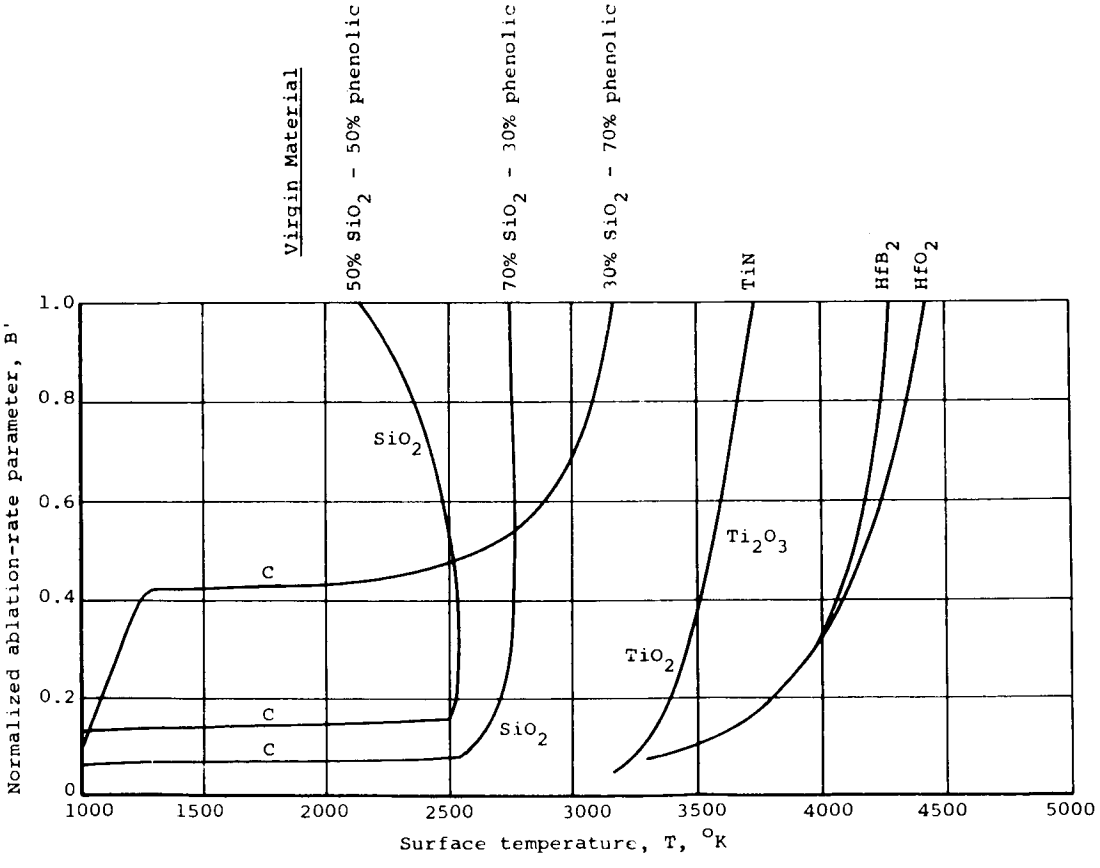


(c) TiB_2, B_4C, W, BeO, HfB_2, and HfO_2.

Figure 15.- Concluded.

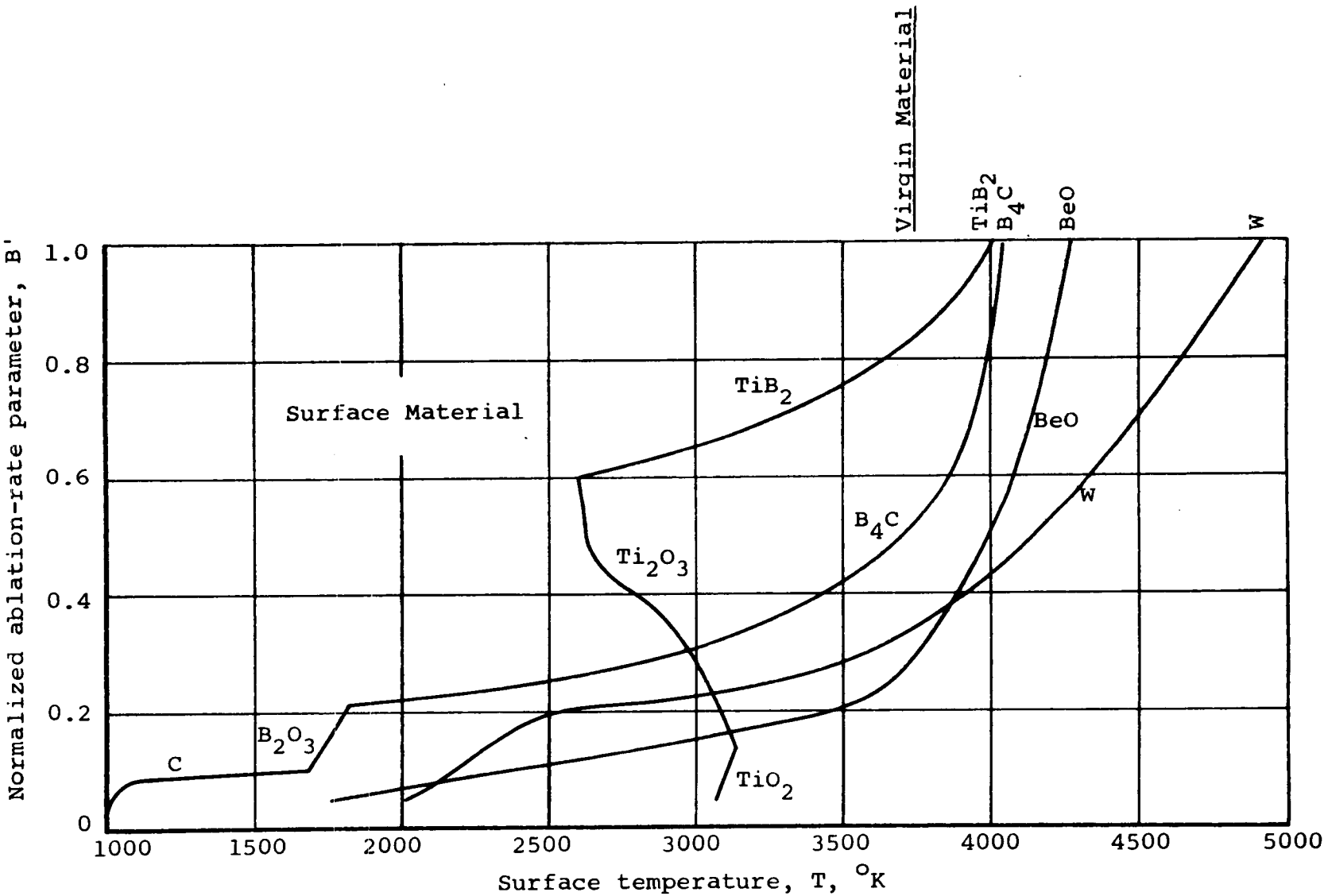


(a) Graphite, graphite phenolic, ZrO_2, ZrN, and ZrC.



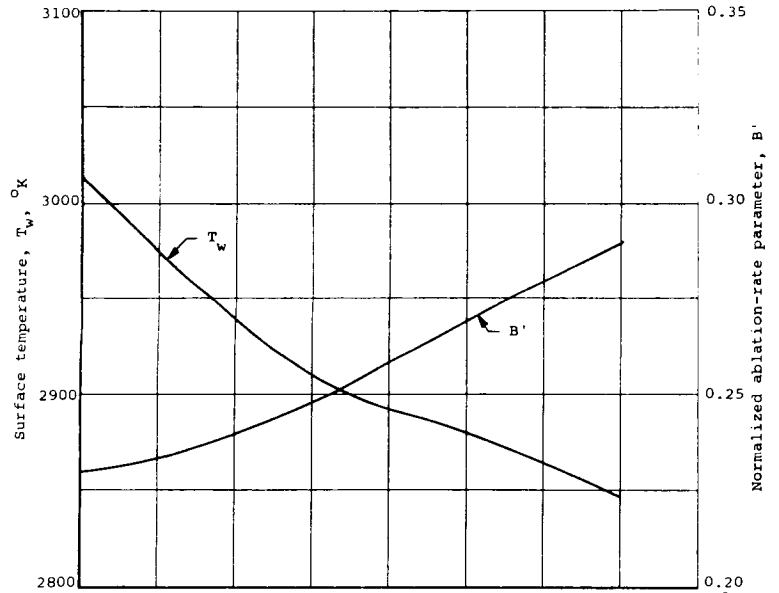
(b) Silica phenolic, TiN, HfB_2, and HfO_2.

Figure 16.- Combined solution of species conservation equations and chemical equilibrium relations for Flox-Methane propellant, O/F = 4.0, pressure = 100 psia.

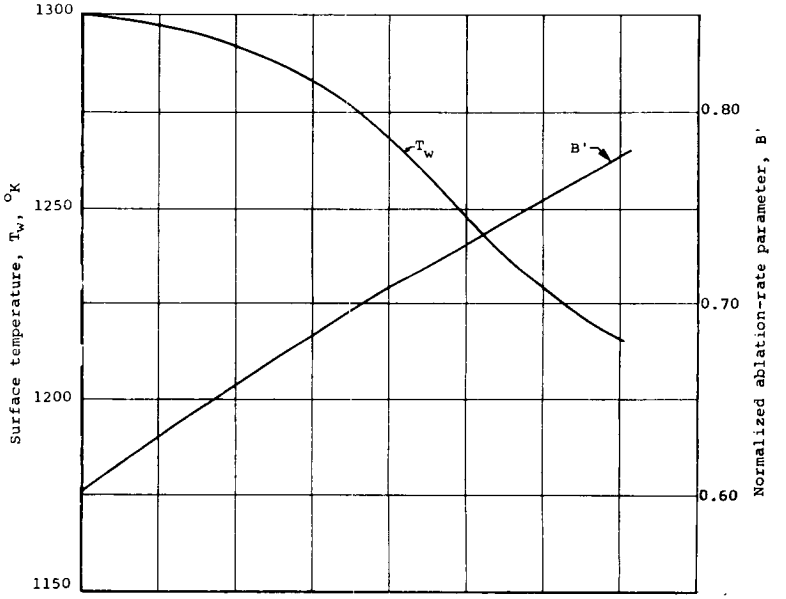


(c) TiB_2, B_4C, BeO, and W.

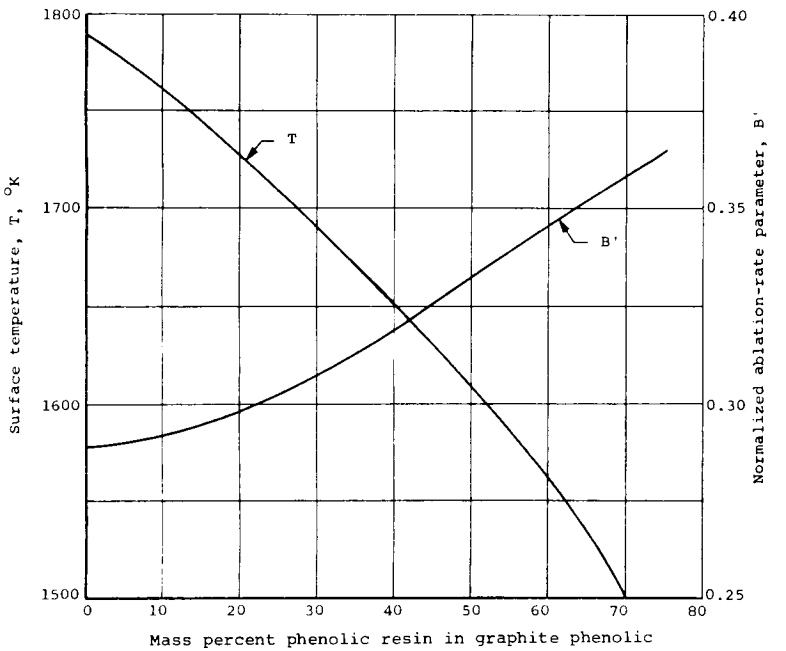
Figure 16.- Concluded.



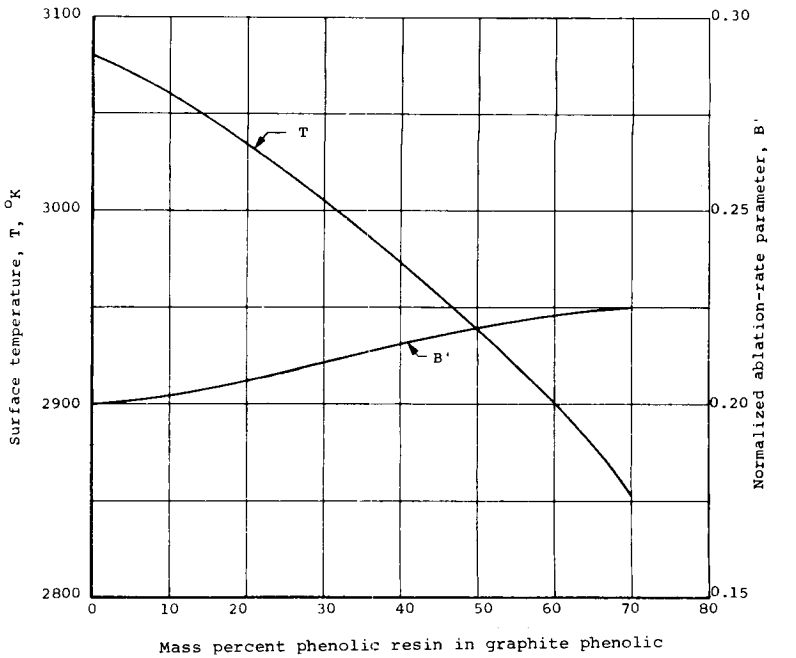
(a) OF_2-B_2H_6 environment, O/F = 3.0, pressure = 100 psia.



(b) O_2-H_2 environment, O/F = 4.0, pressure = 100 psia.



(c) N_2O_4-N_2H_4/UDMH environment, O/F = 2.0, pressure = 100 psia.



(d) Flox-Methane environment, O/F = 4.0, pressure = 100 psia.

Figure 17.- Steady-state energy equation solution for B' and T_w for graphite phenolic material as a function of phenolic content.

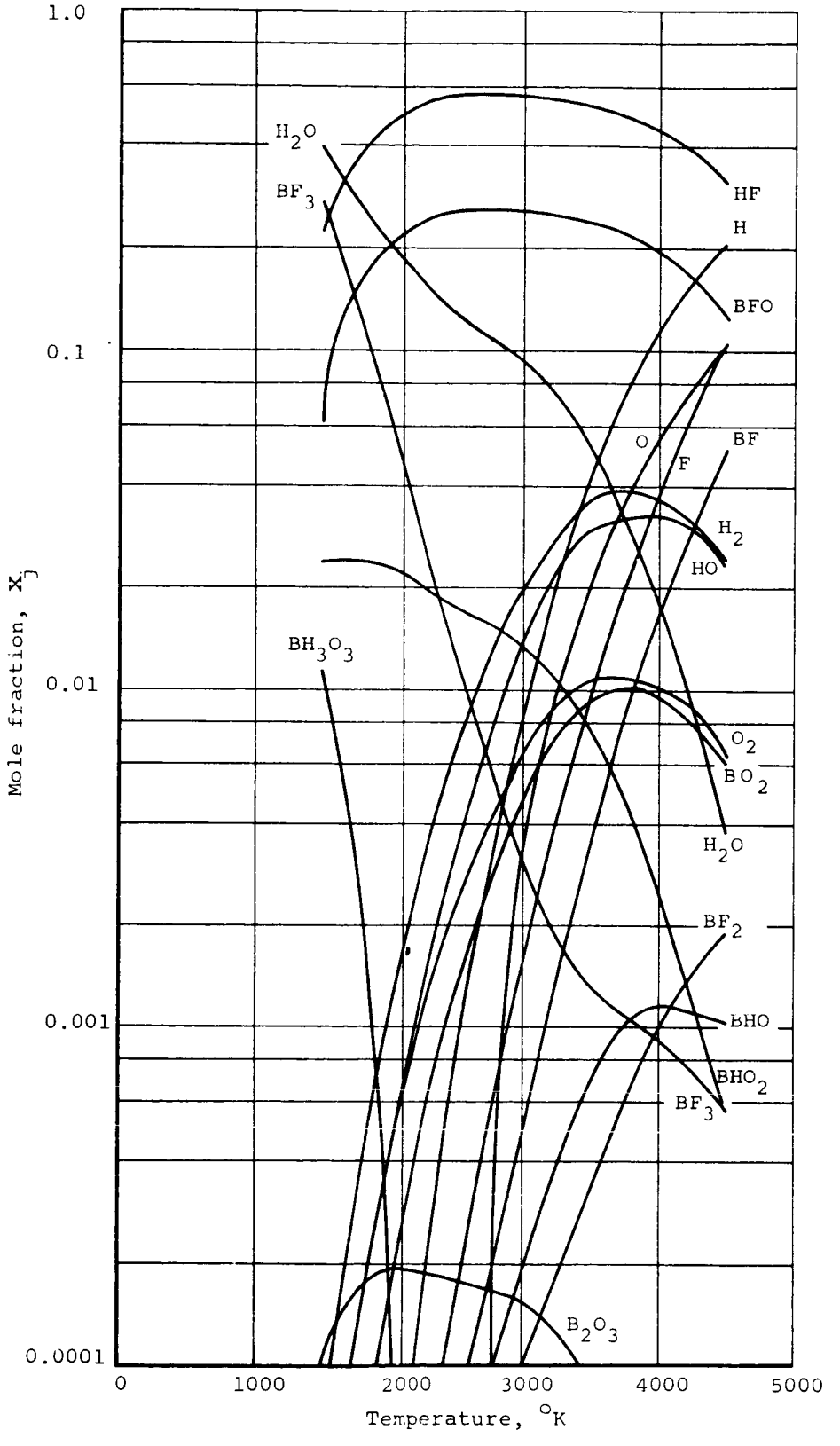


Figure 18.- Equilibrium composition of products of combustion of OF_2-B_2H_6, O/F = 5.85, pressure = 100 psia.

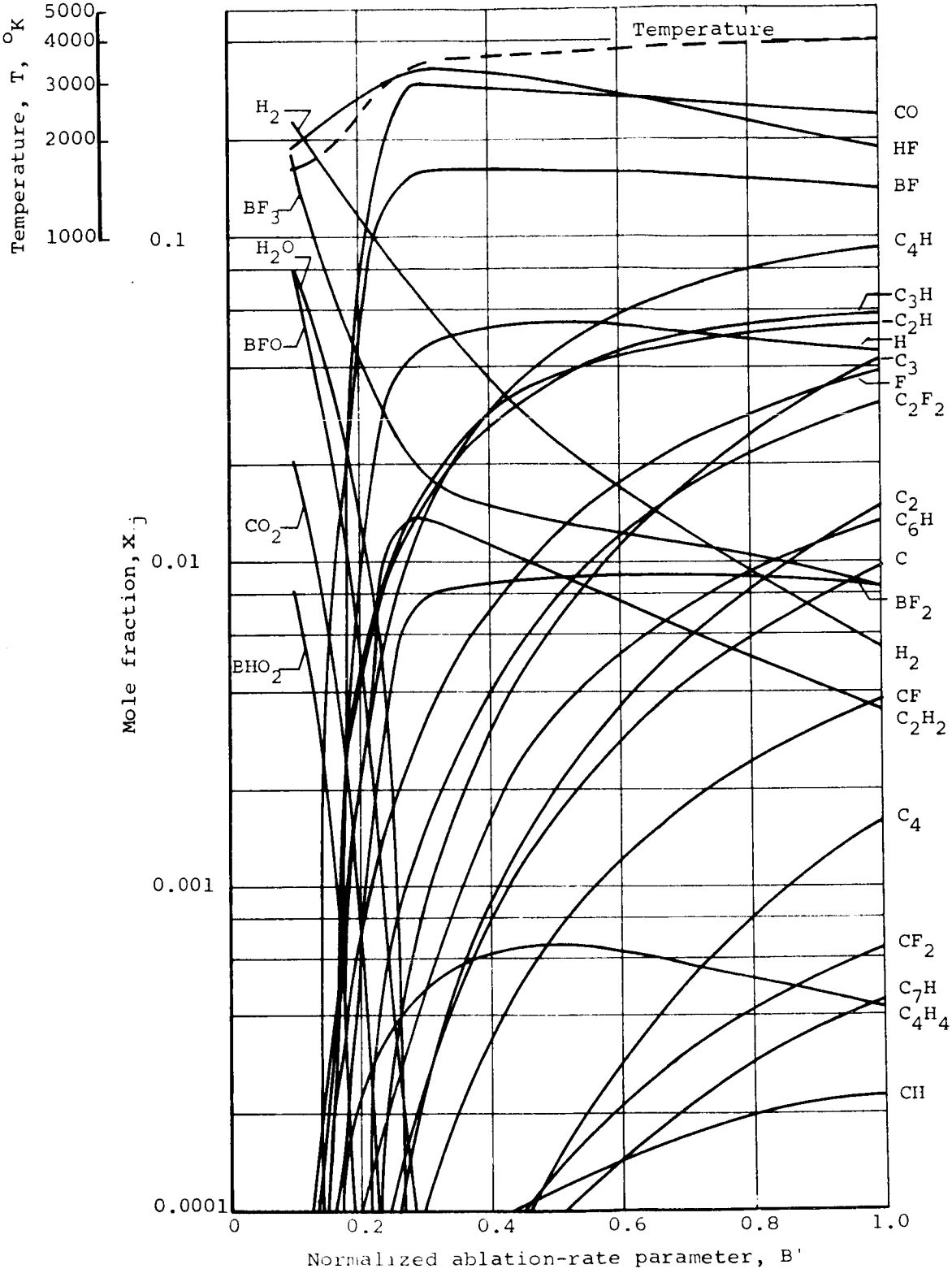


Figure 19.- Equilibrium composition and temperature of products resulting from reactions between OF_2-B_2H_6 and graphite in equilibrium with the graphite surface, O/F = 5.85, pressure = 100 psia.

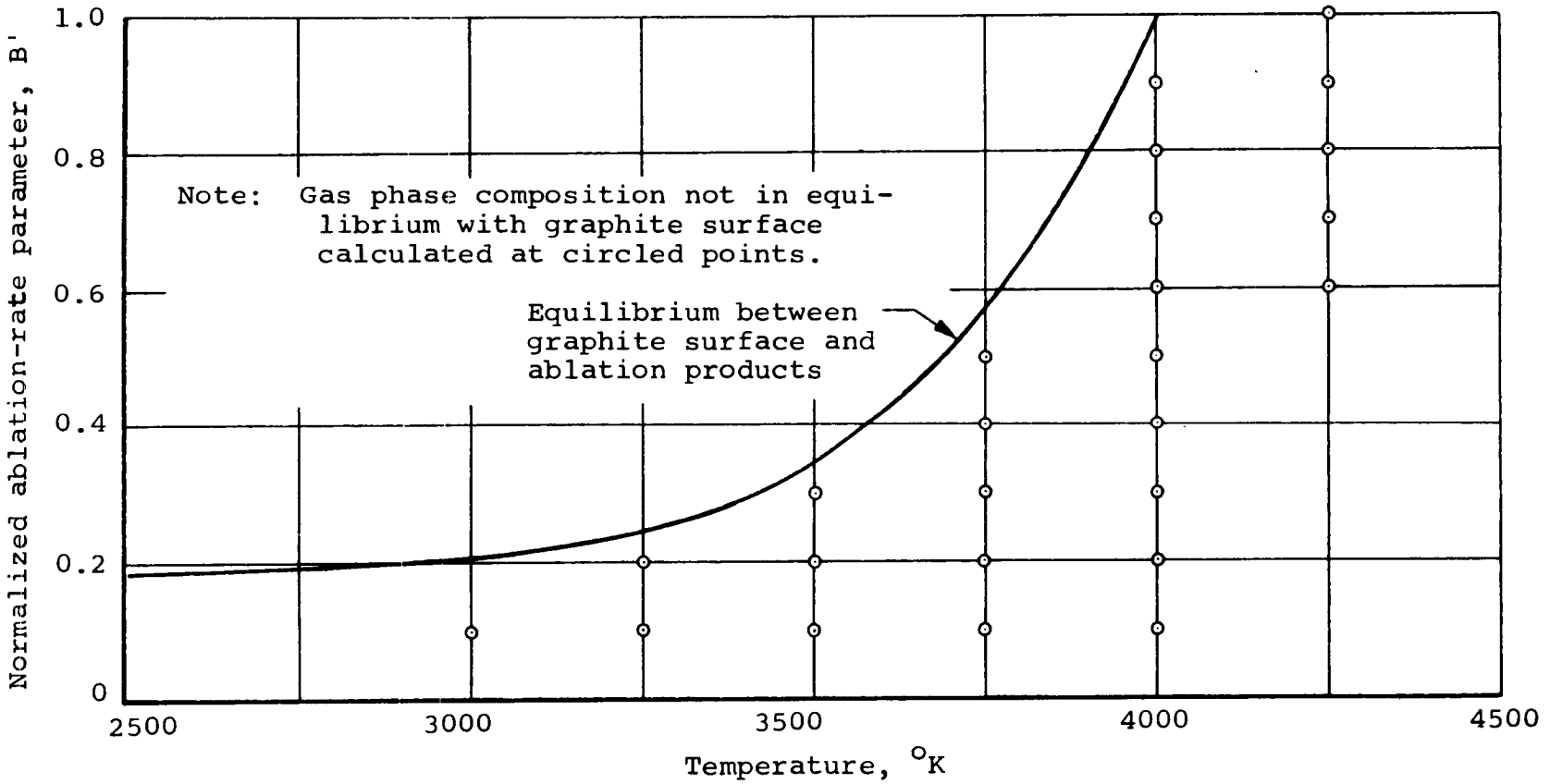
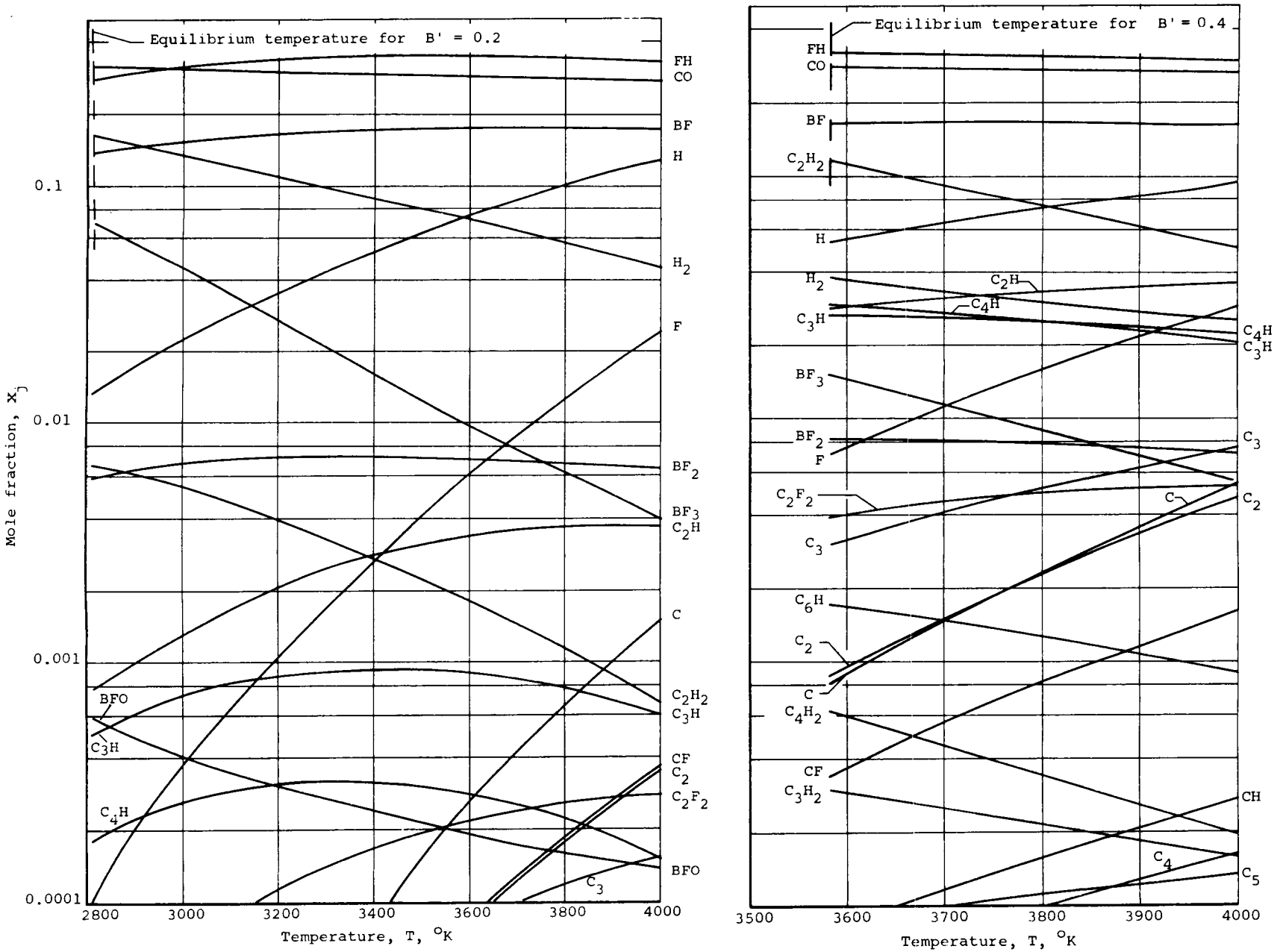


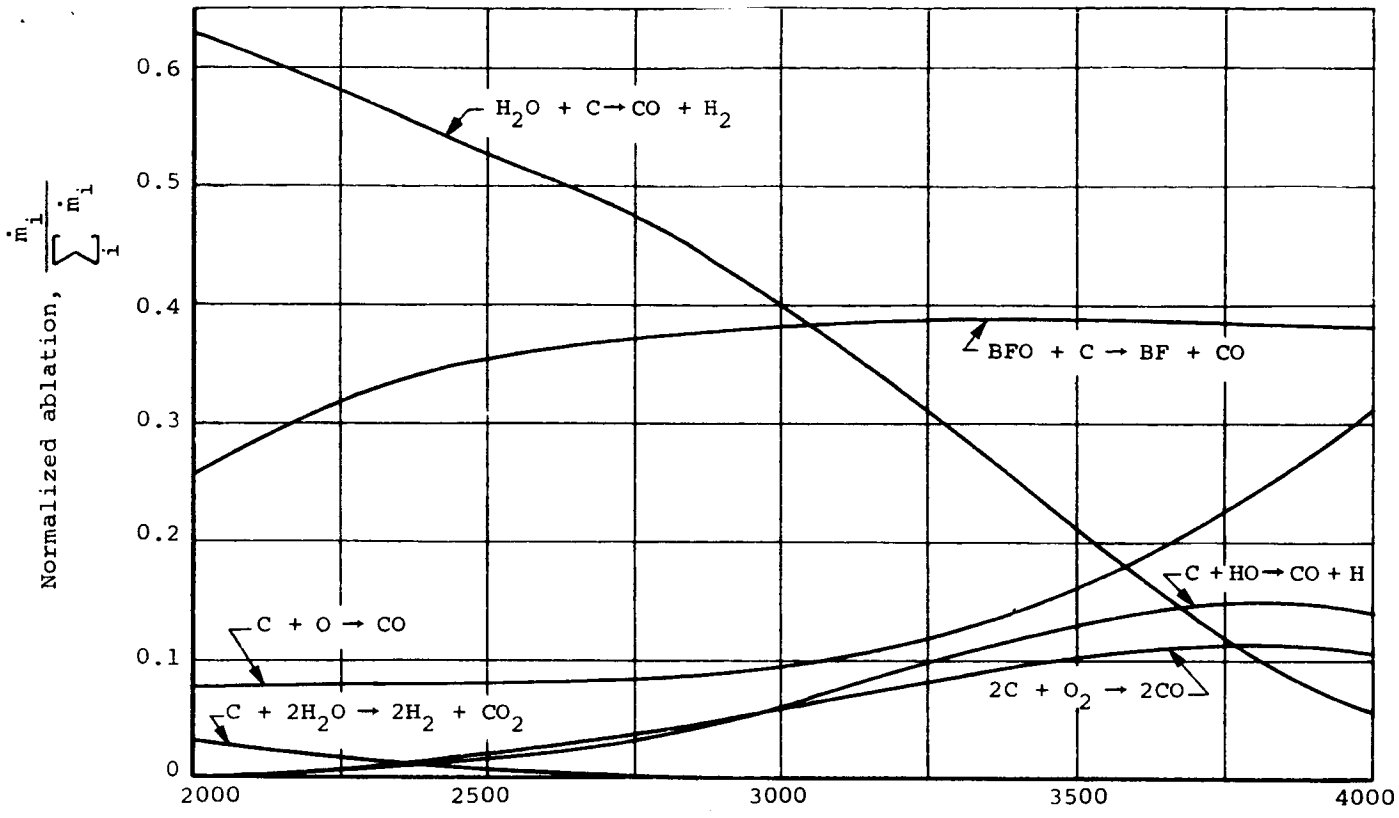
Figure 20.- Equilibrium ablation rate, B', as a function of temperature for graphite in the OF_2- B_2H_6 environment, O/F = 5.85, pressure = 100 psia.



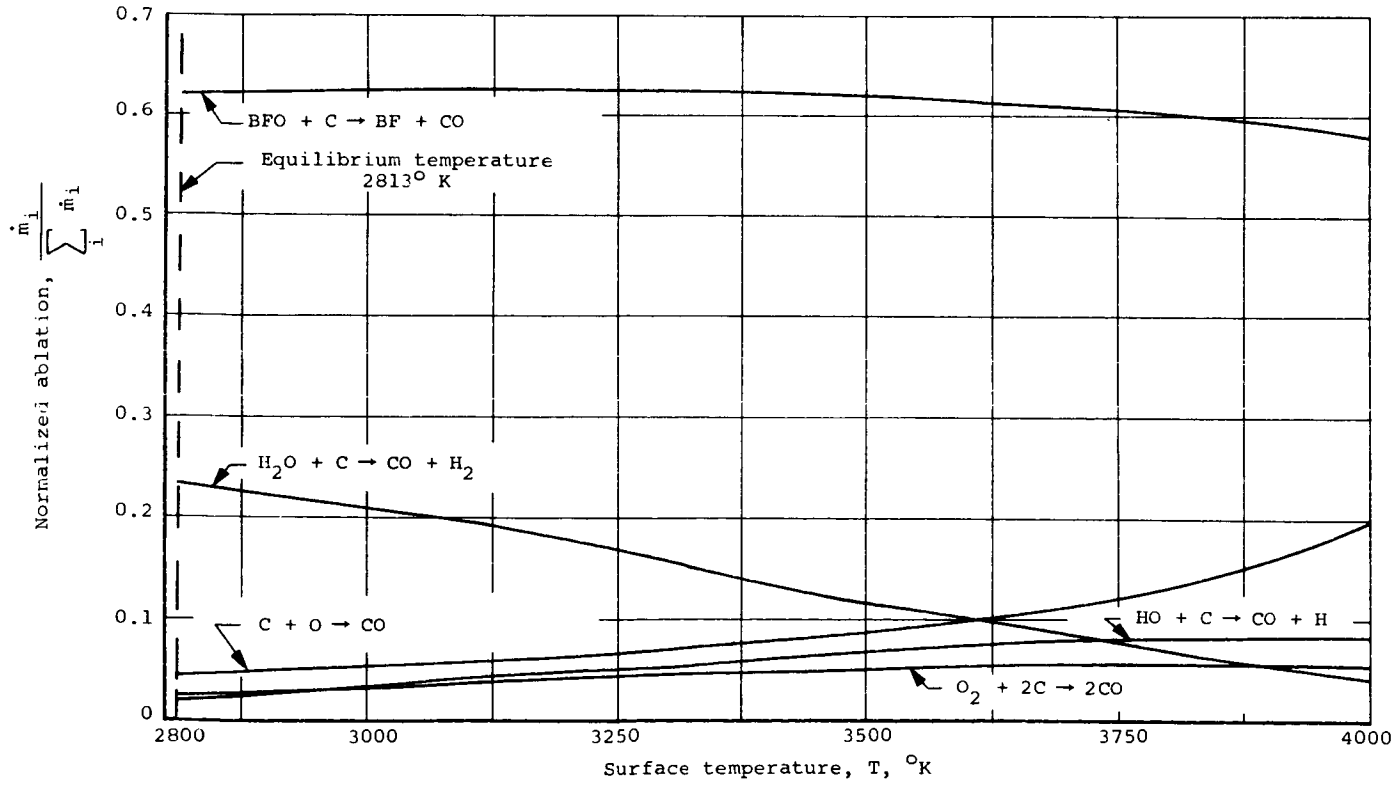
(a) B' = 0.2.

(b) B' = 0.4.

Figure 21.- Gas-phase composition for ablation of graphite in OF_2-B_2H_6, O/F = 5.85, pressure = 100 psia.

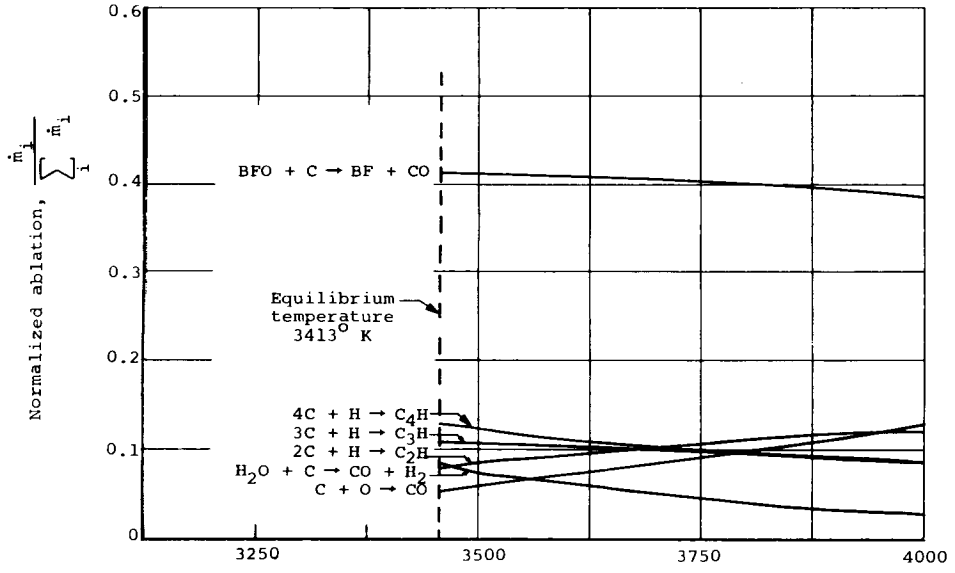


(a) B' = 0.1.

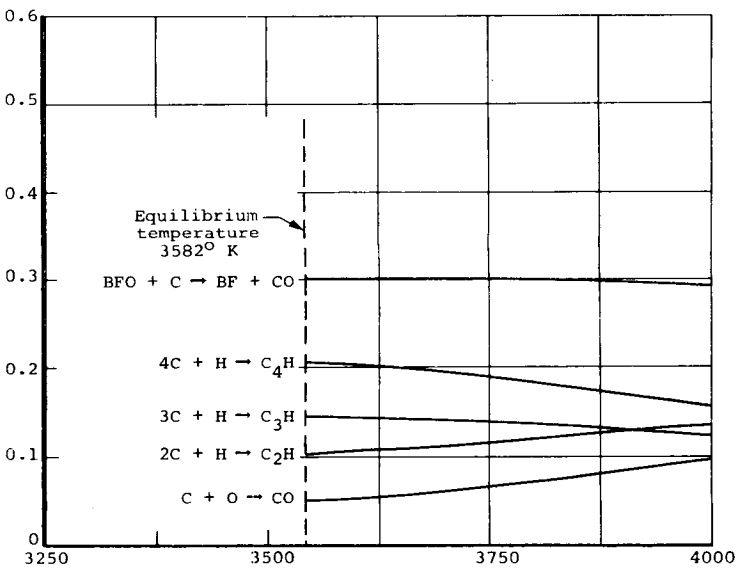


(b) B' = 0.2.

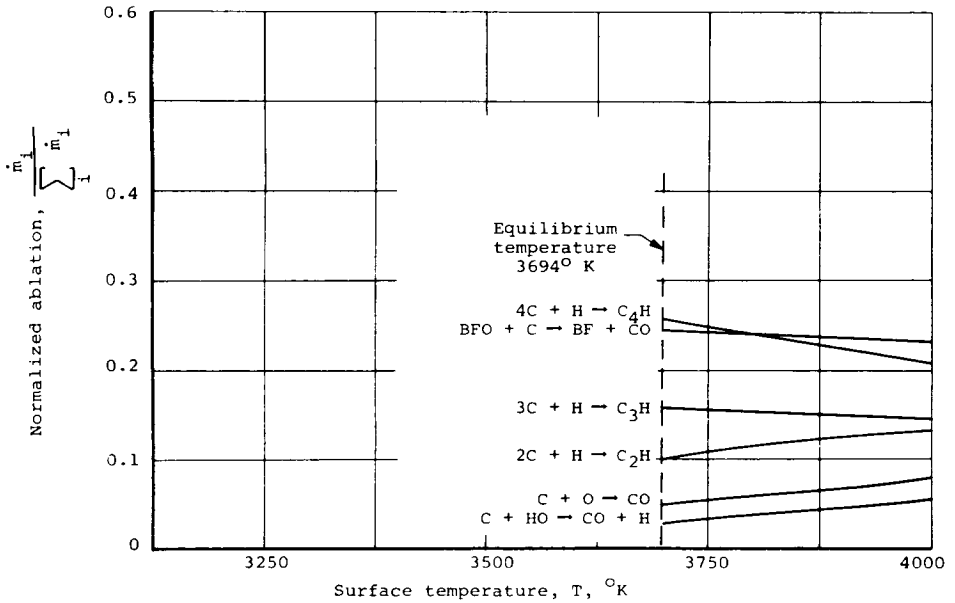
Figure 22.- Importance of various reactions for ablation of graphite in the OF_2- B_2H_6 environment as determined from gas phase equilibrium considerations, O/F = 5.85, pressure = 100 psia.



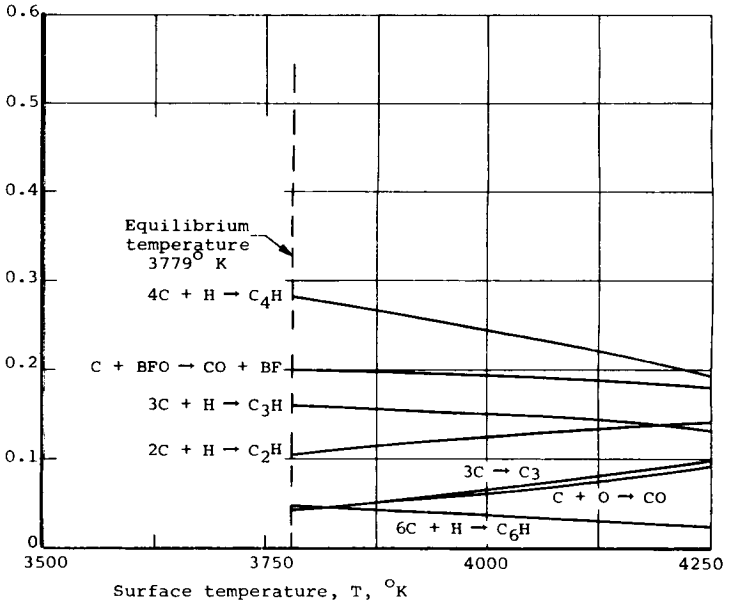
(c) B' = 0.3.



(d) B' = 0.4.



(e) B' = 0.5.



(f) B' = 0.6.

Figure 22.- Continued.

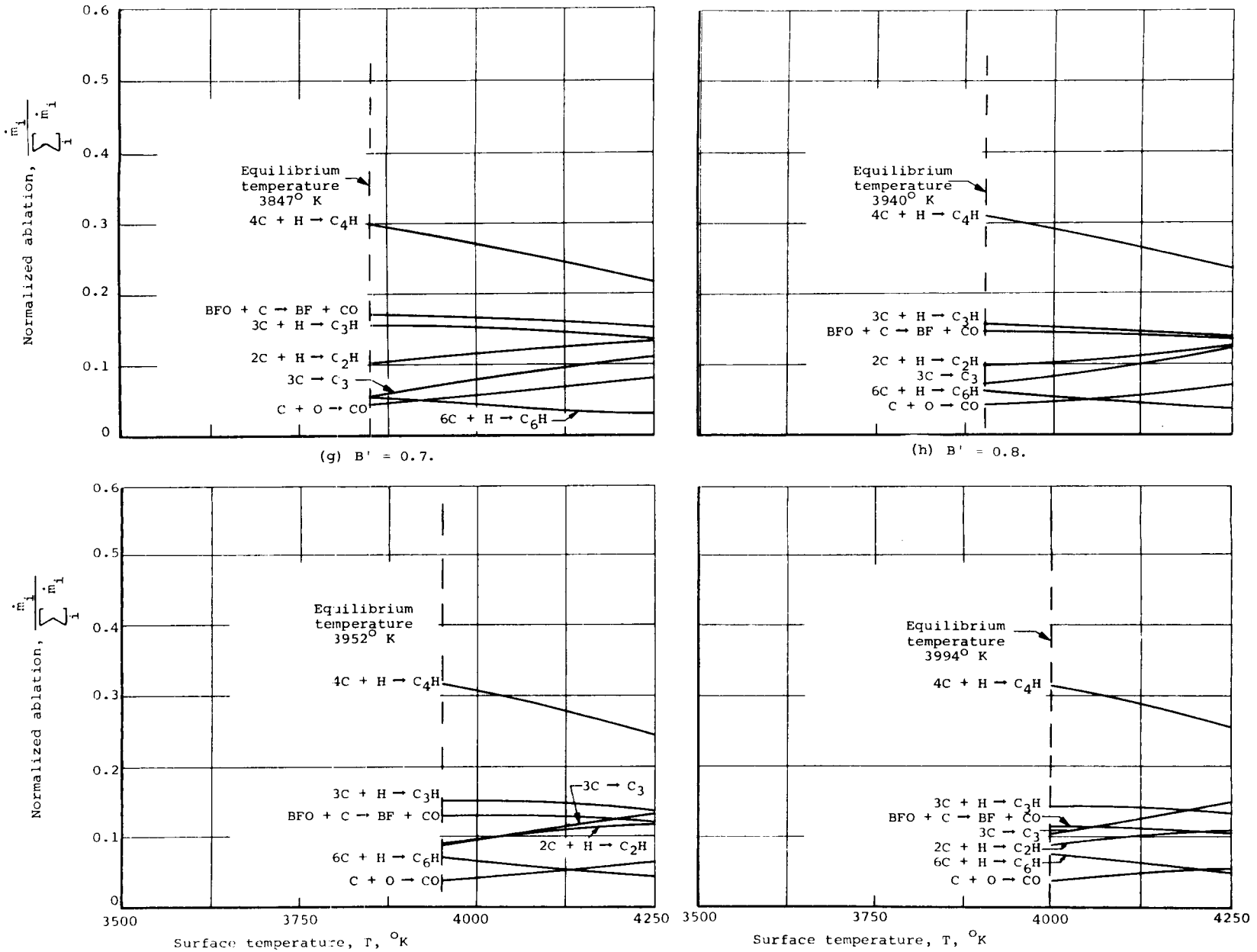
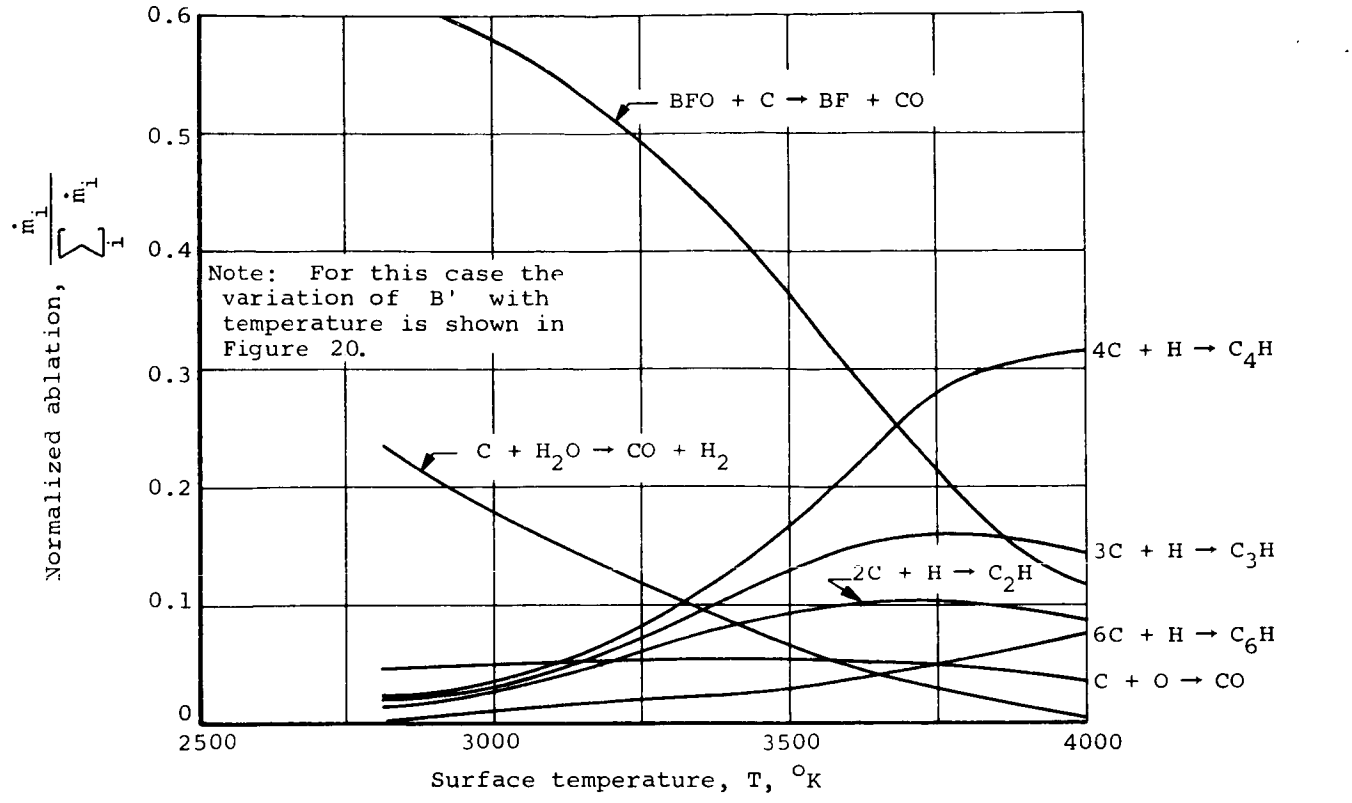
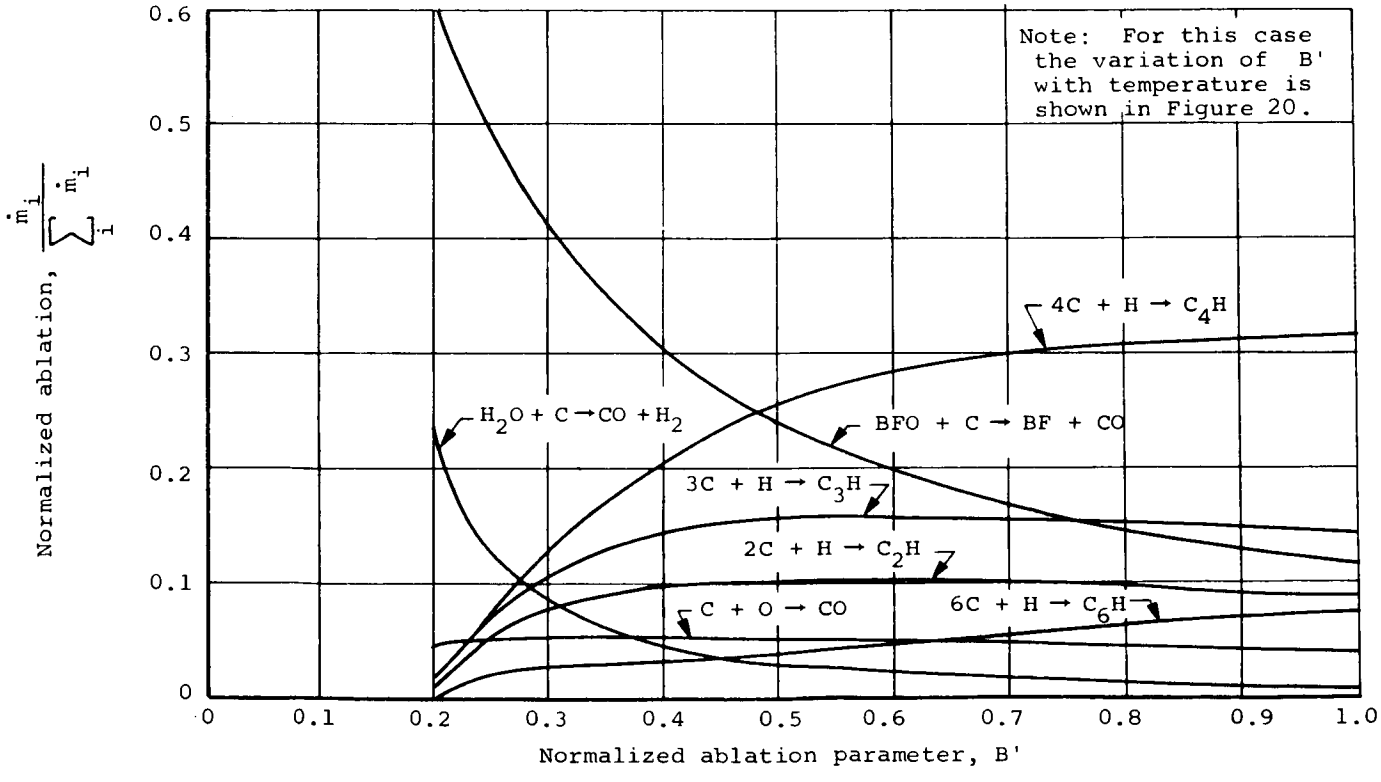


Figure 22.- Concluded.

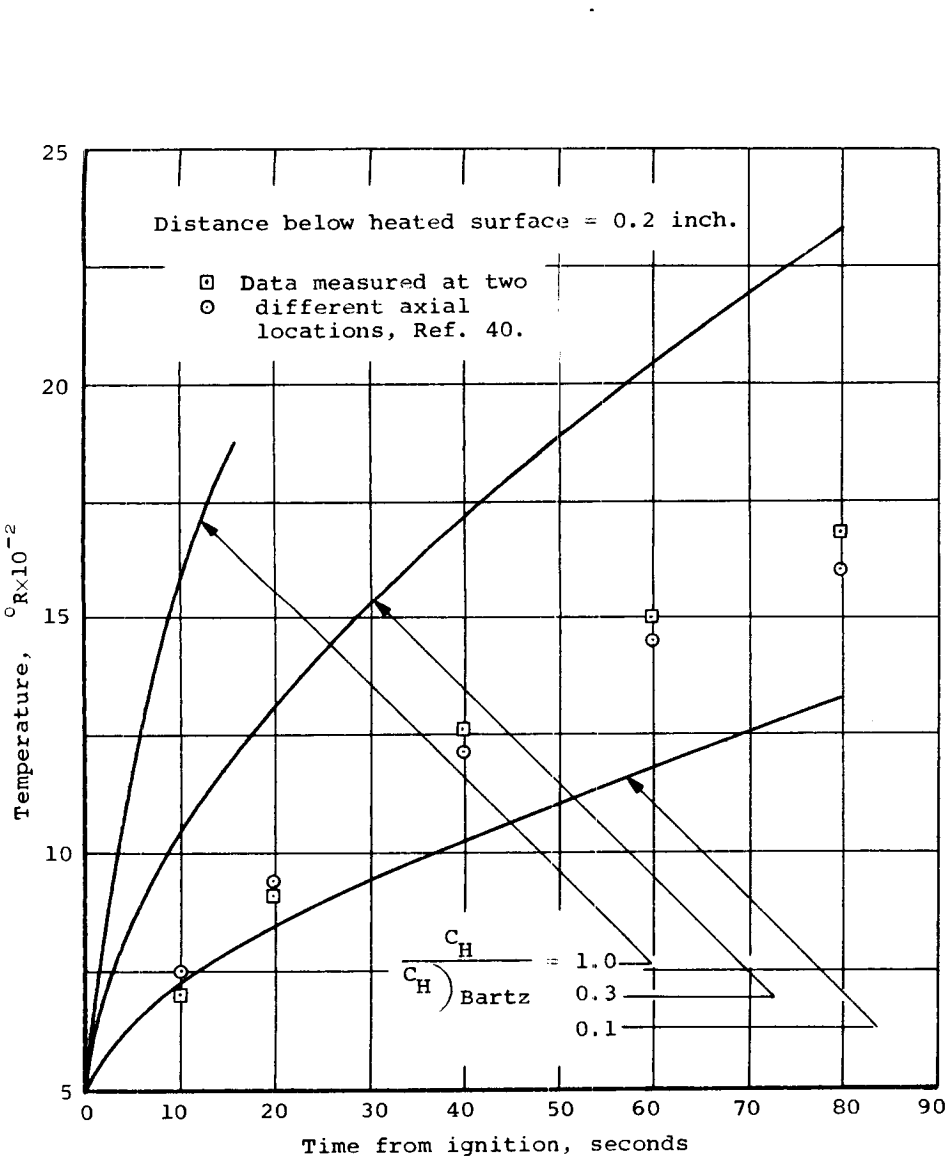


(a) Normalized ablation versus temperature.

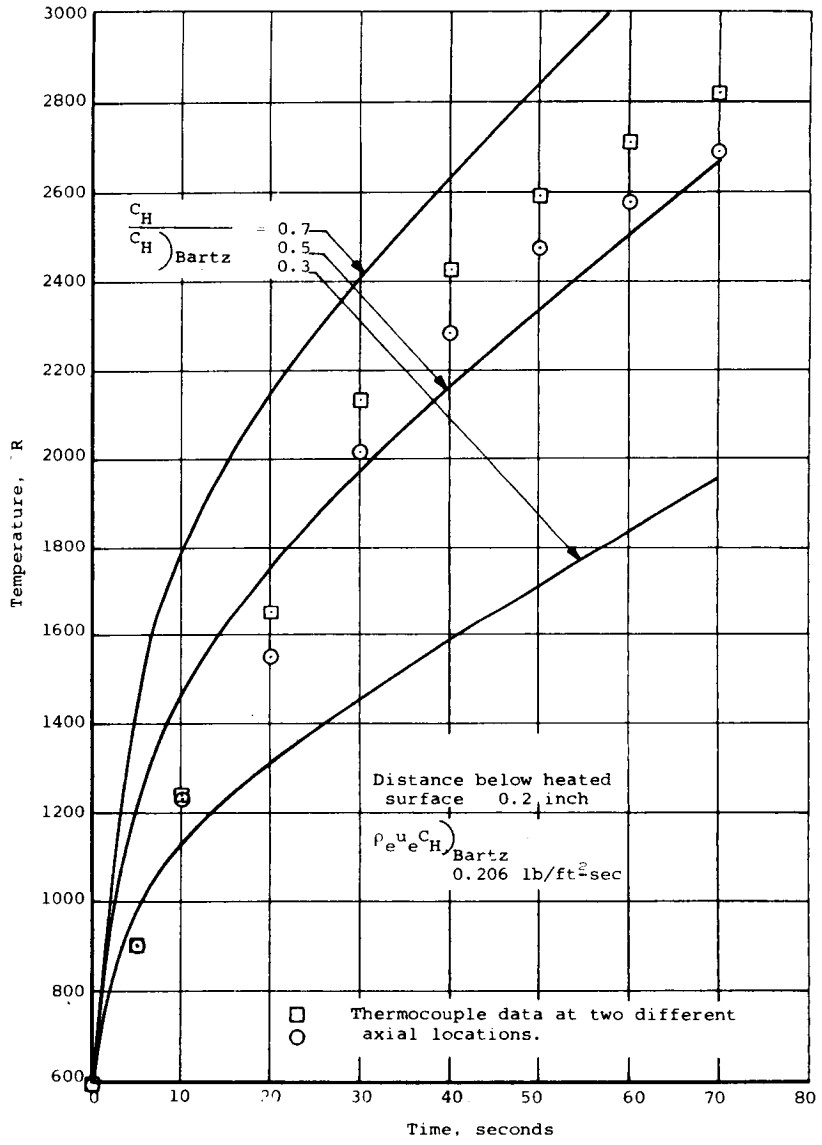


(b) Normalized ablation versus B'.

Figure 23.- Importance of various reactions for ablation of graphite in the OF_2-B_2H_6 environment as determined from gas phase equilibrium considerations, O/F = 5.85, pressure = 100 psia. B' varies such that gas phase is in equilibrium with graphite wall.

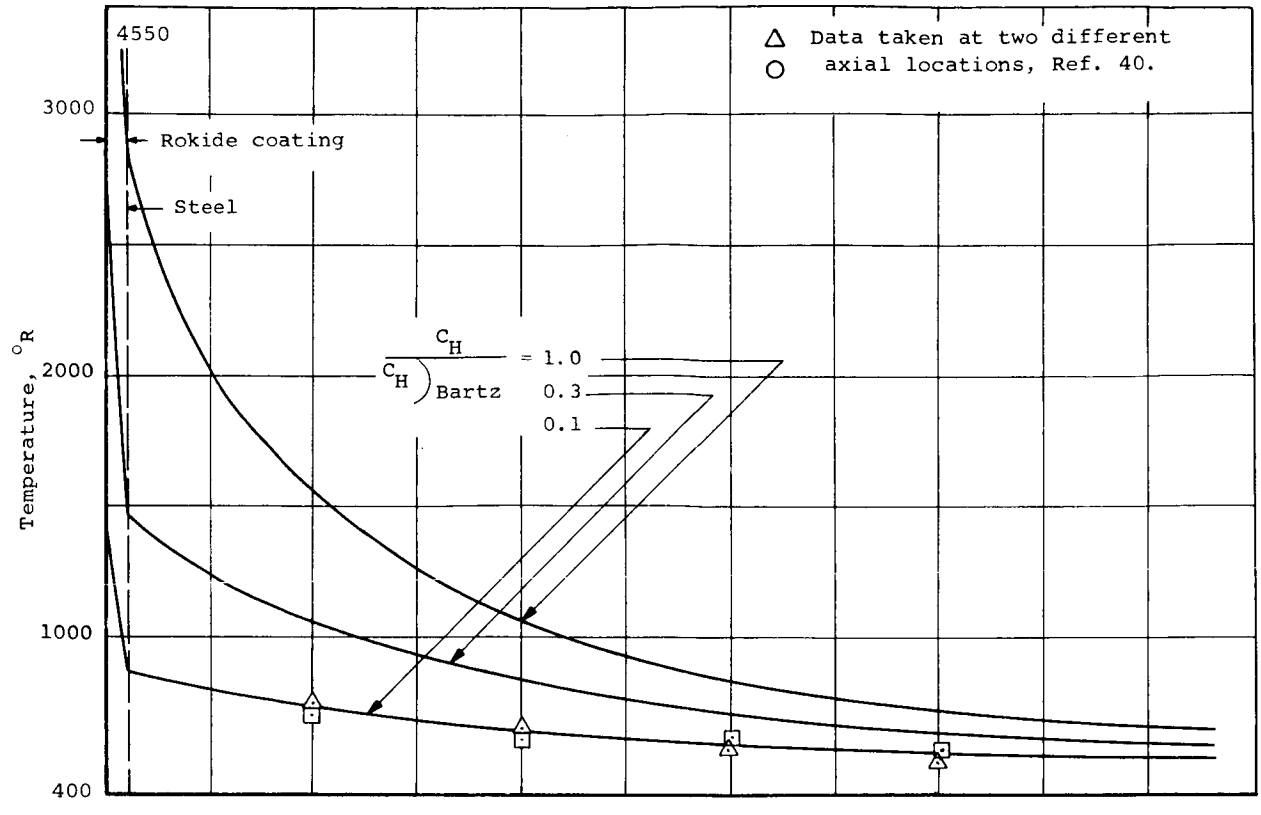


(a) Rokide coated steel nozzle.

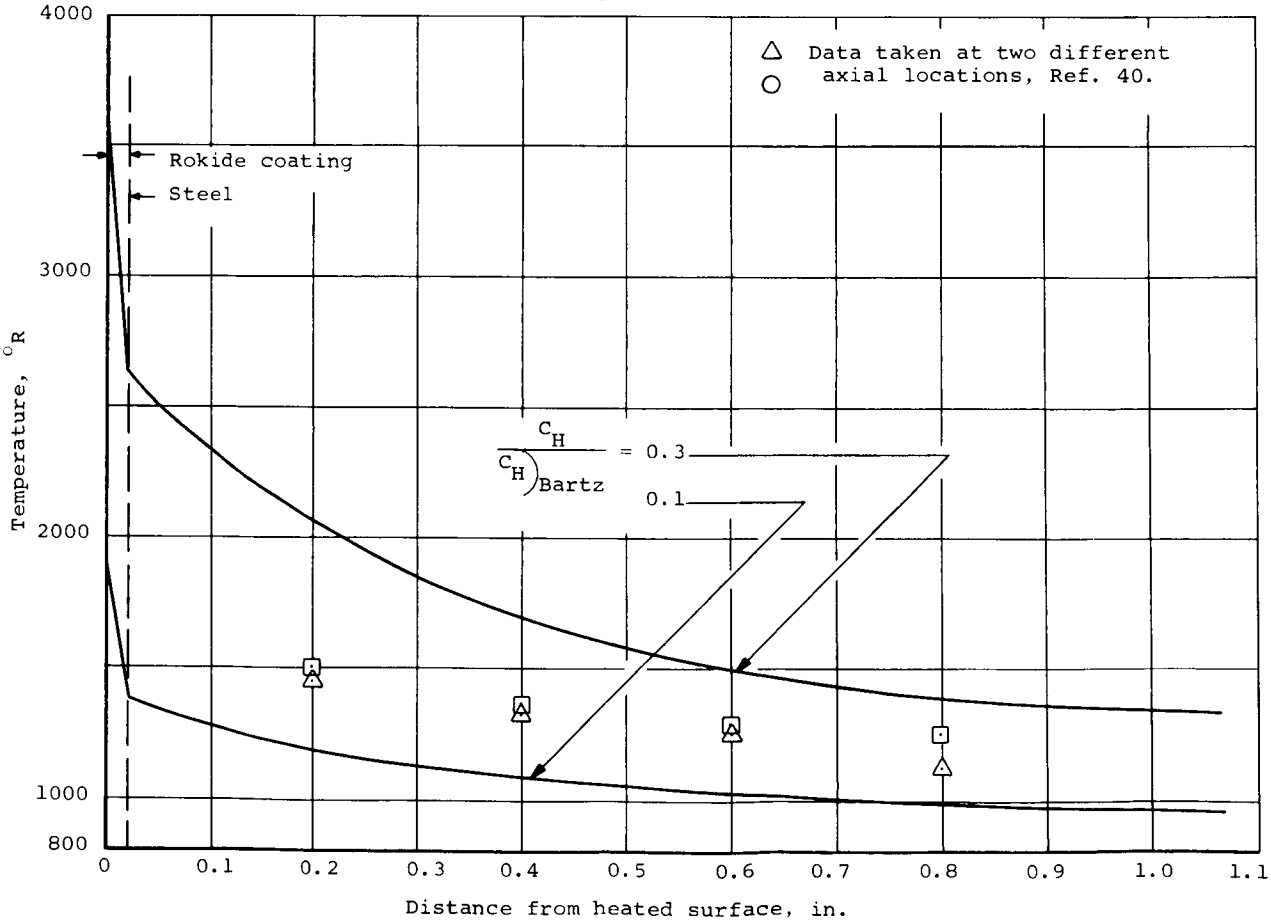


(b) Molybdenum nozzle.

Figure 24.- Comparison of measured temperature histories to those predicted employing different correction factors on theory.



(a) Time from ignition = 10 seconds



(b) Time from ignition = 60 seconds.

Figure 25.- Comparison of measured temperature distributions to those predicted employing different correction factors on theory.

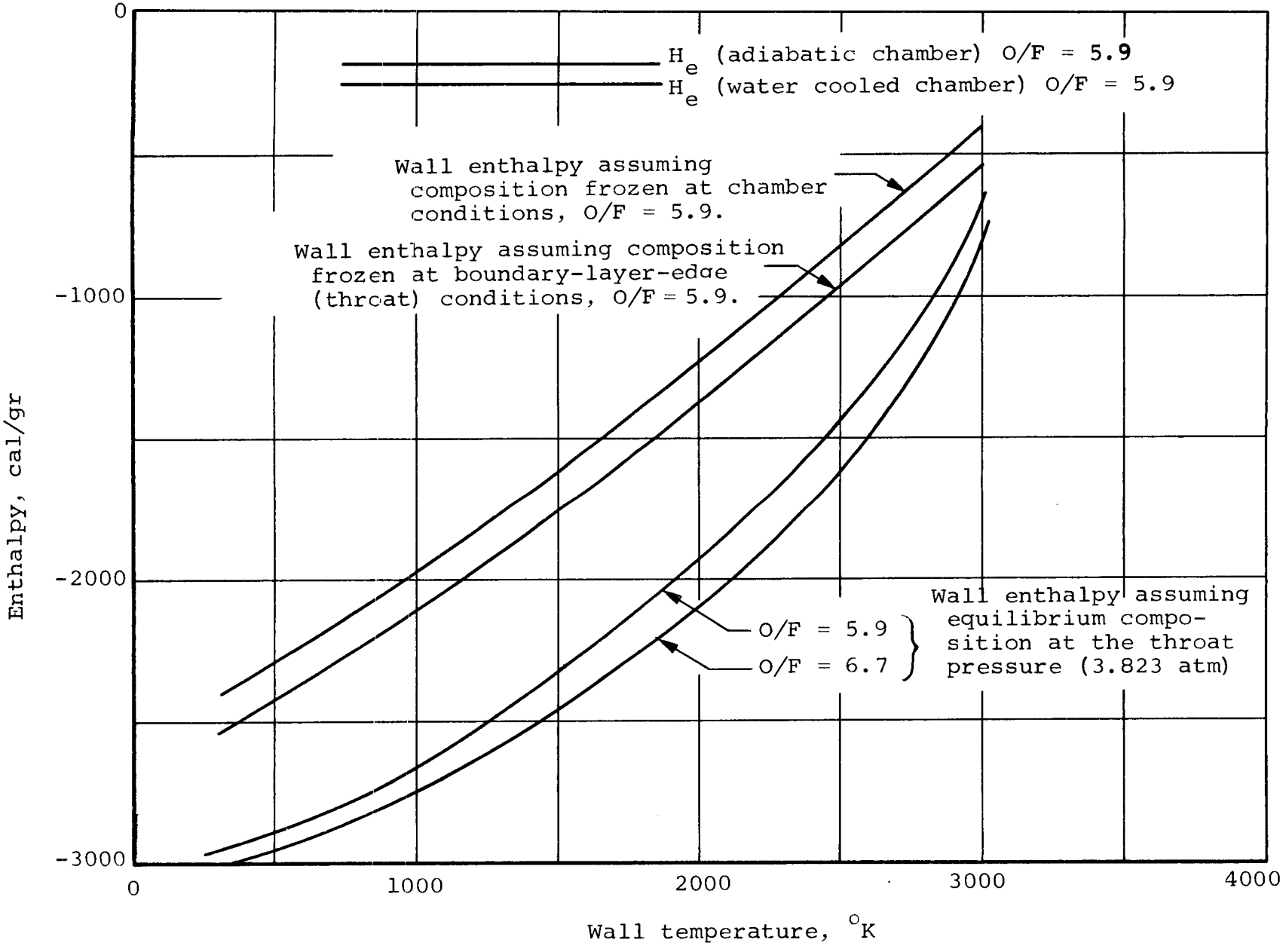
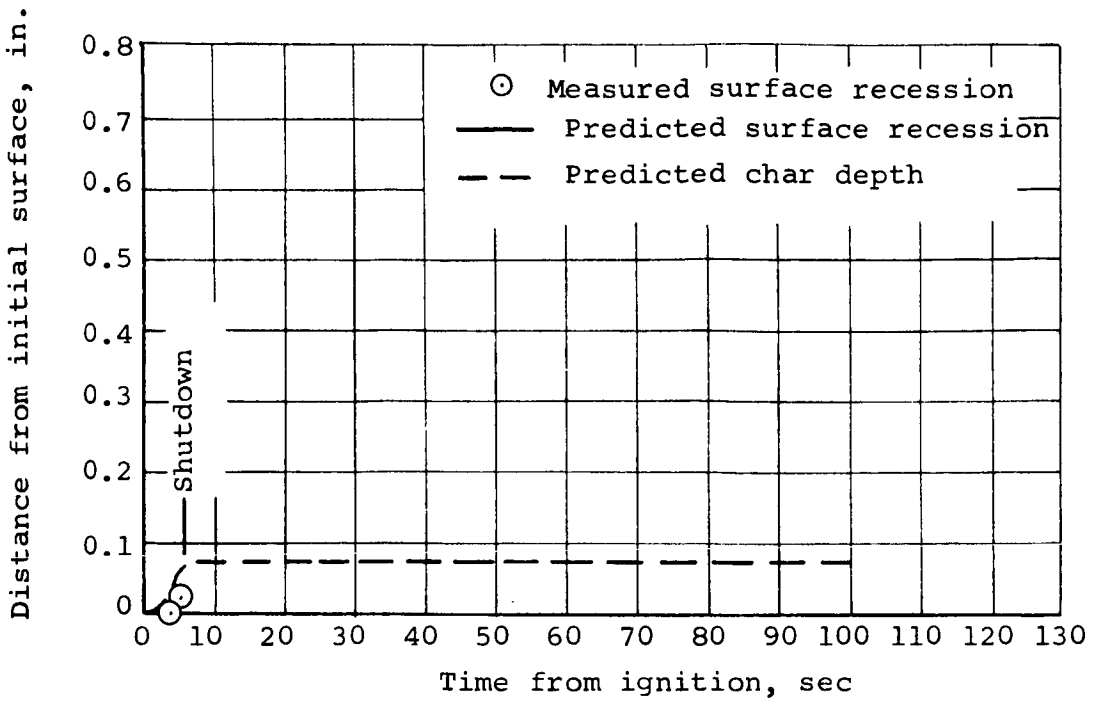
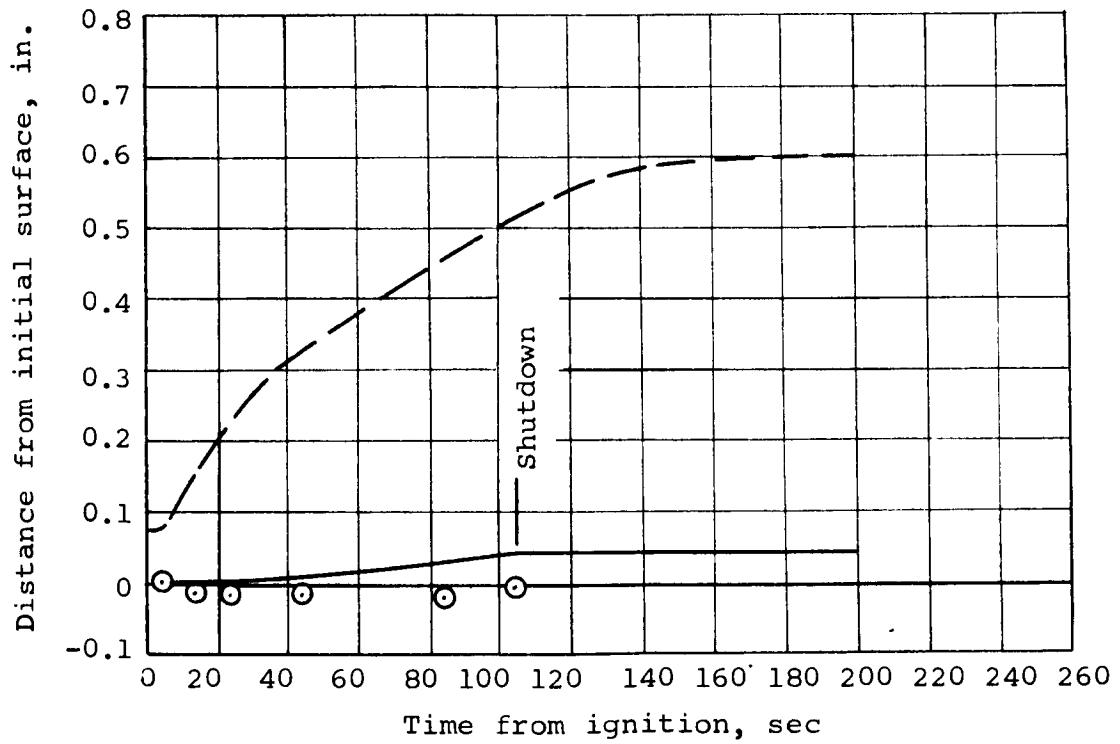


Figure 26.- Enthalpy of gases in O_2-H_2 rocket engine as a function of temperature.

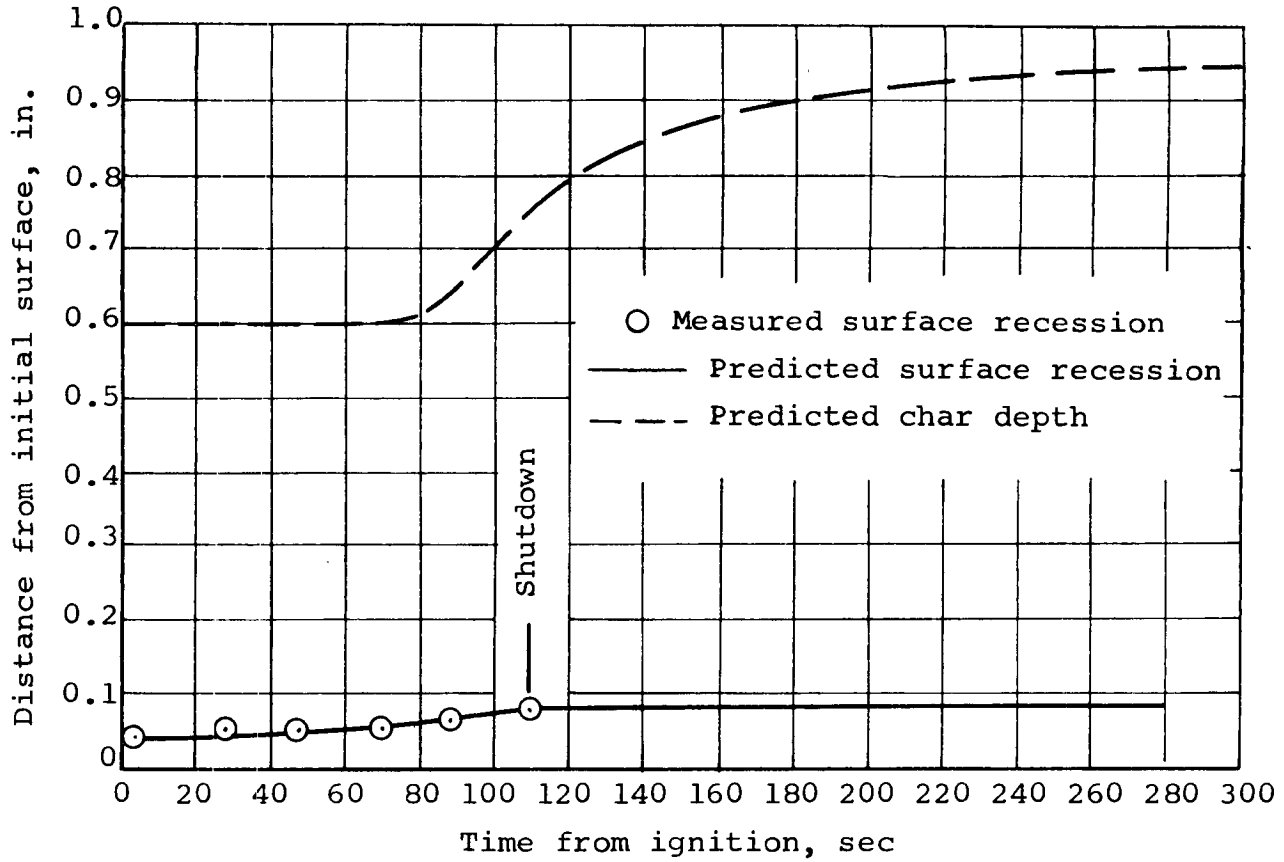


(a) Run No. 89; final ablated depth, predicted, 0 inch, measured, 0.02 inch.



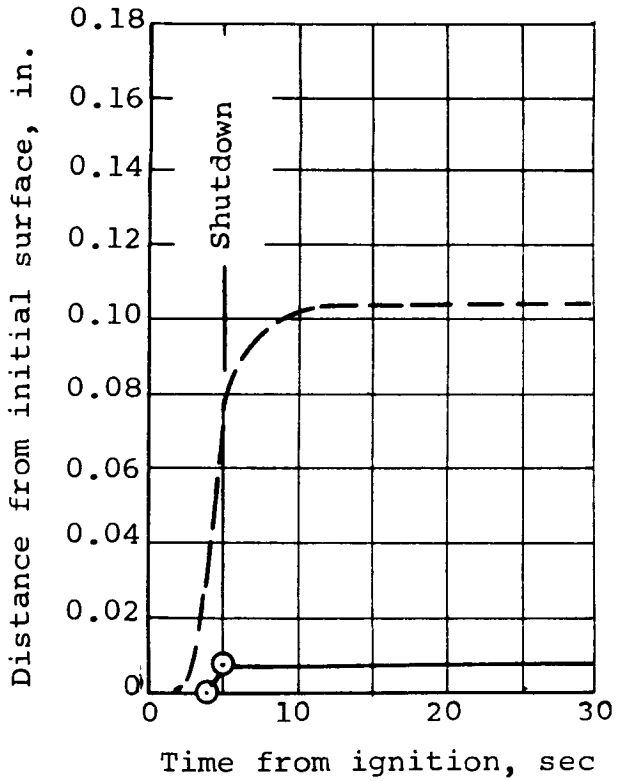
(b) Run No. 90; final ablated depth, predicted, 0.041 inch, measured, -0.013 inch.

Figure 27.- Predicted char depth history and comparison of predicted and measured surface recession for silica phenolic nozzle throat, Engine S-4.

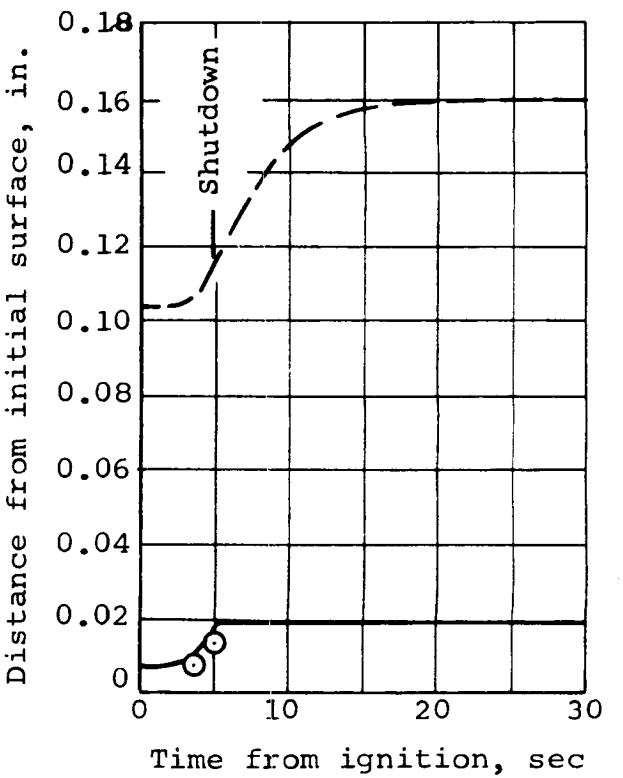


(c) Run No. 91; final ablated depth, predicted, 0.081 inch, measured, 0.073 inch.

Figure 27.- Concluded.

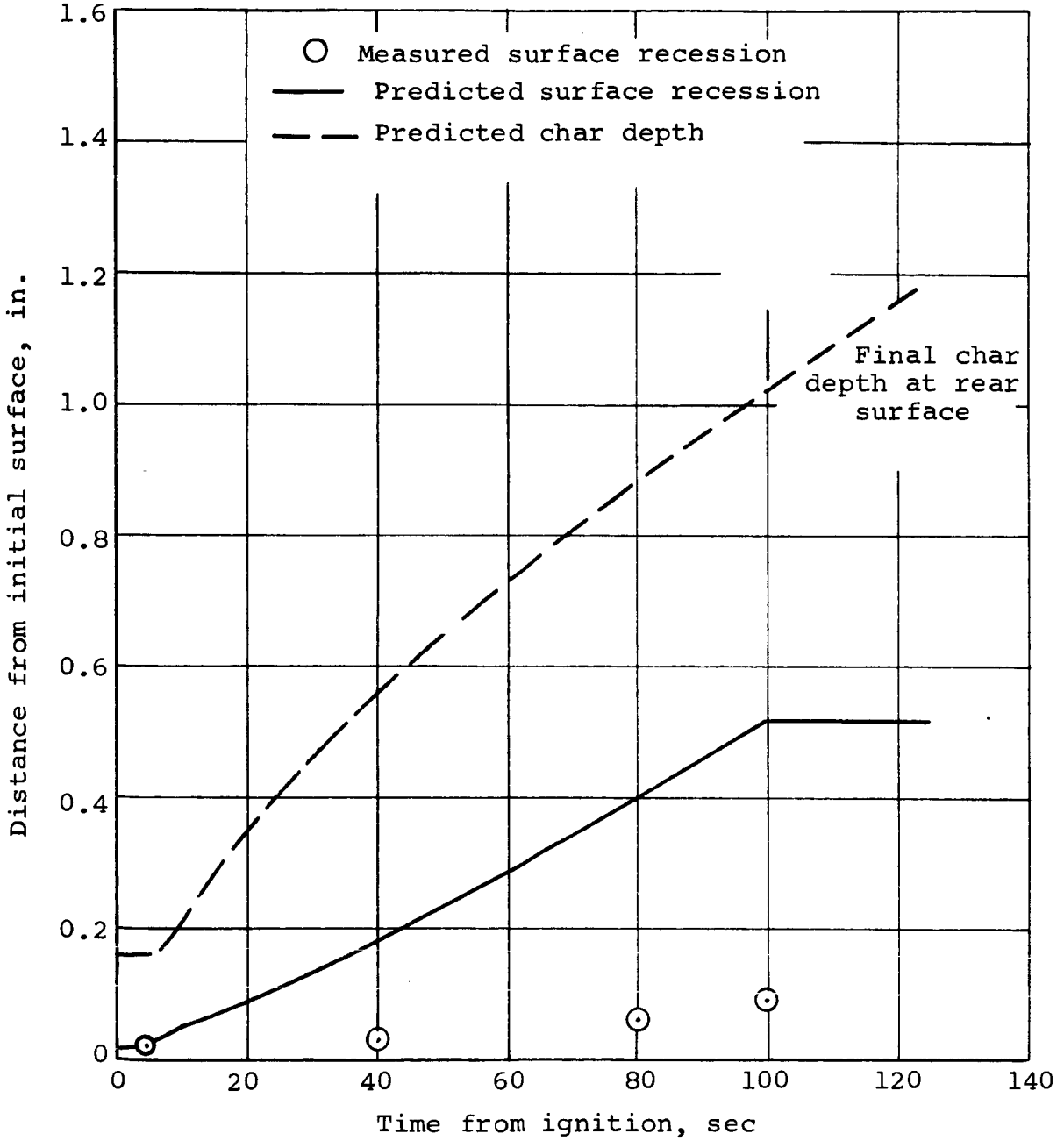


(a) Run No. 64; final ablated depth, predicted, 0.007 inch, measured, 0.007 inch.



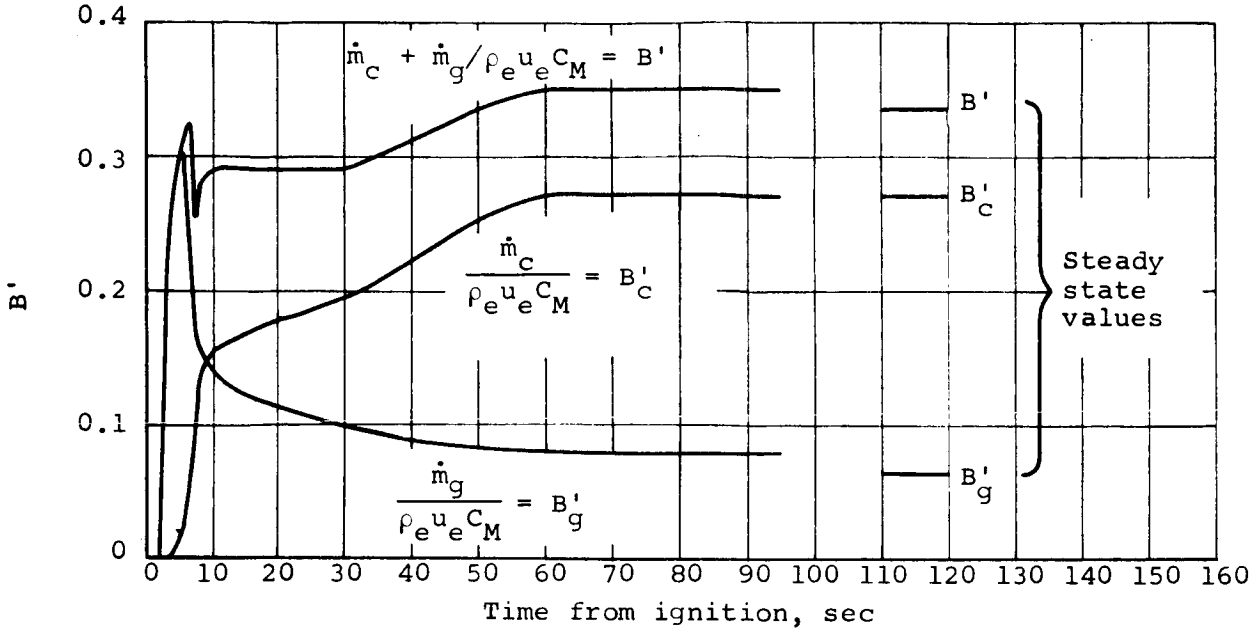
(b) Run No. 65; final ablated depth, predicted, 0.019 inch, measured, 0.013 inch.

Figure 28.- Predicted char depth history and comparison of predicted and measured surface recession for graphite-phenolic nozzle throat, Engine S-10.

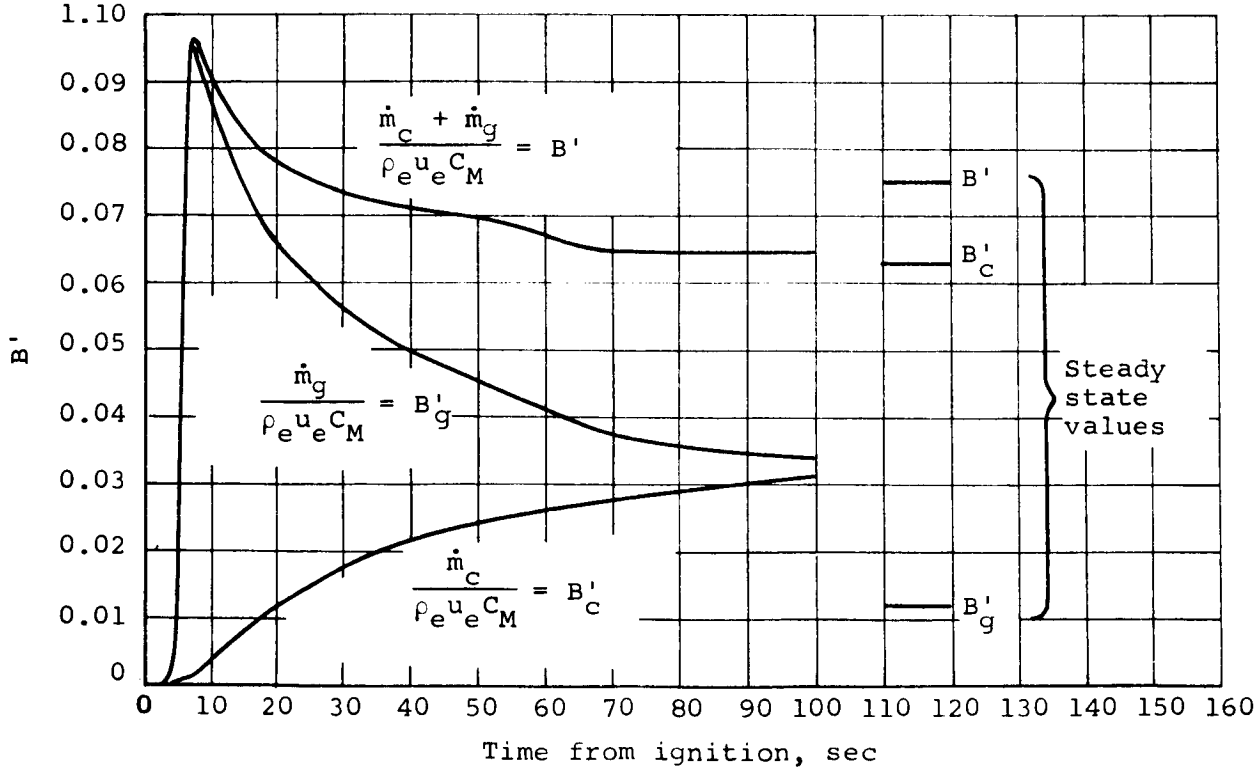


(c) Run No. 66; final ablated depth, predicted, 0.52 inch, measured, 0.09 inch.

Figure 28.- Concluded.

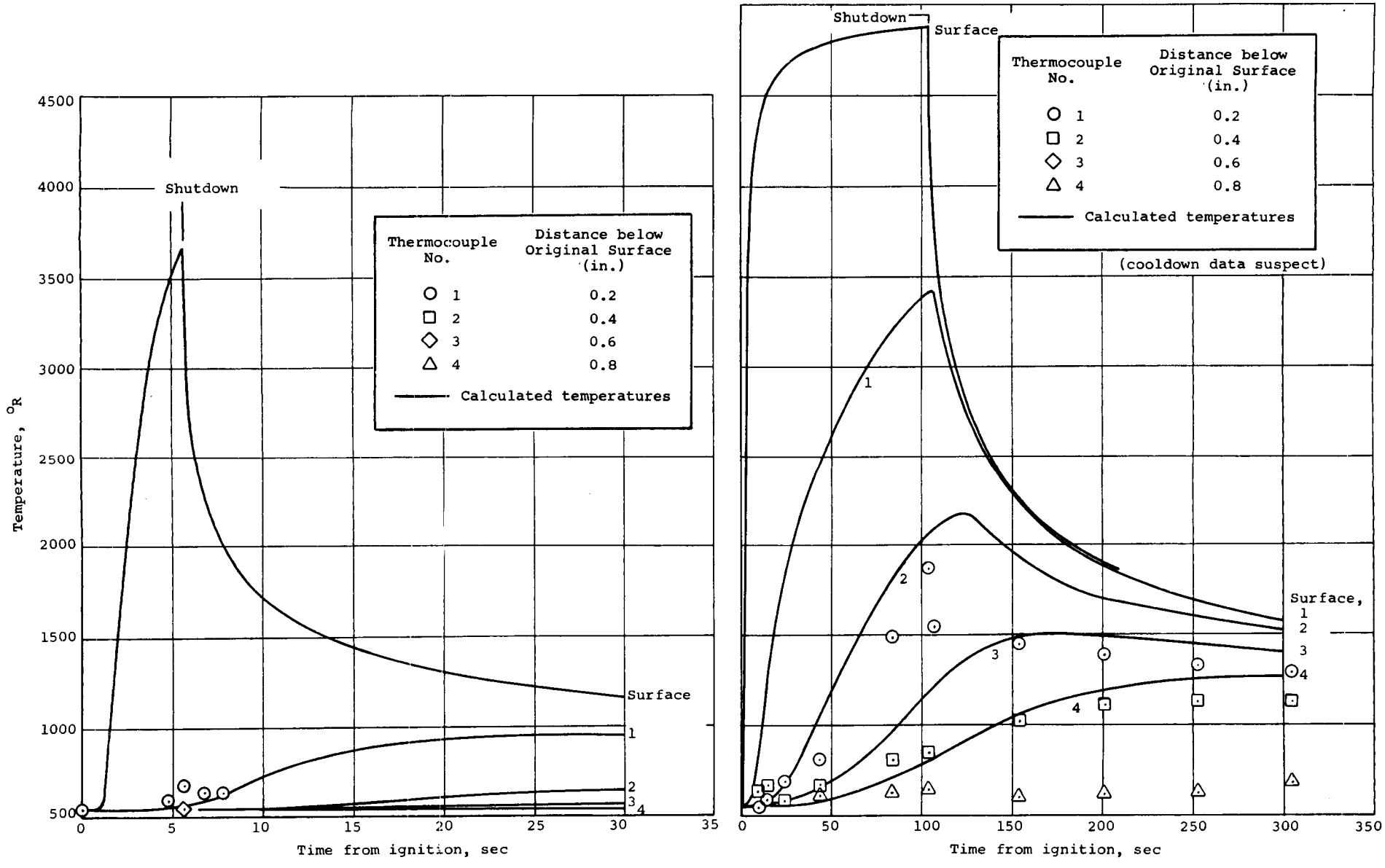


(a) Graphite phenolic, Run No. 66.



(b) Silica phenolic, Run No. 90.

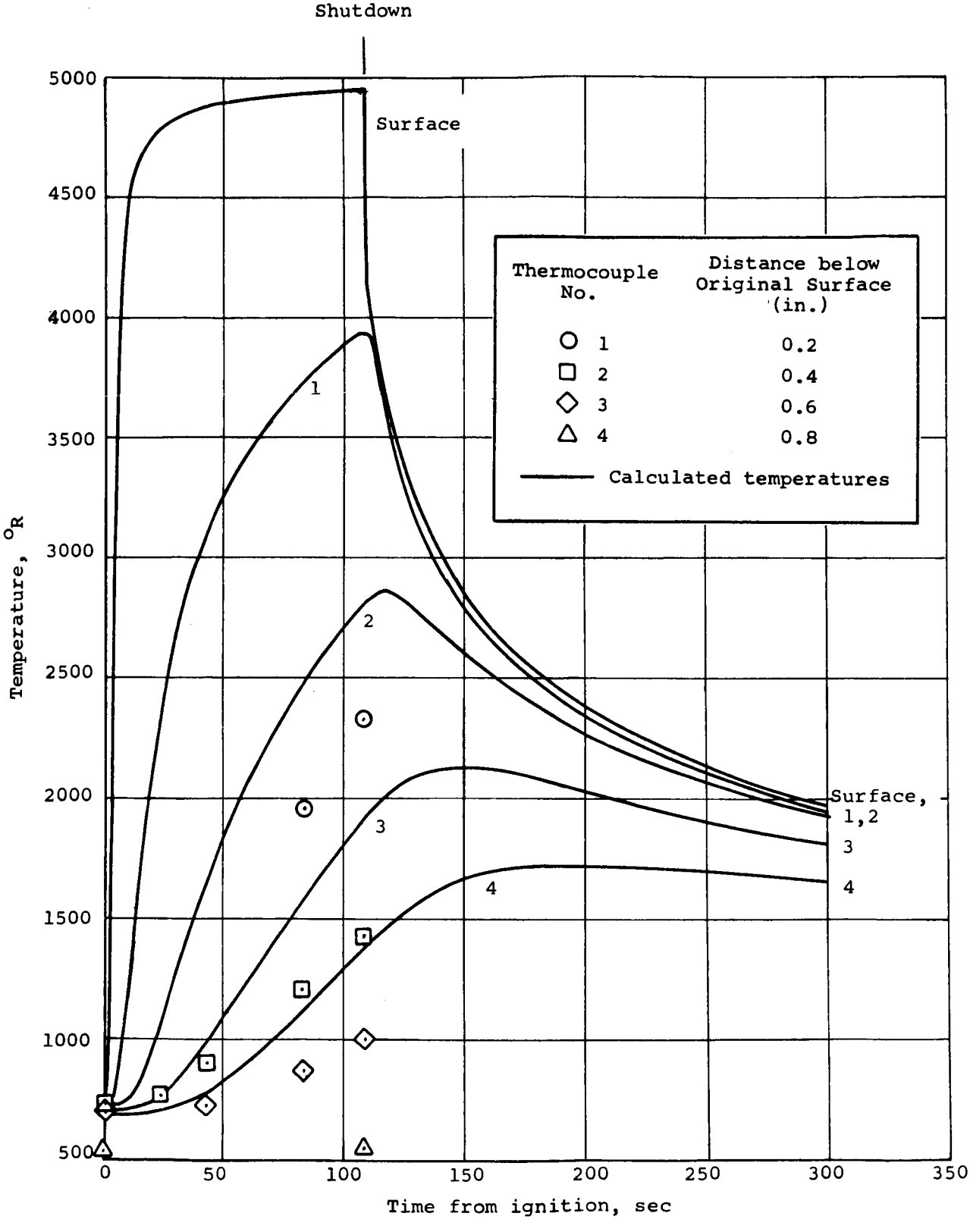
Figure 29.- Comparison of transient and steady-state ablation rates for resin off-gas, char, and total.



(a) Run No. 89.

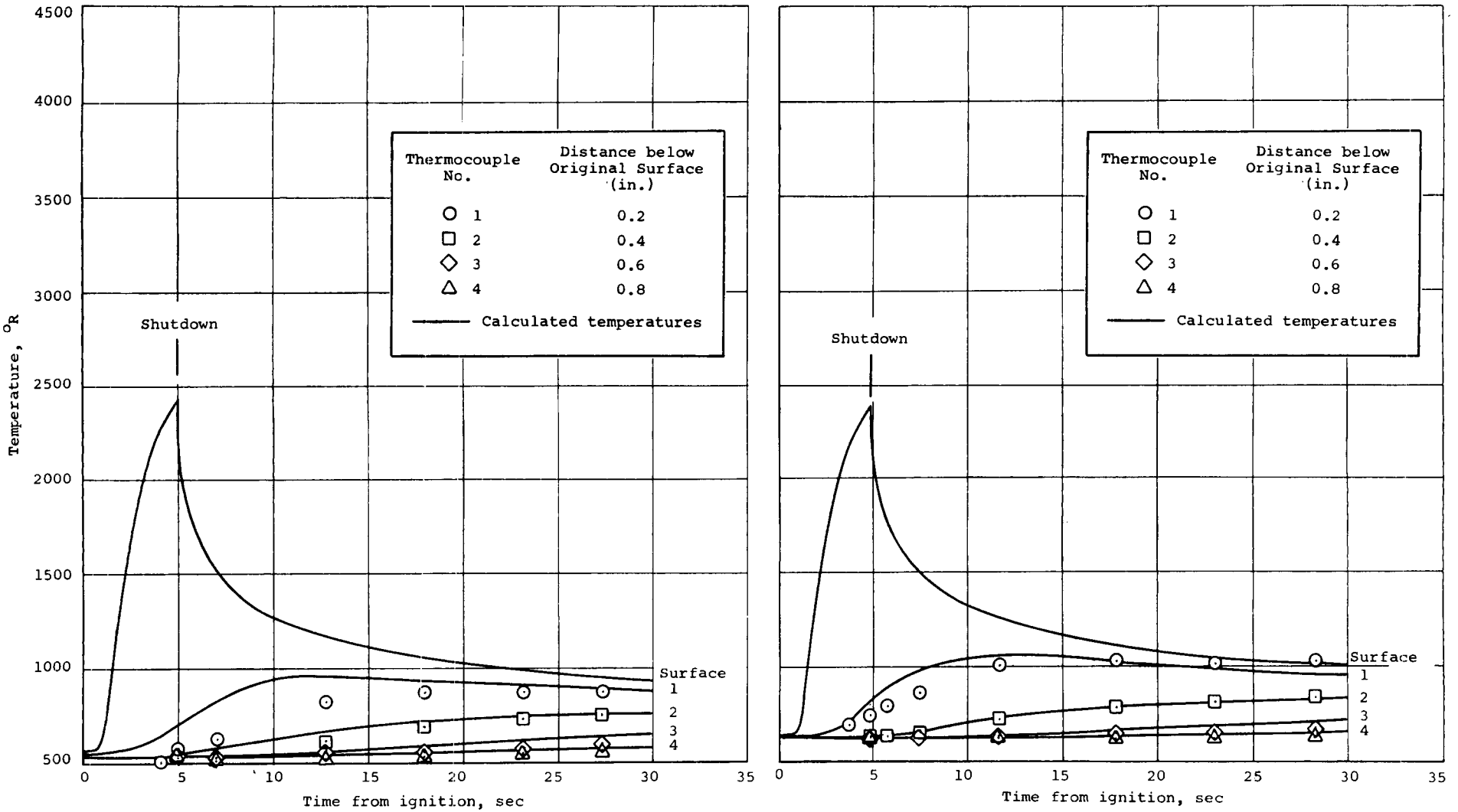
(b) Run No. 90.

Figure 30.- Comparison of predicted to measured temperature histories for the silica-phenolic nozzle throat, Engine S-4.



(c) Run No. 91.

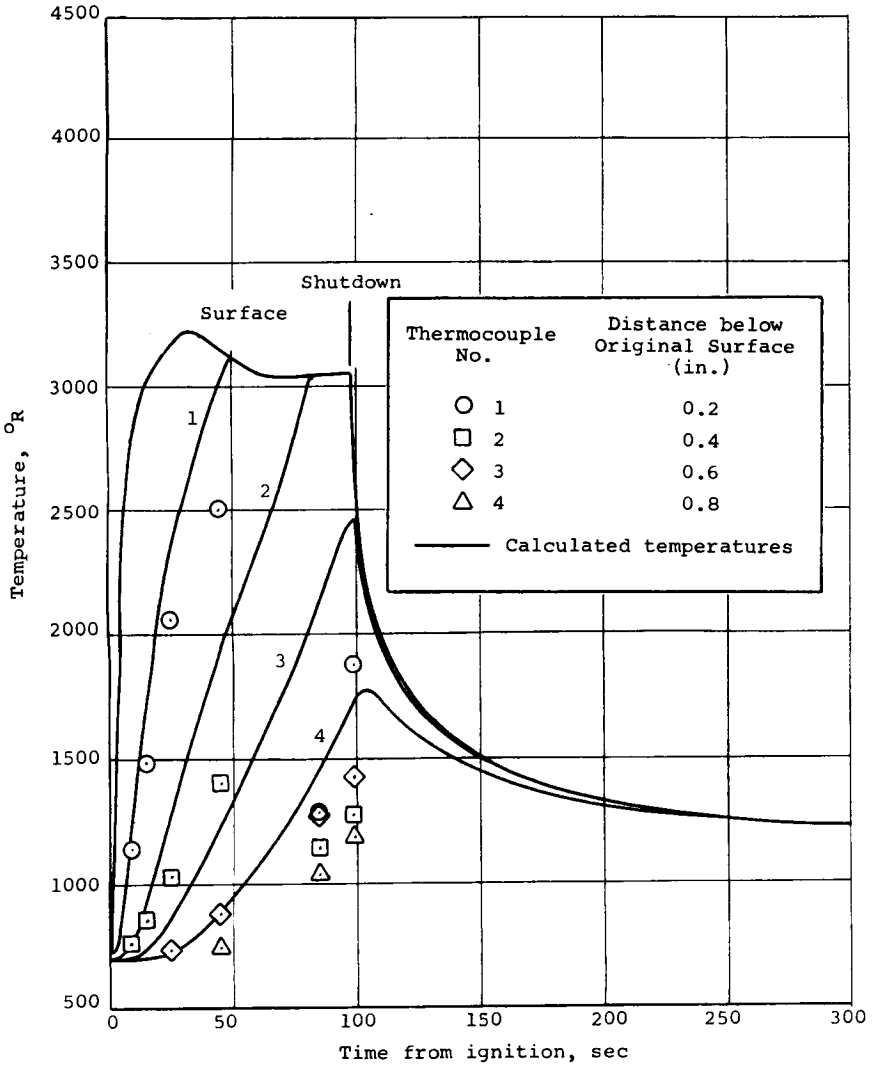
Figure 30.- Concluded.



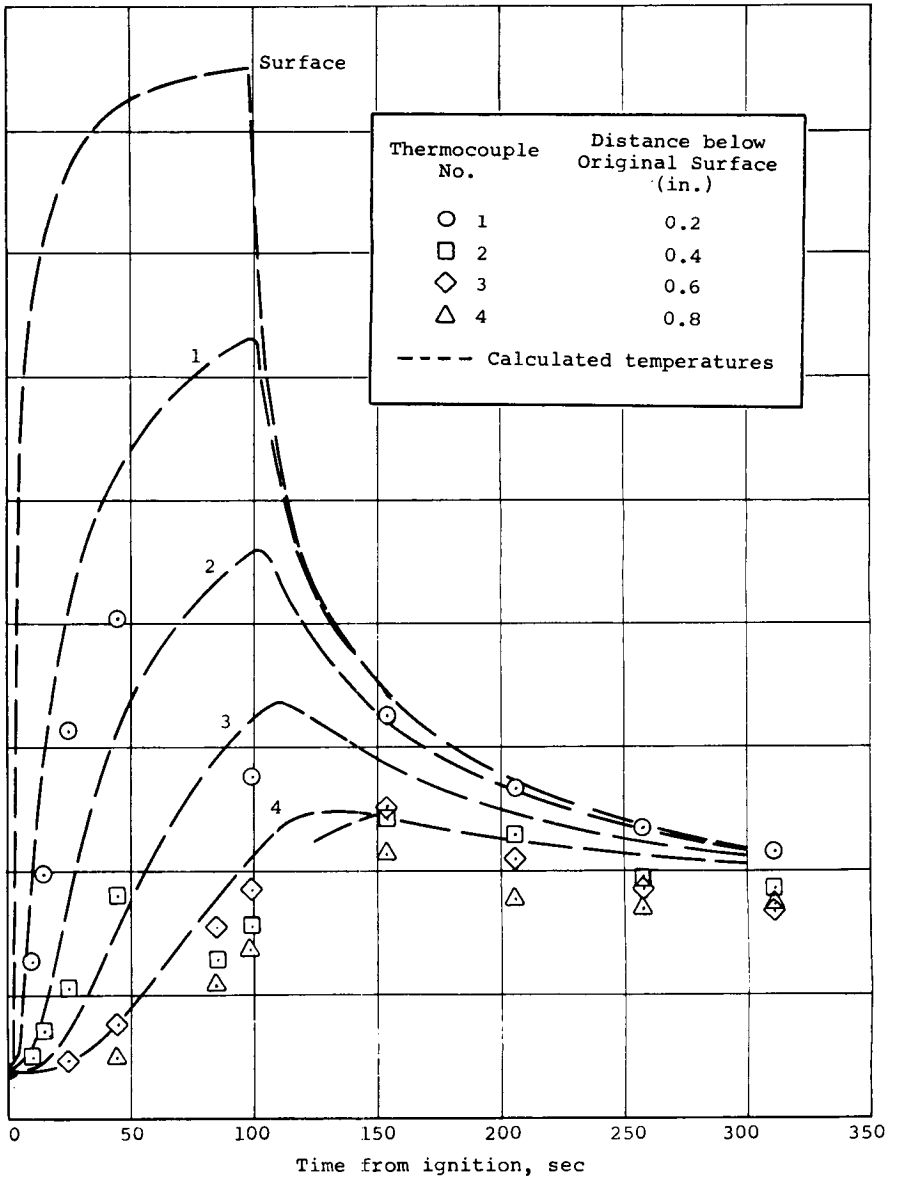
(a) Run No. 64.

(b) Run No. 65.

Figure 31.- Comparison of predicted to measured temperature histories for the graphite-phenolic nozzle throat, Engine S-10.



(c) Run No. 66.



(d) Run No. 66, the surface was not allowed to recede for this prediction.

Figure 31.- Concluded.

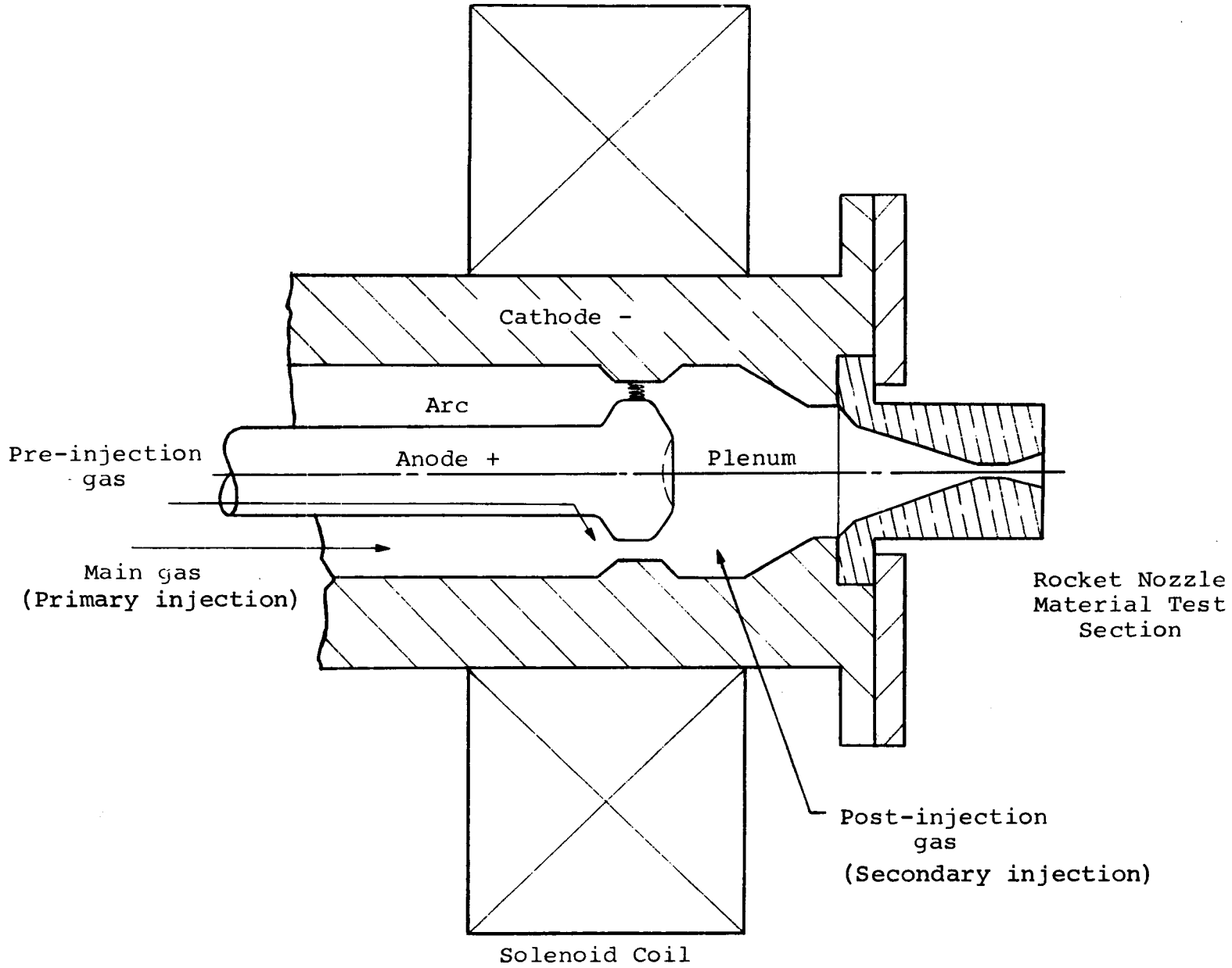


Figure 32.- Schematic of solenoid arc-plasma generator electrode configuration.

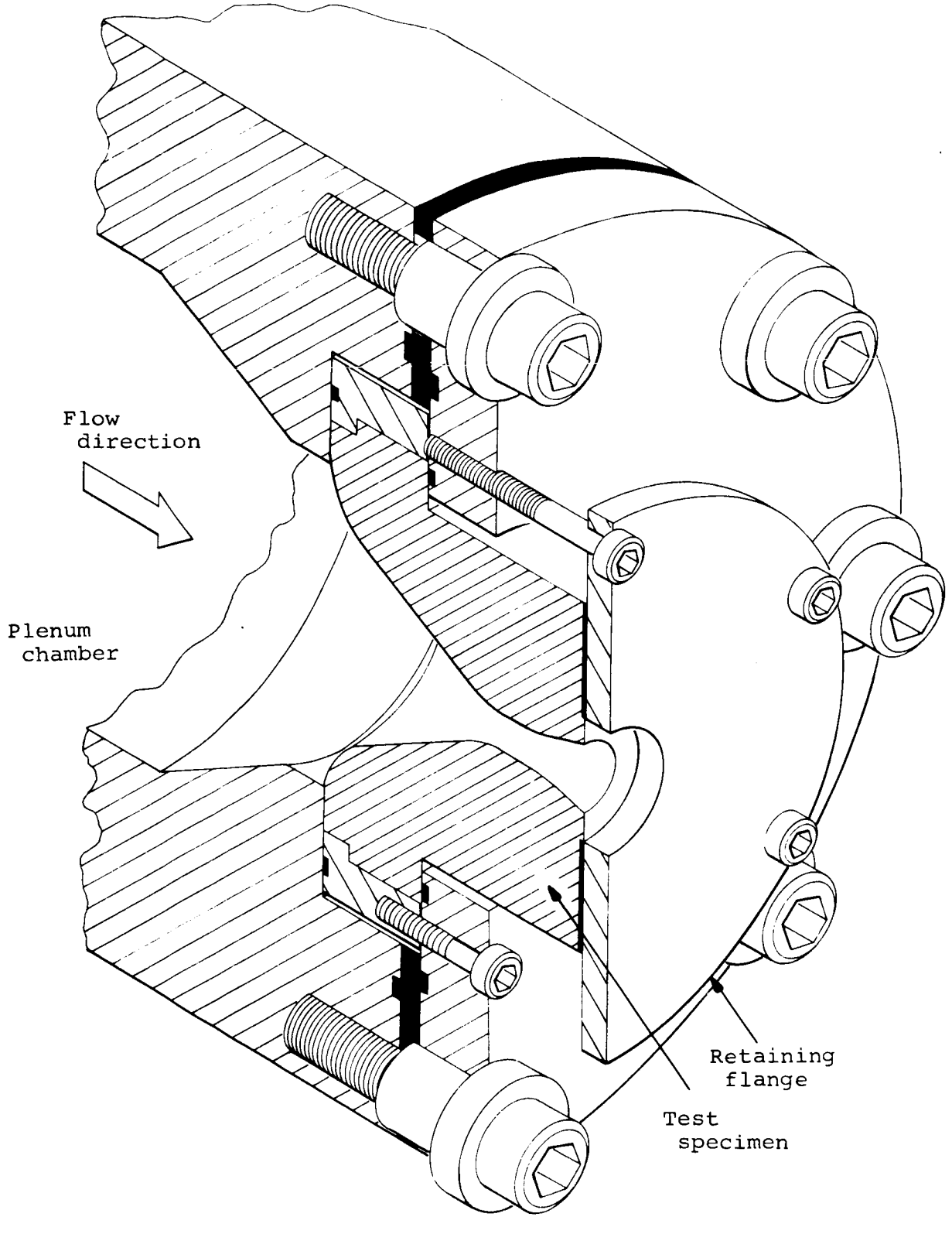


Figure 33.- Rocket-nozzle test model mounting scheme.

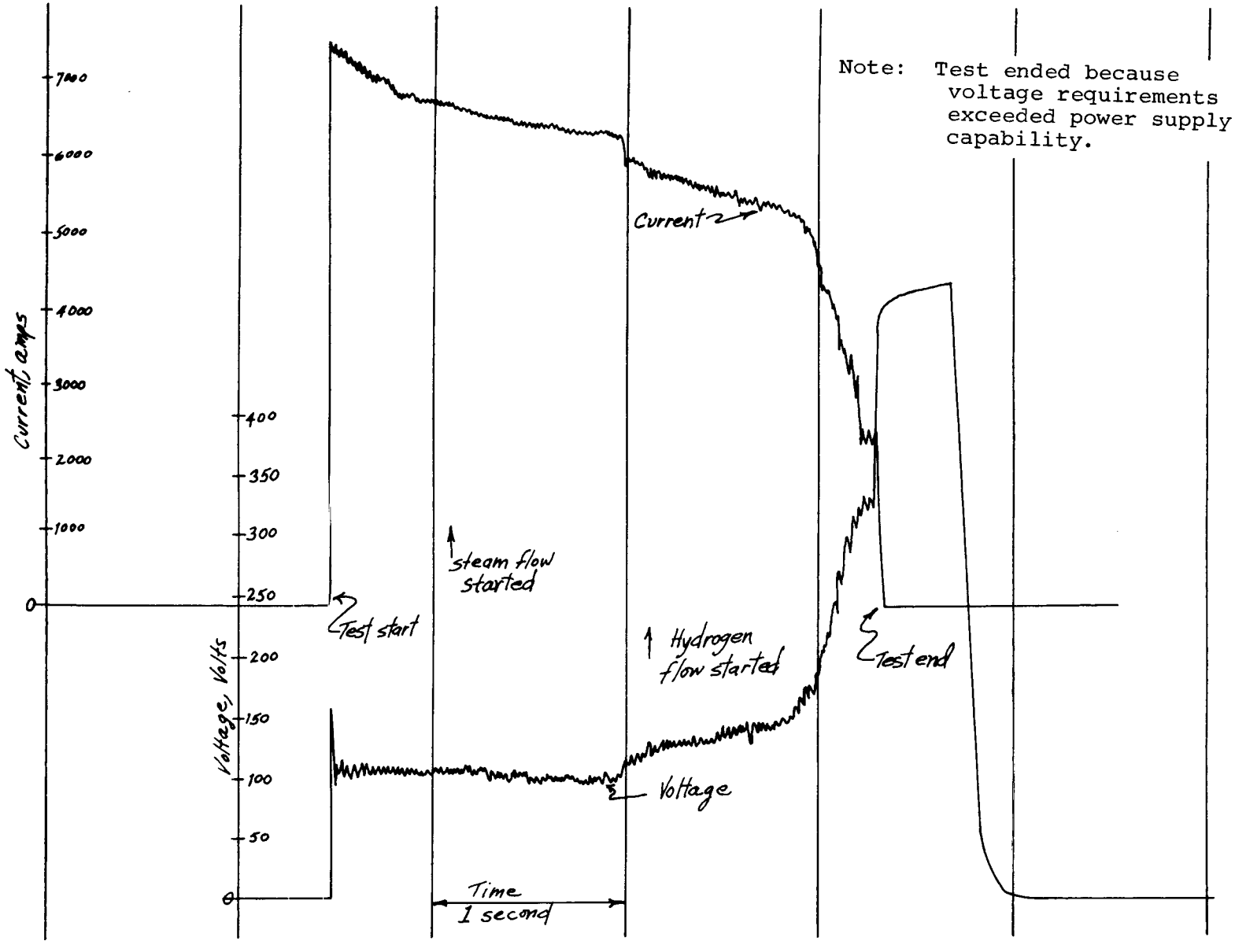


Figure 34.- Oscillograph trace for steam-hydrogen operation showing effect of hydrogen on voltage requirements.

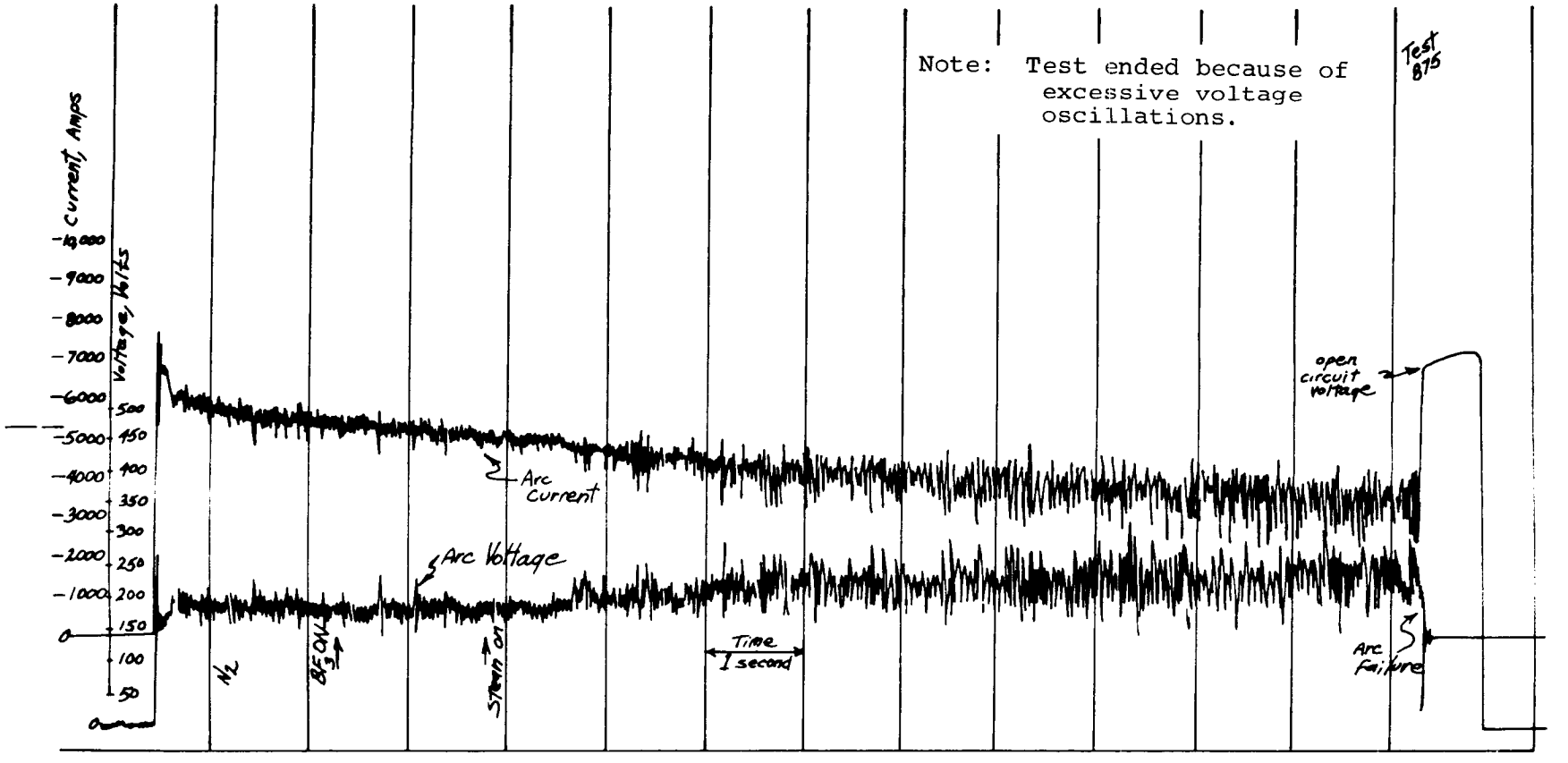


Figure 35.- Oscillograph trace from OF_2-B_2H_6 simulation attempt showing effect of steam on arc operation.

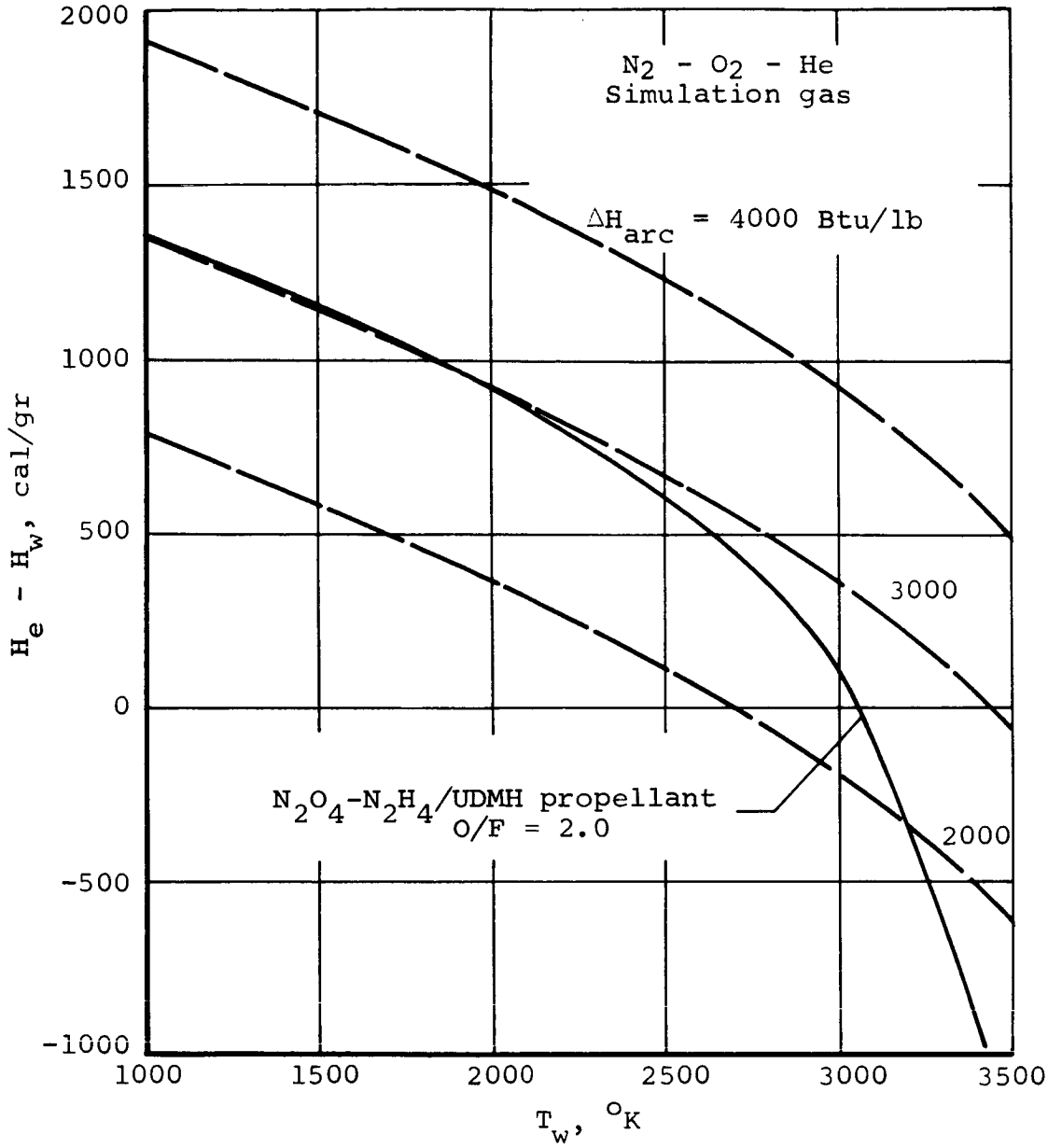


Figure 36.- Comparison of boundary-layer enthalpy potential as a function of wall temperature for the N_2O_4-N_2H_4/UDMH propellant and the N_2-O_2-He simulation gas for different electric energy inputs.

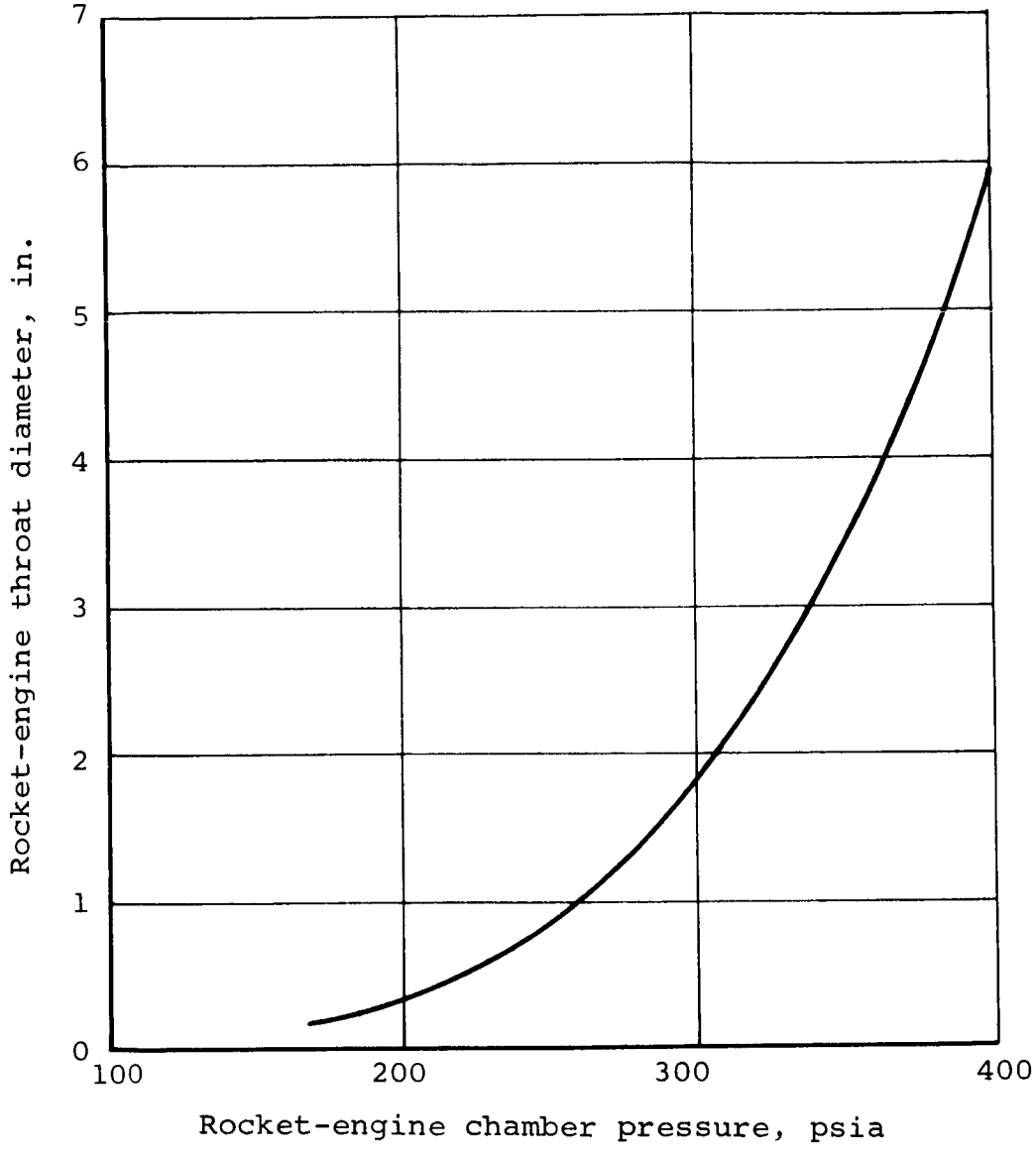


Figure 37.- Range on actual rocket-engine conditions simulated by duplicating enthalpy and oxidation potential of N_2O_4-N_2H_4/UDMH propellant.

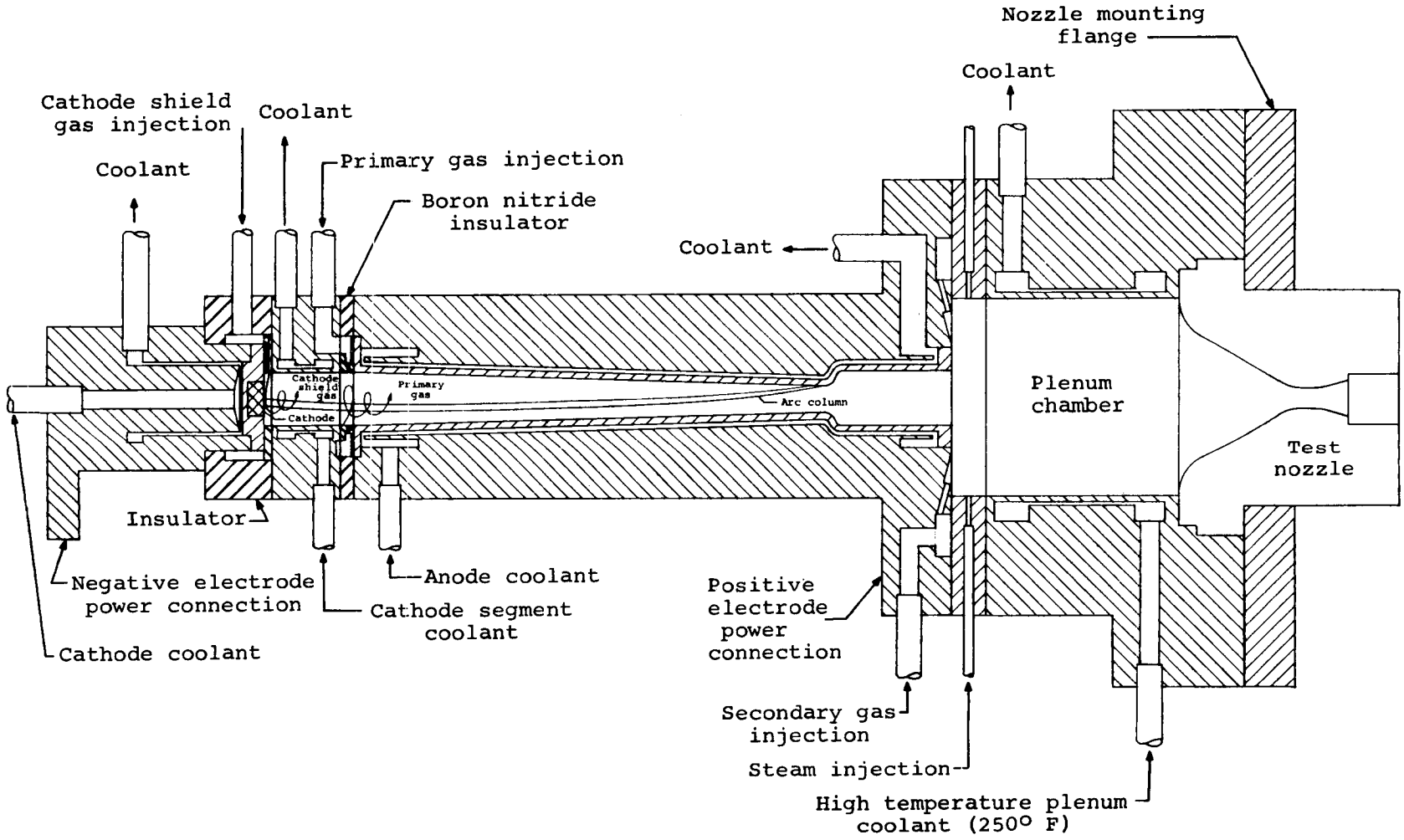


Figure 38.- Constrictor arc-plasma generator rocket-engine environment simulation apparatus.

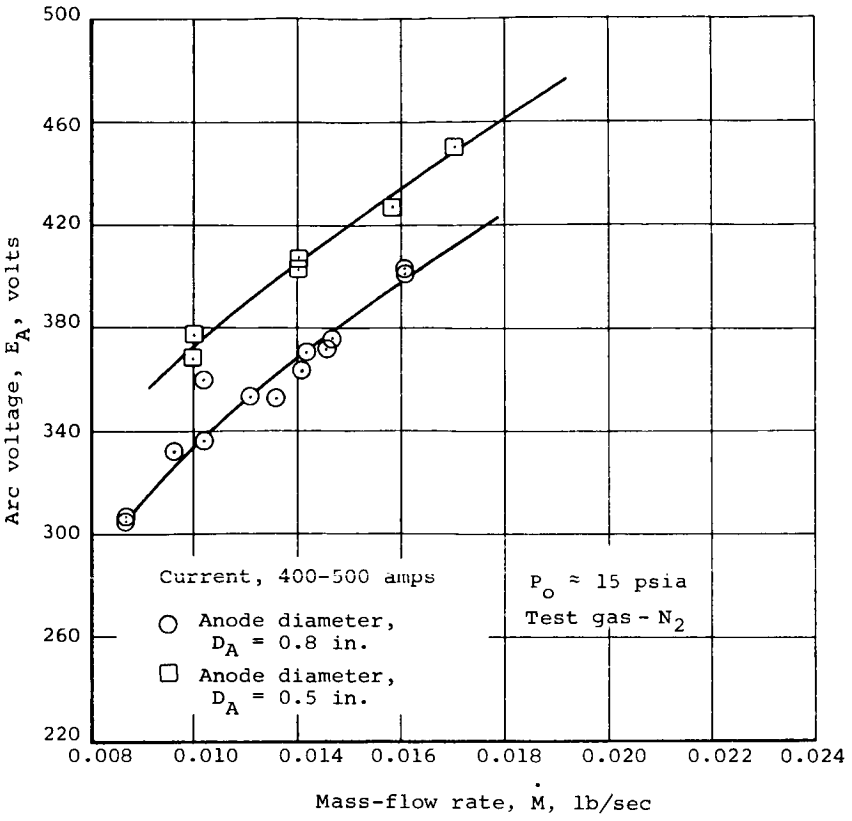


Figure 39.- Arc voltage as a function of mass-flow rate for two anode diameters.

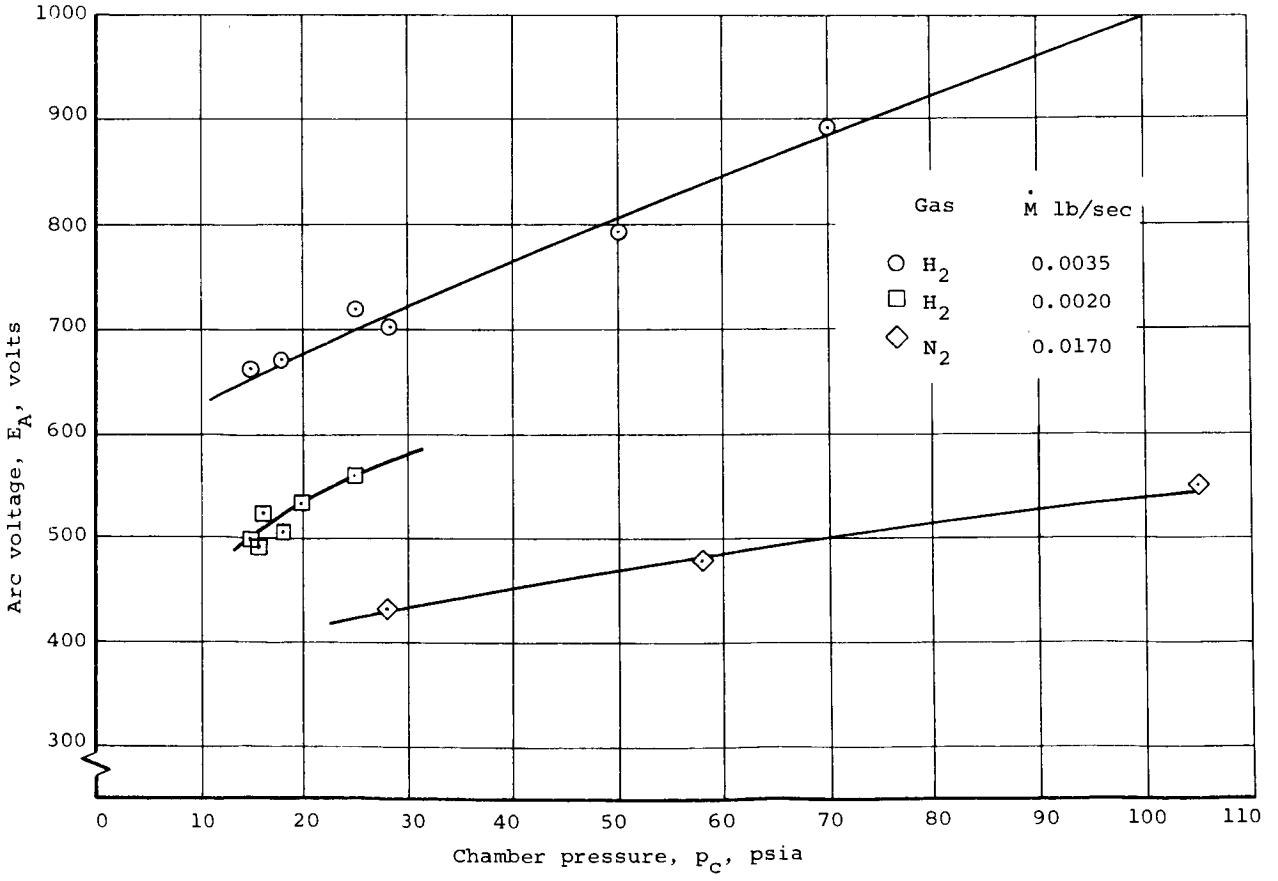


Figure 40.- Arc voltage as a function of chamber pressure for hydrogen and nitrogen operation.

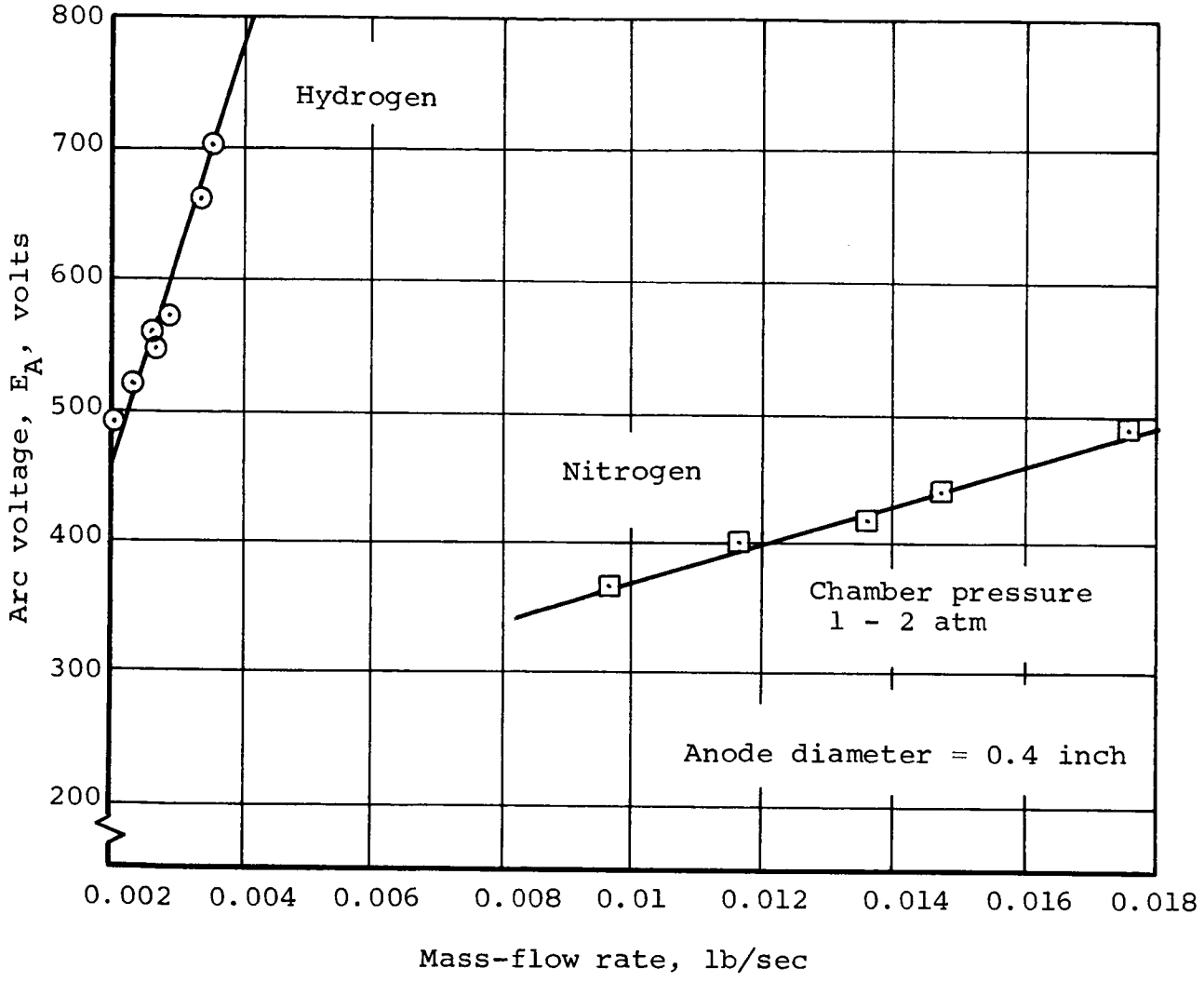


Figure 41.- Arc voltage as a function of mass-flow rate for H_2 and N_2 operation.

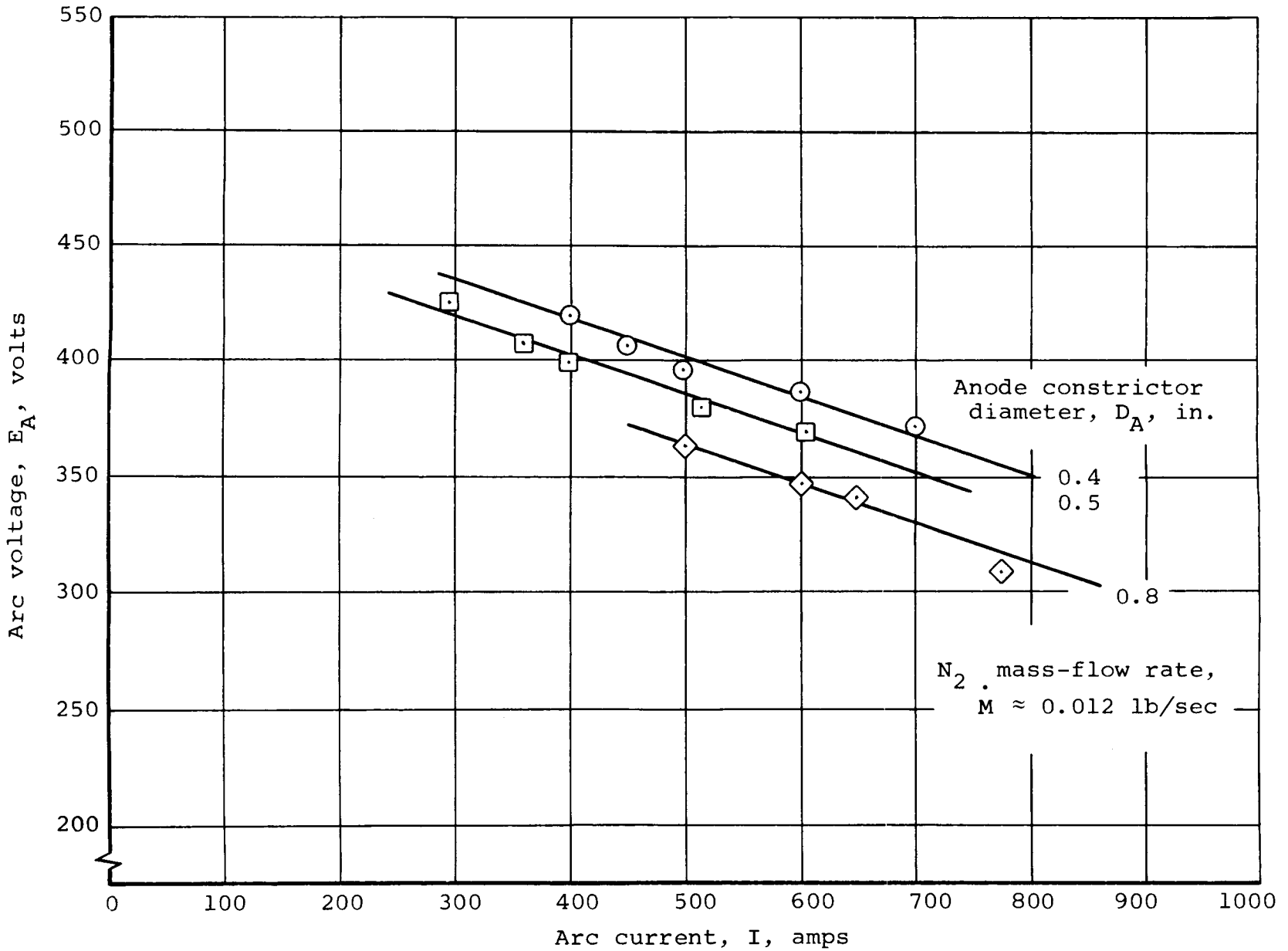


Figure 42.- Effect of anode constrictor diameter on arc voltage.

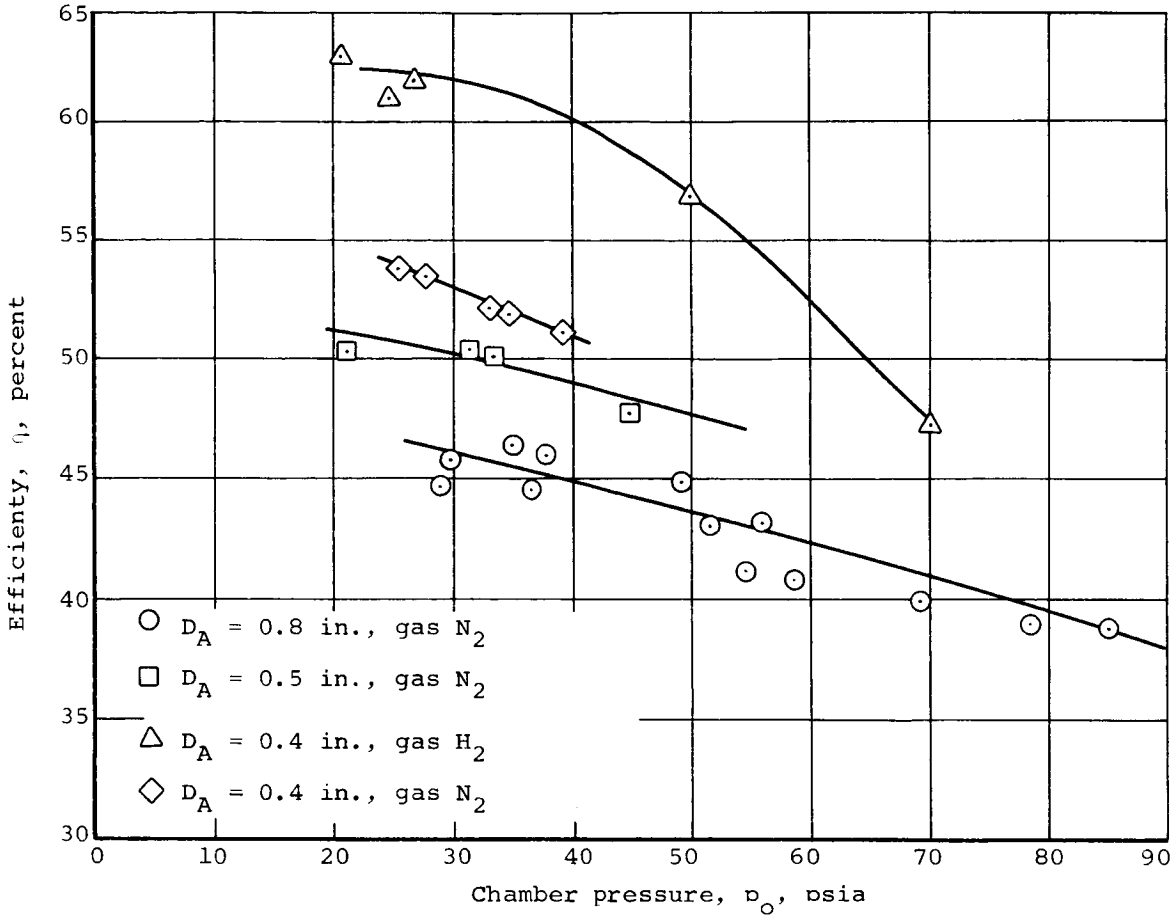


Figure 43.- Arc thermal efficiency as a function of chamber pressure.

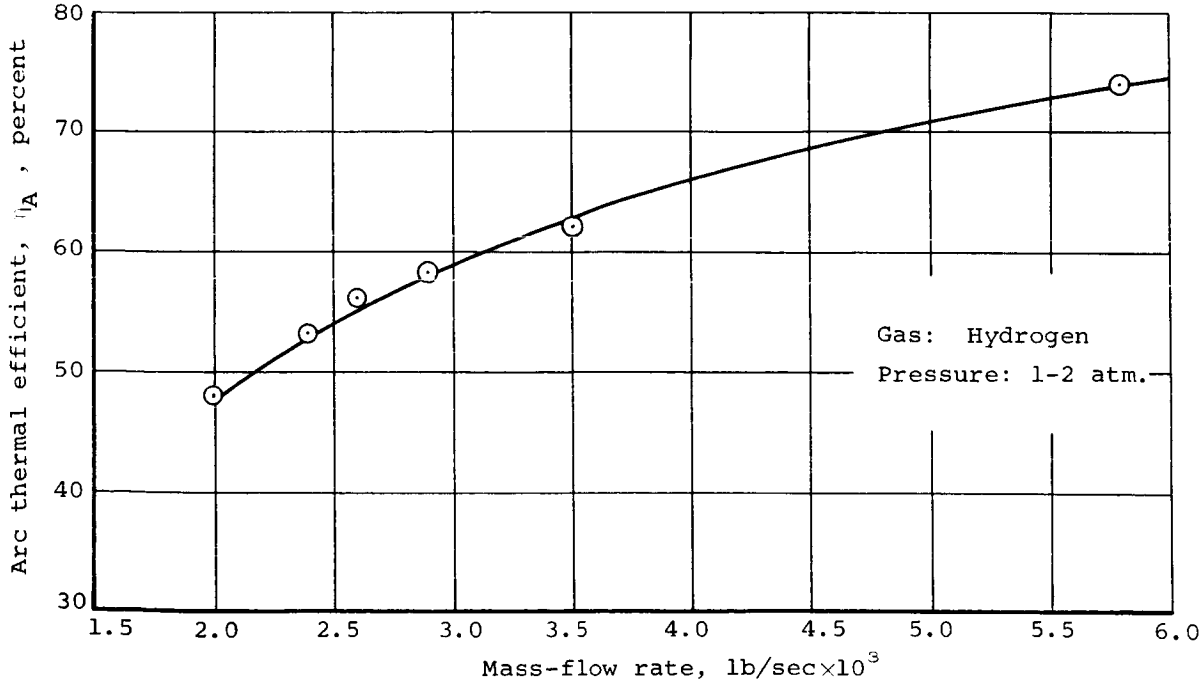


Figure 44.- Arc thermal efficienty as a function of mass-flow rate for hydrogen operation.

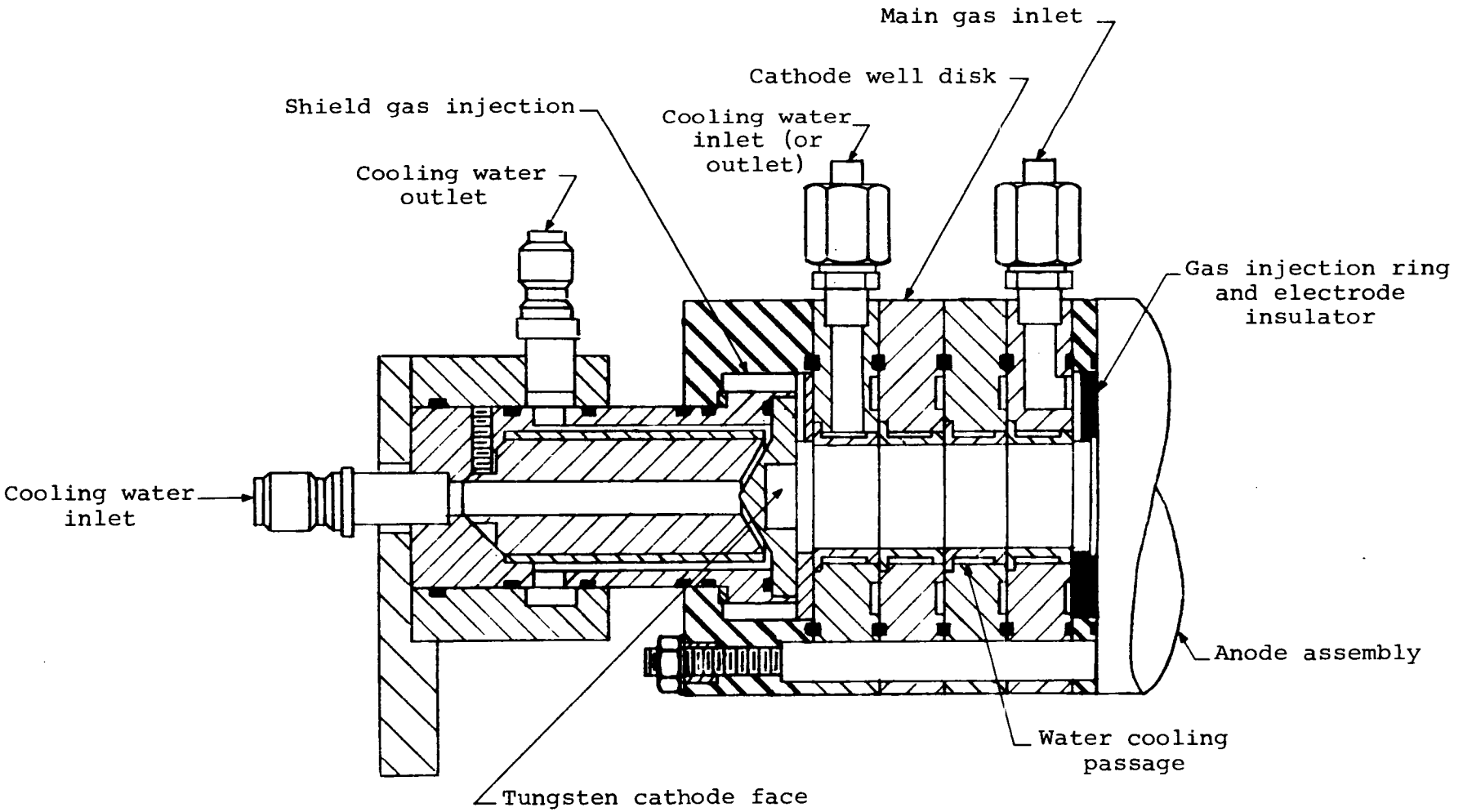


Figure 45.- New cathode configuration, constrictor arc-plasma generator.

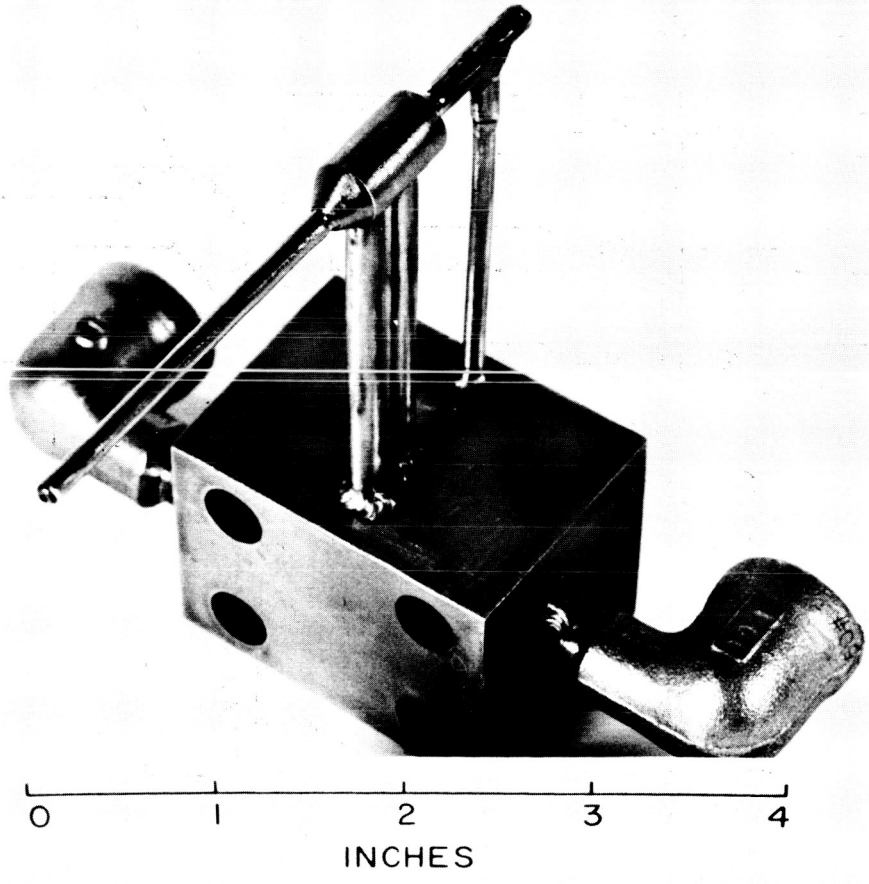


Figure 46.- Water-cooled gas-sampling probe.

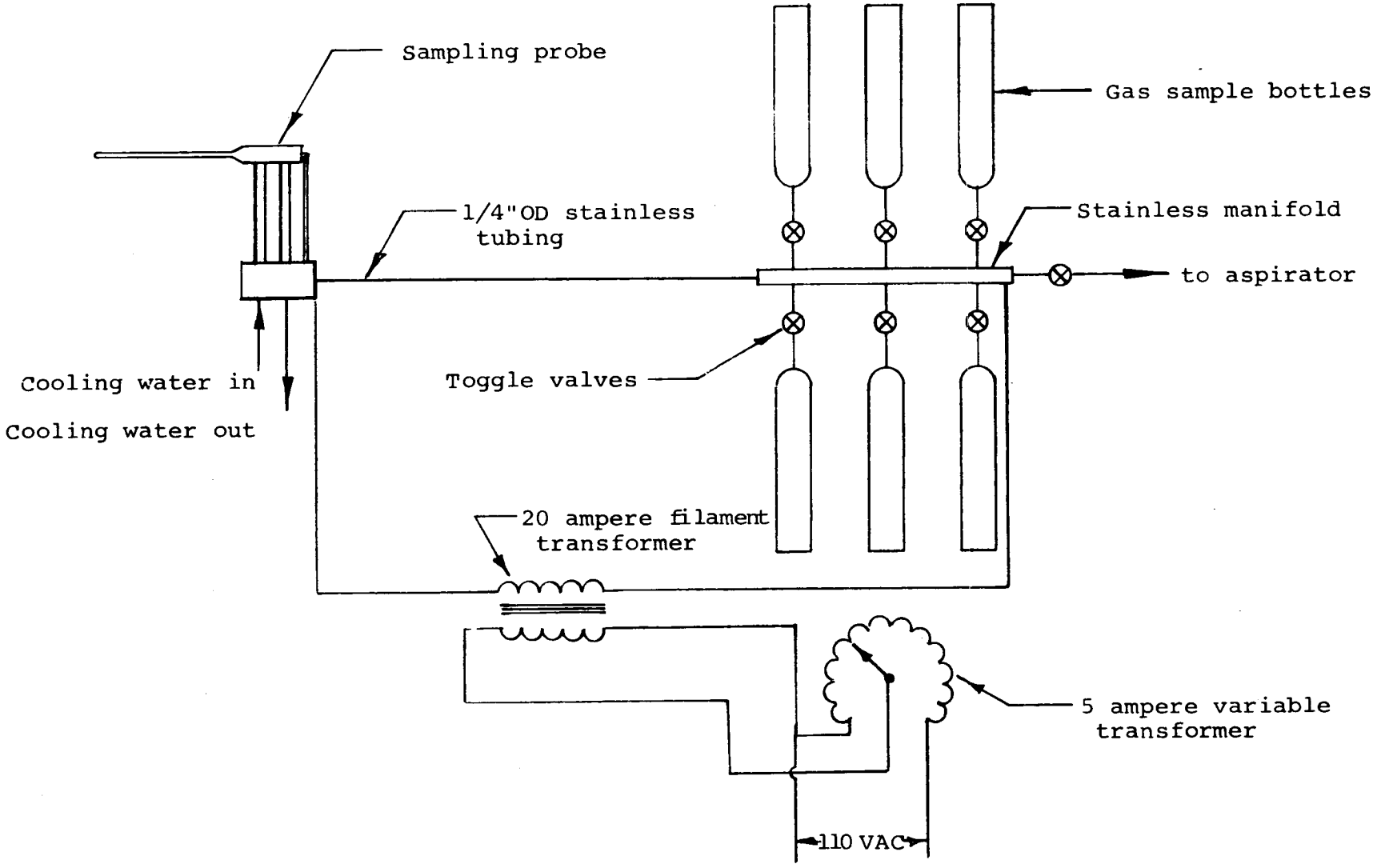
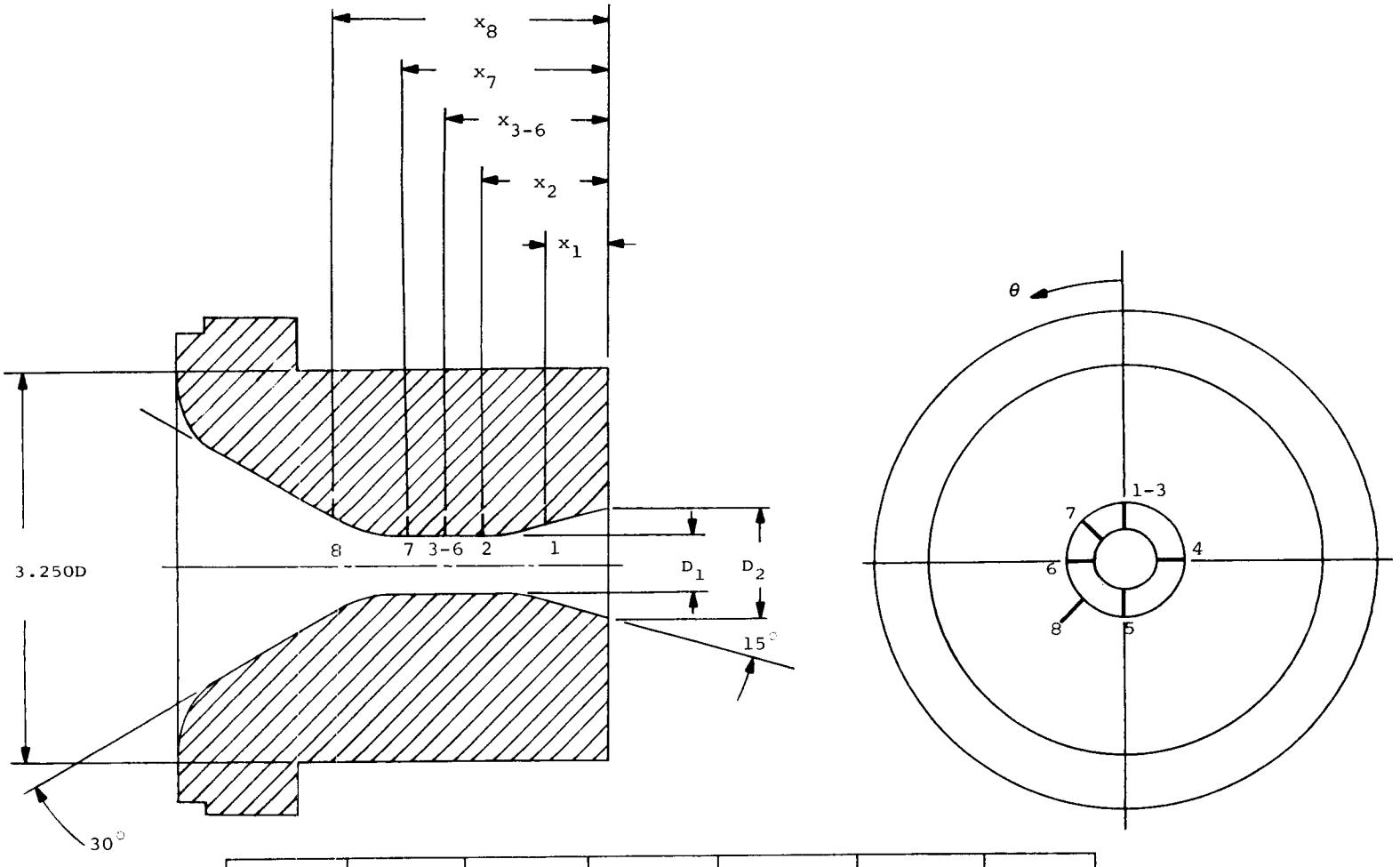


Figure 47.- Schematic representation of the gas-sampling system including the heating method for the sampling tube and manifold.



D_1	D_2	x_1	x_2	x_{3-6}	x_7	x_8
0.300	0.525	0.296	0.599	0.901	1.213	1.703
0.400	0.695	0.375	0.750	1.071	1.382	2.000
0.500	0.875	0.461	0.923	1.235	1.547	2.300
0.700	1.228	0.632	1.256	1.568	1.880	2.896

Figure 48.- Pressure-tap locations in calibration nozzles.

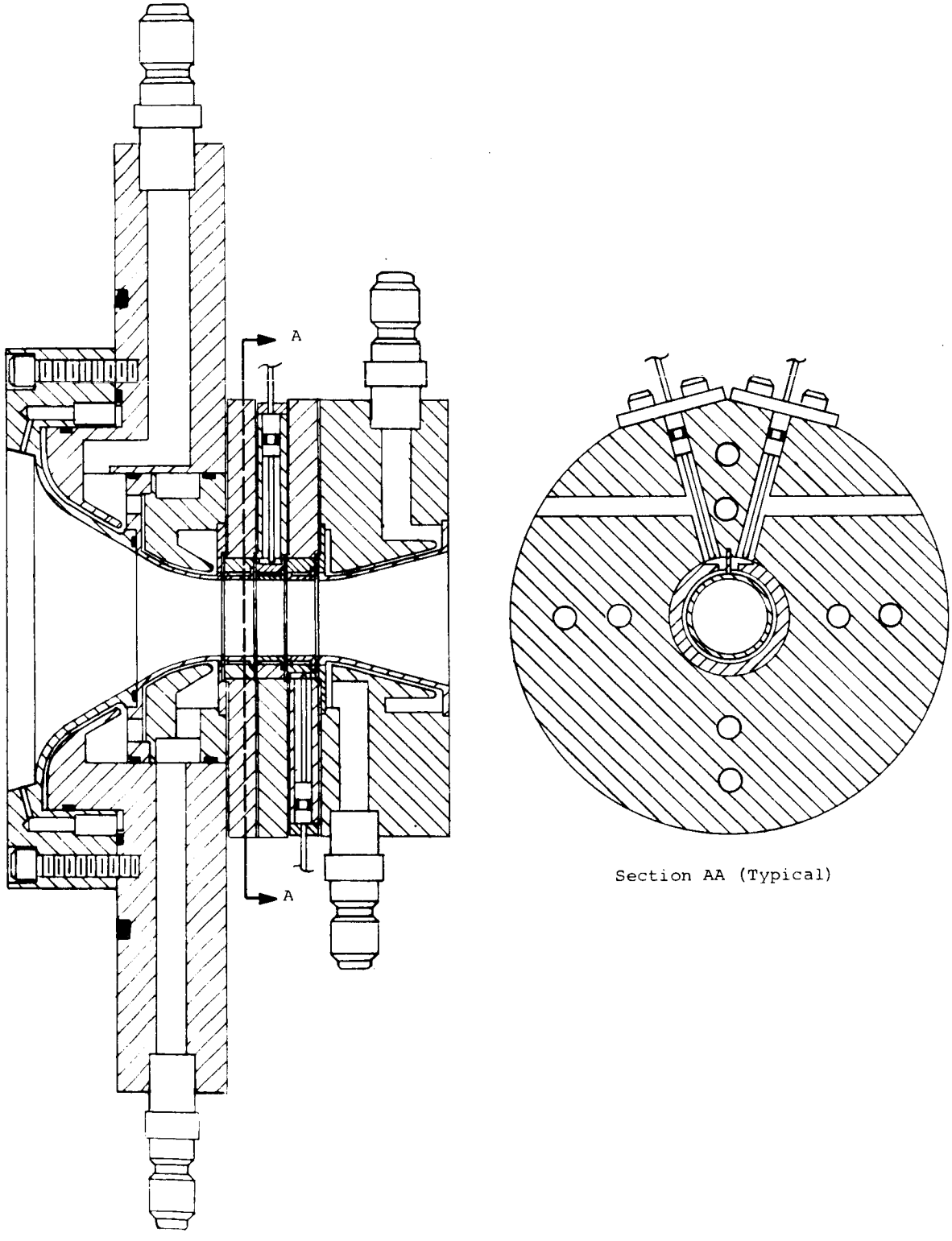


Figure 49.- Schematic drawing of typical heat-transfer calibration nozzle.

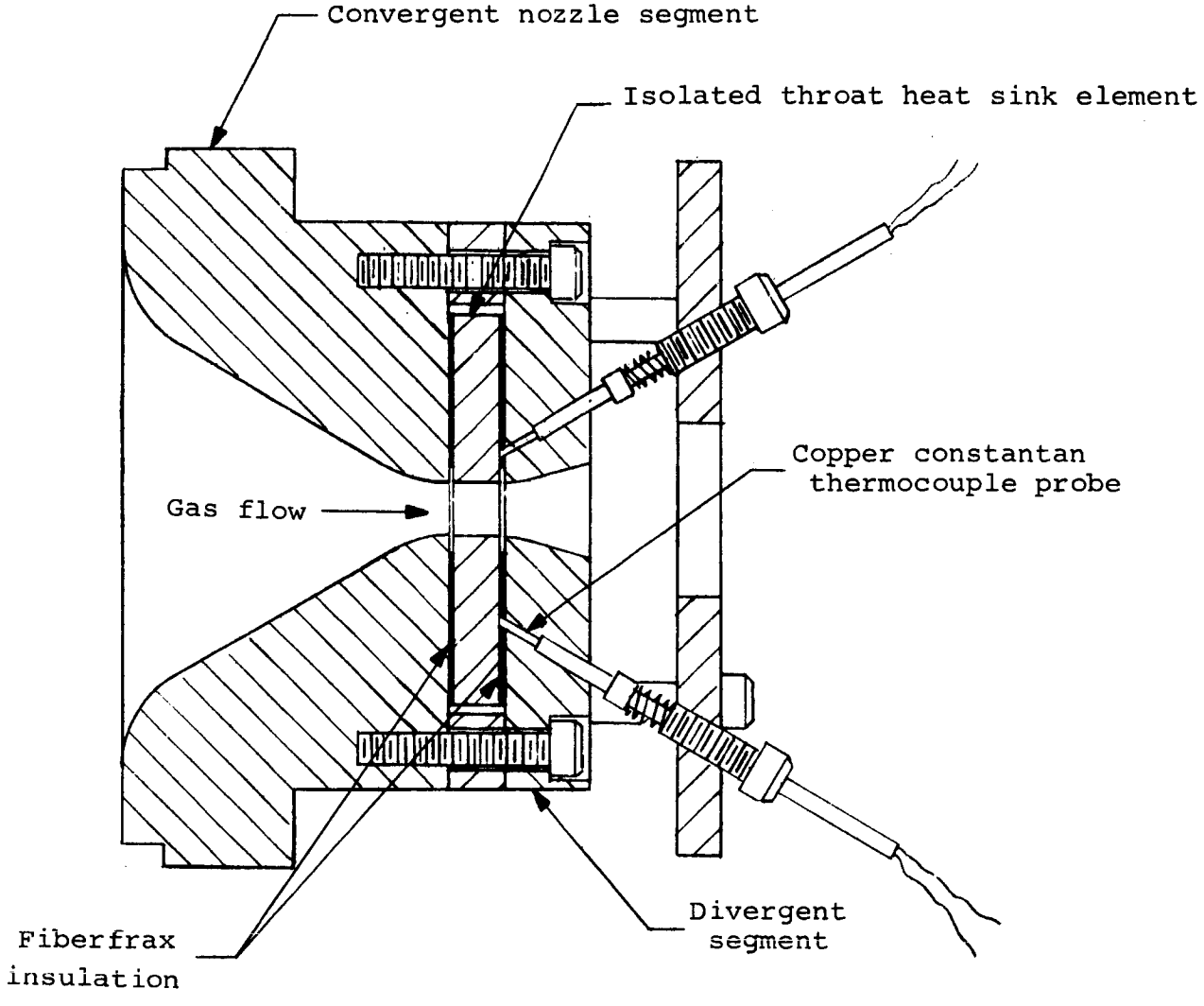


Figure 50.- Section representation of the hot-wall calorimeter model.

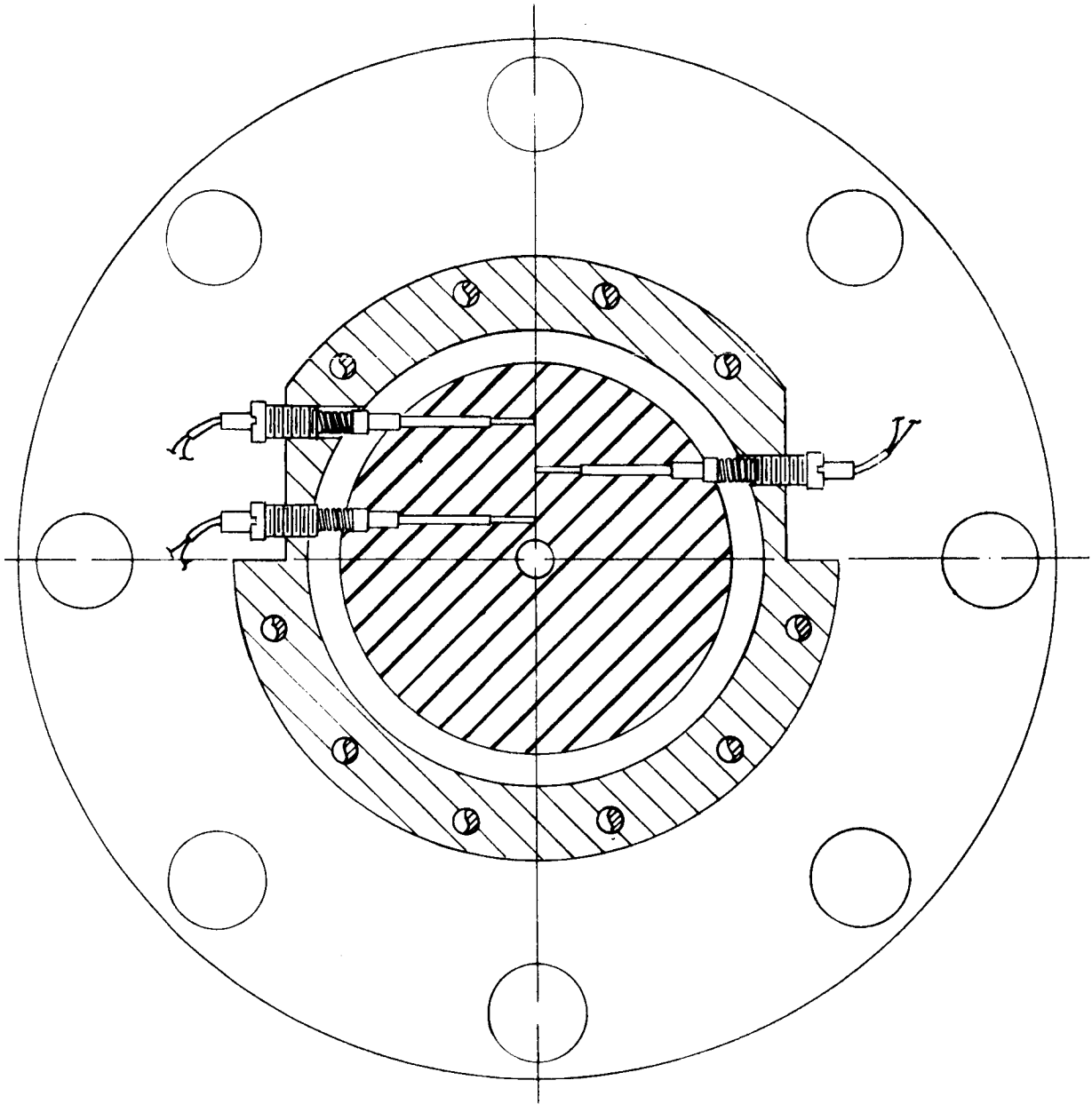


Figure 51.- Thermocouple mounting scheme.

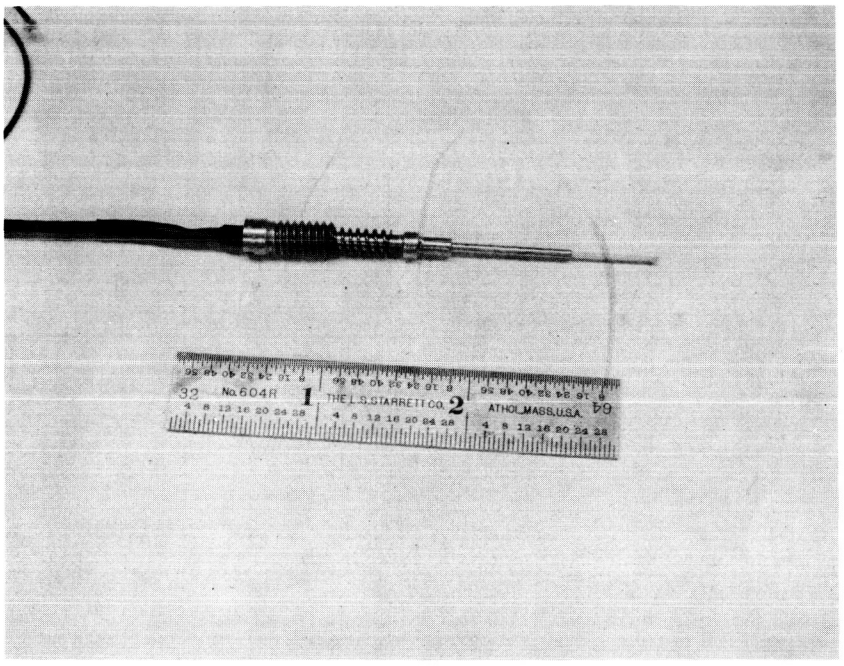


Figure 52.- Thermocouple probe.

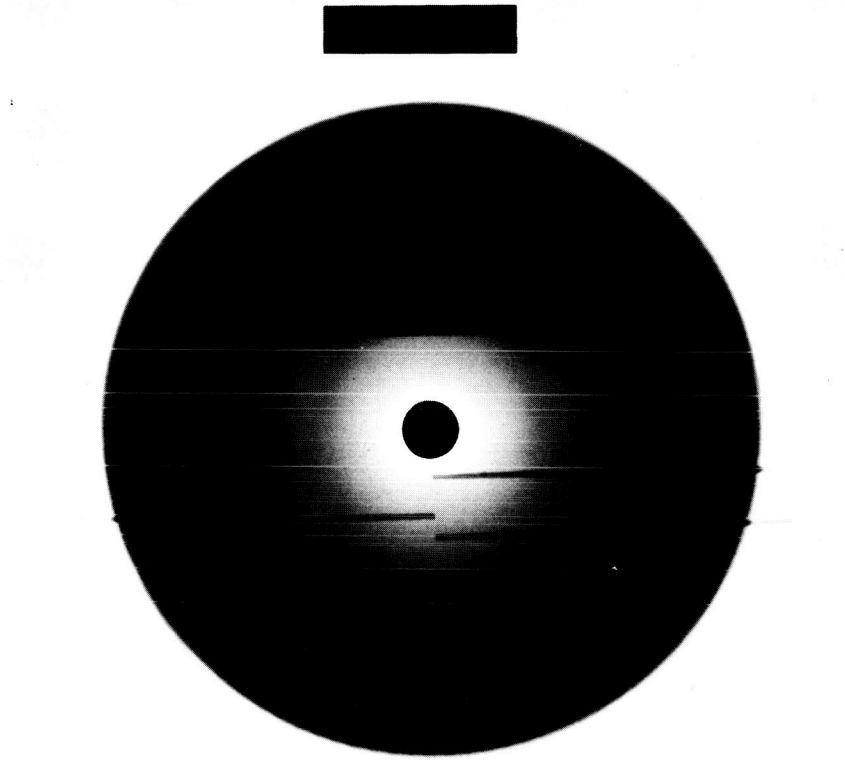


Figure 53.- Typical X-ray photograph of thermocouple-probe locations.

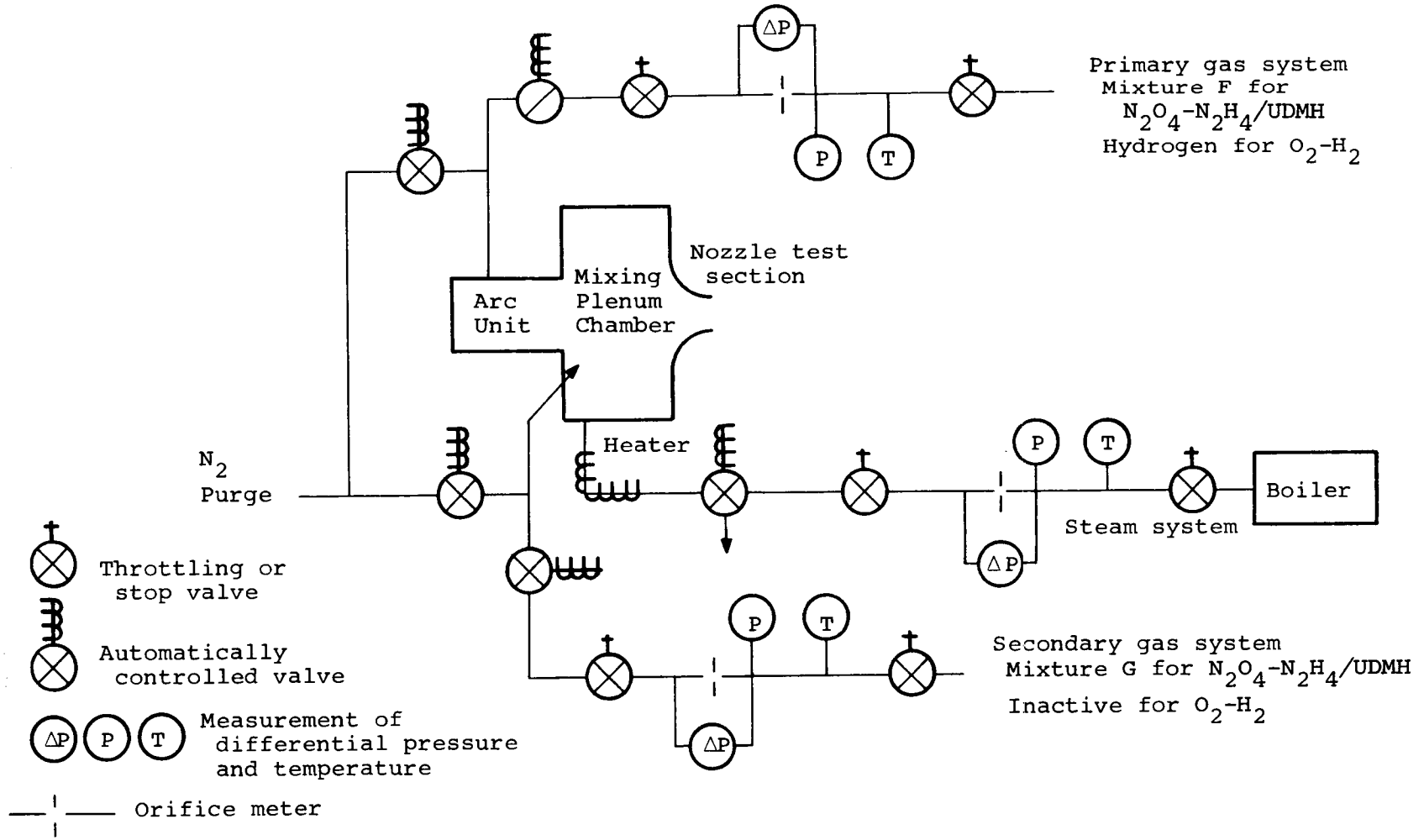
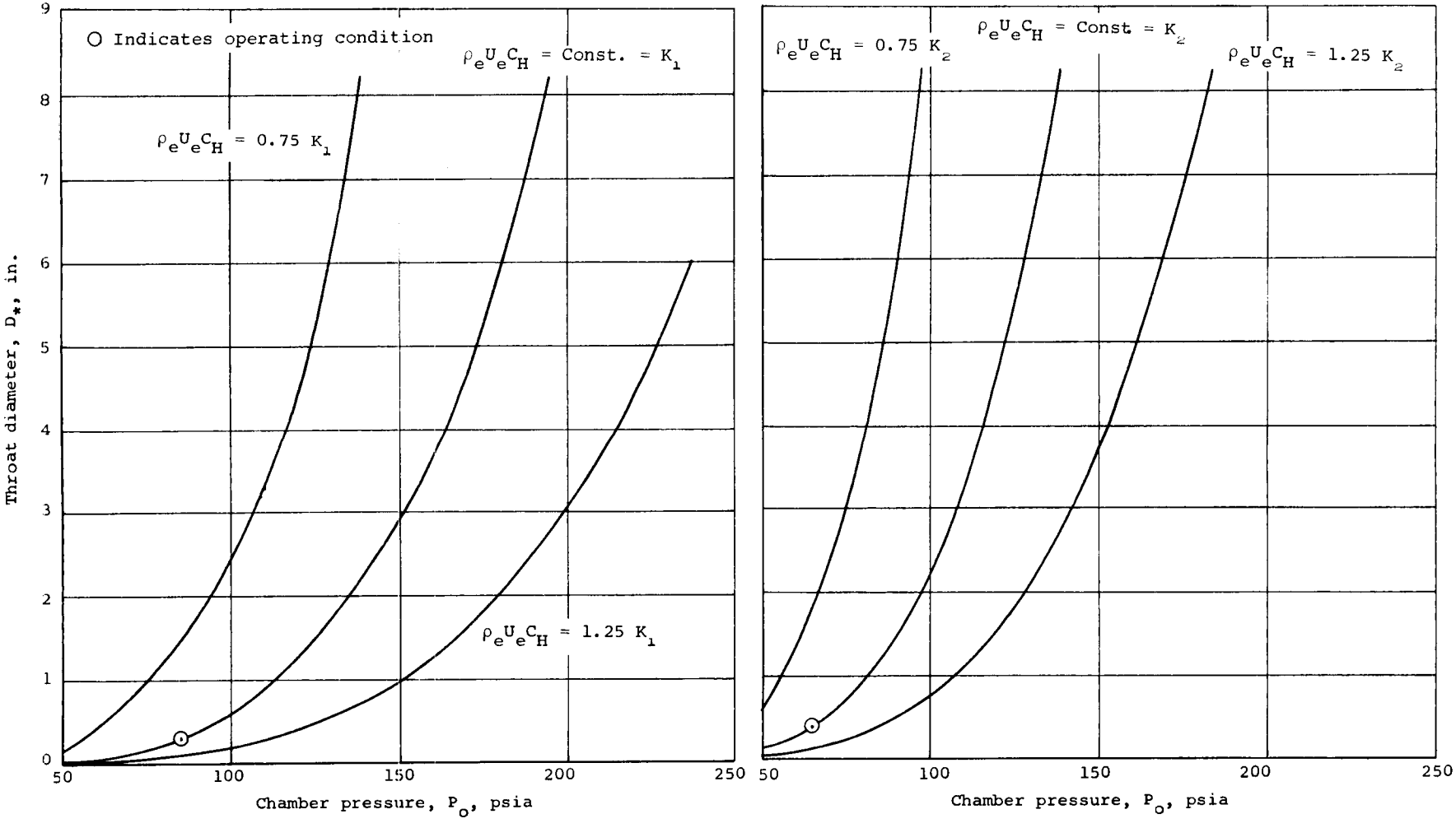


Figure 54.- Schematic of gas systems for liquid engine simulation.



(a) N_2O_4-N_2H_4/UDMH propellant.

(b) O_2-H_2 propellant.

Figure 55.- Comparison of arc-plasma generator simulation capabilities to rocket-engine test conditions.

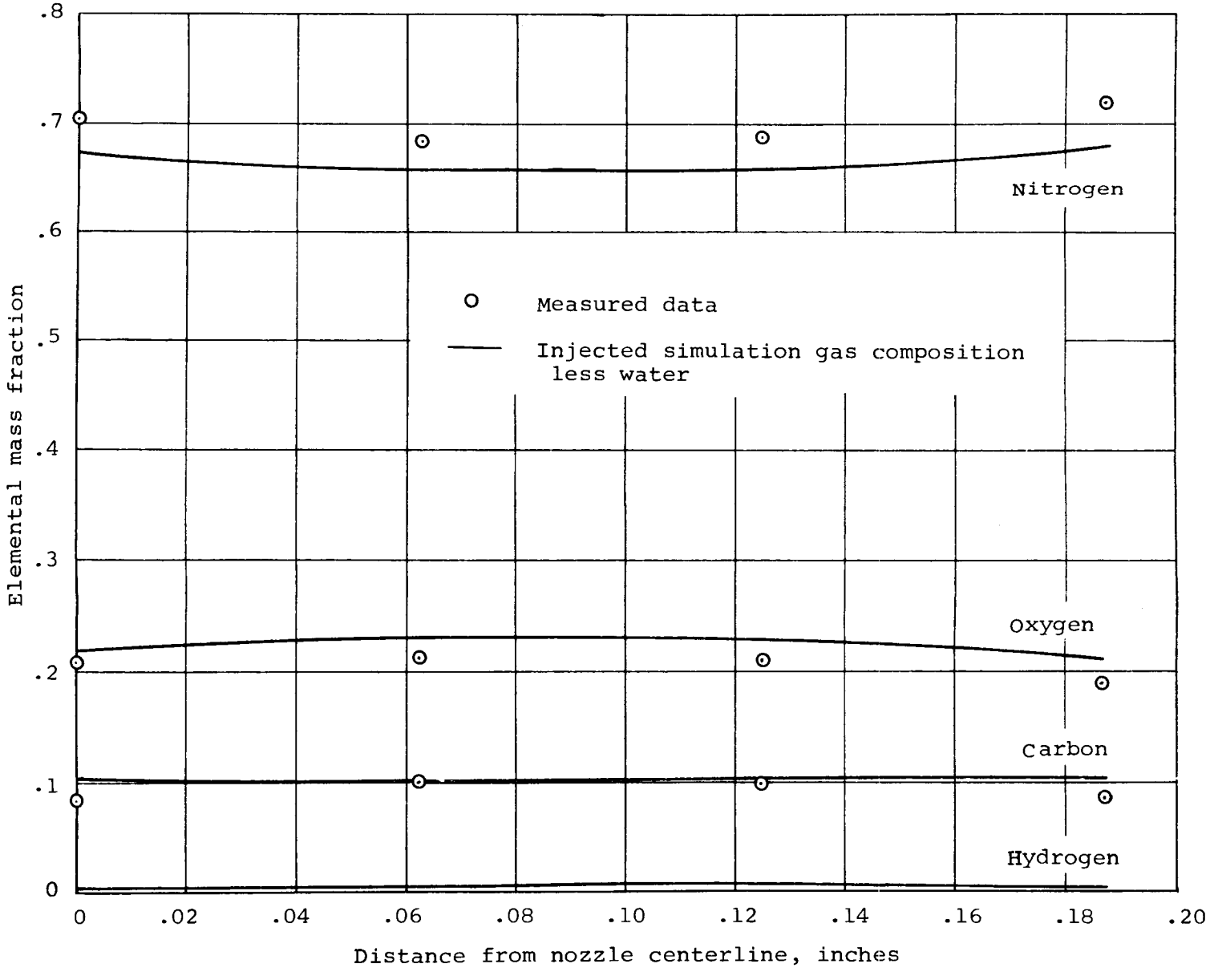


Figure 56.- Comparison of measured gas composition to that which would occur if perfect mixing were obtained. Test No. 252.

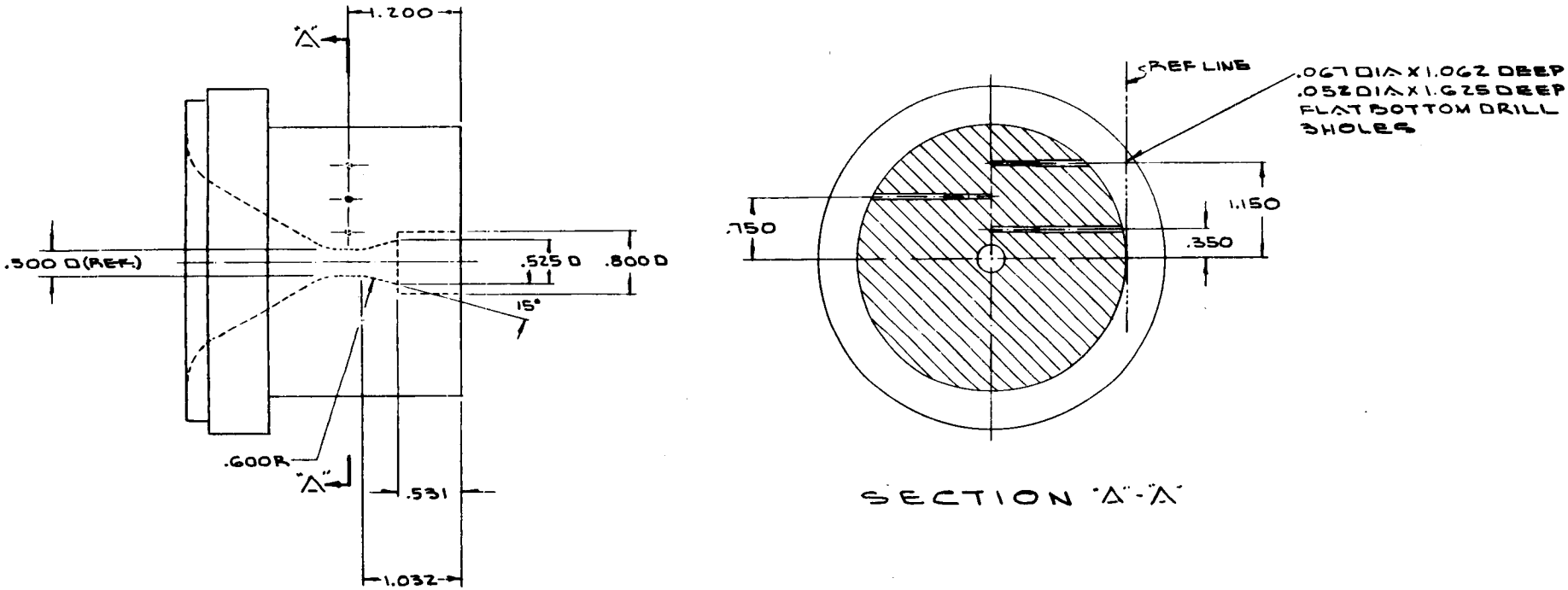


Figure 57.- Typical ablating nozzle configuration; 0.3-inch-diameter nozzle shown.

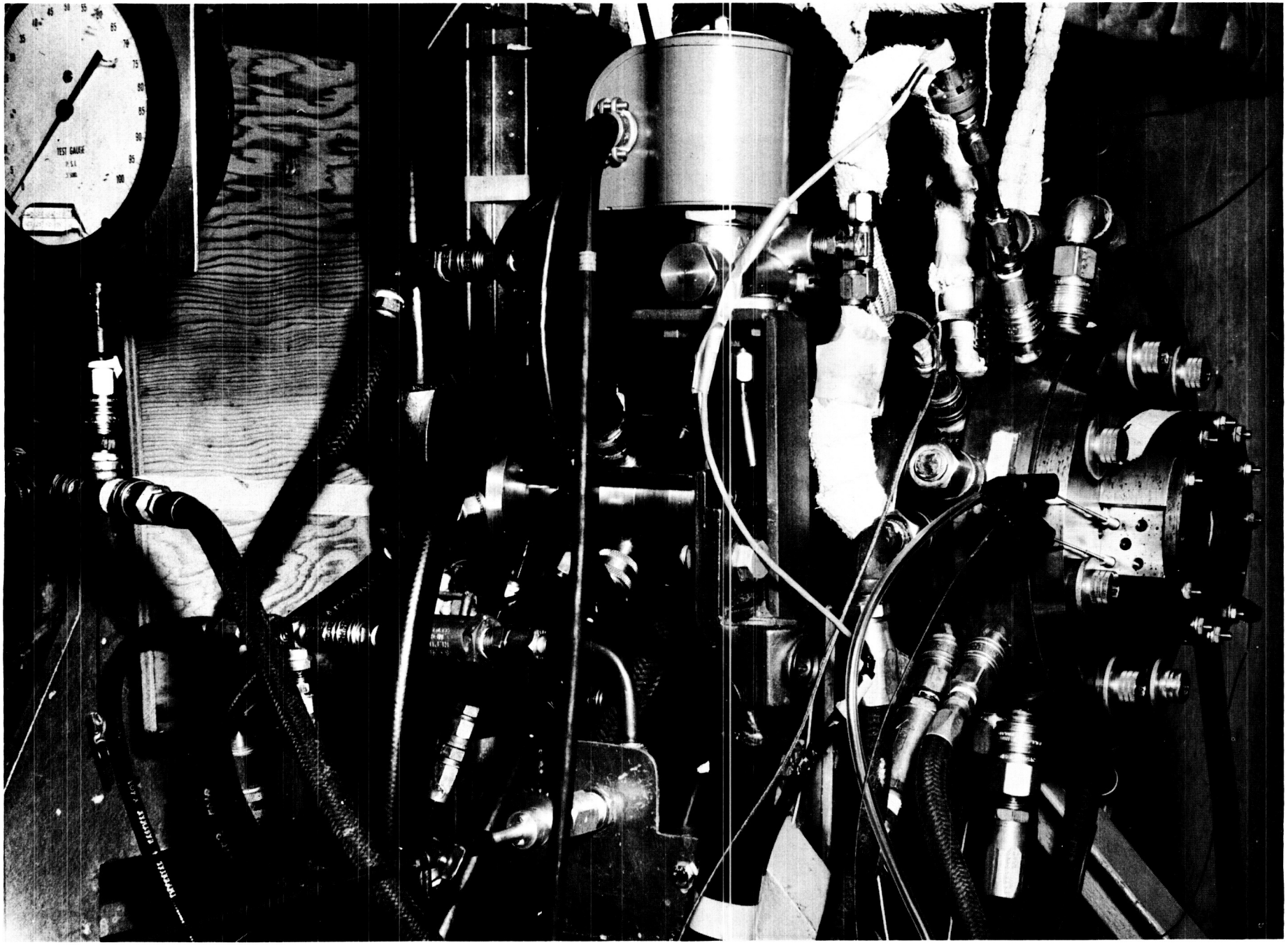
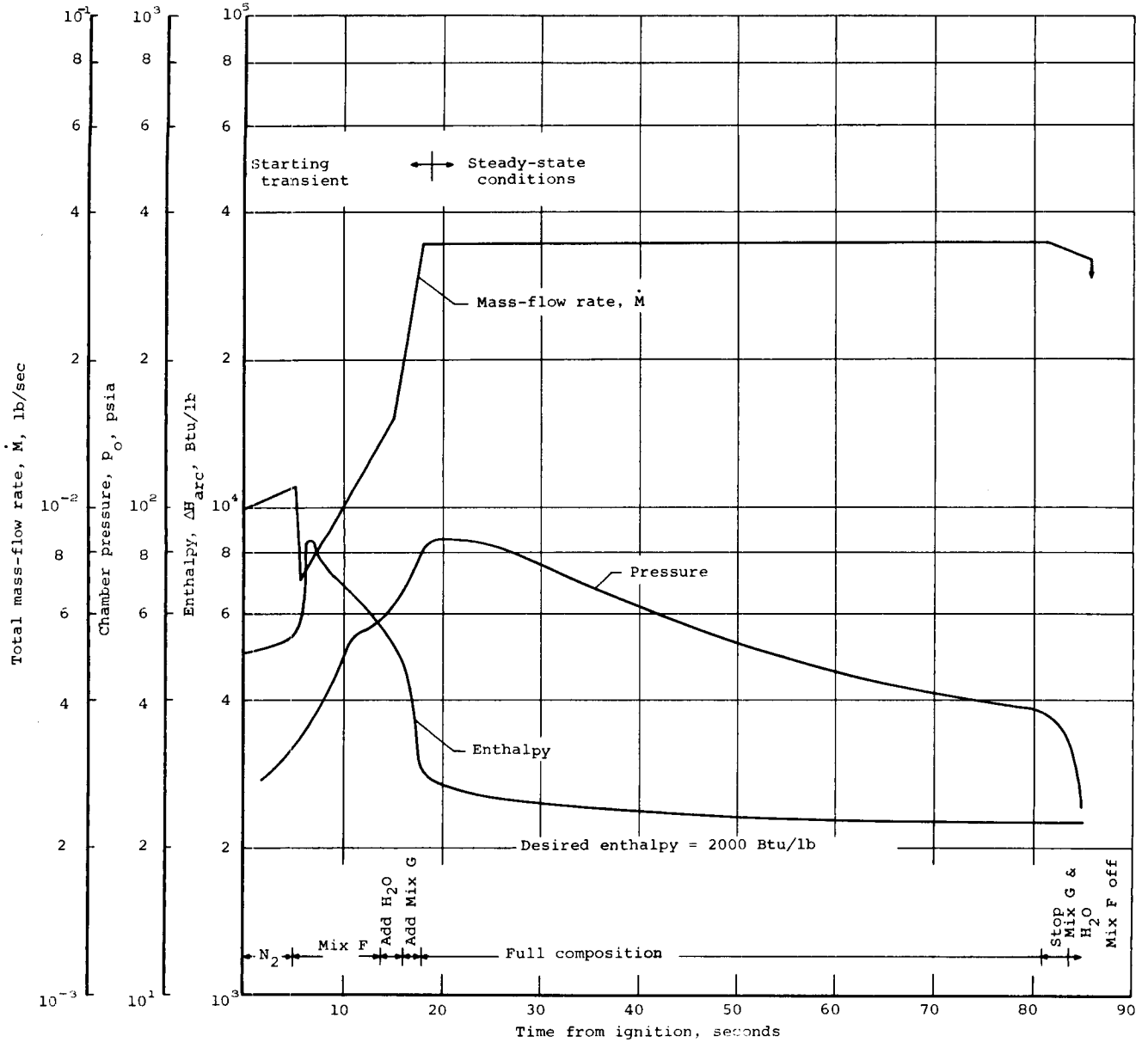
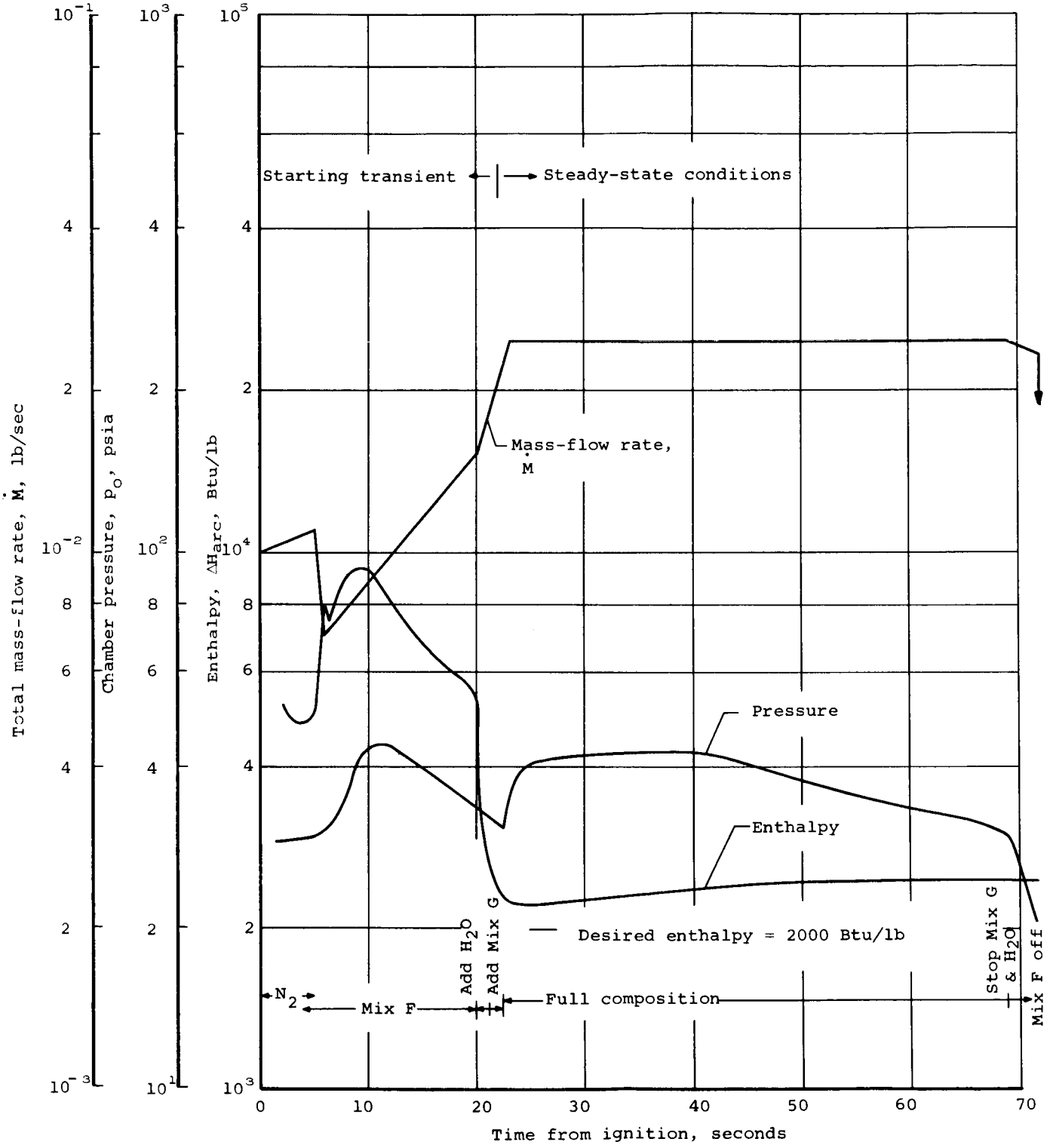


Figure 58.- Constrictor arc-plasma generator with instrumented test nozzle attached.



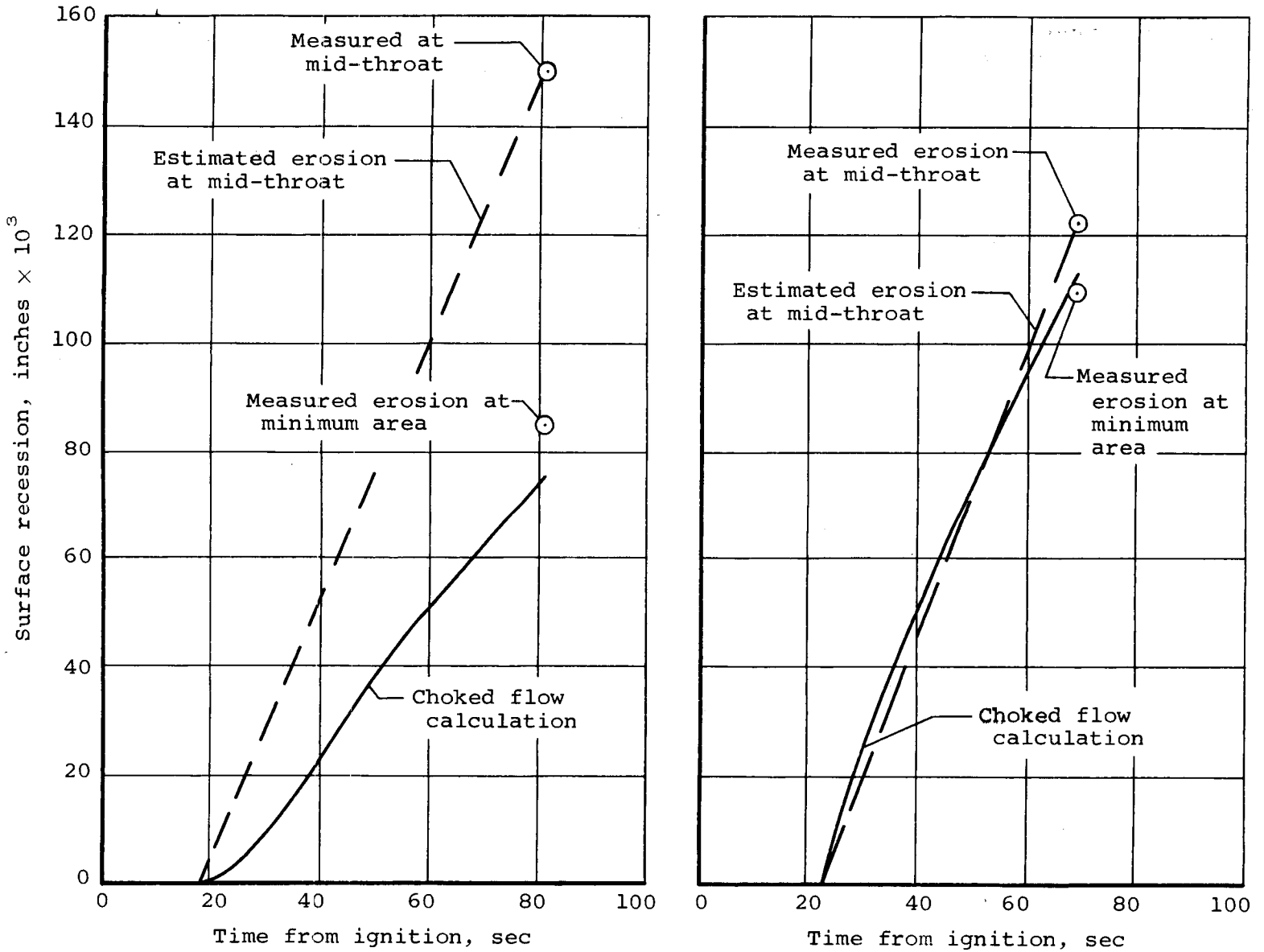
(a) Test No. 295, graphite phenolic, MX 4500.

Figure 59.- Enthalpy, pressure, and mass-flow rate histories for ablation material test in the N_2O_4-N_2H_4/UDMH environment.



(b) Test No. 296, silica phenolic, MX 2600.

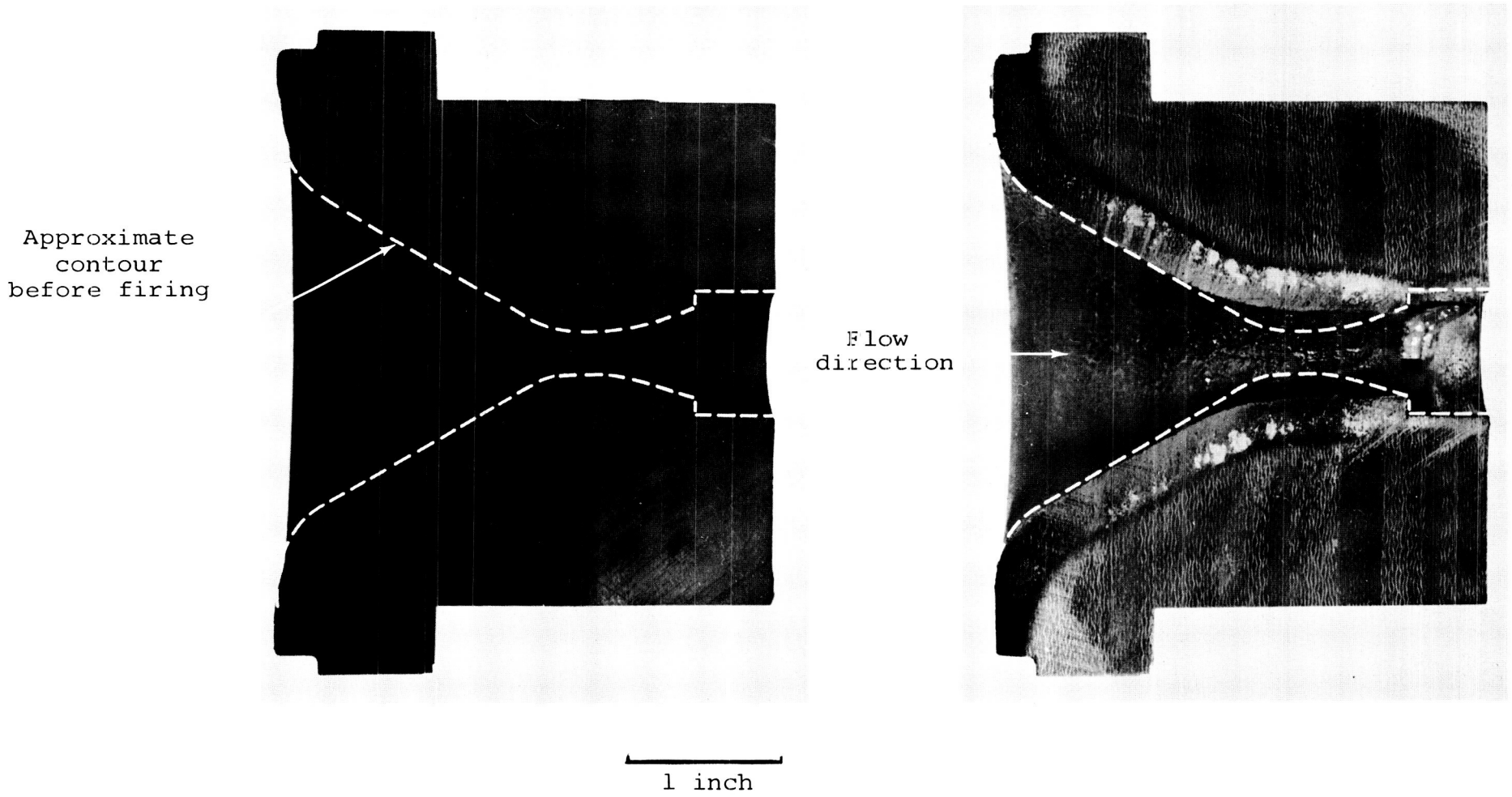
Figure 59.- Concluded.



(a) Test No. 295, graphite phenolic, MX 4500.

(b) Test No. 296, silica phenolic, MX 2600.

Figure 60.- Throat recession data for N_2O_4-N_2H_4/UDMH simulation test series.



(a) Test No. 295, graphite phenolic, MX 4500.

(b) Test No. 296, silica phenolic, MX 2600.

Figure 61.- Post-test view of sectioned nozzles from N_2O_4-N_2H_4/UDMH simulation series.

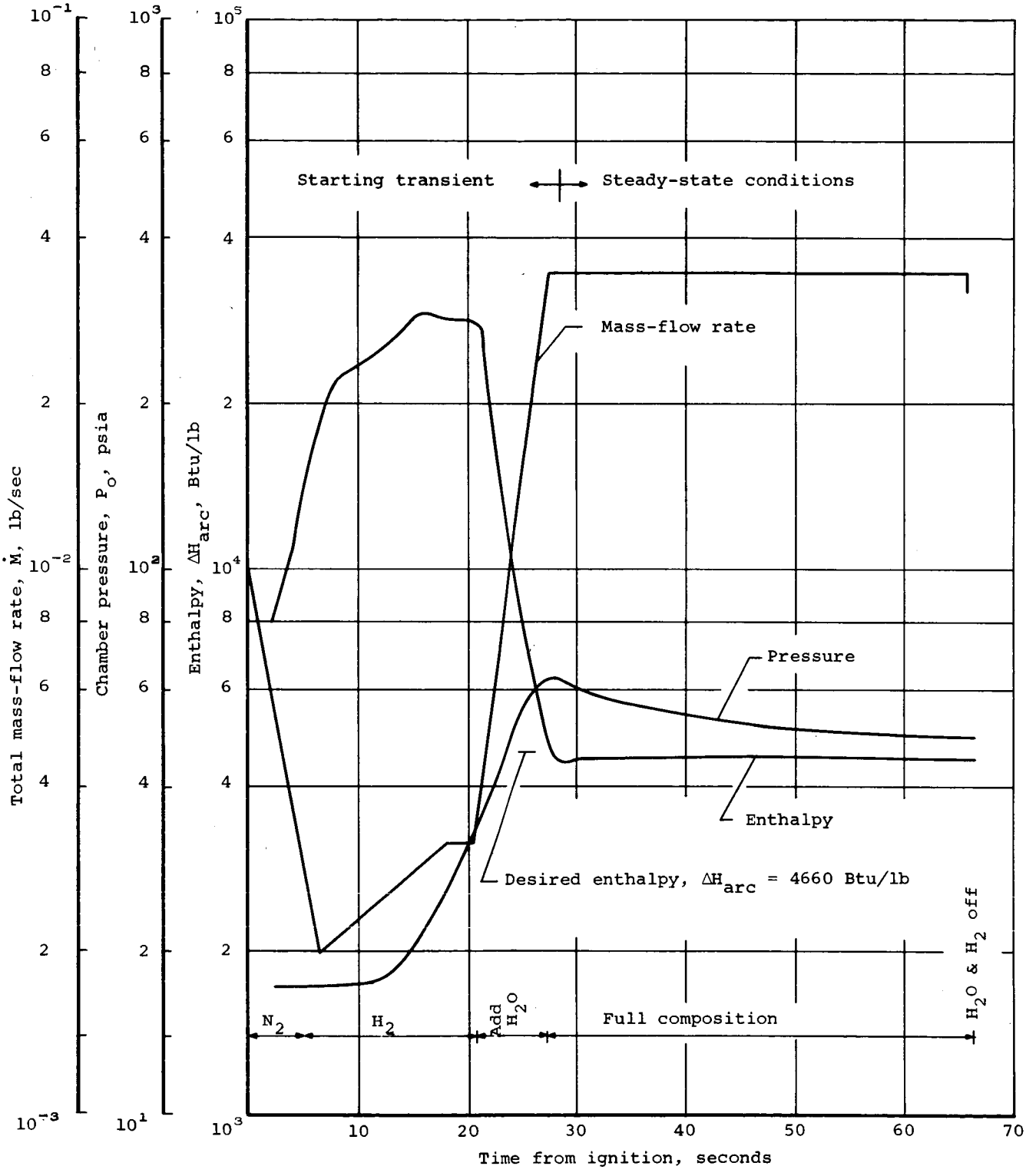


Figure 62.- Enthalpy, pressure, and mass-flow rate histories for ablation material Test No. 290, in the O_2-H_2 environment, silica phenolic, MX 2600.

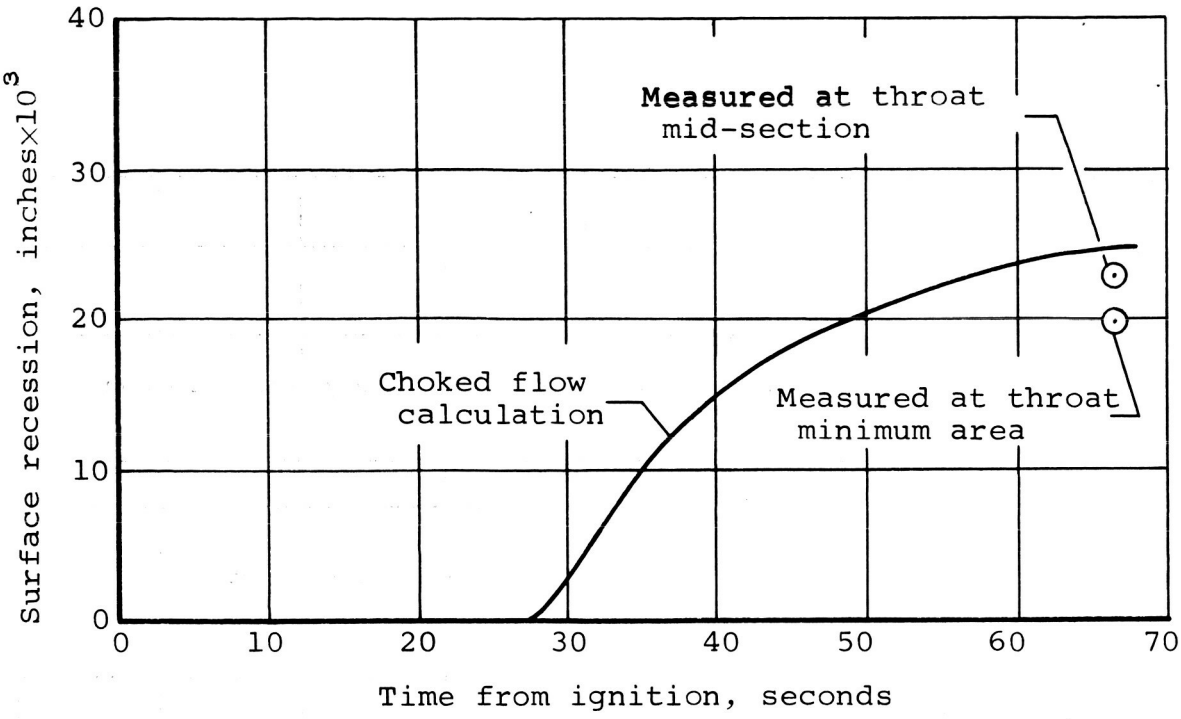


Figure 63.- Throat recession data for O_2-H_2 simulation Test No. 290, silica phenolic, MX 2600.

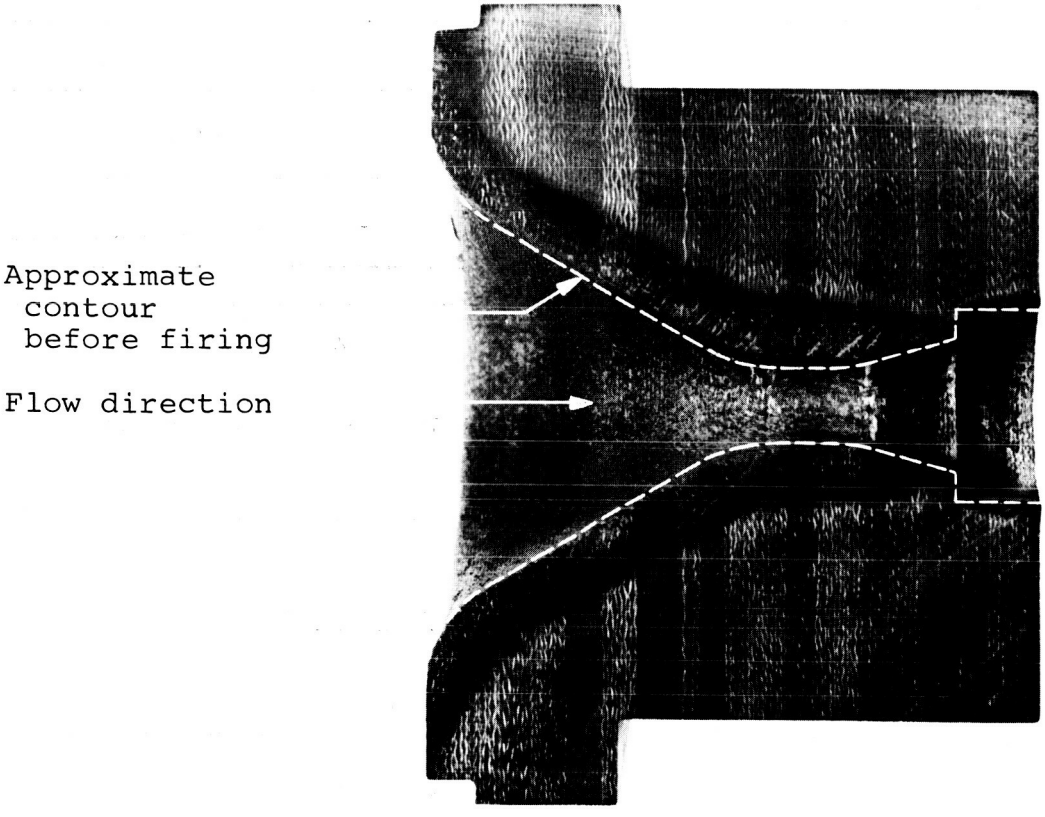


Figure 64.- Post-test view of sectioned nozzles from O_2-H_2 simulation series, silica phenolic, MX 2600.

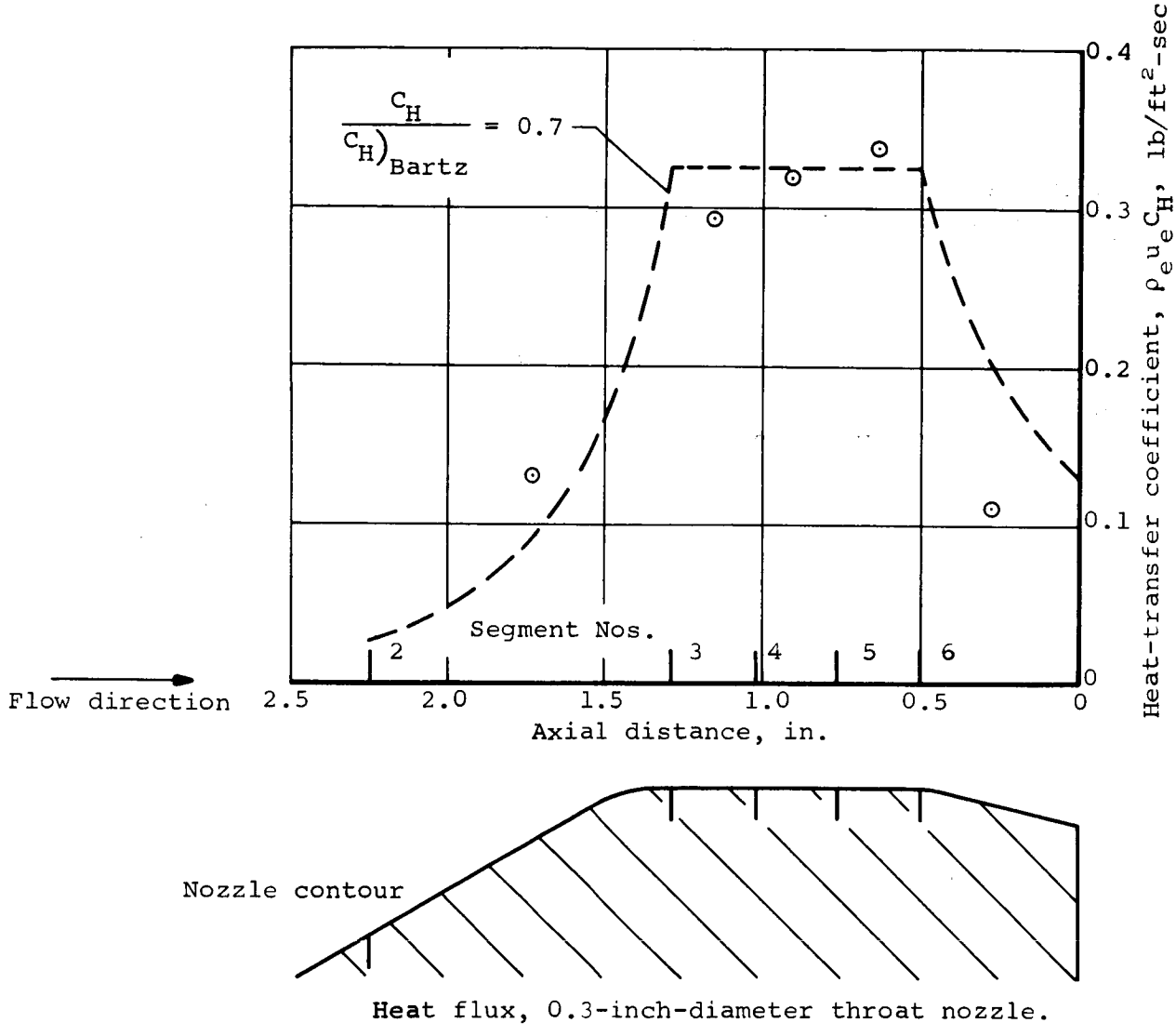
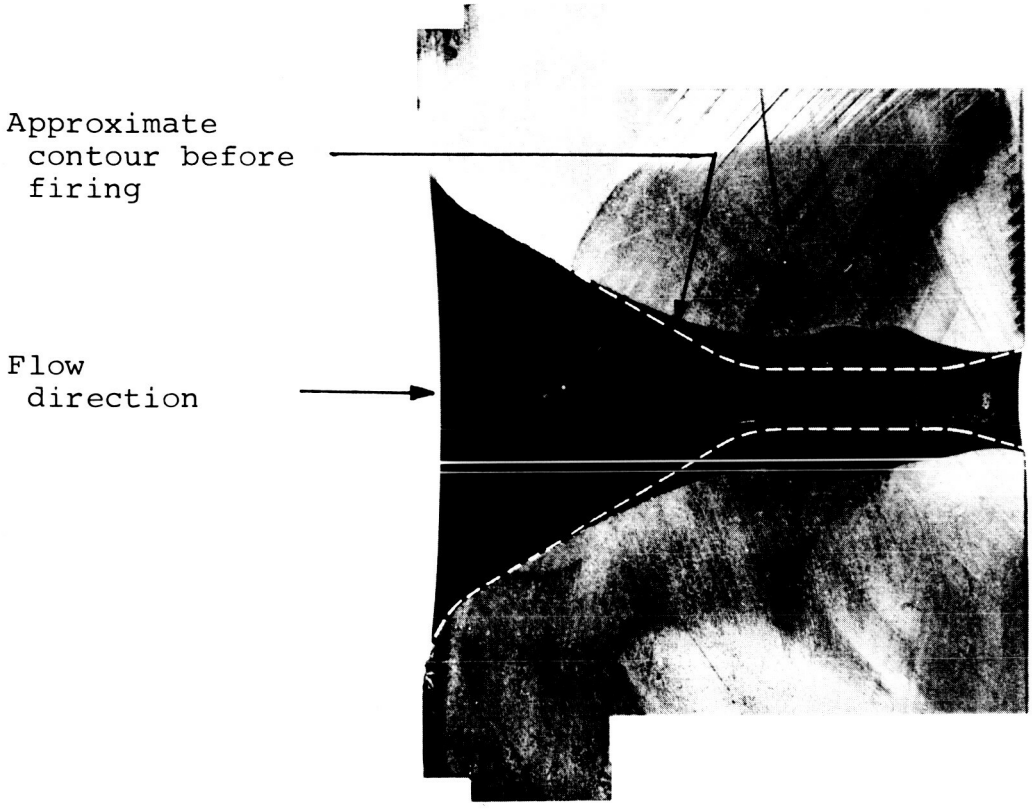
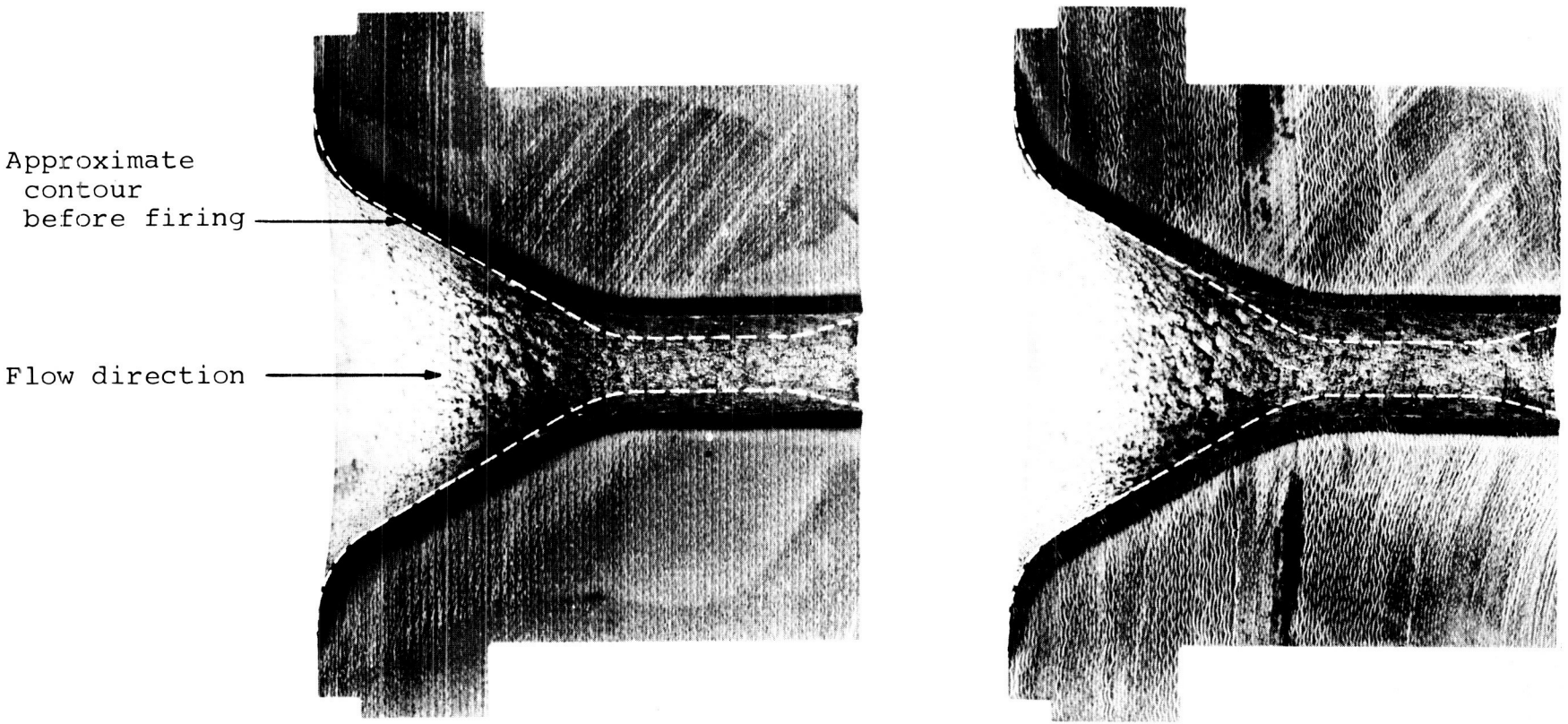


Figure 65.- Comparison of measured and predicted values of $\rho_e U_e C_H$, $D_* = 0.3$ inch, oxidation and enthalpy potential simulation, Test No. 1110.



(a) ATJ graphite, Test No. 1105.

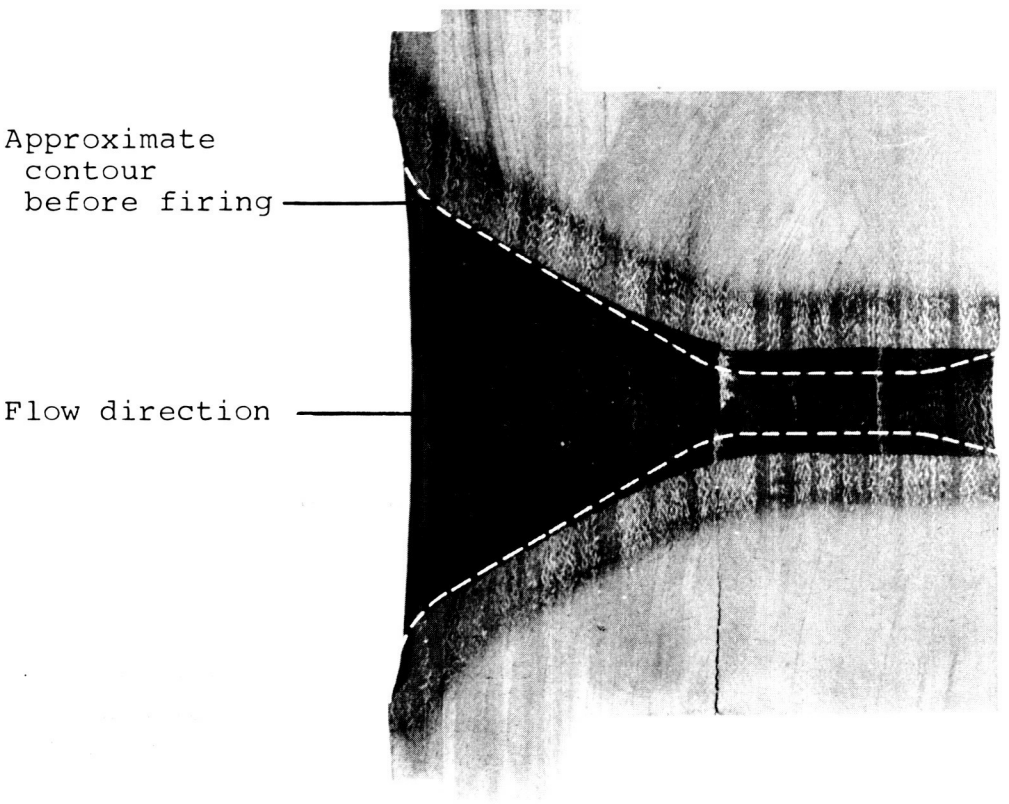
Figure 66.- Post-test view of sectioned nozzle subjected to oxidation and enthalpy potential simulation conditions.



(b) Test No. 1106, silica phenolic, MX 2600.

(c) Test No. 1107, silica phenolic, MXS 75.

Figure 66.- Continued.

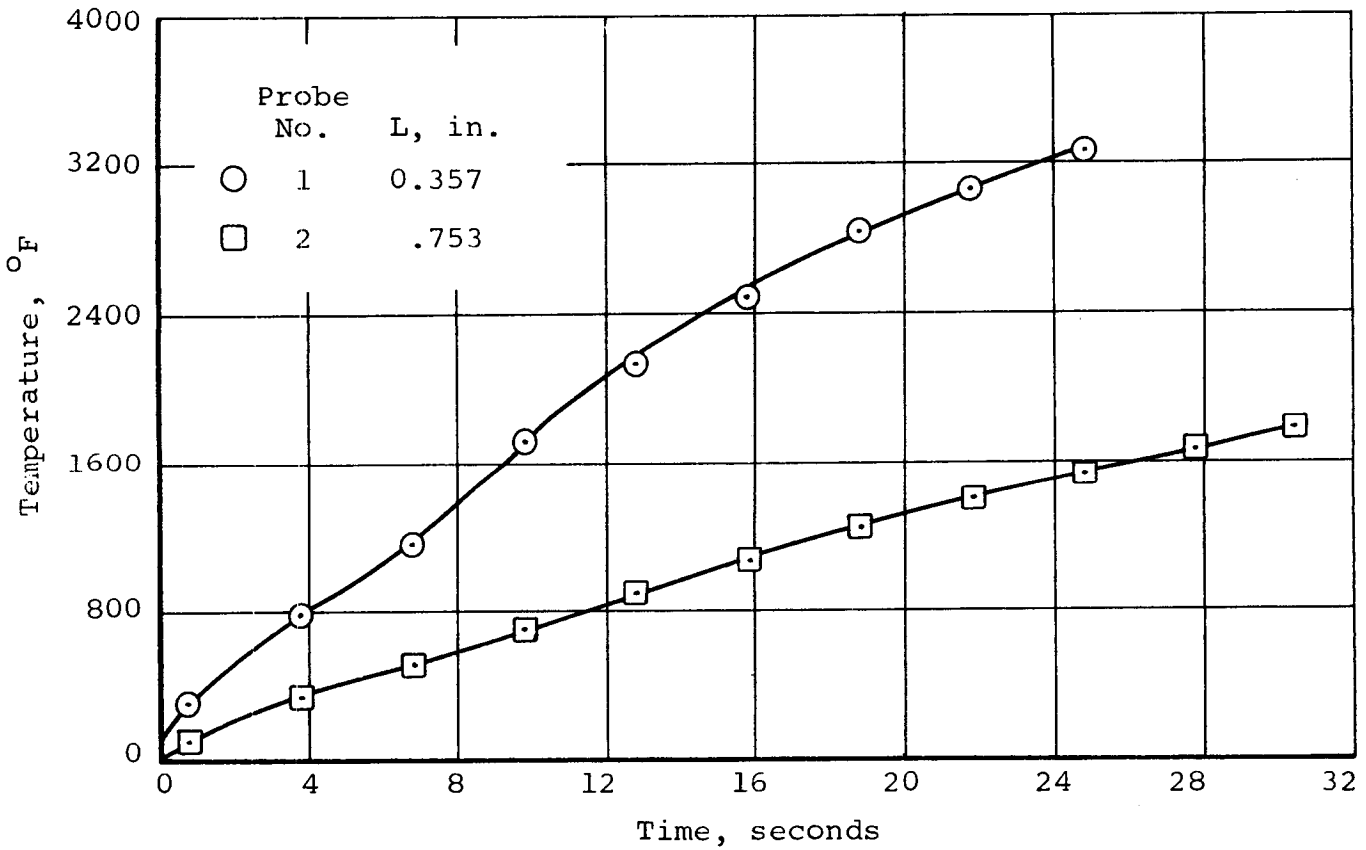


(d) Test No. 1108, graphite phenolic, MX 4500.



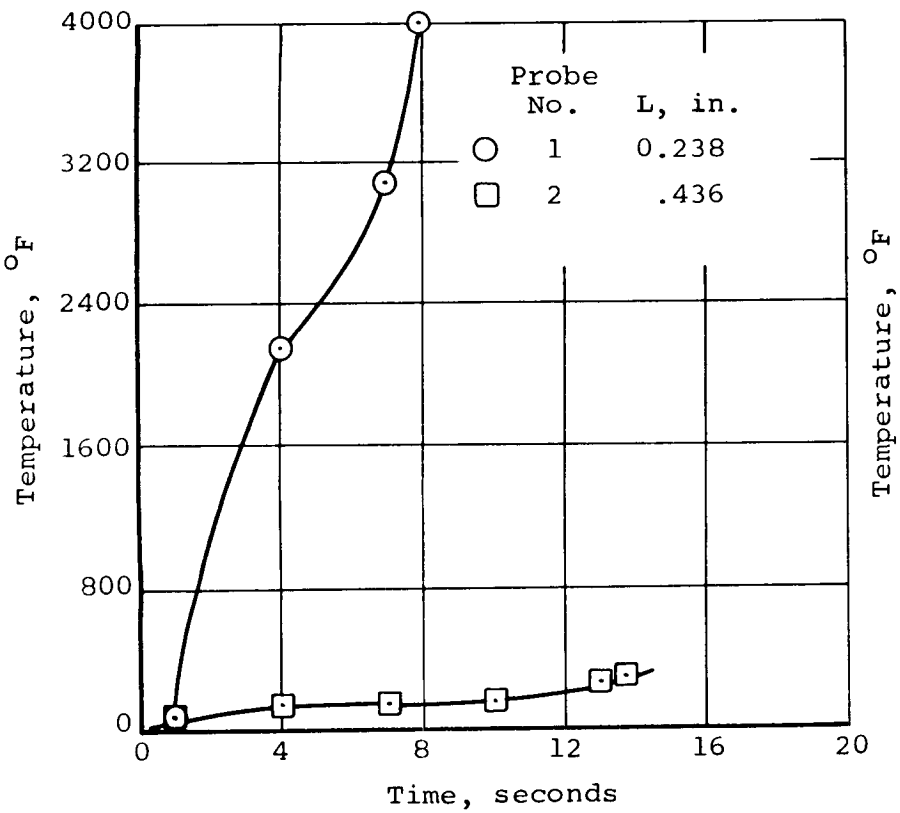
(e) Test No. 1109, silica phenolic, MXS 19.

Figure 66.- Concluded.

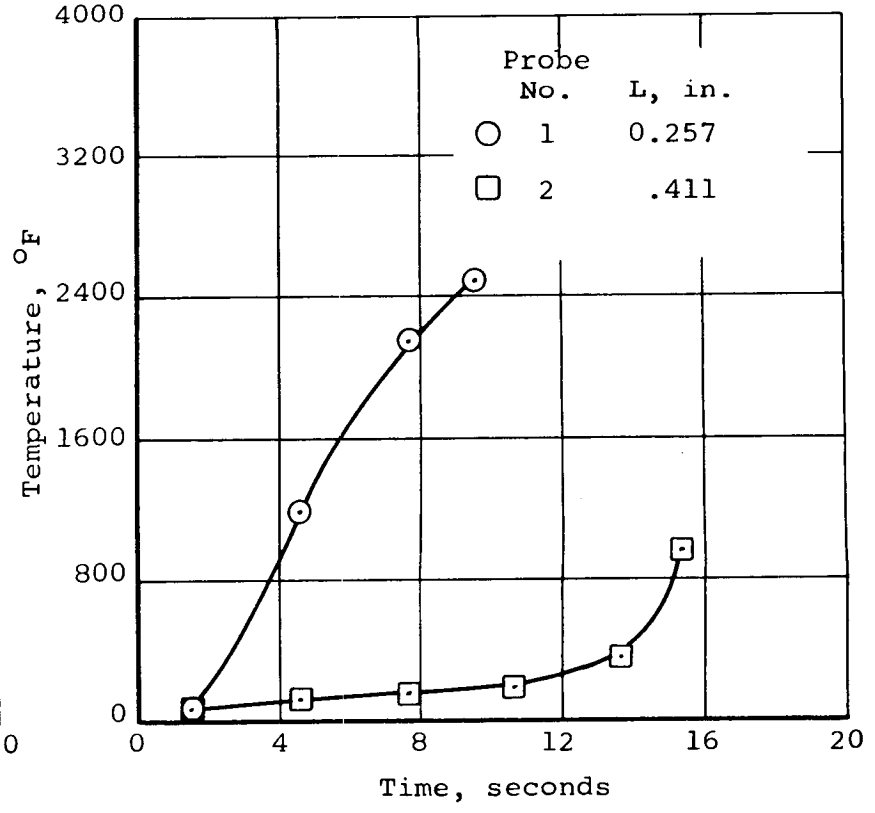


(a) Test No. 1105.

Figure 67.- Internal temperature history, Test Series IV.

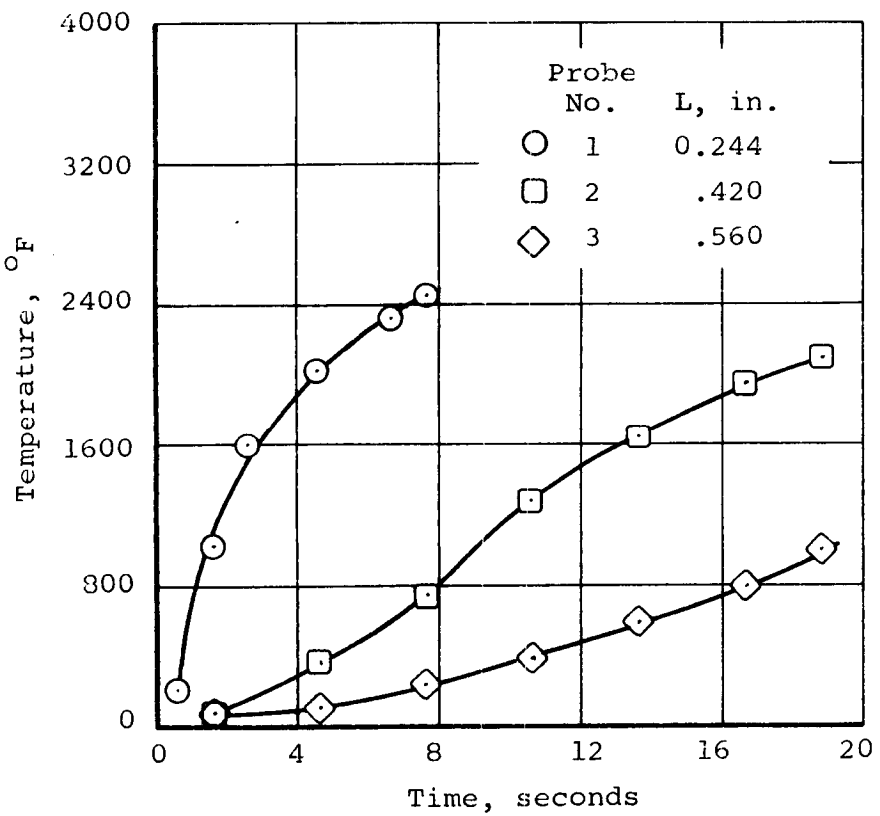


(b) Test No. 1106.

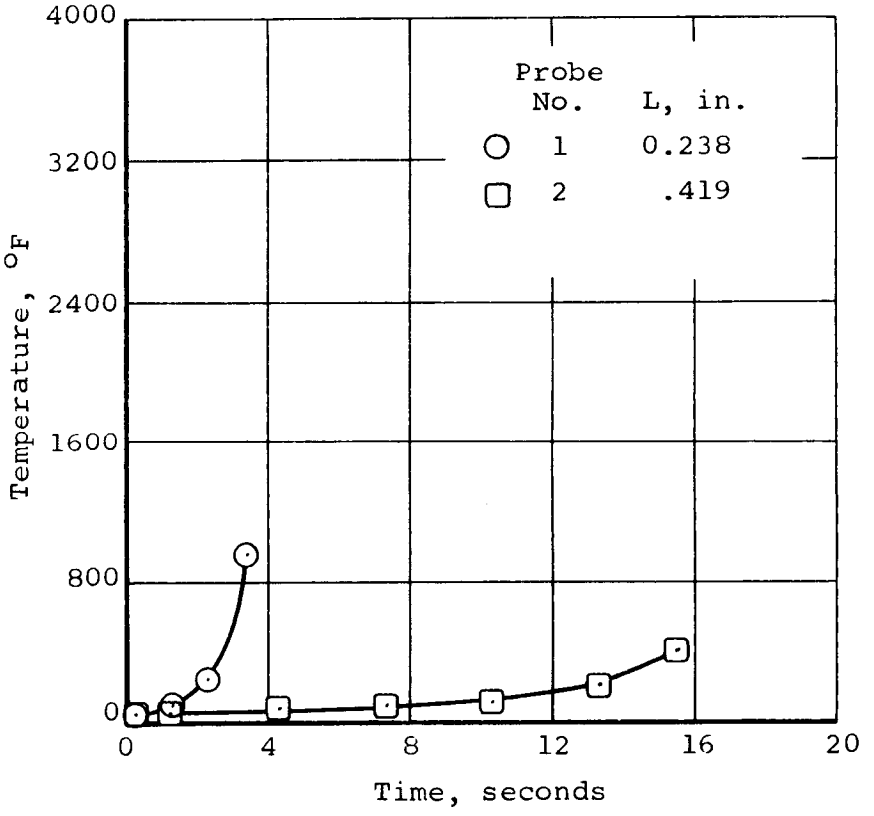


(c) Test No. 1107.

Figure 67.- Continued.

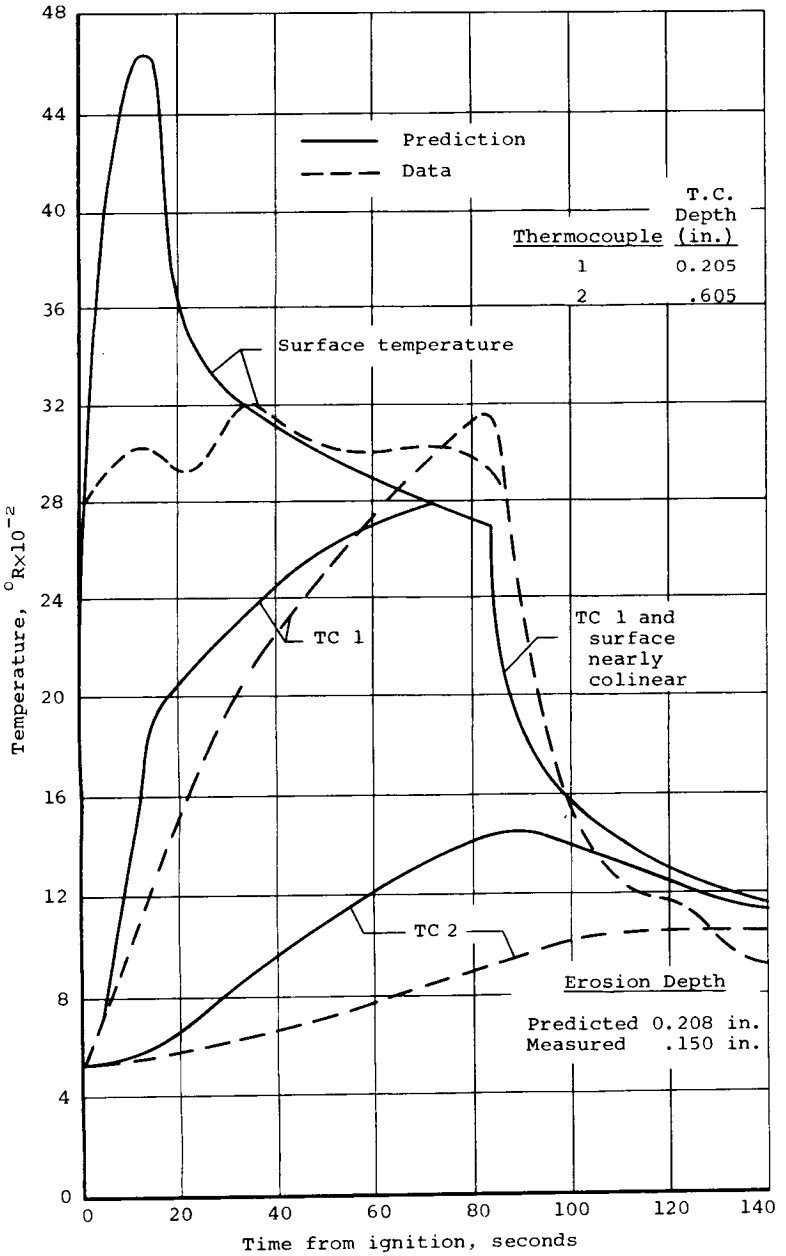


(d) Test No. 1108.

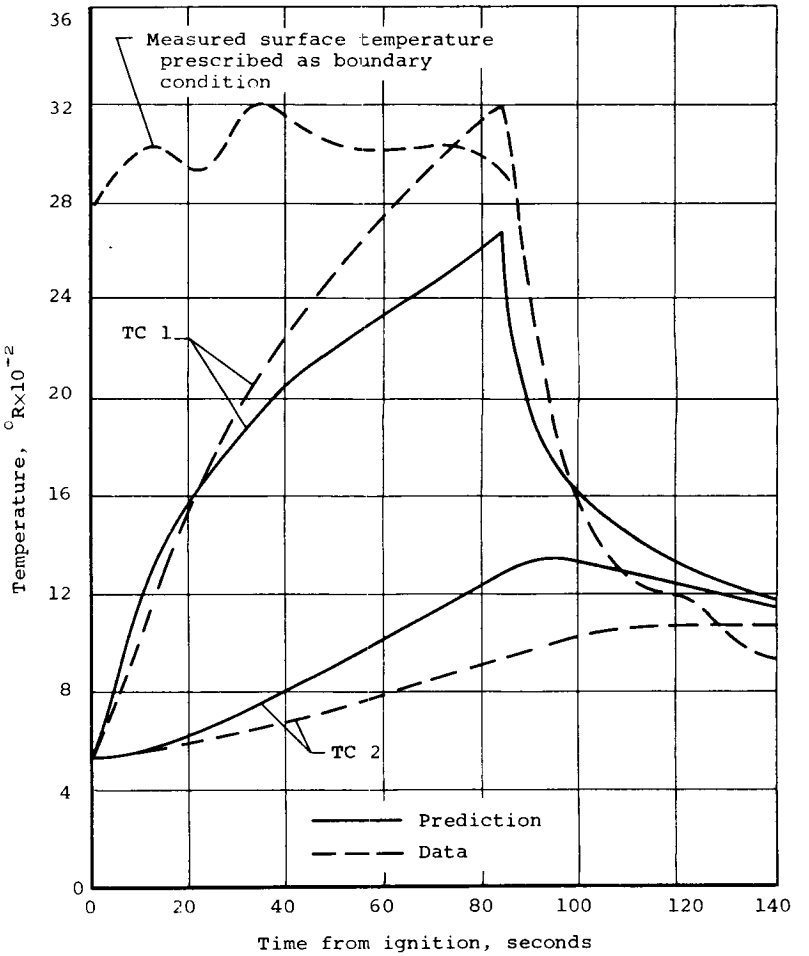


(e) Test No. 1109.

Figure 67.- Concluded.

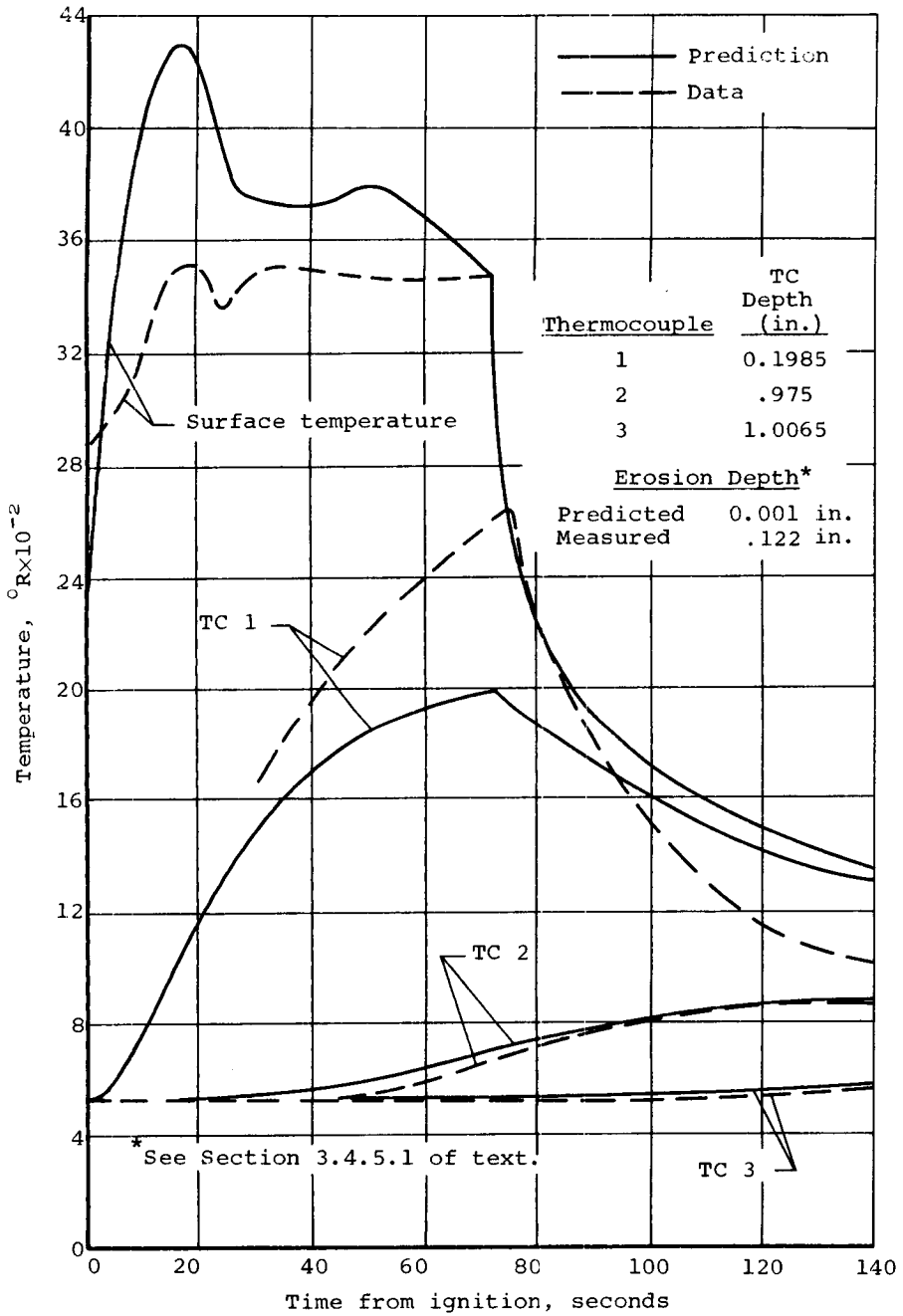


(a) Suface boundary conditions evaluated from chemical equilibrium considerations.

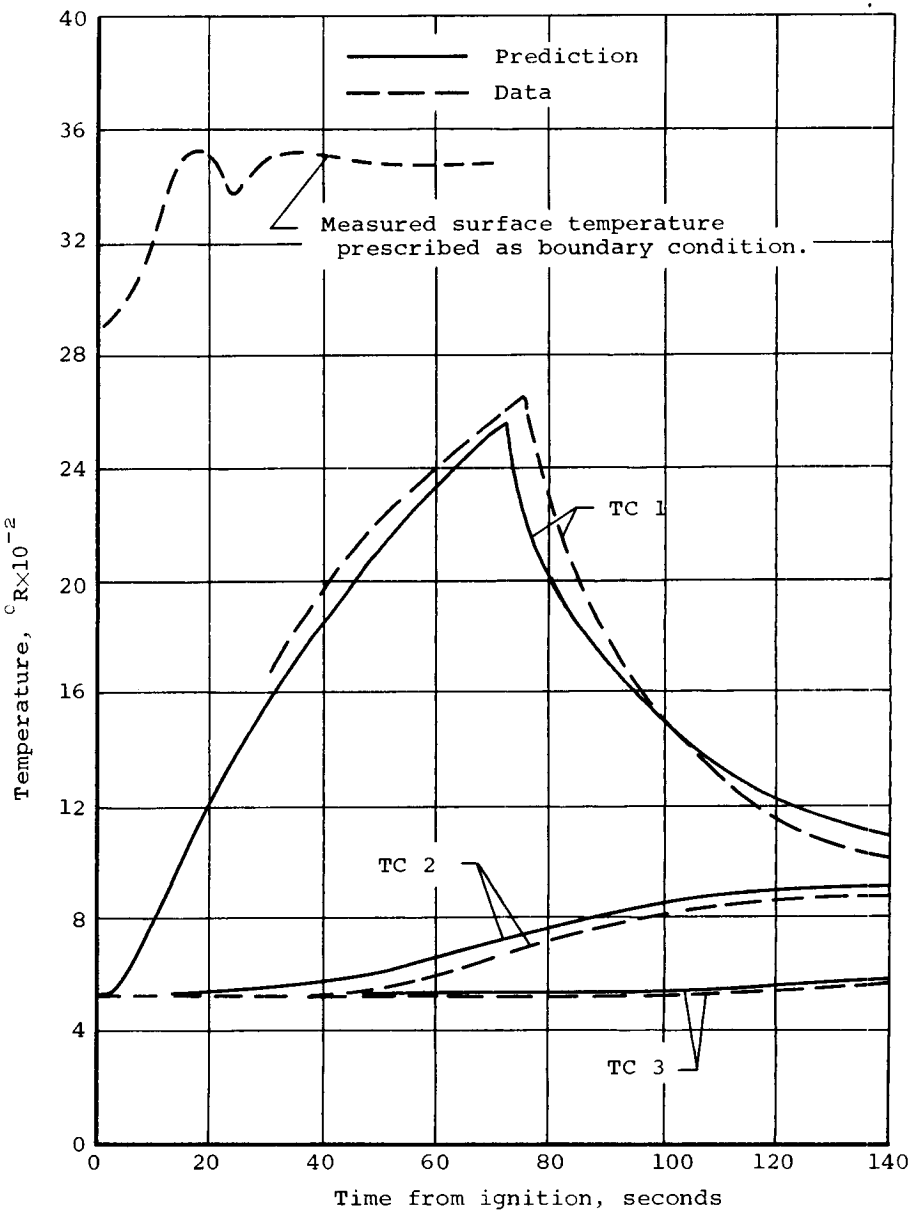


(b) Measured surface temperature and recession rate prescribed as boundary conditions.

Figure 68.- Comparison of predicted and measured response of graphite phenolic (MX 4500) in N_2O_4-N_2H_4/UDMH environment, Test No. 295.



(a) Surface boundary conditions evaluated from chemical equilibrium considerations.



(b) Measured surface temperature and recession rate prescribed as boundary conditions.

Figure 69.- Comparison of predicted and measured response of silica phenolic (MX 2600) in N_2O_4-N_2H_4/UDMH environment, Test No. 296.

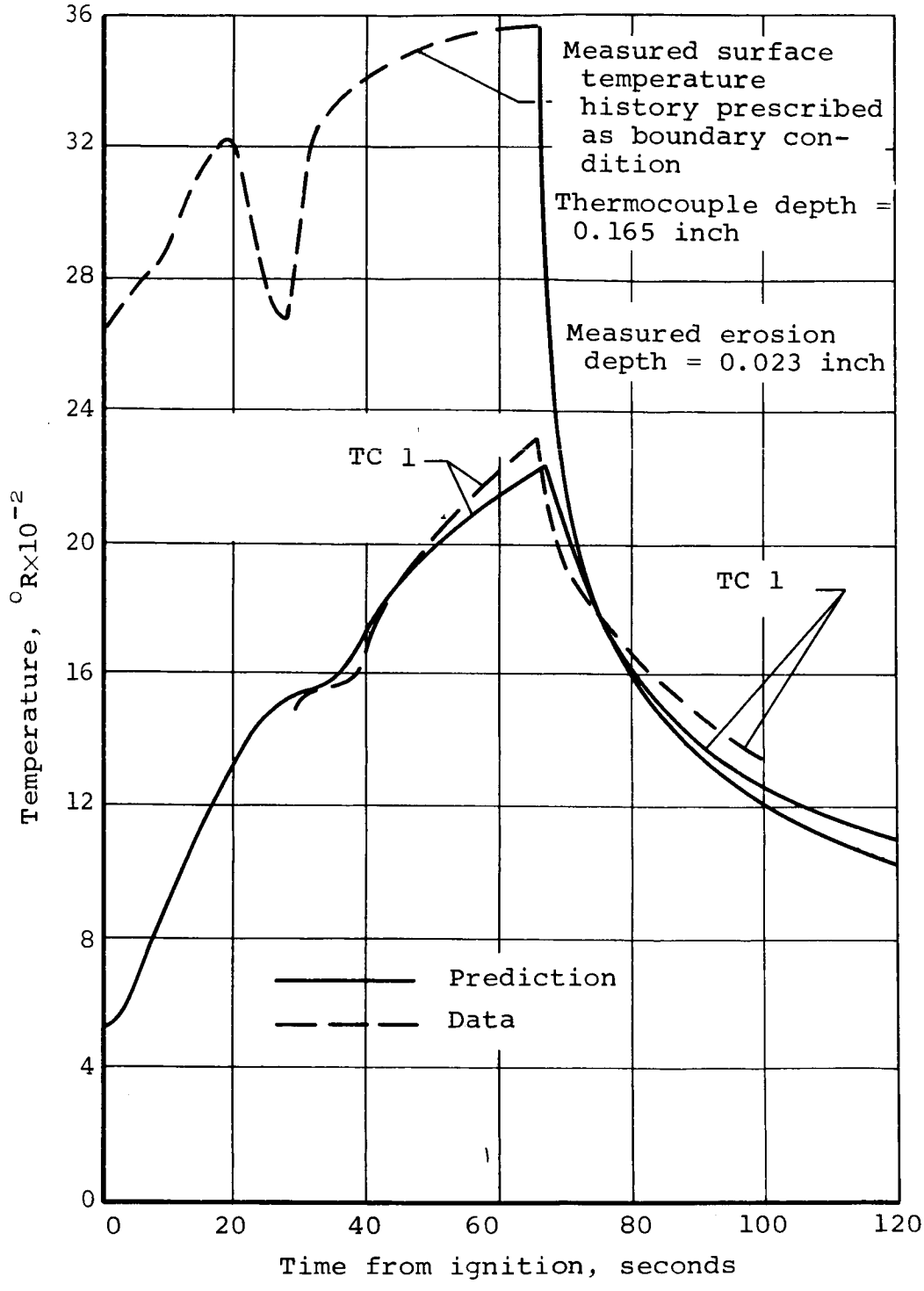


Figure 70.- Comparison of predicted and measured internal-temperature history for silica phenolic (MX 2600) in O_2-H_2 environment, Test No. 290. Measured surface temperature and recession rate prescribed as boundary conditions.

APPENDIX A

HEAT-TRANSFER COEFFICIENT EVALUATION FOR A NONABLATING SURFACE

According to the simplified method proposed by Bartz (Ref. 34) for correlating turbulent heat-transfer data in rocket nozzles, the following equation may be employed to characterize the heat-transfer coefficient to a nonablating surface.

$$h_g = \frac{0.026}{D^{0.2}} \left(\frac{\mu^{0.2} C_p}{Pr^{0.6}} \right)_{am} \left(\rho_{am} U_e \right)^{0.8} \tag{A.1}$$

where the heat-transfer rate to the wall is related to the heat-transfer coefficient and a temperature driving potential.

$$q = h_g (T_o - T_w) \tag{A.2}$$

When chemical reactions are anticipated between conditions at the boundary-layer edge and heated surface, it is convenient to combine the specific heat (C_p) and temperature difference in the above equations in terms of an enthalpy driving potential.

$$q = \rho_e U_e C_H (H_r - H_w) \tag{A.3}$$

where

$$\rho_e U_e C_H = \frac{0.026}{D^{0.2}} \left(\frac{\mu^{0.2}}{Pr^{0.6}} \right)_{am} \left(\rho_{am} U_e \right)^{0.8} \tag{A.4}$$

Utilization of the enthalpy driving potential (Eq. (A.3)) to characterize heat transfer in the chemically reacting boundary layer has been proposed by numerous investigators and has been successfully employed to correlate numerical boundary-layer integrations and experimental data. As indicated in the heat-transfer coefficient equations, the viscosity (μ), Prandtl number (Pr), and density (ρ) should be evaluted at a boundary-layer arithmetric mean temperature (T_{am}). For the chemically reacting boundary layer, the referenc enthalpy condition is more correct and should be utilized. The reference enthalpy is given by (Ref. 35):

$$h' = \frac{h_e + h_w}{2} + 0.22\,(Pr)^{1/3}\,\frac{U_e^2}{2gJ} \qquad (A.5)$$

where $(Pr)^{1/3}$ is the turbulent boundary-layer recovery factor. Considering this reference condition, the heat-transfer coefficient is written:

$$\rho_e U_e C_H = \frac{0.026}{D^{0.2}}\left(\frac{\mu^{0.2}}{Pr^{0.6}}\right)'\left(\rho_e U_e\right)^{0.8}\left(\frac{\rho'}{\rho_e}\right)^{0.8} \qquad (A.6)$$

where the primed quantities are evaluated at boundary-layer reference conditions.

Evaluation of Reference Properties

Because of the dependence of the reference conditions on the chemical composition, and the dependence of the composition on pressure, it is necessary to consider a nominal range of rocket-engine chamber pressures of interest prior to evaluating the reference conditions. For this purpose, consideration is given to the N_2O_4-N_2H_4/UDMH (O/F = 2.0) rocket engine operating in the chamber pressure range 4 to 7 atmospheres. For these conditions, the throat pressure will range from 2 to 4 atmospheres. The chemical composition of the products is shown as a function of temperature in Figure A-1. Corresponding to this composition is the equilibrium temperature as a function of enthalpy in Figure A-2. The boundary-layer-edge velocity at the nozzle throat is given by

$$U_e = \sqrt{\gamma^* g \frac{R}{m^*} T_o \left(\frac{2}{\gamma + 1}\right)} \qquad (A.7)$$

where, for the range of pressure of interest

$\gamma \cong \gamma^* = 1.22$

$m^* \cong 22.2$

$T_o \cong 5550^\circ$ R

$g = 32.17$ Lb_m-ft/Lb_f-sec^2

$R = 1545$ ft-Lb_f/mole-$^\circ$R

$U_e \cong 3700$ ft/sec

For this propellant, the stagnation enthalpy is 58.6 cal/gr = 105 Btu/lb, then

$$h_e = H_o - \frac{U_e^2}{2gJ} = -94 \text{ cal/gr}$$

Assuming a Prandtl number of 0.7 and substituting the above into Equation (A.5), the reference enthalpy at the throat of the N_2O_4-N_2H_4/UDMH engine is given by:

$$h' = \frac{-94 + h_w}{2} + 29.7 \text{ (cal/gr)}$$

referring to Figure (A-2), the enthalpy of the gases adjacent to the wall (h_w) may be obtained as a function of wall temperature. Substituting these values into the above equation yields the reference enthalpy as a function of wall temperature. The result is shown in Figure (A-3).

The reference viscosity (μ') may now be evaluated as a function of reference temperature. The following table gives the viscosity of the primary species as a function of temperature.

T (^oK)	μ(poise) $\times 10^6$				
	H_2O	N_2	CO	CO_2	H_2
1000	359	397	406	393	198
1500	522	518	528	518	258
2000	664	624	637	625	310
2500	791	721	736	721	358
3000	906	811	828	812	403
3500	1013	896	915	899	445

where 1 poise = 1 gr/cm-sec = 0.0672 lb/ft-sec. The reference viscosity of the mixture is obtained as a function of temperature referring to the composition on Figure A-1 and employing the following (relatively accurate) approximation for mixture viscosity.

$$\mu_{mix} = \frac{\sum_j x_j \mu_j m_j^{1/2}}{\sum_j x_j m_j^{1/2}} \qquad (A.8)$$

The variation of μ' with T' is shown in Figure A-4. The ratio of reference density to edge density in Equation (A-6) is obtained from the perfect gas law.

$$\left(\frac{\rho'}{\rho_e}\right) = \left(\frac{m'}{m_e}\right)\left(\frac{T_e}{T'}\right) \tag{A.9}$$

The variation of molecular weight (m) with temperature is shown in Figure A-5. With the above information, the boundary-layer reference conditions may be obtained at the throat of a N_2O_4-N_2H_4/UDMH rocket motor with a chamber pressure in the range of 4 to 7 atm.

Heat-Transfer Coefficient Evaluation

In order to illustrate the details of evaluating the heat-transfer coefficient, an example is considered here. The specific example considered is for the 7.8-inch-diameter throat of a N_2O_4-N_2H_4/UDMH rocket engine having a chamber pressure of 100 psia with a nozzle throat surface temperature of 200° F.

For an isentropic expansion in the free stream, the following equation relates the boundary-layer-edge mass velocity to chamber conditions:

$$\left(\rho_e U_e\right)^* = P_o \sqrt{\frac{g}{R}\frac{\gamma^* m^*}{T_o}} \left(\frac{2}{\bar{\gamma}+1}\right)^{\frac{\bar{\gamma}+1}{2(\bar{\gamma}-1)}} \tag{A.10}$$

where the asterisk pertains to conditions at the throat and the bar pertains to average values between the chamber and the throat. For T_o in $^\circ K$ and P_o in $Lb_f/in.^2$, the above equation becomes

$$\left(\rho_e U_e\right)^* = 15.5\ P_o \sqrt{\gamma^* \frac{m^*}{T_o}} \left(\frac{2}{\bar{\gamma}+1}\right)^{\frac{\bar{\gamma}+1}{2(\bar{\gamma}-1)}} \quad lb/ft^2\text{-sec} \tag{A.11}$$

the variation of isentropic exponent with temperature is shown in Figure A-6 and a Molier chart is shown in Figure A-7. From Figure A-7, for $h_o = 58.6$ cal/gr and $P_o = 100$ psia $= 6.8$ atms, $T_o = 3110^\circ$ K. For evaluating $\bar{\gamma}$, γ^*, and m^*, approximate values of T* and P* will suffice

$$T^* = \frac{T_o}{1 + \frac{\gamma - 1}{2}} \simeq \frac{3110}{1 + \frac{1.235 - 1}{2}} = 2790$$

$$P^* = \frac{6.8}{(1.117)^{\frac{1.235}{0.235}}} = 3.81$$

Then, from Figures A-5 and A-6

$$\gamma^* = 1.220, \quad \bar{\gamma} \simeq 1.225, \quad M^* = 23.1$$

$$\left(\rho_e U_e\right)^* = 15.5\times10^2 \sqrt{1.22\,\frac{23.1}{3110}} \left(\frac{2}{2.225}\right)^{\frac{2.225}{0.45}} = 86.7 \text{ lb/ft}^2\text{-sec}$$

Employing the more accurate $\bar{\gamma}$, the throat temperature is

$$T^* = \frac{3110}{1.112} = 2795^\circ \text{ K}$$

and

$$m^* = 23.0$$

From Equation (A.9), the above, and Figures A-3 and A-5 (for $T_w = 200^\circ$ F)

$$\left(\frac{\rho'}{\rho_e}\right) = \left(\frac{23.6}{23.0}\right)\left(\frac{3110}{2105}\right) = 1.516$$

The reference viscosity for $T' = 2105^\circ$ K is given in Figure A-4.

$$\mu' = 4.44\times10^{-5} \text{ lb/ft-sec}$$

Substituting the above values into Equation (A.6) and assuming Pr = 0.7, yields the heat-transfer coefficient.

$$\rho_e U_e C_H = \frac{0.026}{(7.8/12)^{0.2}} \left[\frac{(4.44\times10^{-5})^{0.2}}{(0.7)^{0.6}}\right] (86.7 \times 1.516)^{0.8}$$

$$= 0.236 \text{ lb/ft}^2\text{-sec}$$

The above detailed calculations would perhaps appear to be inappropriate when consideration is given to the uncertainty associated with the 0.026 factor in the equation. This factor, in fact, is dependent upon the particular nozzle geometry being considered and may vary by 50 percent greater or less for nozzle geometries of practical interest. It is believed that detailed boundary-layer heat-transfer coefficient calculations are appropriate in order to properly account for transport property dependence in the boundary layer. When for particular nozzle geometries of interest, the value of the coefficient is established, the considerations presented herein should enable a more accurate specification of the heat-transfer coefficient including the proper dependence of the significant variables.

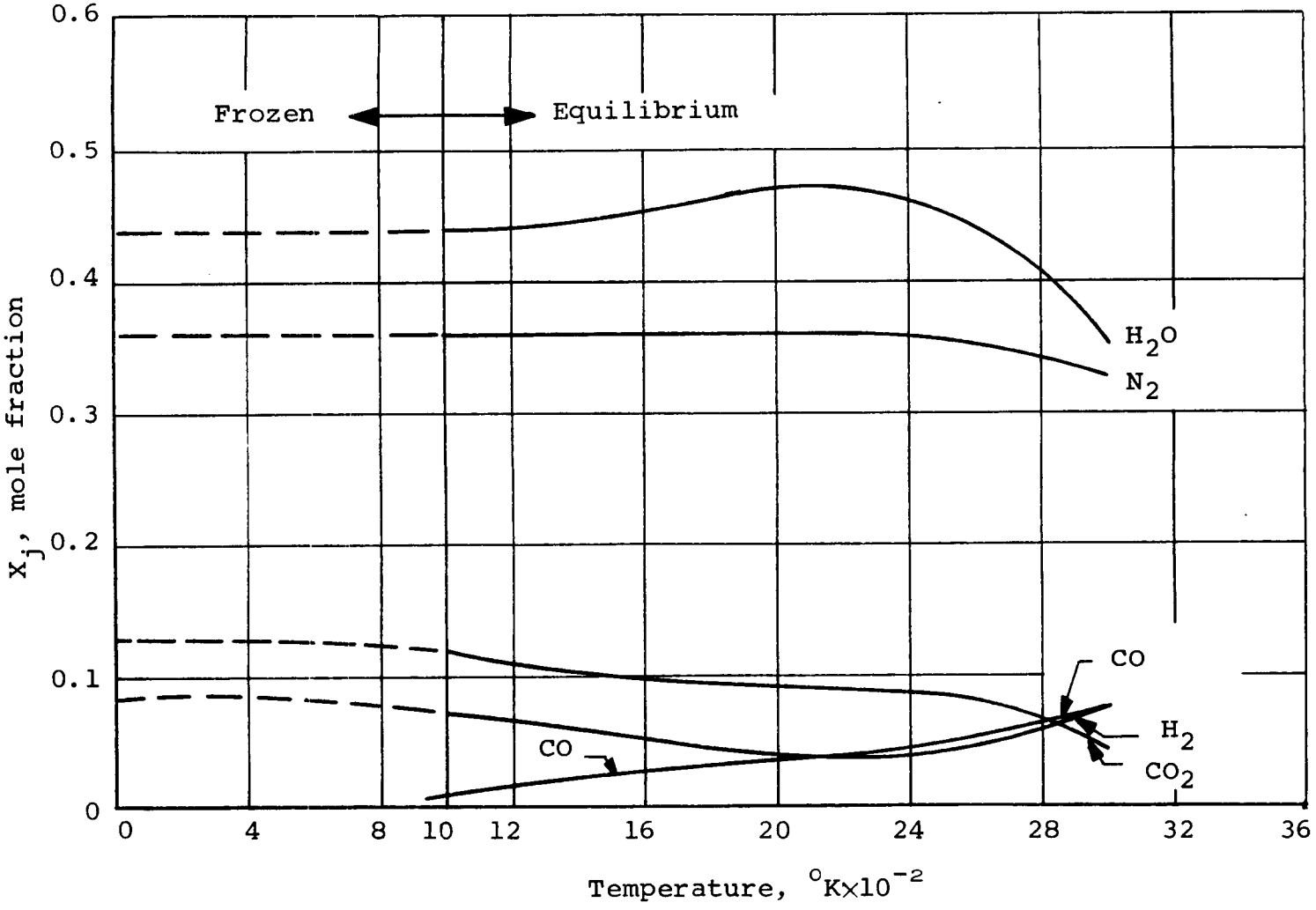


Figure A-1.- Chemical composition of products of combustion of N_2O_4-N_2H_4/UDMH (O/F = 2.0) for a pressure of 2 atm.

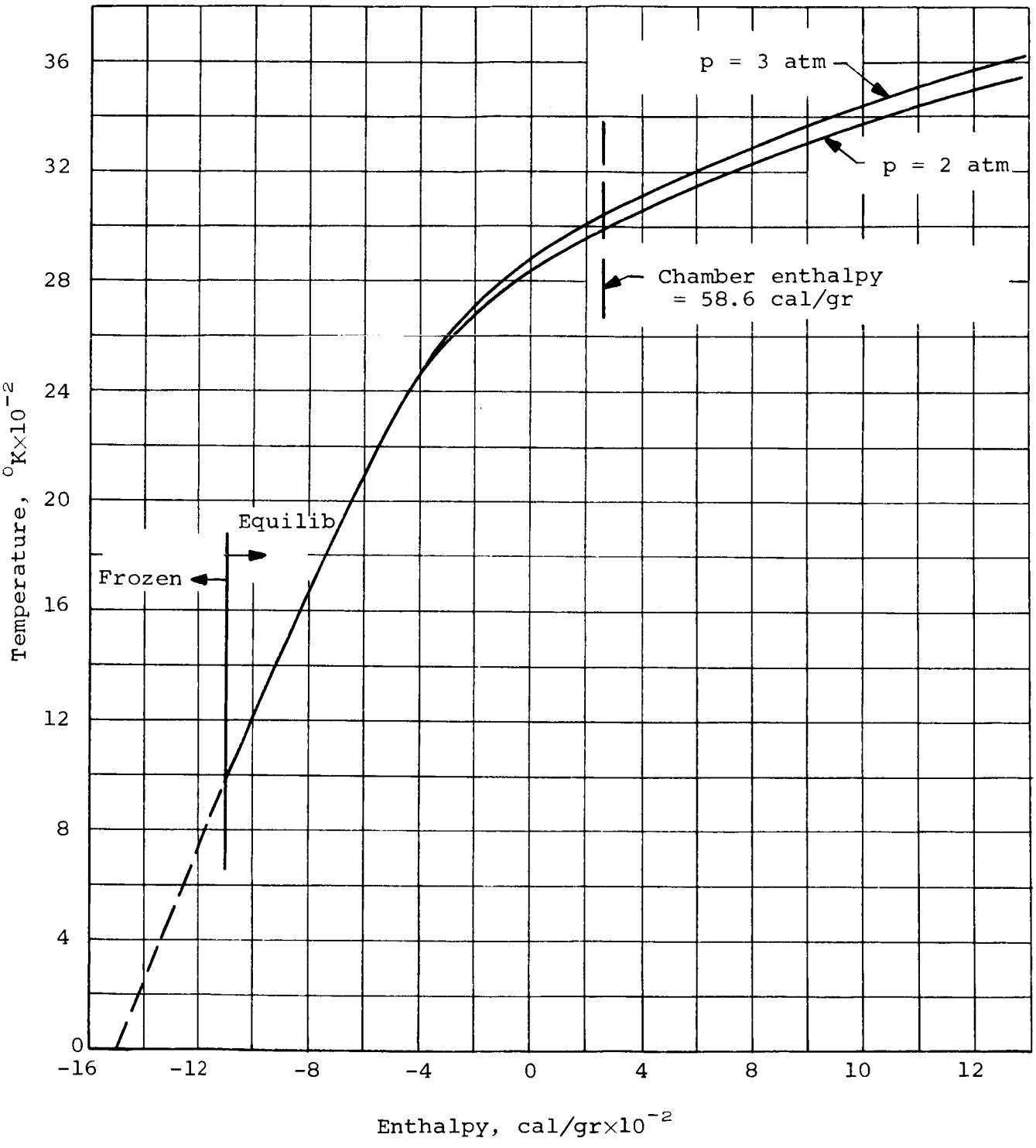


Figure A-2.- Temperature as a function of enthalpy for products of N_2O_4-N_2H_4/UDMH (O/F = 2.0).

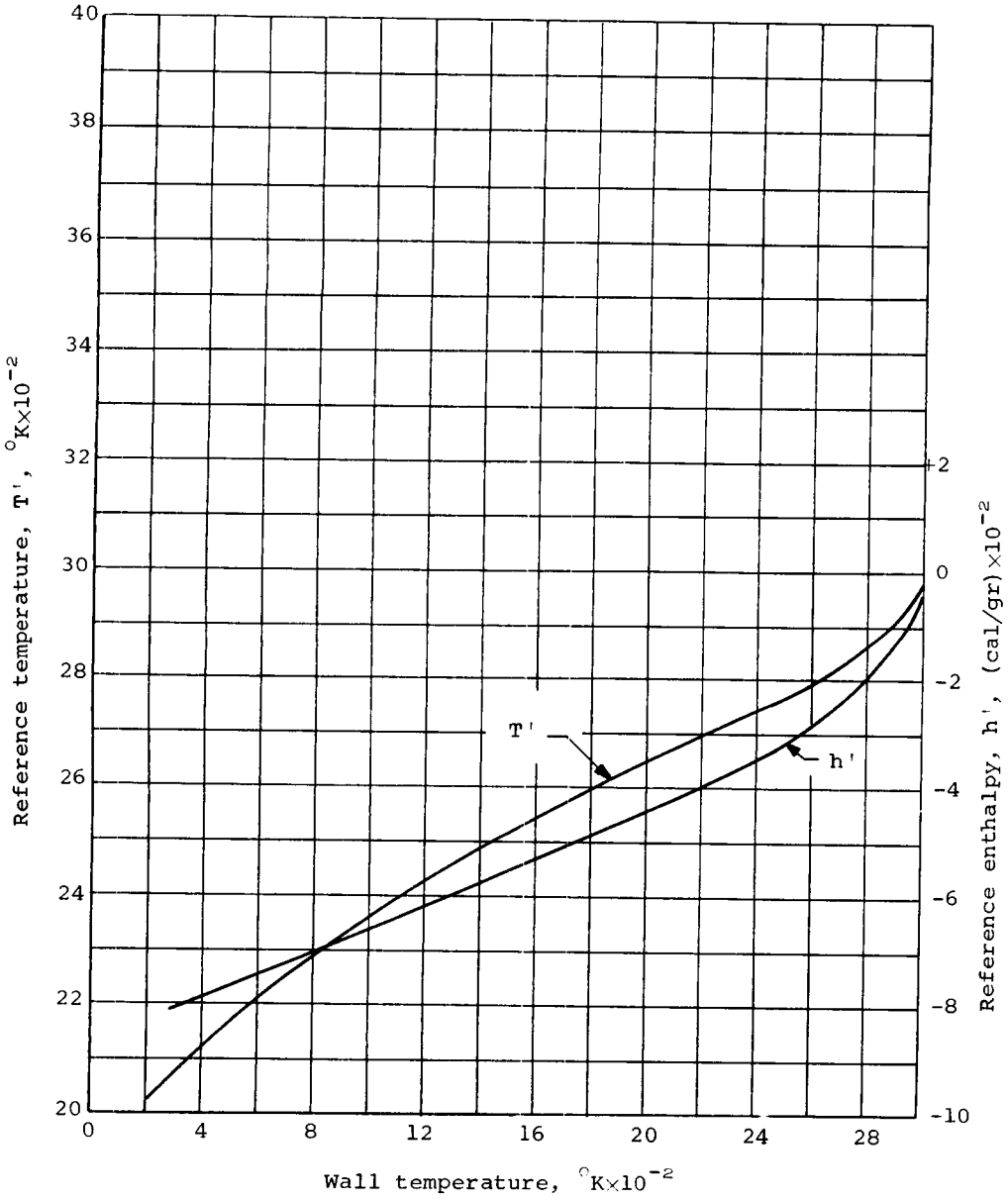


Figure A-3.- Reference enthalpy and temperature as functions of wall temperature N_2O_4-N_2H_4/UDMH nozzle throat (p* = 2.5 atm).

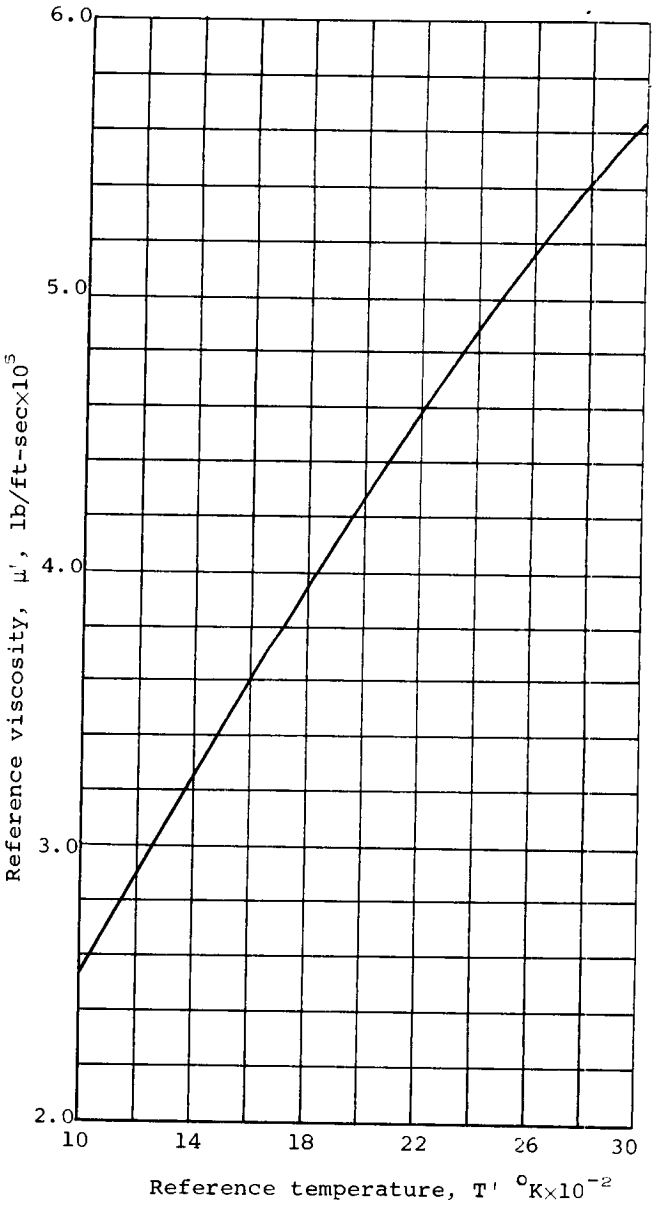


Figure A-4.- Mixture viscosity for N_2O_4-N_2H_4/UDMH environment as a function of temperature.

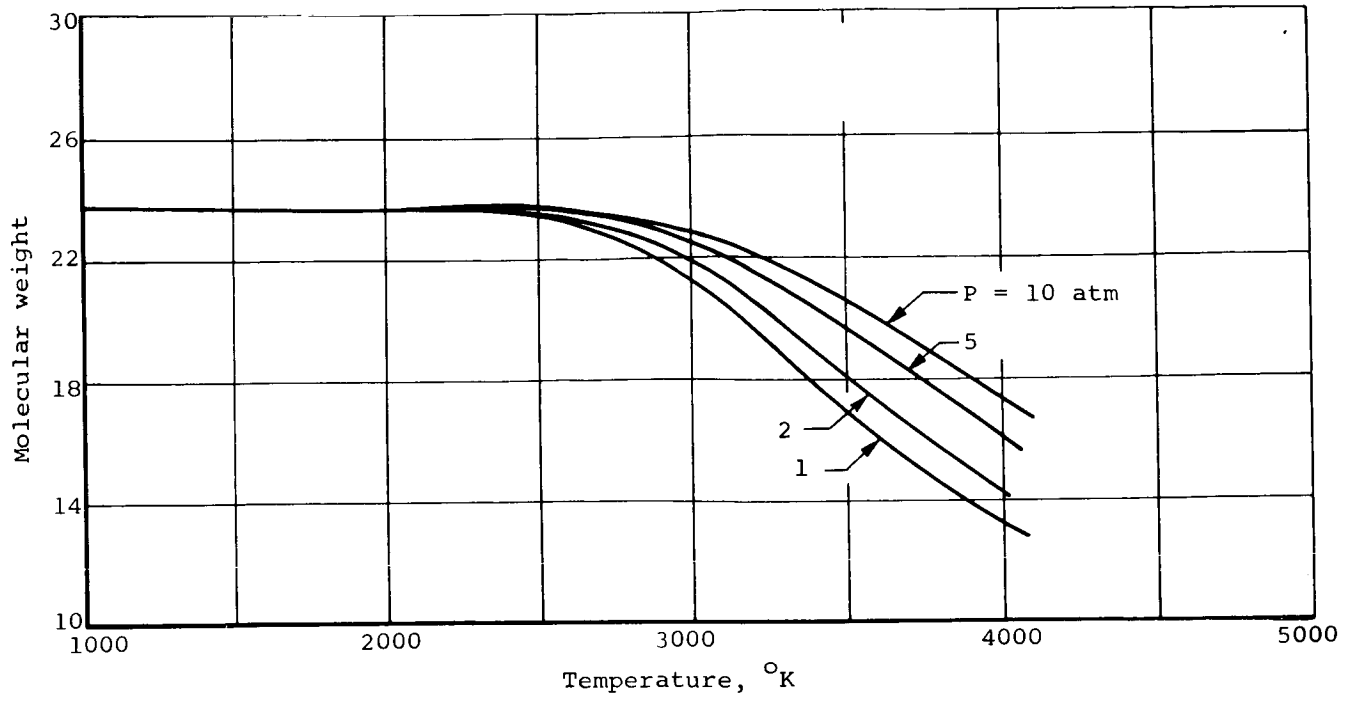


Figure A-5.- Molecular weight as a function of temperature, N_2O_4-N_2H_4/UDMH, O/F = 2.0.

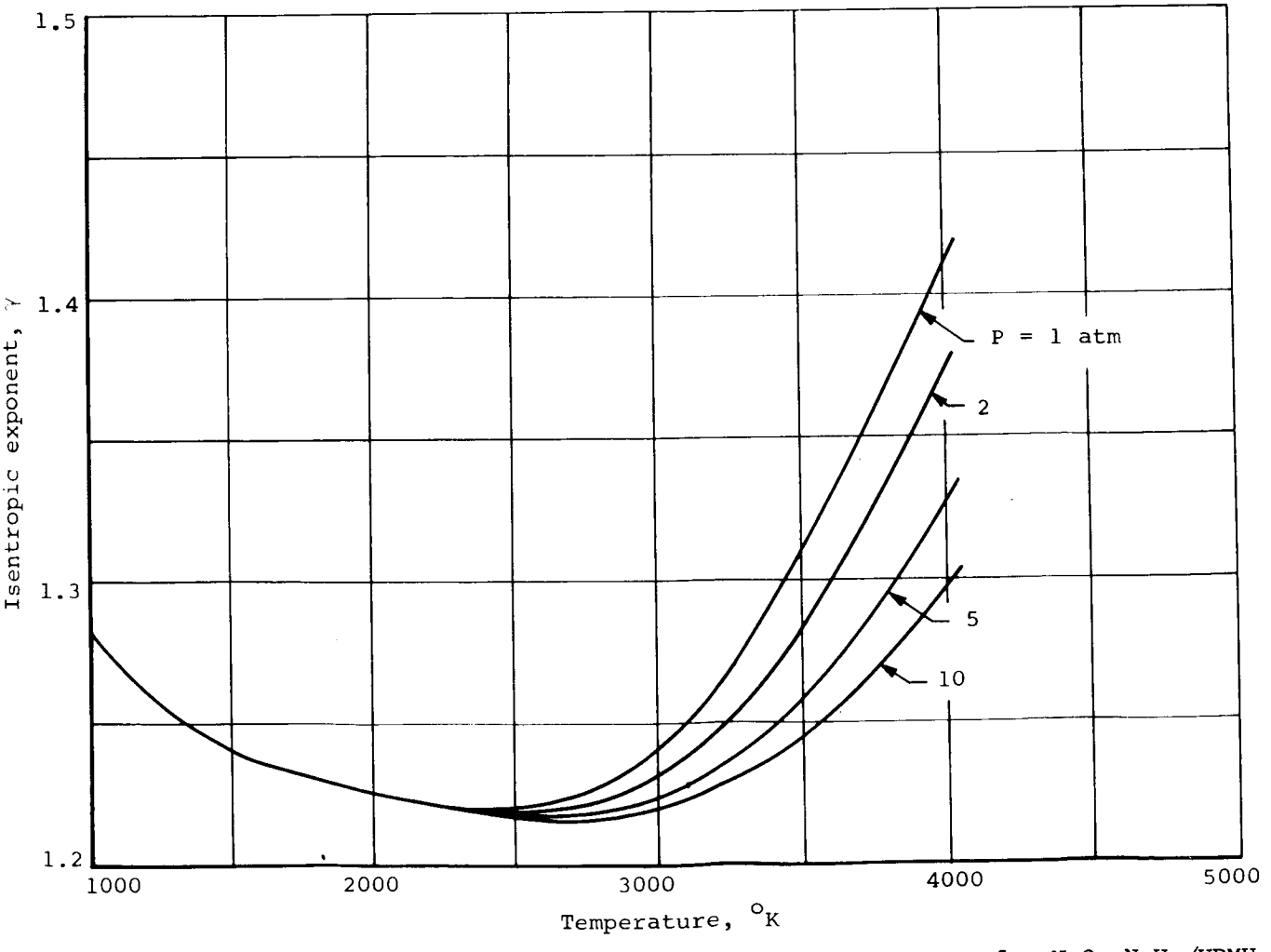


Figure A-6.- Isentropic exponent as a function of temperature for N_2O_4-N_2H_4/UDMH, O/F = 2.0.

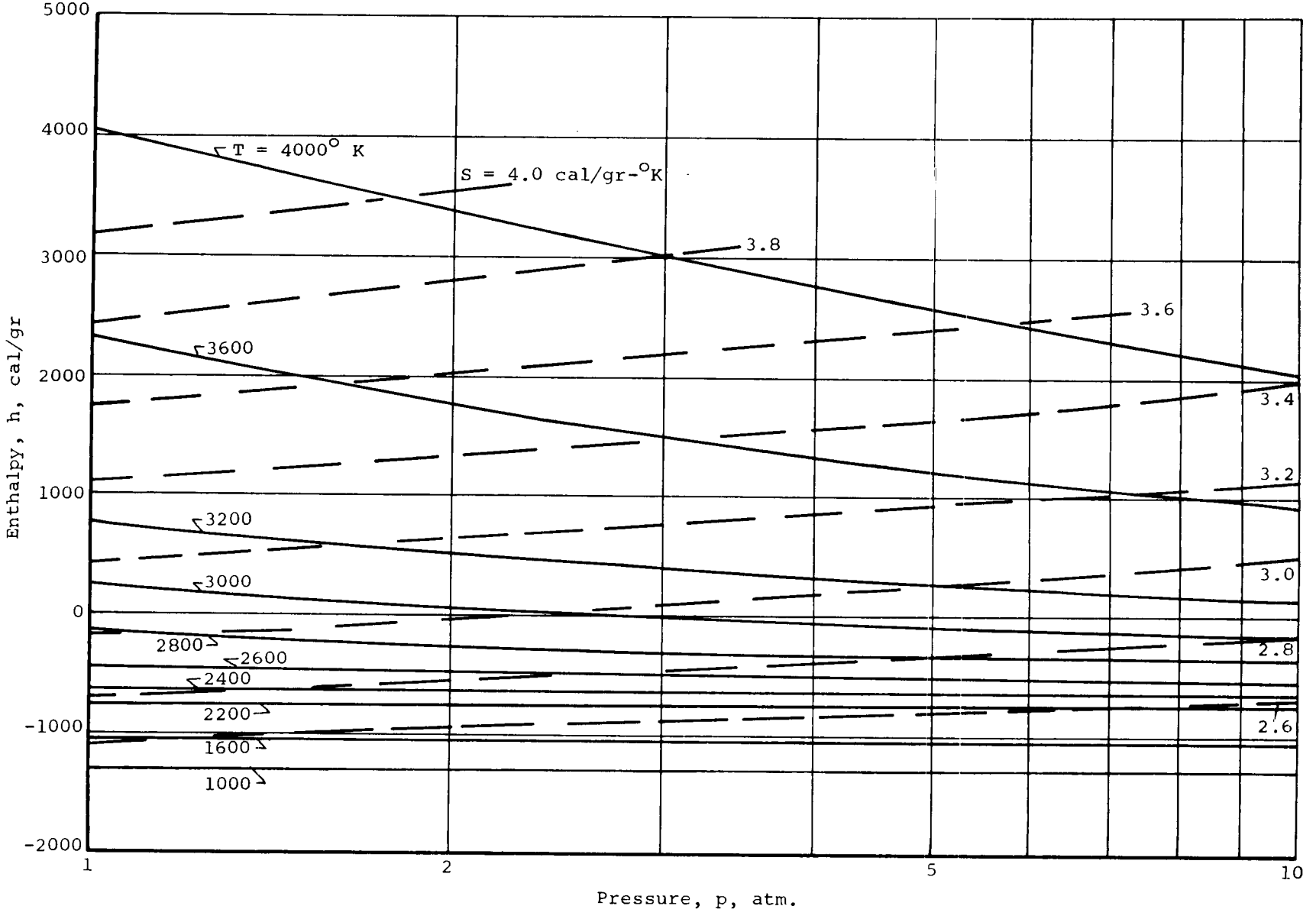


Figure A-7.- Thermodynamic properties for N_2O_4-N_2H_4/UDMH, OF = 2.0.

APPENDIX B

THE ARC-PLASMA FACILITY

The Vidya Arc-Plasma Facility is a complete laboratory for hyperthermal flow experimentation. It houses a Vidya 1-megawatt solenoid arc-plasma generator, a Vidya 400-kilowatt constrictor arc-plasma generator, associated support equipment, and instrumentation for recording and monitoring operating conditions and test material response.

The two types of arc-plasma generators used in the facility operate on different principles; hence, their application varies. The 1-megawatt unit employs concentric water-cooled copper electrodes surrounded by a solenoid coil (see Fig. B-1). The outer electrode serves as the cathode and pressure vessel, while the inner electrode, supported from an insulated rear flange, is the anode. The arc travels in the annulus formed by the two electrodes and is rotated by the magnetic field of the solenoid coil.

The second unit is a 400-kilowatt constrictor arc shown schematically in Figure 38. This employs a tungsten cathode fitted at the bottom of a tubular well, and a tapered, cylindrical anode in line with the cathode. Both the cathode and anode configurations can be easily changed to obtain optimum performance at different test conditions and for different test gases. The gas is introduced tangentially at the insulated interface of the two electrodes causing the arc to run from the tungsten surface to the anode sleeve. In this unit the arc is gas-stabilized rather than magnetic-field-stabilized as in the solenoid unit.

The two arc-plasma generators have different operating characteristics, and thus different (and complementary) capabilities. The 1-megawatt unit is superior at high chamber pressure (above 100 psia) and high mass-flow rate, whereas the 400-kilowatt unit is superior at high enthalpies (above 8000 Btu/lb). The two units also have complementary capabilities for handling the many different types of gases and gas mixtures that have been used for chemical simulation of environments of interest. These gases include nitrogen, air, oxygen, hydrogen, argon, helium, carbon monoxide, carbon dioxide, ammonia, water vapor, and boron trifluoride.

The solenoid arc-plasma generator is nominally rated at an input power level of 1 megawatt. The actual power level spectrum covers the range from 0.45 to 1.2 megawatts. The chamber pressure range, when exhausting to atmosphere, can presently be varied from 1 to 35 atmospheres with nozzle

throat sizes of 1.0 to 0.25-inch diameter, respectively. At these pressures, enthalpy levels up to 8000 Btu/lb are achievable with nitrogen as the test gas. A typical operating envelope for nitrogen at a power level of 850 kilowatts is shown in Figure B-2.

The constrictor arc-plasma generator is nominally rated at an input power level of 400 kilowatts. Its operating spectrum covers the range from 60 to 500 kilowatts. No firm operating envelopes have been obtained for this unit as yet; however, experience to date indicates a maximum enthalpy with simulated air at low chamber pressure of 25,000 Btu/lb or better, and a maximum chamber pressure, at lower enthalpy, of over 8 atmospheres. This unit is currently being used in the simulation of combustion products environments of chemical rockets using hydrogen as the arc heated gas.

The arc power is supplied by battery and diesel electric power supplies. The two arc-plasma generators can be operated from either system independently or with both systems in parallel or series. In general, the constrictor arc can be run directly from the diesel unit, and has unrestricted run time. The large solenoid unit run time is battery limited and has an effective limitation of about 1-1/2 minutes at the 1-megawatt power level. The main battery supply is comprised of 288, 8.5-volt, lead-acid, heavy-duty storage batteries connected in series-parallel arrangements which provide open circuit voltages in 102-volt increments. The diesel-driven generator (Fig. B-3) has a maximum rated output of 500 kilowatts of dc power (660 brake horsepower). The power output and open circuit voltage are continuously variable, the maximum open circuit voltage being 1000 volts. A series combination of the battery and diesel power supplies provides an open-circuit voltage of up to 1800 volts. A ballast resistor provides increments of resistance in series with the arc to control the input power level and electrical circuit stability.

All of the components exposed to the plasma are cooled by high-pressure de-ionied water from a closed-circuit cooling system. The solenoid arc-plasma generator requires about 180 gallons per minute of water flow with an additional 70 gallons per minute required for test fixtures and ballast resistor. A schematic showing the relationship of power, gas, and water supplies to the arc-plasma generator is shown in Figure B-4. The arc-plasma facility control console is shown in Figure B-5.

The arc-plasma generators are instrumented to permit monitoring and continuous recording of the important operating variables required to define the test conditions such as gas enthalpy, chamber pressure, and gas mass-flow

rate. The gas enthalpy is measured by an energy-balance technique in which the losses to the cooling water are deducted from the electrical input energy to determine the net energy transferred to the gas. The accuracy of this technique has been verified by both choked flow calculations and a tubular calorimeter calibration in which the energy imparted to the gas in the generator is recaptured by the water-cooled calorimeter. The chamber pressure is measured by a strain-gauge transducer and the gas mass-flow rate by standard calibrated orifice meters.

The test results for a firing are assessed and calculated from the primary test data and post-test measurements and observations. These results, in addition to the actual firing conditions, include surface recession, surface-temperature history, post-test surface condition, test model weight loss, internal-temperature histories, and, when applicable, post-firing char depth.

The facility instrumentation provides continuous high-speed recording and visual readout of the output from all sensors necessary to monitor the arc operating conditions and model or test section response. An analog-to-frequency converter with paper tape digital printout and a 36-channel oscillograph are used to record all transient data and to provide a time base for testing events. In addition, visual readout is provided at a control console for the monitoring of operating conditions. The recorded test data are reduced on an IBM 1620 computer and the test conditions and results are generally available within 24 hours of test completion.

A variety of high-temperature calorimeters and enthalpy and pressure probes have been developed and used at Vidya for test programs and arc-diagnostic studies. The calorimeters include both steady-state and transient devices capable of evaluating semi-local heating rates to many model shapes.

The photographic coverage used on test programs includes both real time and high-speed motion pictures of models and test sections during test, in addition to still shots both before and after test. A complete photographic laboratory at the facility is used to provide rapid film processing.

Recently the arc-plasma facility has been upgraded to include high altitude and supersonic capability with the use of vacuum pumping equipment. The equipment was placed in operation during September 1965.

The new vacuum pumping system for the Vidya Arc-Plasma Facility consists of a test chamber, a five-stage steam ejector complex, two 110-boiler horsepower steam generators, a cooling tower, and associated control equipment. A partial view of the test chamber and steam ejector system is shown in Figure B-6.

The test chamber consists of a cylindrical steel vessel, 4 feet in diameter by 15 feet long, comprised of three sections. The first is the test chamber proper, which houses the supersonic nozzle and model support system, and contains various ports for test observation and access. This is followed by an after-cooler which houses a heat exchanger to cool the arc-heated gases prior to entering the ejector system. The final section provides a transition from the test chamber diameter to the inlet of the steam-ejector system. Provision for radiant energy-flux simulation equipment is incorporated in the test chamber design.

Steam ejectors were selected as the pumping device because they afford an approximately constant mass-flow rate pumping characteristic and can handle gases too corrosive for mechanical pumping systems. The steam-ejector equipment consists of five ejector stages, two interstage condensers (each with condensate pumps), and an exhaust silencer. The motive steam for the ejector system is supplied by two 110-boiler-horsepower steam generators. The two units together can provide a total steam load of 6000 lb/hr at 240 psi. A recirculating cooling-water system is provided to supply cooling water continuously to the two interstage condensers of the ejector system. The thermal energy in the cooling water is dissipated in a cooling tower.

The flow characteristics of the vacuum pumping system are presented in Figure B-7 as gas mass-flow rate, $\dot{m}$, versus test-section pressure, p_e, which corresponds to the static pressure at the nozzle exit. The system is capable of pumping any flow rates represented within or below the shaded area in the figure. For example, 1 mm Hg pressure can be maintained with a flow rate as high as 2.9×10^{-2} lb/sec. The lower flow rate limit of 5×10^{-3} lb/sec shown in the figure is not a facility or arc-plasma generator limitation, but rather is a value chosen arbitrarily as a convenient lower limit for the purposes of simulation calculations. The test chamber is not capable of operation at pressures exceeding ambient, so the upper limit of test-section pressure is 760 mm Hg, as indicated in the figure.

Also shown in Figure B-7 are the flow rates, m, test-section static pressures, p_e, chamber total pressures, p_{t_1}, and model stagnation pressures, p_{t_2}, corresponding to test-section Mach numbers, M, of 3 and 5 and various test-section (flow) diameters, D_e, all at a stagnation enthalpy, h_o, of 10,000 Btu/lb.[1] It should be pointed out that these lines of constant M, D_e, and h_o represent test conditions which can be obtained within the

[1]These calculations were performed for an idealized gas with $\gamma_{eff} = 1.20$.

constraints of the vacuum system, but the operating limitations imposed by the particular plasma generators are not included in the figure.

The projected envelopes of stagnation point heating rate, $q_o R^{1/2}$ as a function of model stagnation pressure, p_{t_2} for the Vidya arc-plasma generators are presented in Figure B-8. These represent overall envelopes for nozzle exit diameters between 3/4 inch and 10 inches with a Mach number variation of M = 3 to M = 5.

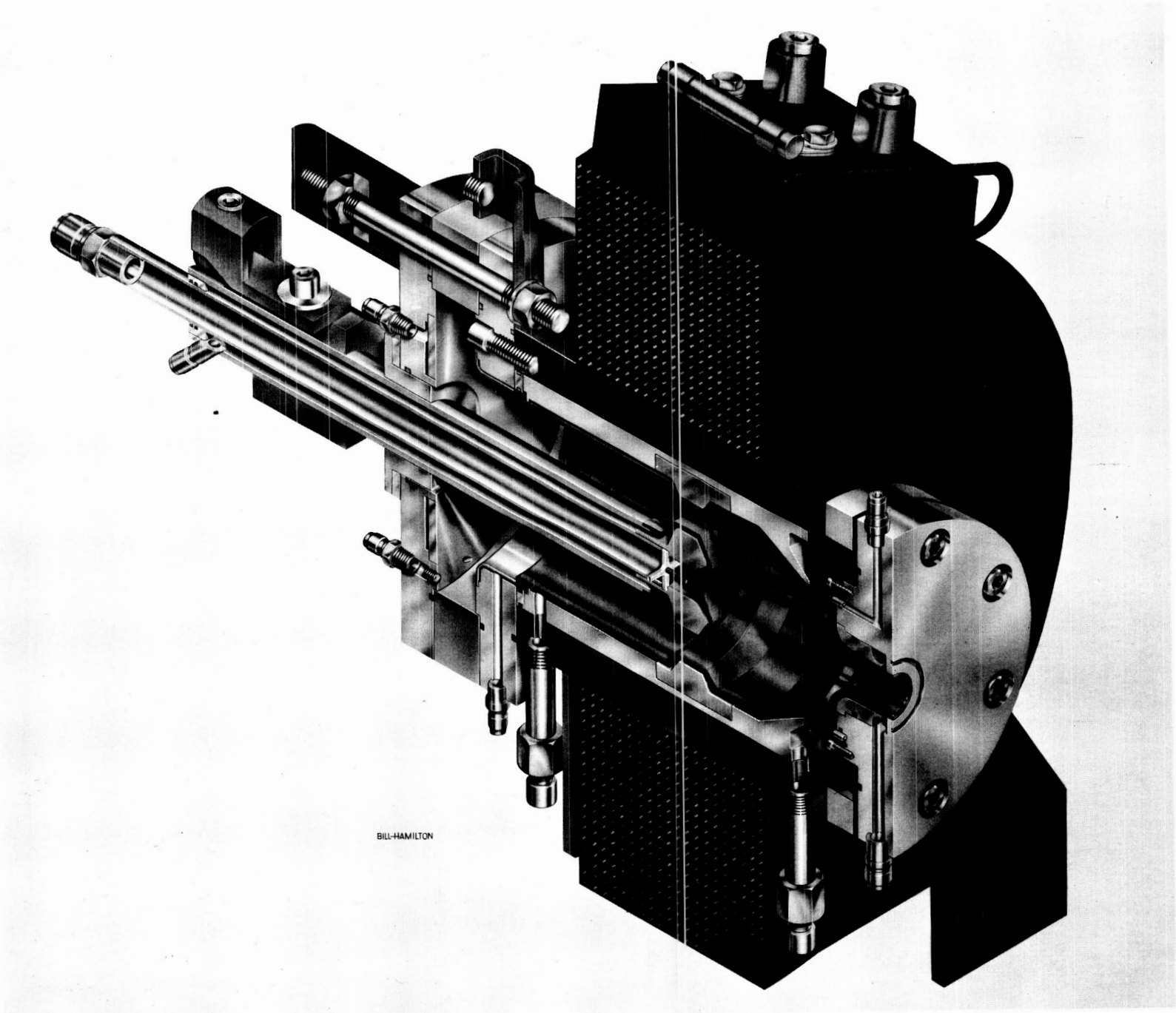


Figure B-1.- Section representation of the solenoid arc-plasma generator.

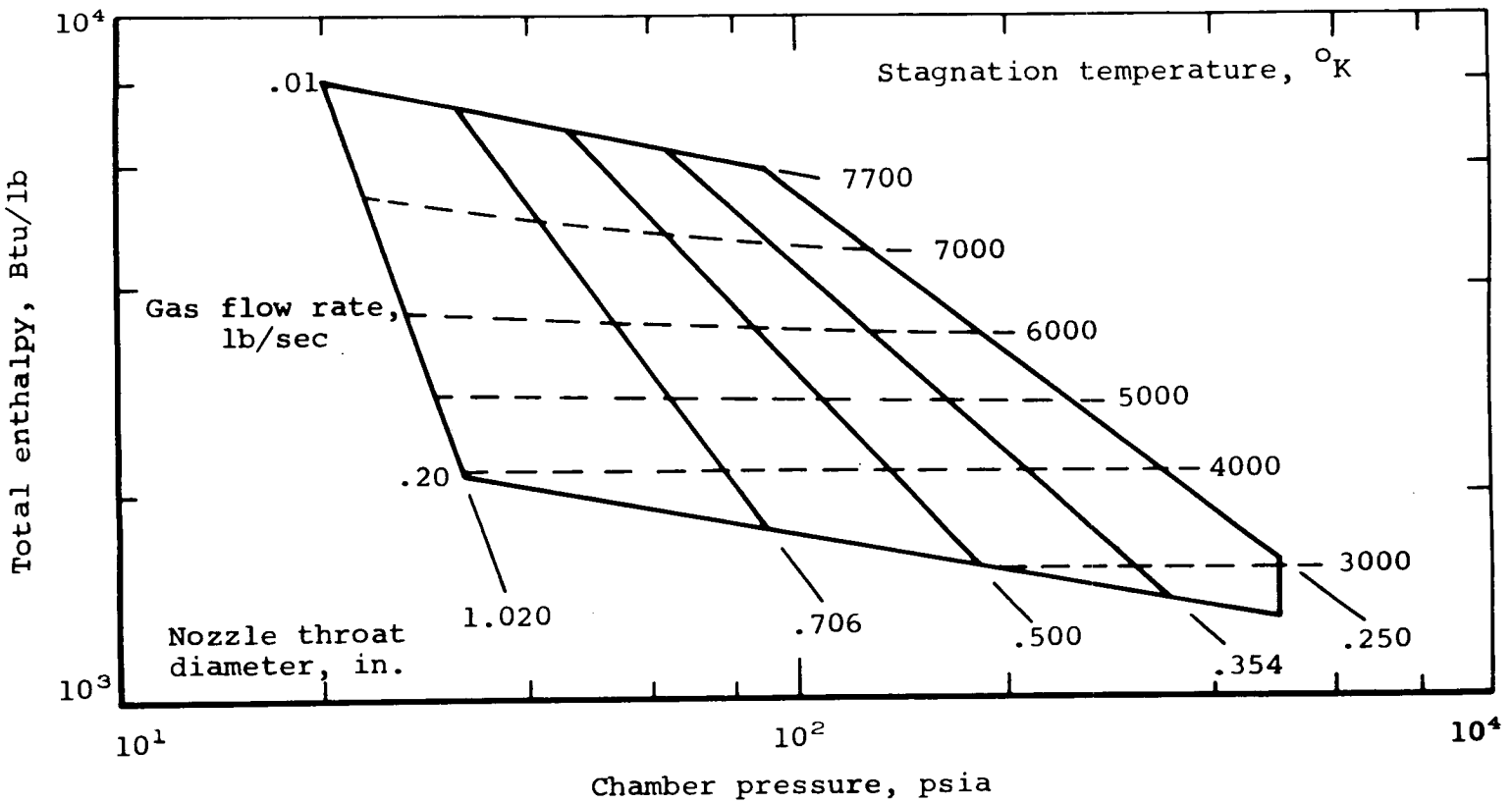


Figure B-2.- Typical operating envelope for the solenoid arc-plasma generator, 850 kw with nitrogen.

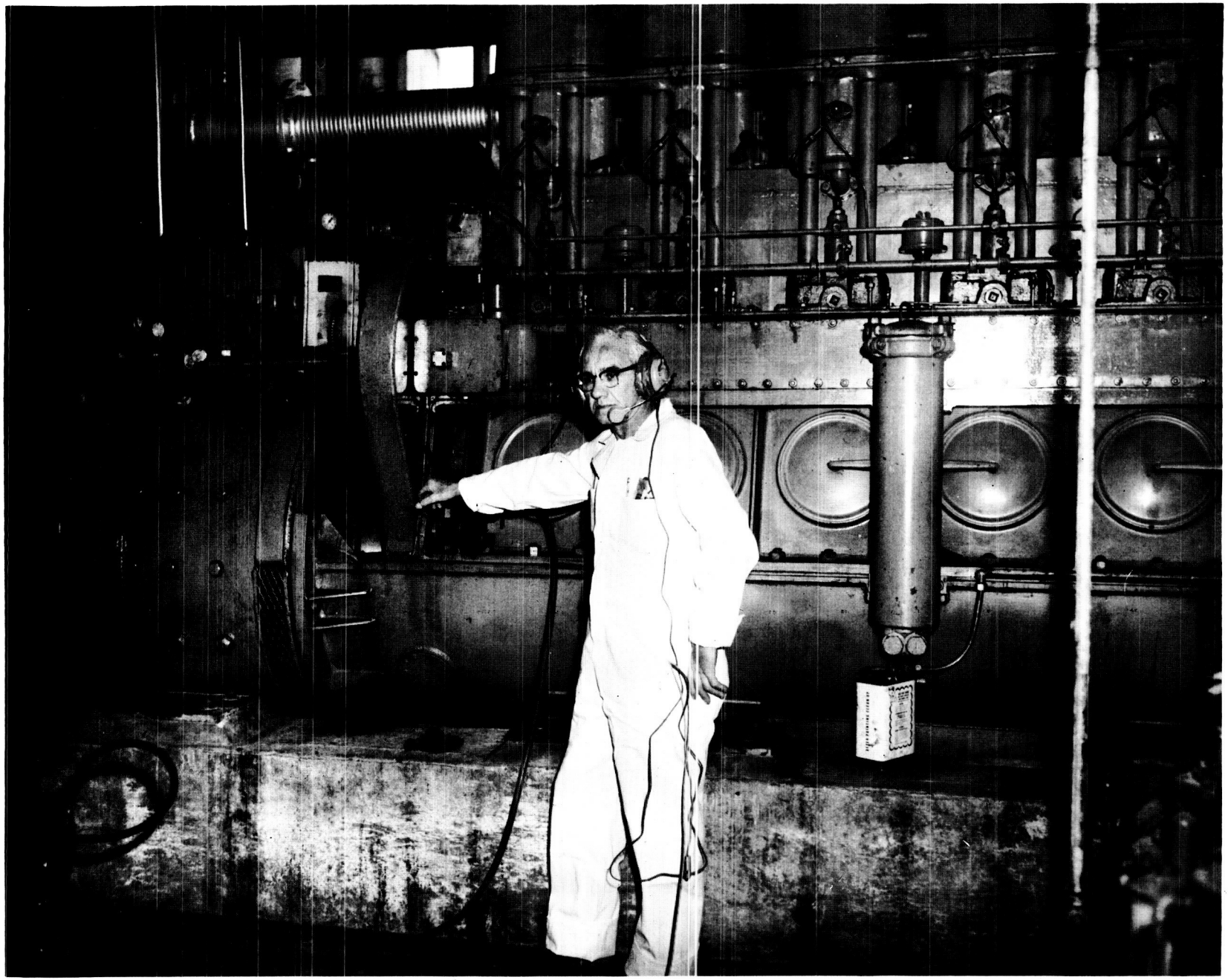


Figure B-3.- Diesel-generator power supply.

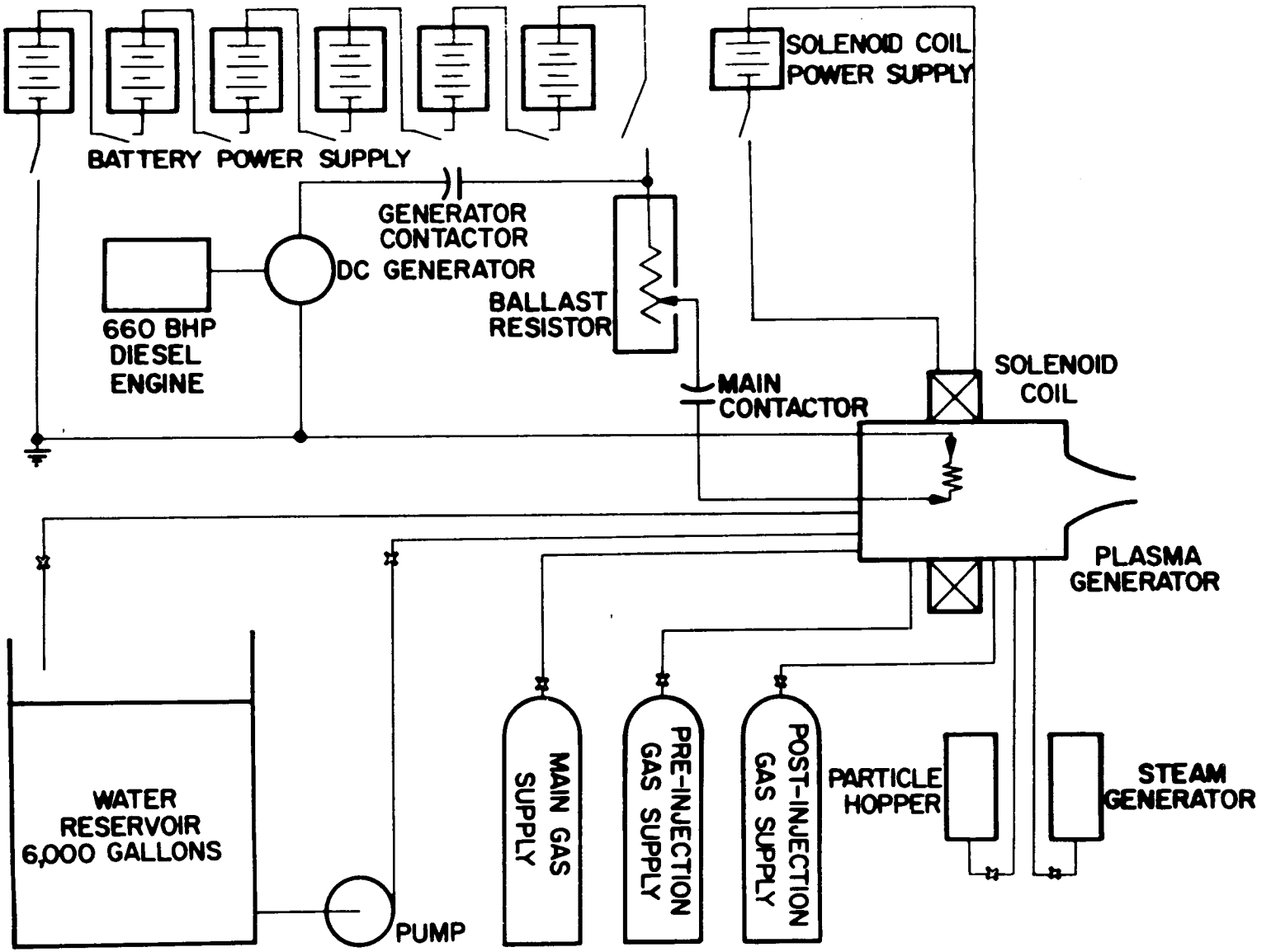


Figure B-4.- Schematic diagram of the arc-plasma facility.

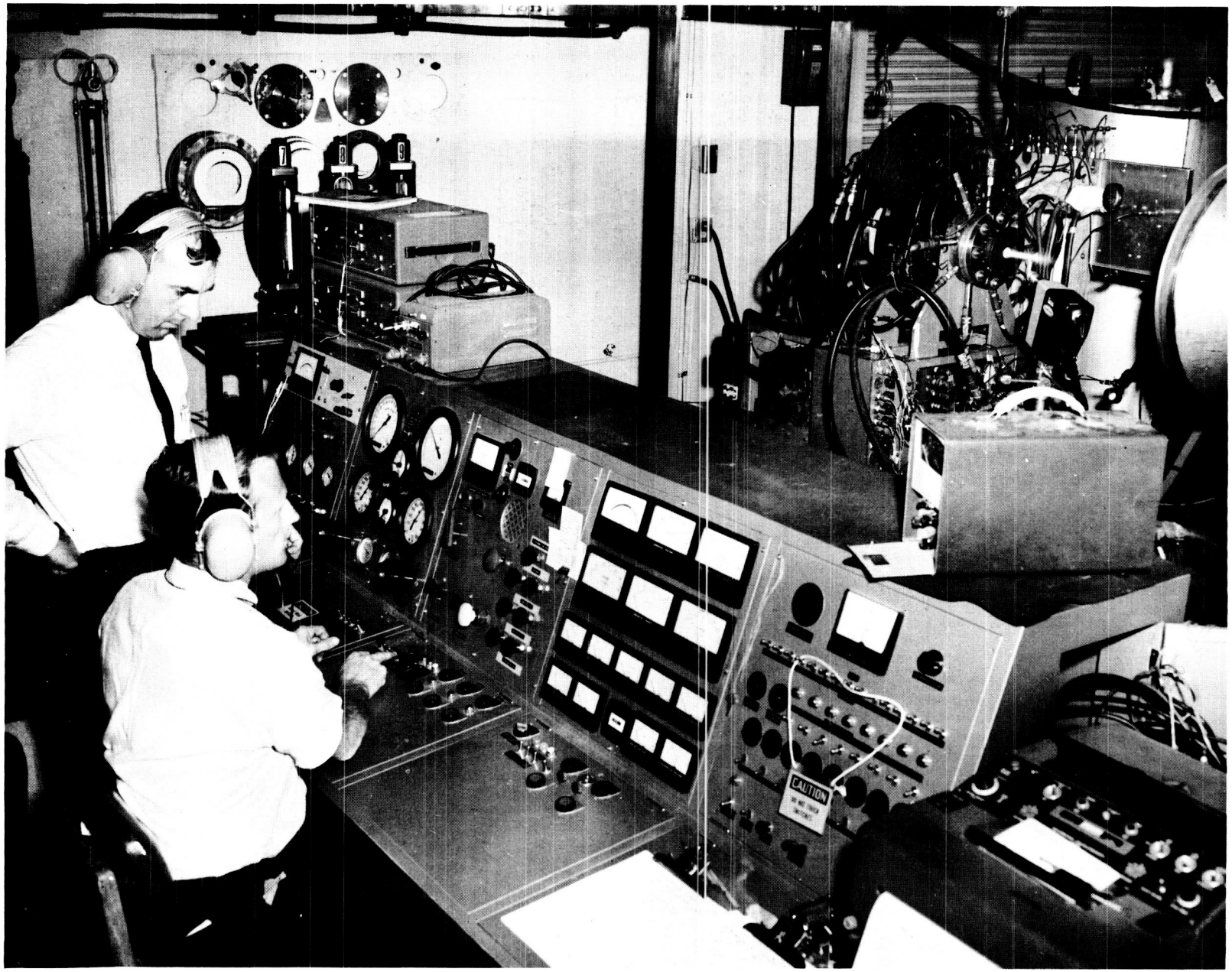


Figure B-5.- Control console.

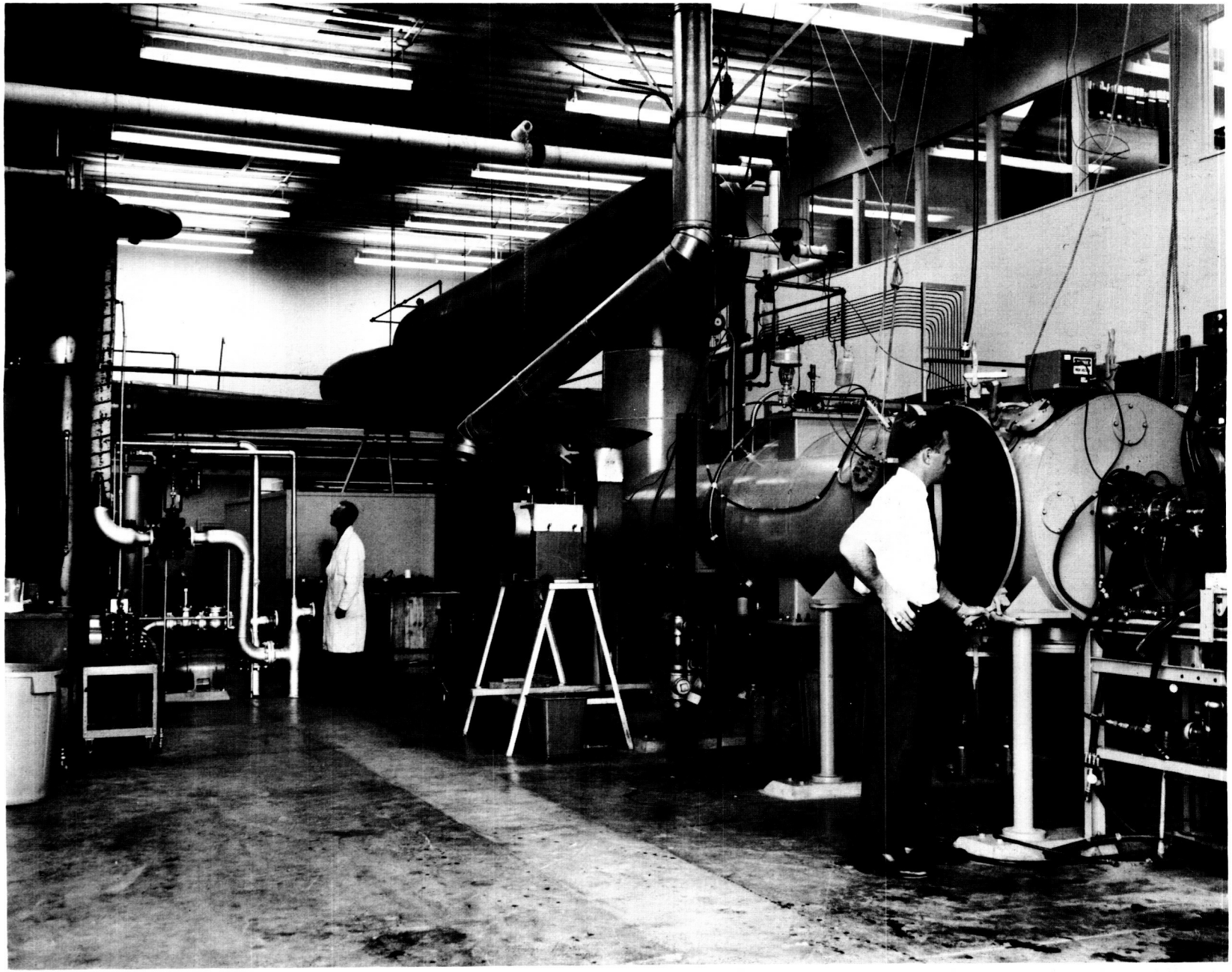


Figure B-6.- A partial view of the Vidya Arc-Plasma Facility showing the test chamber and steam ejectors.

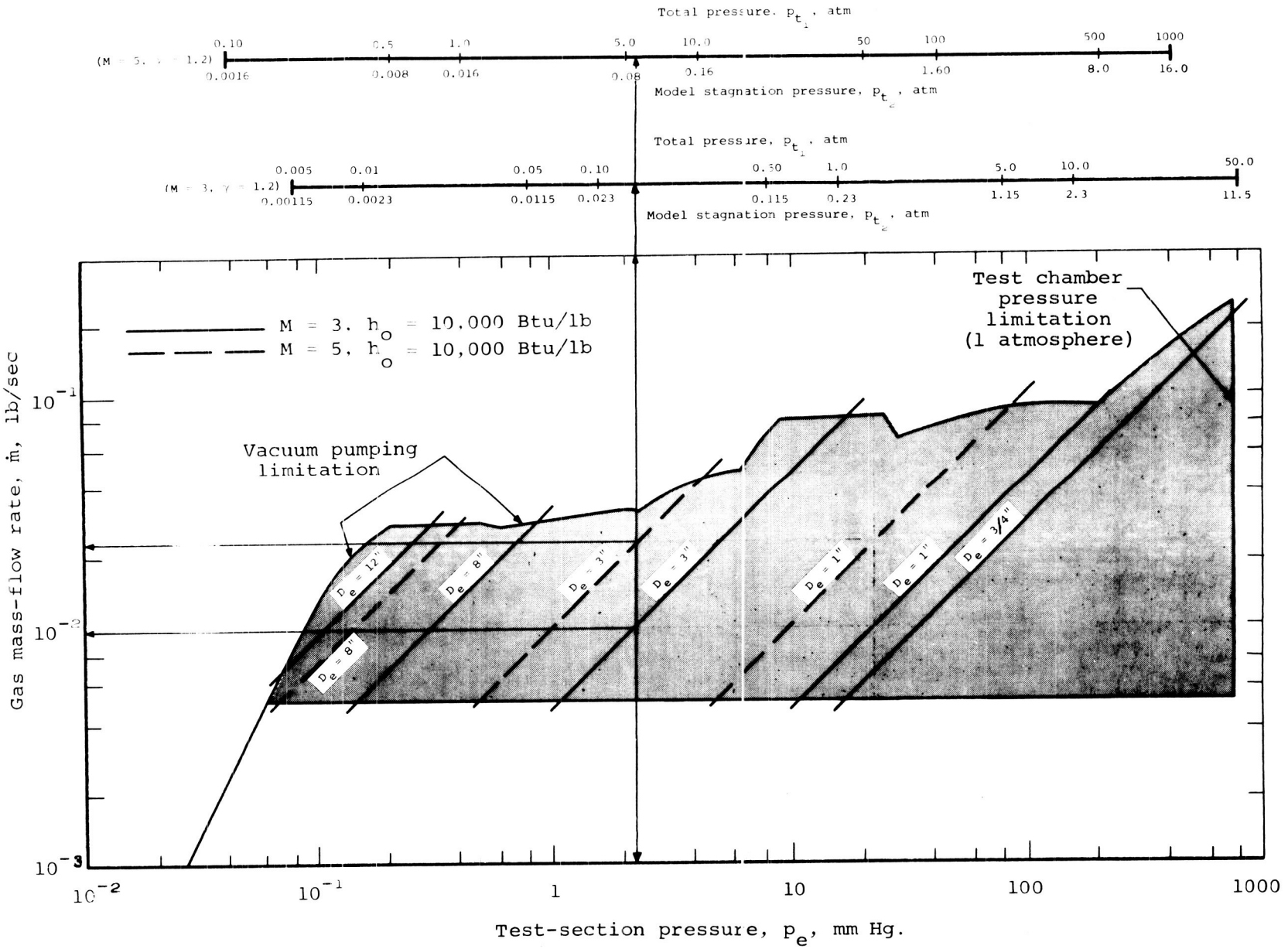


Figure B-7.- Flow characteristics of the Vidya vacuum pumping system.

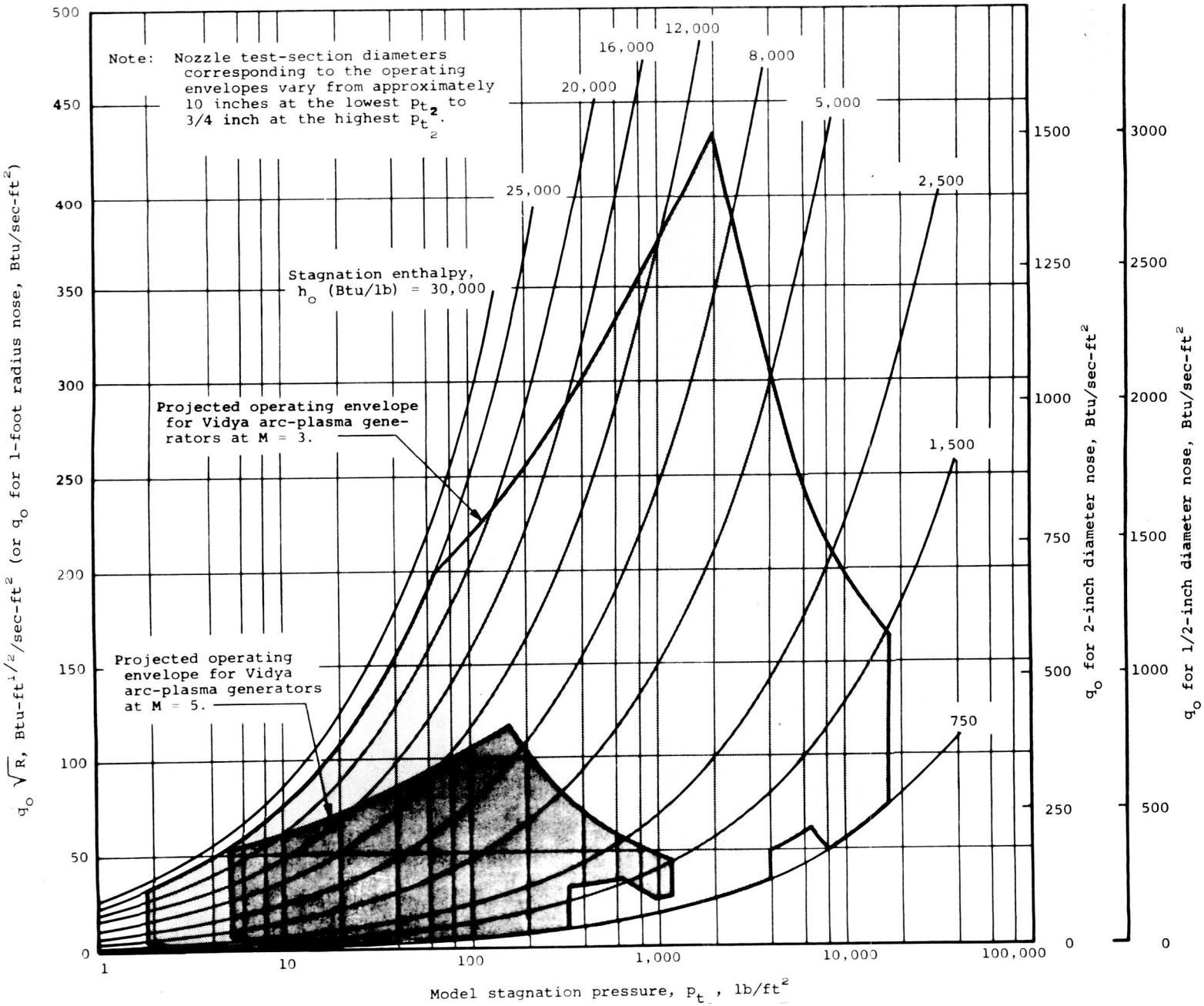


Figure B-8.- Projected stagnation-point heat-flux operating envelopes of Vidya arc-plasma generators at test Mach numbers of 3 and 5.

APPENDIX C

DISTRIBUTION LIST

Contract NAS7-218

NASA Headquarters
Washington, D. C. 20546
Attn: Code RRM/James Gangler (1)
Code RV/Milton B. Ames (1)

NASA Marshall Space Flight Center
Huntsville, Alabama 35812
Attn: Keith Chandler, R-P&VE-PA (1)
Fred Uptagrafft, R-P&VE-ME (1)

NASA Western Operations Office
150 Pico Boulevard
Santa Monica, California 90406
Attn: Office of Technical Information (1)
General Counsel for Patent Matters (1)

NASA Resident Office
Mail Stop 180-603
Jet Propulsion Laboratory
4800 Oak Grove Drive
Pasadena, California 91103
Attn: R. L. McGill, Contracting Officer's Rep. (1)

Chief, Liquid Propulsion Technology, RPL
Office of Advanced Research and Technology
NASA Headquarters
Washington, D. C. 20546
Attn: F. E. Compitello (4)

NASA Scientific and Technical Information Facility
P. O. Box 33
College Park, Maryland 20740 (25)

Mr. Vincent L. Johnson
Director, Launch Vehicles and Propulsion, SV
Office of Space Science and Applications
NASA Headquarters
Washington, D. C. 20546 (1)

Mr. Edward Z. Gray
Director, Advanced Manned Missions, MT
Office of Manned Space Flight
NASA Headquarters
Washington, D. C. 20546 (1)

Mr. Clarence A. Syvertson
Mission Analysis Division
NASA Ames Research Center
Moffett Field, California 24035 (1)

Mr. Erwin A. Edelman,
Technical Monitor
Mail 500-305
NASA Lewis Research Center
21000 Brookpark Road
Cleveland, Ohio 44135 (1)

Mr. J. J. Notardonato
NASA Lewis Research Center
21000 Brookpark Road
Cleveland, Ohio 44135 (1)

NASA Langley Research Center
Langley Station,
Hampton, Virginia 23365
Mail 206/William A. Brooks, Jr. (1)
Mail 214/Robert L. Swain (1)

NASA Ames Research Center
Moffett Field, California 94035
Mail 234-1, Bradford H. Wick (1)
Mail 229-2, Warren Winovich (1)

NASA FIELD CENTERS

Ames Research Center
Moffett Field, California 94035
Attn: Technical Librarian (2)

Goddard Space Flight Center
Greenbelt, Maryland 20771
Attn: Technical Librarian (2)

Jet Propulsion Laboratory
California Institute of Technology
4800 Oak Grove Drive
Pasadena, California 91103
Attn: Technical Librarian (2)

Langley Research Center
Langley Station
Hampton, Virginia 23365
Attn: Technical Librarian (2)

Lewis Research Center
21000 Brookpark Road
Cleveland, Ohio 44135
Attn: Technical Librarian (2)

Marshall Space Flight Center
Huntsville, Alabama 35812
Attn: Technical Librarian (2)

Manned Spacecraft Center
Houston, Texas 77001
Attn: Technical Librarian (2)

Western Operations Office
150 Pico Boulevard
Santa Monica, California 90406
Attn: Technical Librarian (2)

John F. Kennedy Space Center, NASA
Cocoa Beach, Florida 32931
Attn: Technical Librarian (2)

GOVERNMENT INSTALLATIONS

Aeronautical Systems Division
Air Force Systems Command
Wright-Patterson Air Force Base
Dayton, Ohio 45433
Attn: Technical Librarian (1)

Air Force Missile Development Center
Holloman Air Force Base
New Mexico
Attn: Technical Librarian (1)

Air Force Missile Test Center
Patrick Air Force Base, Florida
Attn: Technical Librarian (1)

Air Force Systems Division
Air Force Unit Post Office
Los Angeles 45, California
Attn: Technical Librarian (1)

Arnold Engineering Development Center
Arnold Air Force Station
Tullahoma, Tennessee
Attn: Technical Librarian (1)

Bureau of Naval Weapons
Department of the Navy
Washington, D. C.
Attn: Technical Librarian (1)

Defense Documentation Center Hdqs.
Cameron Station, Building 5
5010 Duke Street
Alexandria, Virginia 22314
Attn: TISIA (1)

Headquarters,
U. S. Air Force
Washington 25, D. C.
Attn: Technical Librarian (1)

Picatinny Arsenal
Dover, New Jersey 07801
Attn: Technical Librarian (1)

Air Force Rocket Propulsion
Laboratory
Research and Technology Division
Air Force Systems Command
Edwards, California 93523
Attn: Technical Librarian (1)

U. S. Atomic Energy Commission
Technical Information Services
Box 62, Oak Ridge, Tennessee (1)
Attn: Technical Librarian (1)

U.S. Army Missile Command
Redstone Arsenal
Alabama 35809
Attn: Technical Librarian (1)

U.S. Naval Ordnance Test Station
China Lake, California 93557
Attn: Technical Librarian

CPIA

Chemical Propulsion Information
Agency
Applied Physics Laboratory
8621 Georgia Avenue
Silver Spring, Maryland 20910
Attn: Technical Librarian (1)

INDUSTRY CONTRACTORS

Aerojet-General Corporation
P.O. Box 296
Azusa, California 91703
Attn: Technical Librarian (1)

Aerojet-General Corporation
P.O. Box 1947
Sacramento, California 95809
Attn: Technical Librarian,
Bldg. 2015, Dept. 2410 (1)

Aeronautronic
Philco Corporation
Ford Road
Newport Beach, California 92663
Attn: Technical Librarian (1)

Aerospace Corporation
2400 East El Segundo Boulevard
P.O. Box 95085
Los Angeles, California 90045
Attn: Technical Librarian (1)

Arthur D. Little, Inc.
20 Acorn Park
Cambridge, Massachusetts 02140
Attn: Technical Librarian (1)

Astropower Laboratory
Douglas Aircraft Company
2121 Paularino
Newport Beach, California 92663
Attn: Technical Librarian (1)

Astrosystems International, Inc.
1275 Bloomfield Avenue
Fairfield, New Jersey 07007
Attn: Technical Librarian (1)

Atlantic Research Corporation
Edsall Road and Shirley Highway
Alexandria, Virginia 22314
Attn: Technical Librarian (1)

Beech Aircraft Corporation
Boulder Division
Box 631
Boulder, Colorado
Attn: Technical Librarian (1)

Bell Aerosystems Company
P. O. Box 1
Buffalo, New York 14240
Attn: Technical Librarian (1)

Bendix Systems Division
Bendix Corporation
3300 Plymouth Road
Ann Arbor, Michigan
Attn: Technical Librarian (1)

Boeing Company
P. O. Box 3707
Seattle, Washington 98124
Attn: Technical Librarian (1)

Missile Division
Chrysler Corporation
P.O. Box 2628
Detroit, Michigan 48231
Attn: Technical Librarian (1)

Wright Aeronautical Division
Curtiss-Wright Corporation
Wood-Ridge, New Jersey 07075
Attn: Technical Librarian (1)

Missile and Space Systems Division
Douglas Aircraft Company, Inc.
3000 Ocean Park Boulevard
Santa Monica, California 90406
Attn: Technical Librarian (1)

Aircraft Missiles Division
Fairchild Hiller Corporation
Hagerstown, Maryland 10
Attn: Technical Librarian (1)

General Dynamics/Astronautics
Library & Information Services(128-00)
P.O. Box 1128
San Diego, California 92112
Attn: Technical Librarian (1)

Re-Entry Systems Department
General Electric Company
3198 Chestnut Street
Philadelphia, Pennsylvania 19101
Attn: Technical Librarian (1)

Advanced Engine & Technology Dept.
General Electric Company
Cincinnati, Ohio 45215
Attn: Technical Librarian (1)

Grumman Aircraft Engineering Corp.
Bethpage, Long Island, New York
Attn: Technical Librarian (1)

Ling-Temco-Vought Corporation
Astronautics
P.O. Box 5907
Dallas, Texas 75222
Attn: Technical Librarian (1)

Lockheed California Company
2555 North Hollywood Way
Burbank, California 91503
Attn: Technical Librarian (1)

Lockheed Missiles and Space Company
P. O. Box 504
Sunnyvale, California 94088
Attn: Technical Information Center (1)

Lockheed Propulsion Company
P. O. Box 111
Redlands, California 92374
Attn: Technical Librarian (1)

The Marquardt Corporation
16555 Saticoy Street
Van Nuys, California 91409
Attn: Technical Librarian (1)

Baltimore Division
Martin Marietta Corporation
Baltimore, Maryland 21203
Attn: Technical Librarian (1)

Denver Division
Martin Marietta Corporation
P. O. Box 179
Denver, Colorado 80201
Attn: Technical Librarian (1)

McDonnell Aircraft Corporation
P. O. Box 516
Municipal Airport
St. Louis, Missouri 63166
Attn: Technical Librarian (1)

Space & Information Systems Division
North American Aviation, Inc.
12214 Lakewood Boulevard
Downey, California
Attn: Technical Librarian (1)

Rocketdyne
North American Aviation, Inc.
6633 Canoga Avenue
Canoga Park, California 91304
Attn: Library (586-306) (1)

Northrop Space Laboratories
3401 West Broadway
Hawthorne, California
Attn: Technical Librarian (1)

Astro-Electronics Division
Radio Corporation of America
Princeton, New Jersey 08540
Attn: Technical Librarian (1)

Reaction Motors Division
Thiokol Chemical Corporation
Denville, New Jersey 07832
Attn: Technical Librarian (1)

Republic Aviation Corporation
Farmingdale Long Island, New York
Attn: Technical Librarian (1)

Space General Corporation
9200 East Flair Avenue
El Monte, California 91734
Attn: Technical Librarian (1)

Stanford Research Institute
333 Ravenswood Avenue
Menlo Park, California 94025
Attn: Technical Librarian (1)

TRW Systems Group
TRW, Incorporated
One Space Park
Redondo Beach, California 90278
Attn: Technical Librarian (1)

TAPCO Division
TRW, Incorporated
23555 Euclid Avenue
Cleveland, Ohio 44117
Attn: Technical Librarian (1)

Thiokol Chemical Corporation
Huntsville Division
Huntsville, Alabama
Attn: Technical Librarian (1)

Research Laboratories
United Aircraft Corporation
400 Main Street
East Hartford, Connecticut 06108
Attn: Technical Librarian (1)

United Technology Center
587 Mathilda Avenue
P. O. Box 358
Sunnyvale, California 94088
Attn: Technical Librarian (1)

Aerospace Operations
Walter Kidde and Company, Inc.
567 Main Street
Belleville, New Jersey 07109
Attn: Technical Librarian (1)

Florida Research and Development
Pratt and Whitney Aircraft
United Aircraft Corporation
P. O. Box 2691
West Palm Beach, Florida 33402
Attn: Technical Librarian

Rocket Research Corporation
520 South Portland Street
Seattle, Washington 98108
Attn: Technical Librarian

Texaco Experiment Inc.
P. O. Box 1-T
Richmond, Virginia 23202
Attn: Technical Librarian